universität wien

DISSERTATION / DOCTORAL THESIS

Titel der Dissertation / Title of the Doctoral Thesis

„Electron-Phonon Interactions Using the Projector-Augmented-Wave Method“

verfasst von / submitted by

Manuel Engel, BSc MSc

angestrebter akademischer Grad / in partial fulfilment of the requirements for the degree of

Doktor der Naturwissenschaften (Dr. rer. nat.)

Wien, 2023 / Vienna, 2023

Studienkennzahl lt. Studienblatt / degree programme code as it appears on the student record sheet:	A 796 605 411
Dissertationsgebiet lt. Studienblatt / field of study as it appears on the student record sheet:	Physik
Betreut von / Supervisor:	Univ.-Prof. Dipl.-Ing. Dr. Georg Kresse
Mitbetreut von / Co-Supervisor:	

Acknowledgements

This project would have not been possible, were it not for the unwavering support of numerous individuals. First and foremost, I want to express my utmost gratitude towards my supervisors, Georg Kresse and Martijn Marsman. They have given me invaluable guidance toward reaching my goal and have blessed me and many of my colleagues with a pleasant yet exciting working environment.

From the bottom of my heart, I also thank my peers and research collaborators, who have made me feel welcome and valued while providing meaningful scientific feedback. Through countless discussions, they have significantly deepened my understanding in the field and improved the quality of my work. In particular, I want to thank Henrique Miranda for providing so much support and guidance. Additionally, I am grateful to Menno Bokdam who, over many years, was a mentor figure to me in more ways than one. Special thanks go to everyone who has proofread my thesis.

I express my sincerest gratitude also to my family and friends who have continuously supported me throughout this challenging journey. Especially my loving wife, Beate Reichl, and my best friend, Maximilian Liebetreu, have never stopped being a constant source of inspiration, motivation and reassurance. I am eternally grateful to be surrounded by such caring individuals.

Finally, I thank the Austrian Science Fund (FWF) for funding parts of this project.

Contents

CHAPTER 1

Introduction

Within the vast and sprawling research area that is condensed-matter physics, few fields are as crucial for our understanding of the physical world as electron-phonon interactions. They underpin many physical phenomena at both zero and finite temperature, from electrical conductivity, thermal conductivity, even superconductivity to optical properties, thermoelectricity and polarons. Alongside the many theoretical accomplishments, the numerical simulation of electron-phonon interactions from first principles, or ab-initio, has become a powerful tool to predict material properties for researchers and engineers. Research in this area has led to countless innovations and the development of new technologies, such as for batteries [1, 2], solar cells [3, 4], organic electronics [5] and thermoelectrics [6–9]. The hunt for ever more efficient and accurate computational techniques is fueled by a rising demand for greater predictive power. It is in this tantalizing research area that this work aims to contribute.

1.1 Band-Structure Renormalization

A key quantity that is affected by electron-phonon interactions is the electronic band structure of solids. It governs many of the important physical properties of the system, such as electrical conductivity, optical absorption and chemical reactivity. Basically, the electronic band structure describes the allowed energy levels of electronic states in the material. In an extended system, such as in solids, these states cover a continuous range of energies, so-called bands. The bands are separated by band gaps, energy ranges where no electronic states are allowed. Depending on the presence, size and location of a band gap in relation to the Fermi level, materials can be grouped into three broad categories: metals, semiconductors and insulators. An example band structure is shown in Fig. 1.1 for the case of LiF, a prototypical insulator featuring a wide band gap.

Semiconductors feature a comparatively small band gap at the Fermi level. These materials have unique electrical and optical properties that have made

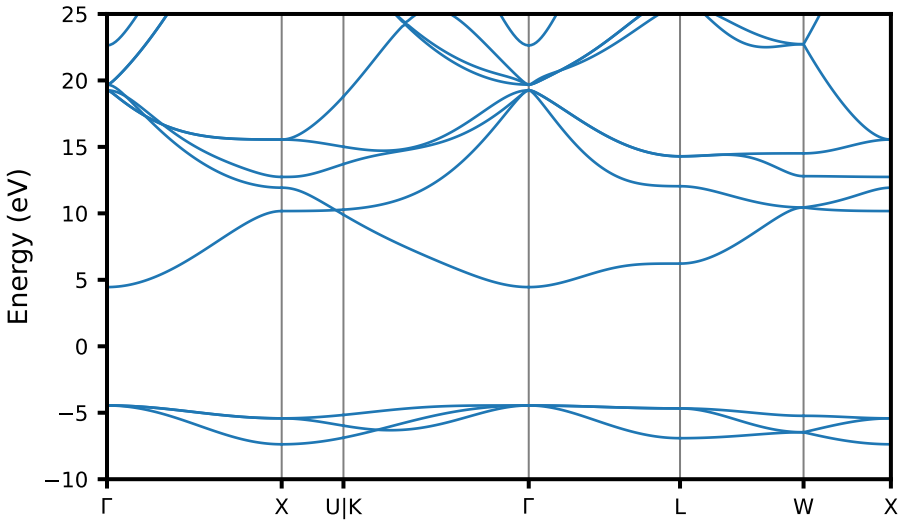

Figure 1.1: Electronic band structure of LiF obtained from density-functional theory (DFT) (see Section 2.1). The bands are plotted along high-symmetry lines (see Fig. 2.2b). The zero of the energy scale is shifted to the Fermi energy lying mid gap. Shown are the three highest-lying states of the valence band and the lowest-lying states of the conduction band.

them indispensable to modern solid-state devices. As the name implies, they have an electrical conductivity that lies somewhere between that of metals and insulators. The electrical conductivity can be tuned by introducing impurities through a process known as doping. This is exploited in diodes and transistors, the building blocks of modern microelectronics. Additionally, the size of the band gap in these materials is often in the range of visible light, making them an attractive option for optoelectronics. It is hard to overemphasize the importance of semiconductor devices in modern technology. They range from light-emitting diodes to lasers, solar cells, batteries and integrated circuits.

Given the prevalence of gapped materials in modern technology, it is only natural that great effort is put into improving the accuracy of ab-initio calculations of the electronic band gap. However, this has proven to be a difficult challenge. For example, implementations based on the popular DFT are prone to underestimating the band gap. This point is discussed in more detail in Section 2.1. An improved band structure can be obtained by including electron-electron interactions using the *GW* method [10–12]. However, these quasiparticle corrections do not account for finite-temperature effects and lattice vibrations. That is the realm of electron-phonon interactions. They explain to a large degree the temperature dependence of the electronic band structure [13–21]. Moreover, even at absolute-zero temperature, quantum-mechanical zero-point vibrations of the crystal lattice affect the band structure. This is known as zero-point renormalization (ZPR). Depending on the material, the ZPR can yield a significant contribu-

tion to the electronic band gap [17–24]. As an example, Fig. 1.2 shows the ZPR of the band gap of diamond. In this case, the ZPR of the indirect band gap is about

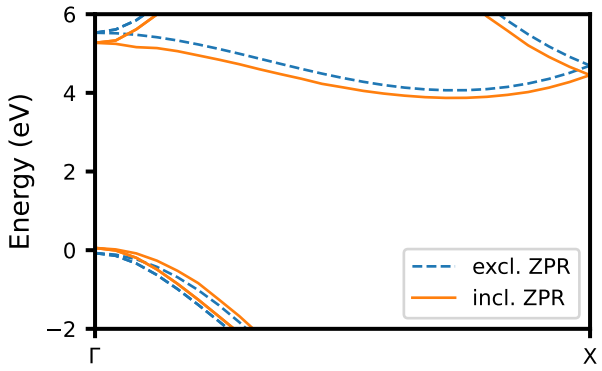

Figure 1.2: Electronic band structure of diamond showing its indirect band gap. Dashed blue lines neglect electron-phonon interactions. Orange lines are renormalized by the ZPR up to second-order in the electron-phonon interaction (see Chapter 4). The size of the band-gap ZPR is about 8 %. The bands are plotted along the $\overline{\Gamma X}$ high-symmetry line (see Fig. 2.2b). The zero of the energy scale is shifted to the Fermi energy.

323 meV, which amounts to about 8 % of the total gap.

In this work, we study the renormalization of the electronic band structure of semiconductors and insulators due to electron-phonon interactions. This interaction is rigorously described in many-body perturbation theory [25], where electrons and phonons interact locally by exchanging momentum. The coupling strength or probability of this fundamental scattering process is given by the electron-phonon matrix element. The goal of the present work is in no small part directly linked to the computation of this quantity from first principles. Ultimately, once the electron-phonon matrix element is known, a plethora of additional observables can be calculated from it. This includes electron and phonon quasiparticle lifetimes, spectral functions and contributions to electrical and heat transport.

1.2 Outline

Starting from theoretical considerations, we build a numerical implementation of electron-phonon interactions that is firmly integrated into the Vienna Ab-initio Software Package (VASP) [26–29]. During the Master thesis Ref. [30], we already undertook an initial implementation effort. However, there are numerous aspects to expand upon.

One of the greatest challenges is to formulate the electron-phonon problem in the framework of the projector-augmented-wave (PAW) method. The PAW method was introduced by Blöchl in 1994 [31] as a way to treat valence electrons

similar to pseudopotential methods. It offers a superior compromise between computational performance and accuracy. The PAW method is an integral part of VASP [32] that we can utilize for the treatment of electron-phonon interactions. Currently, two complementary formulations of the electron-phonon interaction exist in the PAW framework [33, 34]. In addition to the implementation of these two approaches, we provide new theoretical insights relating the two that are supported by numerical evidence [35].

In order to improve the computational performance of calculating electron-phonon matrix elements, we utilize an interpolation scheme first introduced by Giustino *et al.* in 2007 [36, 37]. It relies on the unique spatial properties of localized Wannier orbitals [38, 39]. Interpolation techniques are tried and tested staples in electron-phonon calculations [18, 40–43].

Another aspect of electron-phonon interactions that needs to be accounted for are long-range electrostatic contributions arising from longitudinal optical lattice vibrations in polar materials. Based on early considerations by Vogl [44], Fröhlich [45] developed a model that describes these contributions as an effective coupling strength. Due to the long-range nature of the phenomenon, it is difficult to capture using interpolation techniques. Verdi and Giustino [46] as well as Sjakste *et al.* [47] later independently developed a generalization of the Fröhlich model to the electron-phonon matrix element that captures the electrostatic dipole interaction. This can be used to amend the interpolation scheme in most cases. An extension to quadrupole interactions was recently covered by Brunin *et al.* [48], Jhalani *et al.* [49] and Park *et al.* [50].

An important factor that distinguishes different electron-phonon implementations is how the phonon perturbation is calculated. A popular choice is density-functional perturbation theory (DFPT) [51], a perturbative approach that operates within the unit cell of the crystal lattice. While we also seek to treat the electron-phonon interactions perturbatively, we instead opt to use large supercells. In this case, the phonon perturbation is computed using finite atomic displacements. The advantage of this is twofold. First, finite-displacement methods are comparatively simple to implement. Second, they allow the use of more complicated exchange-correlation functionals with minor additional effort.

There are alternative supercell-based approaches to calculate the renormalization of the electronic band gap. These include Monte-Carlo simulations [52, 53] and molecular dynamics [54, 55]. Both of these categories are stochastic methods that can reach excellent numerical accuracy in exchange for long computation times. There are also adiabatic supercell approaches that rely on specifically chosen, frozen atomic displacements [15–17, 56–59]. These have the advantage that they implicitly include selected higher-order contributions to the electron-phonon interaction. They can also readily be applied to beyond-DFT methods [58]. However, despite their advantages, these methods are usually restricted to the adiabatic regime. This means that they neglect the energy transfer between electrons and phonons during emission or absorption. In addition, due to the aforementioned long-range electrostatic effects, it can be difficult to reach

convergence with respect to the supercell size in polar materials.

The theoretical and numerical research work accumulates in two publications. In the first one, we demonstrate the use of the Wannier-based electron-phonon implementation to calculate the ZPR and temperature dependence of the electronic band structure. For the second publication, an alternative implementation is used. Instead of relying on Wannier orbitals, this approach interpolates only the electron-phonon potential starting from a supercell. The electronic orbitals are obtained from an exact diagonalization of the Hamiltonian in the unit cell. This way, we are able to make accurate statements about the convergence of the ZPR with respect to the number of intermediate states, compare different PAW formulations and test various pseudopotentials in the context of electron-phonon interactions.

The present work is written using the Gaussian cgs unit system and is structured as follows. In Chapter 2, we present the basic concepts of electronic band theory. We show how the complex many-body problem of interacting electrons can be simplified using the famous Kohn-Sham (KS) DFT. In addition, we focus on the technical aspects of dealing with many electrons in practice using the PAW method. As mentioned earlier, the integration of electron-phonon interactions with the PAW method is an integral part of this work.

In Chapter 3, we give a short introduction to the theory of harmonic lattice vibrations. The term phonon refers to the quasiparticle associated with the quantization of these lattice vibrations. We present an interpolation scheme based on the matrix of interatomic force constants (IFC) to obtain the phonon spectrum. Particular emphasis is placed on long-range electrostatic contributions to phonon spectra in polar materials.

Chapter 4 introduces the electron-phonon interaction from the perspective of many-body perturbation theory. We derive two distinct formulations of this problem in the PAW framework and describe their differences. This is the core theoretical aspect of this work. Furthermore, we discuss the treatment of long-range electrostatic effects in this context.

In Chapter 5, we introduce Wannier orbitals. They provide an alternative representation of electronic orbitals in terms of localized functions in real space. We describe how to use their unique spatial properties to interpolate the electronic band structure as well as electron-phonon matrix elements. The interpolation scheme is extended to polar materials.

The numerical results obtained in the scope of this work are summarized in Chapter 6. This includes the two previously mentioned publications on the renormalization of the electronic band structure due to electron-phonon effects. Additionally, we report as yet unpublished results.

Finally, in Chapter 7, we present the conclusion to the research project. After commenting on the achievements and shortcomings of the present work, we establish possible future goals. Hopefully, this work can act as a solid stepping stone for future endeavors.

CHAPTER 2

Electrons in Extended Systems

The dynamics of any closed non-relativistic quantum system are governed entirely by the famous Schrödinger equation,

$$\hat{H}\Psi = \mathrm{i}\hbar\frac{\partial}{\partial t}\Psi. \tag{2.1}$$

Using its time-independent form,

$$\hat{H}\Psi = E\Psi, \tag{2.2}$$

one can in principle find the ground state of any system by minimizing the energy, E. This includes the field of condensed-matter physics, where the electrons and ions interact to form a dense material. Once the ground-state solution has been obtained, a wide variety of material properties can be calculated with great accuracy. One might consider this to be the holy grail of material-physics simulations.

Simple as it may seem, however, solving the Schrödinger equation has proven to be a monumental challenge. This is due to the high complexity encoded in the many-body wave function, Ψ. For a system with N_e electrons and N_n ions, the wave function can be formulated in terms of their position coordinates, $\mathbf{r}_i$ and $\mathbf{R}_i$, respectively:

$$\Psi = \Psi(\mathbf{r}_1, \dots, \mathbf{r}_{N_\mathrm{e}}, \mathbf{R}_1, \dots, \mathbf{R}_{N_\mathrm{n}}). \tag{2.3}$$

For a system with sufficiently many particles, this becomes impossible to handle by any modern computer. Naturally, this is a problem if one wants to simulate an extended system containing thousands of electrons. As such, great effort has been devoted to finding adequate approximations to the general many-body problem.

2.1 Density-Functional Theory

A particularly successful approach to solving the Schrödinger equation in the field of condensed-matter physics is DFT. Even decades after its inception, DFT

plays a pivotal role at the forefront of ab-initio simulations. Due to its simplicity and unmatched computational performance, DFT has managed to remain relevant and is without a doubt the most widespread computational method to predict material properties.

2.1.1 Born-Oppenheimer Approximation

The dynamics of a coupled electron-ion system are described by the Hamiltonian

$$\hat{H}_{\mathrm{en}} = -\sum_{i}^{N_{\mathrm{e}}} \frac{\hbar^2 \Delta_i}{2m_{\mathrm{e}}} - \sum_{i}^{N_{\mathrm{n}}} \frac{\hbar^2 \Delta_i}{2m_i} + \frac{1}{2}\sum_{i}^{N_{\mathrm{e}}}\sum_{j\neq i}^{N_{\mathrm{e}}} \frac{e^2}{|\mathbf{r}_i - \mathbf{r}_j|} + \frac{1}{2}\sum_{i}^{N_{\mathrm{n}}}\sum_{j\neq i}^{N_{\mathrm{n}}} \frac{e^2 Z_i Z_j}{|\mathbf{R}_i - \mathbf{R}_j|} - \sum_{i}^{N_{\mathrm{e}}}\sum_{j}^{N_{\mathrm{n}}} \frac{e^2 Z_j}{|\mathbf{r}_i - \mathbf{R}_j|}, \quad (2.4)$$

where m_{e} is the electron mass and e is the elementary charge. m_i and Z_i are the mass and atomic number of ion i, respectively. Eq. (2.4) features an electron-electron, an ion-ion as well as an electron-ion term. Most of the time, however, the dynamics of the ions develop on a much larger timescale than the dynamics of the electrons. This is directly related to the large difference between m_{e} and a typical nuclear mass, m_i. In this case, it is customary to replace the full many-body wave function with a product between an electronic wave function, $\Psi_{\mathrm{e}}(\mathbf{r}_1, \ldots, \mathbf{r}_{N_{\mathrm{e}}})$, and an ionic wave function, $\Psi_{\mathrm{n}}(\mathbf{R}_1, \ldots, \mathbf{R}_{N_{\mathrm{n}}})$. This is the well-known *Born-Oppenheimer* approximation, which decouples the electronic and ionic subsystems. The electronic Hamiltonian in the Born-Oppenheimer approximation is given as

$$\hat{H}_{\mathrm{BO}} = -\sum_{i}^{N_{\mathrm{e}}} \frac{\hbar^2 \Delta_i}{2m_{\mathrm{e}}} + \frac{1}{2}\sum_{i}^{N_{\mathrm{e}}}\sum_{j\neq i}^{N_{\mathrm{e}}} \frac{e^2}{|\mathbf{r}_i - \mathbf{r}_j|} - \sum_{i}^{N_{\mathrm{e}}}\sum_{j}^{N_{\mathrm{n}}} \frac{e^2 Z_j}{|\mathbf{r}_i - \mathbf{R}_j|}, \quad (2.5)$$

where the nuclear coordinates, $\mathbf{R}_i$, are considered external parameters. In this sense, the electron-ion interaction is described by an effective nuclear potential generated by the charged ions, i.e., the final term in Eq. (2.5).

2.1.2 Hohenberg-Kohn Theorems

The Born-Oppenheimer approximation is a powerful first step in reducing the complexity of the problem. However, the key insight that lays the foundation for DFT is provided by the Hohenberg-Kohn theorems [60]. Let $n(\mathbf{r})$ be the density of a system of N_{e} interacting electrons in an external potential, $V_{\mathrm{ext}}(\mathbf{r})$. Then the following statements hold:

Theorem 1 *$V_{ext}[n(\mathbf{r})]$ is a unique functional. It follows that the Hamiltonian and its spectrum are also uniquely determined by the ground-state density, $n_0(\mathbf{r})$.*

Theorem 2 *$n_0(\mathbf{r})$ minimizes the total-energy functional,*

$$E[n(\mathbf{r})] = F[n(\mathbf{r})] + \int \mathrm{d}^3 r\, V_{ext}(\mathbf{r}) n(\mathbf{r}), \tag{2.6}$$

where $F[n(\mathbf{r})]$ is a universal functional.

Together, the Hohenberg-Kohn theorems imply that all ground-state properties of a system are uniquely determined by the ground-state *density*, $n(\mathbf{r})$. Additionally, the ground-state density can be found by minimizing a universal density functional. Universality in this case means that $F[n(\mathbf{r})]$ does not depend on $V_{\mathrm{ext}}(\mathbf{r})$.

A profound consequence of the Hohenberg-Kohn theorems is that solving the time-independent Schrödinger equation in terms of a many-body wave function is exactly equivalent to finding the ground-state density of the electrons. As the name implies, this is the central idea behind DFT. Compared to the many-body wave function, the density is a much less complicated object, having only three spatial dimensions. All the complexity of the problem, including non-local exchange and correlation effects, is now essentially encoded within the universal functional, $F[n(\mathbf{r})]$. Unfortunately, the exact form of $F[n(\mathbf{r})]$ is unknown. In practice, one has to rely on various approximation strategies.

As a small side note, DFT is not restricted to electrons but extends to all kinds of fermions and bosons. It is in principle an exact reformulation of the many-body problem of interacting particles in an external potential. The practical limitations of DFT arise largely due to approximations of $F[n(\mathbf{r})]$.

2.1.3 Kohn-Sham Equations

In 1965, Kohn and Sham reformulated the DFT total-energy functional such that practical calculations based on DFT became possible. Even today, KS DFT is the most successful and widely used formulation of DFT and acts as the basis for more advanced approaches.

In KS DFT, the fully interacting system is first mapped onto an auxiliary system of non-interacting electrons such that the respective ground-state densities are identical. Each single-particle state is represented as a KS orbital, $|\psi_i\rangle$. The density is then simply given as

$$n(\mathbf{r}) = \sum_i^{N_\mathrm{e}} \langle\psi_i|\mathbf{r}\rangle \langle\mathbf{r}|\psi_i\rangle = \sum_i^{N_\mathrm{e}} |\psi_i(\mathbf{r})|^2, \tag{2.7}$$

where $\psi_i(\mathbf{r})$ is the real-space representation of the respective KS orbital. Having a basis comprised of single-particle states also leads to a trivial form of the kinetic-energy functional of the non-interacting KS electrons:

$$T_{\mathrm{KS}} = -\frac{\hbar^2}{2m_\mathrm{e}} \sum_i^{N_\mathrm{e}} \langle\psi_i|\Delta|\psi_i\rangle\,. \tag{2.8}$$

The kinetic energy, together with the well-known electrostatic Hartree energy,

$$E_{\mathrm{H}}[n(\mathbf{r})] = \frac{e^2}{2} \iint \mathrm{d}^3 r \; \mathrm{d}^3 r' \; \frac{n(\mathbf{r}) n(\mathbf{r}')}{|\mathbf{r} - \mathbf{r}'|}, \tag{2.9}$$

can be extracted from the universal density functional,

$$F[n(\mathbf{r})] = T_{\mathrm{KS}}[n(\mathbf{r})] + E_{\mathrm{H}}[n(\mathbf{r})] + E_{\mathrm{xc}}[n(\mathbf{r})], \tag{2.10}$$

where $E_{\mathrm{xc}}[n(\mathbf{r})]$ is known as the exchange-correlation functional. Essentially, $E_{\mathrm{xc}}[n(\mathbf{r})]$ contains all remaining non-classical contributions, such as exchange and correlation energy, that are not captured by $T_{\mathrm{KS}}[n(\mathbf{r})]$ and $E_{\mathrm{H}}[n(\mathbf{r})]$.

At this point, minimization of the total-energy functional in Eq. (2.6) leads to the famous KS equations:

$$\hat{H}_{\mathrm{KS}} |\psi_i\rangle = \left(-\frac{\hbar^2 \Delta}{2 m_{\mathrm{e}}} + v_{\mathrm{KS}}(\mathbf{r}) \right) \psi_i(\mathbf{r}) = \varepsilon_i \psi_i(\mathbf{r}), \tag{2.11}$$

where the effective KS potential,

$$v_{\mathrm{KS}}(\mathbf{r}) \equiv V_{\mathrm{ext}}(\mathbf{r}) + v_{\mathrm{H}}(\mathbf{r}) + v_{\mathrm{xc}}(\mathbf{r}), \tag{2.12}$$

is the sum of the external potential, $V_{\mathrm{ext}}(\mathbf{r})$, the Hartree potential,

$$v_{\mathrm{H}}(\mathbf{r}) \equiv \frac{\delta E_{\mathrm{H}}[n(\mathbf{r})]}{\delta n(\mathbf{r})} = e^2 \int \mathrm{d}^3 r' \; \frac{n(\mathbf{r}')}{|\mathbf{r} - \mathbf{r}'|}, \tag{2.13}$$

and the exchange-correlation potential,

$$v_{\mathrm{xc}}(\mathbf{r}) \equiv \frac{\delta E_{\mathrm{xc}}[n(\mathbf{r})]}{\delta n(\mathbf{r})}. \tag{2.14}$$

The derivatives appearing in Eqs. (2.13) and (2.14) are understood as functional derivatives with respect to the density. The total energy functional that needs to be minimized can be expressed as follows:

$$E[n(\mathbf{r})] = \sum_i^{N_{\mathrm{e}}} \varepsilon_i - E_{\mathrm{H}}[n(\mathbf{r})] + E_{\mathrm{xc}}[n(\mathbf{r})] - \int \mathrm{d}^3 r \, v_{\mathrm{xc}}(\mathbf{r}) n(\mathbf{r}). \tag{2.15}$$

Due to Eq. (2.7), everything that depends on the density also implicitly depends on the KS orbitals. Therefore, Eq. (2.11) can be solved self-consistently to obtain the KS orbitals, $|\psi_i\rangle$, and KS eigenvalues, ε_i, which allows us to calculate the density using Eq. (2.7). In other words, the variational quantities in KS DFT are the KS orbitals. The eigenvalues will be discussed in more detail in the context of the electronic band structure in Section 2.3.

The introduction of the KS equations has transformed the complicated many-body problem into a system of independent particles moving in an effective potential. The only approximation at this point is the Born-Oppenheimer approximation. Otherwise, DFT is in principle an exact theory. However, there is one remaining issue that needs to be addressed.

The exchange-correlation energy, E_{xc}, contains the unknown parts of the universal density functional. To this day, its exact form remains a mystery. Therefore, one has to rely on approximations for E_{xc}. The history of KS DFT is in a way directly linked to the history of density-functional approximations. Ever since its inception, the success of DFT was driven by an ever-expanding library of more accurate exchange-correlation functionals. However, it has proven to be exceedingly difficult to make systematic improvements upon prior approximations. Here, we briefly mention the two most basic functionals that are still in widespread use today, but refrain from going into detail.

The earliest approximation to E_{xc} is the local-density approximation (LDA). It is based on the uniform electron gas. The idea is that, at each point in space, the exchange-correlation energy density is locally approximated to be the same as for the uniform electron gas with the same electron density. The exchange part is known analytically [61], whereas the correlation part can be based on sophisticated Monte-Carlo simulations [62, 63]. This approximation works surprisingly well.

Another popular choice is the so called generalized-gradient approximation (GGA). The GGA was designed to improve upon the LDA by also introducing the local gradient of the electron density in the exchange-correlation functional. Many different GGA functionals exist that are built upon this concept. A particularly popular flavor of GGA functional is the one proposed by Perdew, Burke and Ernzerhof (PBE) [64, 65]. This is the exchange-correlation functional of choice for the majority of this work.

2.2 Bloch Orbitals

Up until this point, we considered a scenario where the electrons move in an external potential, V_{ext}, generated by a *general* arrangement of nuclei. However, in this work we are interested in solids, which we idealize as infinitely extended periodic systems. The ionic structure of such a system can be described by a Bravais lattice, such that each ion has a position $\mathbf{R}_{l\kappa} = \mathbf{R}_l + \boldsymbol{\tau}_\kappa$. $\mathbf{R}_l$ is the position of the primitive unit cell l and $\boldsymbol{\tau}_\kappa$ is the relative position of the ion κ within the basis of that cell. This is illustrated in Fig. 2.1. The set of all lattice points $\mathbf{R}_l$ comprises the direct lattice.

A primitive unit cell is any unit cell spanned by three lattice vectors, $\mathbf{a}_1$, $\mathbf{a}_2$ and $\mathbf{a}_3$, such that it contains exactly one lattice point, $\mathbf{R}_l$, while obeying the translational symmetries of the crystal. The volume $V_{\text{pc}} = \mathbf{a}_1 \cdot (\mathbf{a}_2 \times \mathbf{a}_3)$ of the primitive unit cell is the smallest of any possible unit cell. Fig. 2.2a shows the conventional unit cell for a face-centered cubic (fcc) lattice together with a possible choice for the primitive lattice vectors. The fcc lattice is an important Bravais lattice type commonly found in ionic crystals and semiconductors. It is also the underlying lattice type for the diamond and zincblende structures.

Let $\mathbf{R}$ be an arbitrary linear combination of primitive lattice vectors with inte-

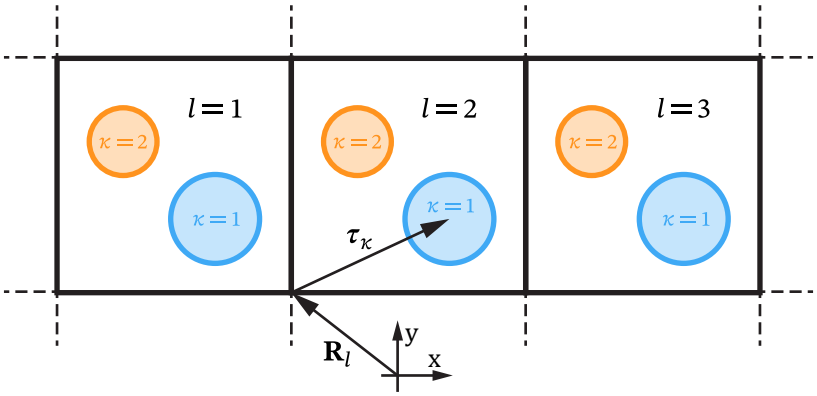

Figure 2.1: Unit cells of a crystal lattice illustrated in two dimensions. The vectors $\mathbf{R}_l$ point to the different unit cells. Orange and blue circles correspond to different atoms in the crystal basis. τ_κ are the basis vectors relative to each unit cell.

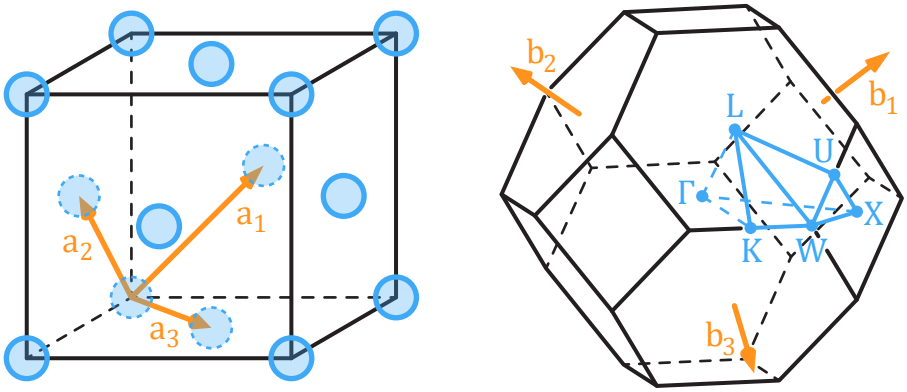

(a) Conventional unit cell of the fcc lattice. Indicated in blue are the positions of the lattice points. A possible choice for the primitive-cell lattice vectors $\mathbf{a}_i$ is shown in orange.

(b) FBZ of the fcc lattice in reciprocal space. The *directions* of the primitive reciprocal-lattice vectors $\mathbf{b}_i$ are indicated in orange. The blue dots are high-symmetry points and are labeled by letters. Γ is at the zone center. The blue lines between the points are high-symmetry lines.

Figure 2.2: Unit cells of the fcc lattice in real and reciprocal space.

ger coefficients. Then, the crystal structure is invariant under translations along $\mathbf{R}$ and so is the nuclear potential, $V_{\text{ext}}(\mathbf{r})$. This has important consequences for the solutions of the KS equations. In particular, we can invoke the Bloch theorem, named after Felix Bloch who introduced the idea in 1929 [66]:

Theorem 3 *The solutions to a single-particle Schrödinger equation with a lattice-*

periodic external potential are of the form

$$\psi_{n\mathbf{k}}(\mathbf{r}) = u_{n\mathbf{k}}(\mathbf{r})e^{i\mathbf{k}\cdot\mathbf{r}}, \tag{2.16}$$

where $u_{n\mathbf{k}}(\mathbf{r}+\mathbf{R}) = u_{n\mathbf{k}}(\mathbf{r})$ *is lattice-periodic.*

We call $|\psi_{n\mathbf{k}}\rangle$ a Bloch orbital, n the band index and $\mathbf{k}$ the Bloch vector. It is quite natural to represent the cell-periodic part of the Bloch orbital in terms of plane waves [67]:

$$u_{n\mathbf{k}}(\mathbf{r}) = \sum_{\mathbf{G}} c_{n\mathbf{k}-\mathbf{G}} \mathrm{e}^{-\mathrm{i}\mathbf{G}\cdot\mathbf{r}}. \tag{2.17}$$

Both $\mathbf{k}$ and $\mathbf{G}$ are vectors in reciprocal space. The former is in general a continuous variable while the latter belongs to the reciprocal lattice. The basis vectors of the reciprocal lattice, $\mathbf{b}_1$, $\mathbf{b}_2$ and $\mathbf{b}_3$, are defined as:

$$\mathbf{b}_1 = \frac{2\pi}{V_{\mathrm{pc}}}\mathbf{a}_2 \times \mathbf{a}_3, \tag{2.18}$$

$$\mathbf{b}_2 = \frac{2\pi}{V_{\mathrm{pc}}}\mathbf{a}_3 \times \mathbf{a}_1, \tag{2.19}$$

$$\mathbf{b}_3 = \frac{2\pi}{V_{\mathrm{pc}}}\mathbf{a}_1 \times \mathbf{a}_2. \tag{2.20}$$

The volume spanned by these three vectors,

$$\Omega_{\mathrm{BZ}} = \frac{(2\pi)^3}{V_{\mathrm{pc}}} = \mathbf{b}_1 \cdot (\mathbf{b}_2 \times \mathbf{b}_3), \tag{2.21}$$

is also the volume of the first Brillouin zone (FBZ), a uniquely determined unit cell that is the Wigner-Seitz cell of the reciprocal lattice [67]. A visualization of the FBZ of the fcc lattice is provided in Fig. 2.2b. An arbitrary reciprocal-lattice vector $\mathbf{G}$ can always be written as a linear combination of the $\mathbf{b}_i$ with integer coefficients, similar to $\mathbf{R}$ for the direct lattice. The reciprocal lattice so defined is dual to the direct lattice:

$$\mathbf{a}_i \cdot \mathbf{b}_j = 2\pi\delta_{ij} \quad \Rightarrow \quad \mathrm{e}^{\mathrm{i}\mathbf{G}\cdot\mathbf{R}} = 1. \tag{2.22}$$

Using the plane-wave representation in Eq. (2.17), we see that the Bloch orbitals are periodic functions in the Bloch vector, $\mathbf{k}$, with respect to the reciprocal lattice:

$$\begin{aligned}\psi_{n\mathbf{k}+\mathbf{G}}(\mathbf{r}) &= \mathrm{e}^{\mathrm{i}\mathbf{k}\cdot\mathbf{r}} \sum_{\mathbf{G}'} c_{n\mathbf{k}+\mathbf{G}-\mathbf{G}'} \mathrm{e}^{-\mathrm{i}(\mathbf{G}'-\mathbf{G})\cdot\mathbf{r}} \\ &= \mathrm{e}^{\mathrm{i}\mathbf{k}\cdot\mathbf{r}} \sum_{\mathbf{G}''} c_{n\mathbf{k}-\mathbf{G}''} \mathrm{e}^{-\mathrm{i}\mathbf{G}''\cdot\mathbf{r}} \\ &= \psi_{n\mathbf{k}}(\mathbf{r}).\end{aligned} \tag{2.23}$$

Consequently, we can restrict the Bloch vector to the FBZ without loss of generality. The Bloch orbitals form an orthogonal set. If we choose

$$\int_{V_{\mathrm{pc}}} \mathrm{d}^3 r \, u^*_{m\mathbf{k}}(\mathbf{r}) u_{n\mathbf{k}}(\mathbf{r}) = \delta_{mn} \tag{2.24}$$

as the normalization convention, then the Bloch orbitals are normalized with respect to the unit cell:

$$\langle \psi_{m\mathbf{k}'} | \psi_{n\mathbf{k}} \rangle = \Omega_{\mathrm{BZ}} \delta_{mn} \delta^{(3)}(\mathbf{k} - \mathbf{k}'). \tag{2.25}$$

In this case, the Bloch orbitals obey the following completeness relation:

$$\sum_n \int_{\Omega_{\mathrm{BZ}}} \frac{\mathrm{d}^3 k}{\Omega_{\mathrm{BZ}}} \, |\psi_{n\mathbf{k}}\rangle \langle \psi_{n\mathbf{k}}| = \mathbb{1}, \tag{2.26}$$

where n runs over all occupied *and* unoccupied bands. The integration boundary, Ω_{BZ}, indicates that the integral is taken over the FBZ.

As a side remark, we like to mention that, in addition to the global phase freedom inherent to all quantum systems, Bloch orbitals exhibit additional *local* phase freedom. In other words, if $|\psi_{n\mathbf{k}}\rangle$ is a solution to the Schrödinger equation and $\varphi(\mathbf{k})$ is an arbitrary $\mathbf{k}$-dependent phase, then $|\psi_{n\mathbf{k}}\rangle \, \varphi(\mathbf{k})$ is an equally valid solution. In particular, there are no continuity requirements on the complex phase, $\varphi(\mathbf{k})$.

The Bloch orbitals offer a natural way of representing the solutions to the KS equations, Eq. (2.11), for solids. In the case of an infinitely extended system, $\mathbf{k}$ is a continuous variable confined to the FBZ. In this context, $\mathbf{k}$ is sometimes interpreted as the momentum of a single-particle electron state. This provides an intuitive description for the electronic single-particle states, being characterized by a band index n and a crystal momentum, $\mathbf{k}$. However, we like to remind of the fact that the fictitious KS states obtained by solving Eq. (2.11) are just that, fictitious. They do not correspond to true eigenstates of the momentum operator.

The use of Bloch orbitals as solutions to the KS equations can act as the basis for numerical implementations of DFT. Let us exemplify the core idea on the electronic charge density, $n(\mathbf{r})$. The completeness relation in Eq. (2.26) allows us to write the density in terms of Bloch orbitals:

$$n(\mathbf{r}) = \sum_n \int_{\Omega_{\mathrm{BZ}}} \frac{\mathrm{d}^3 k}{\Omega_{\mathrm{BZ}}} f_{n\mathbf{k}} \, \langle \mathbf{r} | \psi_{n\mathbf{k}} \rangle \langle \psi_{n\mathbf{k}} | \mathbf{r} \rangle \,, \tag{2.27}$$

where $f_{n\mathbf{k}}$ are the occupancies of the corresponding orbitals. This means that the total electronic density is a sum of single-particle KS densities of the *occupied* orbitals. Therefore, the highest value for n is in practice of the same order of magnitude as the number of electrons per unit cell. This is a tremendous improvement over the number of electrons within a macroscopic solid (about 10^{23}).

However, the Bloch vector $\mathbf{k}$ is still a continuous variable, offering an uncountably infinite number of possible solutions to the KS equations. Fortunately, the KS Bloch orbitals, $|\psi_{n\mathbf{k}}\rangle$, usually depend very smoothly on $\mathbf{k}$. Therefore, integrals such as in Eq. (2.27) are evaluated by means of sampling the FBZ at specific values of $\mathbf{k}$, for example, on a regular grid. The required grid sizes depend on the material and on the quantities one wishes to calculate. In practice, the $\mathbf{k}$-point convergence must be reached by systematically increasing the sampling density.

2.3 Electronic Band Structure

After solving the KS equations, Eq. (2.11), for a solid, one obtains a set of Bloch orbitals, $|\psi_{n\mathbf{k}}\rangle$, as well as a set of KS eigenvalues, $\varepsilon_{n\mathbf{k}}$. $\varepsilon_{n\mathbf{k}}$ is a complicated function of the Bloch vector, $\mathbf{k}$. In its entirety, it describes the relationship between allowed energies and Bloch vectors of the KS states. This is commonly referred to as the electronic band structure. It governs many of the electronic and optical properties of the system.

The electronic band structure can feature regions in energy where no states are allowed. As alluded to in Chapter 1, these band gaps are important distinguishing features between different classes of materials. In particular, the location of band gaps in relation to the Fermi level allows distinguishing between metals, semiconductors and insulators. The Fermi level, ε_F, is defined as the amount of energy required to add an electron to the system. It is also known as the chemical potential.

If ε_F is situated within a band, the material is generally considered a metal. Electrons can easily reach energetically higher-lying states, contributing significantly to the electrical conductivity. In metals at finite temperature, states at the Fermi level have on average a 50 % probability of being occupied. In the ground state of metals, the Fermi level coincides with the Fermi energy, the energy of the highest occupied single-electron orbital.

If, on the other hand, ε_F is situated within a band gap, the material is either an insulator or a semiconductor. In this case, we call the band below the gap the valence band and the one above the gap the conduction band. Accordingly, we call the respective extrema of these bands the vallence-band maximum (VBM) and conduction-band minimum (CBM). Insulators are defined by a large band gap with ε_F situated mid gap, far below the CBM. In these materials, typical thermal fluctuations are too low in energy to excite sufficient charge carriers in the conduction band. Thus, insulators generally feature high electrical resistivities. Semiconductors feature a comparatively small band gap. This allows charge carriers to be present at finite temperatures. For semiconductors, in particular, the location and size of the band gap in relation to the Fermi level has huge consequences on its electrical and optical properties. There are many levels of detail to this that we choose to withhold for brevity.

Unfortunately, it is well-known that density-functional approximations (such

as LDA and GGA) systematically underestimate the band gap of insulators and semiconductors [68–72]. Nonetheless, the band structure obtained by DFT calculations is often used as an initial step for higher-level methods. There are ongoing efforts to design new density functionals specifically tailored towards solids and the reproduction of the electronic band gap [73]. However, in order to achieve greater accuracy, one has to include the phonon-induced renormalization of the electronic band structure as well.

2.4 The Projector Augmented-Wave Method

In Section 2.2, we have seen that Bloch orbitals are suitable solutions to the KS equations for periodic systems. In addition, Eq. (2.17) provides a natural representation of these Bloch orbitals in terms of plane-waves. This leads to a simple form of the KS equations that is easily implemented in ab-initio software. However, a naive implementation purely based on a plane-wave basis is extremely inefficient. We will quickly outline the problem and then proceed to provide a state-of-the-art solution, the PAW method.

The eigenfunctions of the KS equations are orbitals that form an orthonormal set. In this particular sense, they are not independent of each other as they have to obey the orthogonality constraint in Eq. (2.25). In order to maintain this orthogonality, the wave functions of higher-lying states must feature radial nodes. The more nodes there are, the more rapidly the wave function oscillates. This is similar to atomic orbitals, where the 1s orbital is nodeless, the 2s features one node, the 3s two nodes, and so on.

The problem with a plane wave basis arises when trying to represent both core and valence states at the same time. Core states are the energetically lowest-lying states that sit deep within the potential well generated by the nucleus. They have the character of an atomic orbital, such as the 1s, and are well localized around the nucleus. Because of this, their contribution to chemical bonding is usually negligible. However, the orthogonality constraint forces higher lying valence states to exhibit nodes close to the nucleus. In this context, we call them all-electron (AE) orbitals due to the fact that they have to be orthogonal to the core orbitals. This is not to be confused with the many-body wave function. AE orbitals are single-particle states.

The rapid oscillations caused by the nodes in AE orbitals require many high-frequency plane-wave components to be represented accurately. This renders their plane-wave representation prohibitively expensive. A common solution is to replace the bare nuclear Coulomb potential together with the dynamics of the core electrons by an effective potential, a pseudopotential. While not strictly necessary, the dynamics of the core electrons are usually completely neglected. This is known as the frozen-core approximation. The idea is that the pseudopotential can be constructed in such a way that the valence wave functions become nodeless below a certain matching radius, r_c, while remaining identical to the

AE orbitals beyond r_c. The resulting orbitals, known as pseudo (PS) orbitals, are much smoother and require fewer plane-wave components to be represented accurately than their AE counterparts. This is illustrated in Fig. 2.3. The radius r_c is chosen such that the chemical bonding region is largely unaffected by the pseudization while maximizing the smoothness of the PS orbitals.

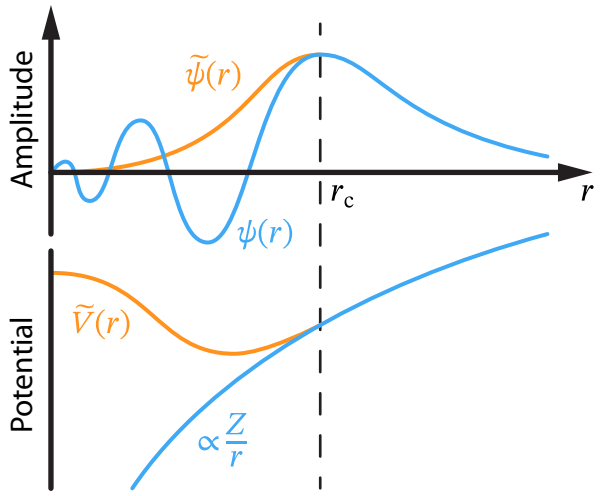

Figure 2.3: Illustration of the pseudopotential method. The Z/r Coulomb potential generates AE solutions at higher energies that exhibit rapid oscillations, shown in blue as $\psi(r)$. A pseudopotential, $\widetilde{V}(r)$, instead generates PS solutions without nodes, shown in orange as $\widetilde{\psi}(r)$, that are much smoother. Beyond the matching radius, r_c, AE and PS are identical.

One issue with the original pseudopotential method is that some AE information is lost and cannot be easily recovered, in particular the core-valence orthogonality and the nodal structure of the valence orbitals. This can be an issue if one is interested in, e.g., electron-core interactions where the exact shape of the AE orbitals is crucial. As it turns out, this is important also for electron-phonon interactions, where the derivative of the nuclear potential is required. More details are provided in Section 4.4.2.

A modern state-of-the-art generalization of the pseudopotential method that addresses its shortcomings is the PAW method [31, 32]. It follows the same basic principles of introducing a pseudopotential but fully retains the AE information using a dual-basis approach. The method is much more involved on paper but delivers an excellent compromise between computational performance and accuracy. The former is comparable to traditional pseudopotential calculations while the latter is competitive with the much more expensive FLAPW method [74].

The main idea of the PAW method is to map the complicated AE orbitals, $|\psi_n\rangle$ onto computationally convenient PS orbitals, $|\widetilde{\psi}_n\rangle$. This is accomplished via a linear transformation:

$$|\psi_n\rangle = \hat{\mathcal{T}}\,|\widetilde{\psi}_n\rangle\,, \tag{2.28}$$

where we have introduced the PAW transformation operator, $\hat{\mathcal{T}}$. For brevity, here and for the remainder of this chapter, the Bloch vector, band and spin indices are absorbed into a composite index, n.

To draw the parallel to the pseudopotential method, let us use the abstract PAW transformation to pseudize the AE orbitals in Eq. (2.11):

$$\hat{H}\hat{\mathcal{T}}\,|\widetilde{\psi}_n\rangle = \varepsilon_n \hat{\mathcal{T}}\,|\widetilde{\psi}_n\rangle\,. \tag{2.29}$$

After multiplying with $\hat{\mathcal{T}}^\dagger$ from the left and defining

$$\widetilde{H} \equiv \hat{\mathcal{T}}^\dagger \hat{H} \hat{\mathcal{T}}, \tag{2.30}$$

$$\tilde{S} \equiv \hat{\mathcal{T}}^\dagger \hat{\mathcal{T}}, \tag{2.31}$$

the KS equations transform into a generalized eigenvalue problem:

$$\widetilde{H}\,|\widetilde{\psi}_n\rangle = \varepsilon_n \tilde{S}\,|\widetilde{\psi}_n\rangle\,. \tag{2.32}$$

These are referred to as the PAW KS equations. $\widetilde{H}$ and $\tilde{S}$ are the PAW Hamiltonian and the PAW overlap operator, respectively. More explicit expressions for these operators are given in Section 2.4.2.

Eq. (2.32) suggests solving the KS equations self-consistently using the smooth PS orbitals as variational quantities instead of the computationally more demanding AE orbitals. Just like in the pseudopotential method, this allows for an efficient computational scheme. However, in contrast, the AE information is not discarded but is contained within the PAW transformation, i.e., within $\widetilde{H}$ and $\tilde{S}$. The trick is to find a computationally convenient representation of this AE information using local basis functions. In order to understand how this works, first, a detailed look at the transformation operator is required.

2.4.1 The Transformation Operator

The problem one aims to solve with the PAW method is the difficulty of treating the rapid oscillations of the AE orbitals close to the nuclei. It is therefore quite reasonable to distinguish between regions of space immediately surrounding each nucleus, usually referred to as the augmentation region, and an interstitial region.

The augmentation region consists of so-called augmentation spheres, each with a radius, $r_{c,a}$, that can depend on the atom type, as indicated by the atom-index, a. We assume that the spheres are large enough to encompass the detailed nodal structure of the orbitals, including the nodes arising from the orthogonality to the core states.

The PAW transformation is chosen such that the resulting PS orbitals differ from the AE orbitals only within the augmentation region. Therefore, it can be represented as a sum over atom-centered contributions:

$$\hat{\mathcal{T}} = \mathbb{1} + \sum_a \hat{\mathcal{T}}_a, \tag{2.33}$$

where $\hat{\mathcal{T}}_a$ only acts within the augmentation sphere corresponding to atom a. $\hat{\mathcal{T}}_a$ determines the form of the PS orbital inside the sphere and should be chosen such that they are computationally convenient. To this end, the PS orbitals are expanded into a complete set of so-called PS partial waves, $|\widetilde{\phi}_{ai}\rangle$, in each augmentation sphere:

$$|\widetilde{\psi}_n\rangle = \sum_i c_{nai} |\widetilde{\phi}_{ai}\rangle \quad \text{within} \quad r_{c,a}, \tag{2.34}$$

with yet undetermined coefficients c_{nai}. For now, the index i can be thought of as a quantum number to an atomic orbital similar to the angular-momentum quantum number, l.

Analogously, the AE orbital can be expanded into a set of AE partial waves,

$$|\psi_n\rangle = \sum_i c_{nai} |\phi_{ai}\rangle \quad \text{within} \quad r_{c,a}. \tag{2.35}$$

The AE partial waves, $|\phi_{ai}\rangle$, are the solutions to the radial scalar relativistic non-spin-polarized Schrödinger equation for the spherical atom at a certain energy. These solutions are obtained numerically for each atom type. The PS partial waves are related to the AE partial waves via the PAW transformation,

$$|\phi_{ai}\rangle = \hat{\mathcal{T}} |\widetilde{\phi}_{ai}\rangle, \tag{2.36}$$

and therefore both feature the same expansion coefficients. This is used to construct a suitable set of PS partial waves. It is worth noting that the domain of the partial waves need not necessarily be restricted to the respective augmentation spheres. However, in the interstitial region, the AE partial waves must be identical to the PS partial waves.

At this point, we can draw a qualitative picture of how the PAW method decomposes an AE orbital. First, a smooth pseudo orbital is constructed that correctly describes the tail of the AE orbital in the interstitial region. Second, PS partial waves are subtracted from these orbitals to remove the artificially introduced smoothness inside the augmentation region. Third, AE partial waves are added to restore the AE character of the orbitals inside the augmentation region. This process is illustrated graphically in Fig. 2.4.

The only missing piece is the determination of the expansion coefficients. As the name implies, the PAW method defines these by means of projection of the PS orbitals onto atom-centered projector functions, $\widetilde{p}_{ai}$:

$$c_{nai} \equiv \langle \widetilde{p}_{ai} | \widetilde{\psi}_n \rangle, \tag{2.37}$$

where each PAW projector, $|\widetilde{p}_{ai}\rangle$, corresponds to one pair of partial waves, $|\phi_{ai}\rangle$ and $|\widetilde{\phi}_{ai}\rangle$. This choice is justified since $\hat{\mathcal{T}}$ was chosen to be linear. The overlap matrix in Eq. (2.37) is sometimes called *orbital character* in the context of the PAW method. The projector functions are chosen such that they are orthogonal to the respective PS partial waves:

$$\langle \widetilde{p}_{ai} | \widetilde{\phi}_{aj} \rangle = \delta_{ij}. \tag{2.38}$$

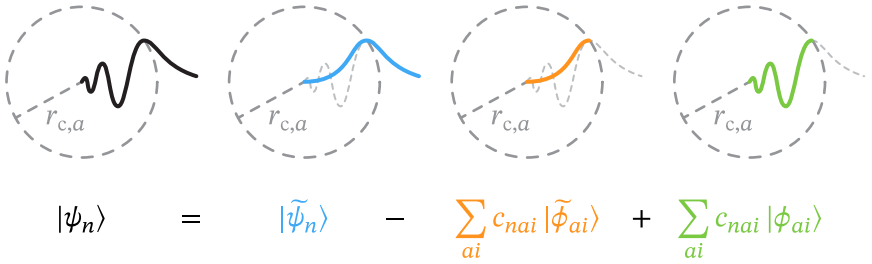

Figure 2.4: Graphical illustration of how the PAW AE orbital, $|\psi_n\rangle$ (black), is expanded in terms of a PS orbitals, $|\tilde{\psi}_n\rangle$ (blue), AE partial waves, $|\phi_{ai}\rangle$ (orange), and PS partial waves, $|\tilde{\phi}_{ai}\rangle$ (green). In each case, the dashed circle represents the augmentation sphere with radius $r_{c,a}$. The solid line represents the real-space wave function of each contribution.

In other words, the projector functions live in a space that is dual to that of the PS partial waves. Under the assumption that the PAW basis is complete inside the augmentation region, it follows immediately from Eq. (2.38) that

$$\sum_i |\tilde{\phi}_{ai}\rangle\langle\tilde{p}_{ai}| = \mathbb{1}_a^{\text{aug}}, \tag{2.39}$$

where we have defined the identity operator $\mathbb{1}_a^{\text{aug}}$ that only acts within the augmentation sphere of atom a and is zero otherwise.

Finally, we are able to specify how the AE orbital is formally described in the PAW method:

$$|\psi_n\rangle = |\tilde{\psi}_n\rangle + \sum_{ai}\Big(|\phi_{ai}\rangle - |\tilde{\phi}_{ai}\rangle\Big)\langle\tilde{p}_{ai}|\tilde{\psi}_n\rangle\,, \tag{2.40}$$

which fully defines the PAW transformation

$$\hat{\mathcal{T}} = \mathbb{1} + \sum_{ai}\Big(|\phi_{ai}\rangle - |\tilde{\phi}_{ai}\rangle\Big)\langle\tilde{p}_{ai}|\,, \tag{2.41}$$

given $|\phi_{ai}\rangle$, $|\tilde{\phi}_{ai}\rangle$ and $|\tilde{p}_{ai}\rangle$. From a practical perspective, this result on its own may not appear to be exceptionally useful. However, the true power of the PAW method lies in the fact that the partial waves can be represented using a different basis set than the pseudo orbitals. Since the partial waves are symmetrically centered around atoms, a natural choice is to expand them into radial basis functions and spherical harmonics. The radial part is represented on a logarithmic grid that allows an accurate description of the complicated AE features close to the nucleus. Meanwhile, the PAW projectors are described in the same basis as the pseudo orbitals, for example in terms of plane waves. This dual-basis aspect lies at the heart of the PAW method, and we will see in the following section how it allows us to efficiently compute the expectation values of operators within this framework. The process of generating adequate PAW basis sets for different reference atomic species is profoundly intricate and is discussed elsewhere [32].

2.4.2 Operators and Expectation Values

While the variational quantity might have formally changed from the AE orbital to the soft PS orbital in the PAW method, the expectation values of physical observables must remain the same. To understand how this works, let us examine the expectation value of a local Hermitian operator $\hat{A}$ as it is expressed in the basis of AE states:

$$\langle \hat{A} \rangle = \sum_n f_n \langle \psi_n | \hat{A} | \psi_n \rangle \,. \tag{2.42}$$

Here, f_n is the occupation number of the corresponding state labeled by n. Expanding the AE states in Eq. (2.42) using the PAW transformation, Eq. (2.28), the expectation value reads

$$\langle \hat{A} \rangle = \sum_n f_n \langle \widetilde{\psi}_n | \hat{\mathcal{T}}^\dagger \hat{A} \hat{\mathcal{T}} | \widetilde{\psi}_n \rangle = \sum_n f_n \langle \widetilde{\psi}_n | \widetilde{A} | \widetilde{\psi}_n \rangle \,, \tag{2.43}$$

where we have implicitly defined $\widetilde{A}$ as the PAW representation of the operator $\hat{A}$. This was already hinted at earlier in Eqs. (2.30) and (2.31), yet this result is true for any (semi)-local operator. Careful readers might have spotted the fact that the Hamiltonian is generally not a local operator. How it can still be accurately described and how non-locality is addressed in this context is discussed elsewhere [32].

By expanding the PAW transformation operators in Eq. (2.43) using Eq. (2.41), we can derive the general form of an operator in the PAW method. Following, for example, Ref. [32], and assuming that the PAW completeness relation in Eq. (2.39) is fulfilled, $\widetilde{A}$ takes the form

$$\widetilde{A} \equiv \hat{A} + \sum_{aij} |\widetilde{p}_{ai}\rangle \left(\langle \phi_{ai} | \hat{A} | \phi_{aj} \rangle - \langle \widetilde{\phi}_{ai} | \hat{A} | \widetilde{\phi}_{aj} \rangle \right) \langle \widetilde{p}_{aj} | \,. \tag{2.44}$$

The operator is now split into three parts. The first part is simply the original $\hat{A}$ that acts directly on the PS orbitals. The second and third parts are AE and PS one-center contributions. The term *one-center* refers to the fact that the expectation values between partial waves are evaluated at the same nuclear site. This is a consequence of the locality of $\hat{A}$. In the case of the one-center terms, the PS orbitals are first projected into the augmentation region via the $|\widetilde{p}_{ai}\rangle$.

The most important detail from a practical point of view is the fact that objects residing on the radial grid, i.e. partial waves, never directly interact with objects residing on the plane-wave grid, i.e. projectors and PS orbitals. The separation into these two domains is what enables the PAW method to work efficiently in the first place.

A particularly important operator, that was already introduced earlier, is the PAW overlap operator, $\tilde{S}$. It can be considered to be the PAW representation of the identity operator. Using Eq. (2.44), we can immediately see the form it takes:

$$\tilde{S} \equiv \mathbb{1} + \sum_{aij} |\widetilde{p}_{ai}\rangle \, Q_{aij} \, \langle \widetilde{p}_{aj}| \,, \tag{2.45}$$

where we have introduced the augmentation charges, Q_{aij},

$$Q_{aij} \equiv \langle \phi_{ai} | \phi_{aj} \rangle - \langle \widetilde{\phi}_{ai} | \widetilde{\phi}_{aj} \rangle \,. \tag{2.46}$$

Similarly, we can write down the general form of the PAW Hamiltonian operator, $\widetilde{H}$:

$$\widetilde{H} \equiv -\frac{\hbar^2}{2m_\mathrm{e}}\Delta + \sum_{aij} |\widetilde{p}_{ai}\rangle \, D_{aij} \, \langle \widetilde{p}_{aj}| \,, \tag{2.47}$$

$$D_{aij} \equiv \langle \phi_{ai}| - \frac{\hbar^2}{2m_\mathrm{e}}\Delta + v_\mathrm{KS}|\phi_{aj}\rangle - \langle \widetilde{\phi}_{ai}| - \frac{\hbar^2}{2m_\mathrm{e}}\Delta + v_\mathrm{KS}|\widetilde{\phi}_{aj}\rangle \,, \tag{2.48}$$

where the D_{aij} are known as PAW strength parameters, or PAW strengths for short. Note that this is an oversimplified picture. In general, Eq. (2.48) also contains non-local compensation charges. The same is true for the charge density. For details, we refer to Ref. [32].

CHAPTER 3

Lattice Dynamics

The Born-Oppenheimer approximation allows us to separate the dynamics of the electrons from the dynamics of the ions comprising the crystal lattice. Up until this point, we have focused purely on the electronic side. In this chapter, we change point of view in order to provide a short introduction to lattice dynamics.

3.1 Force Constants and Dynamical Matrix

The theory of lattice dynamics describes the collective vibrational motion of the crystal ions. We assume that the crystal is described by a Bravais lattice, where each atom is uniquely identified by a primitive-cell index l and a basis index κ. The former labels all primitive-cells in the crystal while the latter distinguishes between different atoms in the primitive-cell basis. In equilibrium, the coordinates of each atom are written as

$$\mathbf{R}_{l\kappa} = \mathbf{R}_l + \boldsymbol{\tau}_\kappa, \tag{3.1}$$

where $\mathbf{R}_l$ is a lattice vector that indicates the location of primitive cell l and $\boldsymbol{\tau}_\kappa$ denotes the atomic position within the basis.

We now allow each atom $(l\kappa)$ to move about its equilibrium position as a function of time. In general, the resulting dynamics can be quite complicated. Since the fast-moving electrons screen most of the electrostatic Coulomb interaction between the positively charged ions, it is often quite reasonable to assume that the ions are only weakly coupled to each other. As a consequence, the average displacement of an ion from its equilibrium position will be small and the potential energy of the system can be expanded into a Taylor series with respect to the displacements, $\mathbf{u}_{l\kappa}$:

$$U = U_0 + \sum_{l\kappa\alpha} \left(\frac{\partial U}{\partial u_{l\kappa\alpha}} \right)_0 u_{l\kappa\alpha} + \frac{1}{2} \sum_{\substack{l\kappa\alpha \\ l'\kappa'\beta}} \left(\frac{\partial^2 U}{\partial u_{l\kappa\alpha}\, \partial u_{l'\kappa'\beta}} \right)_0 u_{l\kappa\alpha} u_{l'\kappa'\beta} + \dots, \tag{3.2}$$

where U_0 denotes the potential energy in the equilibrium configuration. The evaluation of the derivatives at 0 is a shorthand notation to indicate evaluation in the equilibrium configuration of the lattice. The first-order term in Eq. (3.2) is proportional to the net force, $F_{l\kappa\alpha}$, on each displaced atom:

$$F_{l\kappa\alpha} = -\frac{\partial U}{\partial u_{l\kappa\alpha}}. \tag{3.3}$$

However, since the net force in equilibrium is zero by definition, the first-order term vanishes. This leaves the second-order term as the dominant contribution to the potential energy. It is worth noting that third and higher-order terms, which we term *anharmonic*, can still yield sizable contributions under certain circumstances [75–78]. Nevertheless, from here on out, we employ the harmonic approximation and consider only perturbations up to second order in the atomic displacements.

The Hessian matrix in Eq. (3.2) is the IFC matrix, $\Phi_{l\kappa\alpha,l'\kappa'\beta}$:

$$\Phi_{l\kappa\alpha,l'\kappa'\beta} \equiv \left(\frac{\partial^2 U}{\partial u_{l\kappa\alpha}\,\partial u_{l'\kappa'\beta}}\right)_0 = -\left(\frac{\partial F_{l\kappa\alpha}}{\partial u_{l'\kappa'\beta}}\right)_0. \tag{3.4}$$

It describes the linear change of the net force on atom $(l\kappa)$ when atom $(l'\kappa')$ is displaced by a small amount out of equilibrium. This is mathematically equivalent to an elastic spring with a spring constant $\Phi_{l\kappa\alpha,l'\kappa'\beta}$ connecting the two atoms. As such, the IFC matrix can be understood as a generalization of the classical spring constant to a three-dimensional crystal. Obviously, this intuitive explanation does not apply to the self-interaction terms, where $(l\kappa) = (l'\kappa')$, but we will see how these terms can be calculated later.

The IFC matrix exhibits translational invariance with respect to discrete translations along primitive-lattice vectors:

$$\mathbf{R}_{l'} - \mathbf{R}_l = \mathbf{R}_{l''} - \mathbf{R}_0 \quad \Rightarrow \quad \Phi_{l\kappa\alpha,l'\kappa'\beta} = \Phi_{0\kappa\alpha,l''\kappa'\beta}. \tag{3.5}$$

Furthermore, the IFC matrix is symmetric in the following sense:

$$\Phi_{l\kappa\alpha,l'\kappa'\beta} = \Phi_{l'\kappa'\beta,l\kappa\alpha}. \tag{3.6}$$

These symmetry-related properties follow naturally from Eq. (3.4), given that the total ionic potential in equilibrium is cell-periodic and differentiation is commutative.

The IFC matrix has a deep connection to the vibrational properties of the system via its Fourier transform, the so-called *dynamical matrix*:

$$D_{\kappa\alpha,\kappa'\beta,\mathbf{q}} \equiv \frac{1}{\sqrt{m_\kappa m_{\kappa'}}} \sum_l \Phi_{l\kappa\alpha,0\kappa'\beta} e^{-i\mathbf{q}\cdot\mathbf{R}_l}, \tag{3.7}$$

where m_κ is the mass of atom κ and $\mathbf{q}$ is a wave vector inside the FBZ of the lattice. The dynamical matrix as defined in Eq. (3.7) is Hermitian in the following sense:

$$D_{\kappa\alpha,\kappa'\beta,\mathbf{q}} = D^*_{\kappa'\beta,\kappa\alpha,\mathbf{q}}. \tag{3.8}$$

3.2 Phonons

The vibrational properties of the system can be obtained by diagonalizing the dynamical matrix:

$$\sum_{\kappa'\beta} D_{\kappa\alpha,\kappa'\beta,\mathbf{q}} e_{\kappa'\beta,\nu\mathbf{q}} = \omega^2_{\nu\mathbf{q}} e_{\kappa\alpha,\nu\mathbf{q}}. \tag{3.9}$$

In this context, we call $\mathbf{q}$ the *phonon wave vector* as it relates to the momentum of the quasiparticle associated with the collective excitation, the *phonon*. The index ν is the so-called branch index which labels the different vibrational normal modes corresponding to a particular phonon wave vector. In three dimensions, the three phonon modes with the lowest frequencies are commonly called *acoustic* modes. The acoustic modes describe an in-phase motion, meaning that neighboring atoms predominantly oscillate in the same directions. These modes are primarily responsible for the propagation of sound waves through the solid, hence the name *acoustic*. The remaining, higher-lying modes are called *optical* modes and only exist in crystals with more than one atom in the basis. These modes describe an out-of-phase motion, where neighboring atoms predominantly oscillate in opposite directions. In polar materials, where the atoms in the basis belong to different atomic species, the motion produced by optical phonon modes can polarize the material and couple to an electromagnetic field, hence the name *optical*.

The eigenvalues, $\omega^2_{\nu\mathbf{q}}$, of the dynamical matrix are the squared angular frequencies. We will henceforth refer to the angular frequencies, $\omega_{\nu\mathbf{q}}$, as *phonon frequencies*. Finally, the eigenvectors, $e_{\kappa\alpha,\nu\mathbf{q}}$, provide information about the atomic displacement pattern of the lattice wave. In fact, the time-dependent displacement of a particular atom is directly proportional to the corresponding phonon eigenvector:

$$\mathbf{u}_{l\kappa,\nu\mathbf{q}}(t) = \frac{u^0_{\nu\mathbf{q}}}{\sqrt{m_\kappa}} \mathbf{e}_{\kappa,\nu\mathbf{q}} \mathrm{e}^{\mathrm{i}\left(\mathbf{q}\cdot\mathbf{R}_l - \omega_{\nu\mathbf{q}} t\right)}, \tag{3.10}$$

where $u^0_{\nu\mathbf{q}}$ is just a proportionality factor.

The displacement is rigorously defined in the framework of second quantization in terms of the phonon creation and annihilation operators, $\hat{b}^\dagger_{\nu\mathbf{q}}$ and $\hat{b}_{\nu\mathbf{q}}$, respectively. We have previously shown the second-quantized form of the free-phonon Hamiltonian using the canonical quantization technique [30]. Thus, here we simply provide a short summary.

In reciprocal space, the respective canonical displacement and momentum fields, $\hat{\mathbf{u}}_{l\kappa,\nu\mathbf{q}}$ and $\hat{\boldsymbol{\pi}}_{l\kappa,\nu\mathbf{q}}$, corresponding to a lattice excitation with phonon wave vector $\mathbf{q}$ and branch index ν are given as

$$\hat{\mathbf{u}}_{l\kappa,\nu\mathbf{q}} = \sqrt{\frac{\hbar}{2m_\kappa \omega_{\nu\mathbf{q}}}} \mathbf{e}_{\kappa,\nu\mathbf{q}} \mathrm{e}^{\mathrm{i}\mathbf{q}\cdot\mathbf{R}_l} \left(\hat{b}_{\nu\mathbf{q}} + \hat{b}^\dagger_{\nu,-\mathbf{q}}\right), \tag{3.11}$$

$$\hat{\boldsymbol{\pi}}_{l\kappa,\nu\mathbf{q}} = \mathrm{i}\sqrt{\frac{\hbar m_\kappa \omega_{\nu\mathbf{q}}}{2}} \mathbf{e}^*_{\kappa,\nu\mathbf{q}} \mathrm{e}^{-\mathrm{i}\mathbf{q}\cdot\mathbf{R}_l} \left(\hat{b}^\dagger_{\nu\mathbf{q}} - \hat{b}_{\nu,-\mathbf{q}}\right). \tag{3.12}$$

By definition, the creation and annihilation operators obey the following commutation relations:

$$\left[\hat{b}_{\nu\mathbf{q}}, \hat{b}^\dagger_{\nu'\mathbf{q}'}\right] = \Omega_{\mathrm{BZ}}\delta_{\nu\nu'}\delta^{(3)}(\mathbf{q}'-\mathbf{q})\mathbb{1}, \tag{3.13}$$

$$\left[\hat{b}_{\nu\mathbf{q}}, \hat{b}_{\nu'\mathbf{q}'}\right] = 0, \tag{3.14}$$

$$\left[\hat{b}^\dagger_{\nu\mathbf{q}}, \hat{b}^\dagger_{\nu'\mathbf{q}'}\right] = 0. \tag{3.15}$$

Additionally, the field operators obey the so-called *canonical* commutation relations in reciprocal space:

$$\left[\hat{u}_{\kappa\alpha,\mathbf{q}}, \hat{\pi}_{\kappa'\beta,\mathbf{q}'}\right] = \mathrm{i}\hbar\Omega_{\mathrm{BZ}}\mathbb{1}\delta_{\kappa,\kappa'}\delta_{\alpha\beta}\delta^{(3)}(\mathbf{q}'-\mathbf{q}), \tag{3.16}$$

$$\left[\hat{u}_{\kappa\alpha,\mathbf{q}}, \hat{u}_{\kappa'\beta,\mathbf{q}'}\right] = 0, \tag{3.17}$$

$$\left[\hat{\pi}_{\kappa\alpha,\mathbf{q}}, \hat{\pi}_{\kappa'\beta,\mathbf{q}'}\right] = 0, \tag{3.18}$$

with

$$\hat{\mathbf{u}}_{\kappa,\mathbf{q}} \equiv \sum_{l\nu} \hat{\mathbf{u}}_{l\kappa,\nu\mathbf{q}}, \tag{3.19}$$

$$\hat{\boldsymbol{\pi}}_{\kappa,\mathbf{q}} \equiv \sum_{l\nu} \hat{\boldsymbol{\pi}}_{l\kappa,\nu\mathbf{q}}. \tag{3.20}$$

The harmonic lattice Hamiltonian can now be written using the reciprocal-space field operators by promoting the canonical position and momentum variables to quantum fields. This results in

$$\hat{H}_{\mathrm{p}} = \int_{\Omega_{\mathrm{BZ}}} \frac{\mathrm{d}^3q}{\Omega_{\mathrm{BZ}}} \sum_{\kappa\alpha} \frac{1}{2m_\kappa} \hat{\pi}^\dagger_{\kappa\alpha,\mathbf{q}}\hat{\pi}_{\kappa\alpha,\mathbf{q}} + \int_{\Omega_{\mathrm{BZ}}} \frac{\mathrm{d}^3q}{\Omega_{\mathrm{BZ}}} \sum_{\kappa\alpha,\kappa'\beta} \frac{\sqrt{m_\kappa m_{\kappa'}}}{2} \hat{u}^\dagger_{\kappa\alpha,\mathbf{q}} D_{\kappa\alpha,\kappa'\beta,\mathbf{q}} \hat{u}_{\kappa'\beta,\mathbf{q}}, \tag{3.21}$$

which can be expressed in terms of the creation and annihilation operators using Eqs. (3.11) and (3.12):

$$\hat{H}_{\mathrm{p}} = \sum_\nu \int_{\Omega_{\mathrm{BZ}}} \frac{\mathrm{d}^3q}{\Omega_{\mathrm{BZ}}} \frac{1}{2}\hbar\omega_{\nu\mathbf{q}}\left(\hat{b}^\dagger_{\nu\mathbf{q}}\hat{b}_{\nu\mathbf{q}} + \hat{b}_{\nu\mathbf{q}}\hat{b}^\dagger_{\nu\mathbf{q}}\right), \tag{3.22}$$

and after using the commutation relations in Eq. (3.13), the phonon Hamiltonian reads:

$$\hat{H}_{\mathrm{p}} = \sum_\nu \int_{\Omega_{\mathrm{BZ}}} \frac{\mathrm{d}^3q}{\Omega_{\mathrm{BZ}}} \left(\hat{n}^{\mathrm{p}}_{\nu\mathbf{q}} + \frac{1}{2}\right)\hbar\omega_{\nu\mathbf{q}}, \tag{3.23}$$

$$\hat{n}^{\mathrm{p}}_{\nu\mathbf{q}} \equiv \hat{b}^\dagger_{\nu\mathbf{q}}\hat{b}_{\nu\mathbf{q}}. \tag{3.24}$$

The operator $\hat{n}^{\mathrm{p}}_{\nu\mathbf{q}}$ measures the number of phonons with ν and $\mathbf{q}$ in the corresponding multi-particle state and is thus called the *number operator*. Eq. (3.23) describes the system in terms of independent harmonic oscillators. The term $\frac{1}{2}\hbar\omega_{\nu\mathbf{q}}$ is the ground-state energy contribution per phonon.

3.3 Acoustic Sum Rule

In the limit of vanishing phonon wave vector, $\mathbf{q} \to 0$, the acoustic modes describe rigid translations of the entire lattice and the corresponding phonon frequencies become 0:

$$\omega_{\nu\mathbf{0}} = 0 \qquad \forall \quad \nu \leq 3. \tag{3.25}$$

This is a direct consequence of translational invariance. By the same token, the optical modes at $\mathbf{q} \to 0$ become standing waves, i.e., the center of mass in any given unit cell must be stationary with respect to that unit cell:

$$\sum_{\kappa} m_\kappa \mathbf{u}_{\kappa,\nu\mathbf{0}}(t) = 0 \qquad \forall \quad \nu > 3 \tag{3.26}$$

$$\Rightarrow \quad \sum_{\kappa} \sqrt{m_\kappa}\mathbf{e}_{\kappa,\nu\mathbf{0}} = 0 \qquad \forall \quad \nu > 3, \tag{3.27}$$

where we used Eq. (3.10) to express the atomic displacements in terms of the phonon eigenvectors. This allows us to formulate an important sum rule starting from Eq. (3.9):

$$\sum_{\kappa'\beta} D_{\kappa\alpha,\kappa'\beta,\mathbf{0}} e_{\kappa'\beta,\nu\mathbf{0}} = \omega^2_{\nu\mathbf{0}} e_{\kappa\alpha,\nu\mathbf{0}}, \tag{3.28}$$

$$\sum_{\kappa}\sum_{\kappa'\beta} \sqrt{m_\kappa} D_{\kappa\alpha,\kappa'\beta,\mathbf{0}} e_{\kappa'\beta,\nu\mathbf{0}} = \underbrace{\omega^2_{\nu\mathbf{0}} \sum_{\kappa} \sqrt{m_\kappa} e_{\kappa\alpha,\nu\mathbf{0}}}_{=0}, \tag{3.29}$$

$$\sum_{\kappa}\sum_{\kappa'\beta} \sqrt{m_\kappa} D_{\kappa\alpha,\kappa'\beta,\mathbf{0}} \underbrace{\sum_{\nu} e_{\kappa'\beta,\nu\mathbf{0}} e^*_{\kappa''\gamma,\nu\mathbf{0}}}_{=\delta_{\kappa'\kappa''}\delta_{\beta\gamma}} = 0, \tag{3.30}$$

which results in one of multiple manifestations of the acoustic sum rule (ASR):

$$\sum_{\kappa} \sqrt{m_\kappa m_{\kappa'}} D_{\kappa\alpha,\kappa'\beta,\mathbf{0}} = \sum_{\kappa'} \sqrt{m_\kappa m_{\kappa'}} D_{\kappa\alpha,\kappa'\beta,\mathbf{0}} = 0. \tag{3.31}$$

Using Eq. (3.7), we can easily rewrite the ASR in terms of the IFC matrix:

$$\sum_{l\kappa} \Phi_{l\kappa\alpha,l'\kappa'\beta} = \sum_{l'\kappa'} \Phi_{l\kappa\alpha,l'\kappa'\beta} = 0. \tag{3.32}$$

This allows for the calculation of the on-site or self-interaction terms:

$$\Phi_{l\kappa\alpha,l\kappa\beta} = -\sum_{l'\kappa'\neq l\kappa} \Phi_{l'\kappa'\alpha,l\kappa\beta}. \tag{3.33}$$

3.4 Phonon Dispersion Relation

In principle, knowledge of the IFC matrix fully determines the phonon dispersion relation, $\omega_\nu(\mathbf{q})$, in the entire FBZ using Eqs. (3.7) and (3.9). However, in

practice the IFC matrix is only known for a limited set of unit cells, for example, in a supercell calculation. Therefore, the Fourier transform in Eq. (3.7) is strictly valid only for a limited set of q-vectors. If the force constants belong to a given supercell, these q-vectors are the ones *commensurate* with the supercell, i.e., they belong to its reciprocal lattice. The Γ-point is a possible exception to this in the case of polar materials as is shown in Section 3.5.

A common practice to get around this limitation is to interpolate the dynamical matrix between the commensurate q-points. To this end, we can exploit the fact that the IFC matrix decays as a function of distance between atoms. If this decay happens smoothly and exponentially fast, i.e., the force constants are negligible beyond a certain cutoff radius, then the dynamical matrix becomes amenable to Fourier interpolation. The concept of Fourier interpolation is of paramount importance as it is utilized heavily throughout this work.

The interpolation procedure used here works as follows. First, the IFC matrix is constructed in a given Born-von-Karmann supercell [79] by means of finite displacements. This automatically truncates the IFC matrix at about half the physical extent of the supercell due to the periodic boundary conditions. Second, the IFC matrix is transformed to reciprocal space and interpolated by evaluating Eq. (3.7) at an arbitrary q-point. Finally, the resulting dynamical matrix is diagonalized according to Eq. (3.9) to retrieve the phonon frequencies and eigenvectors. In principle, this allows the calculation of the phonon dispersion relation everywhere in the FBZ.

As an example, Fig. 3.1 shows the interpolated phonon dispersion relation for diamond. Since there are two atoms per unit cell in the diamond structure, we

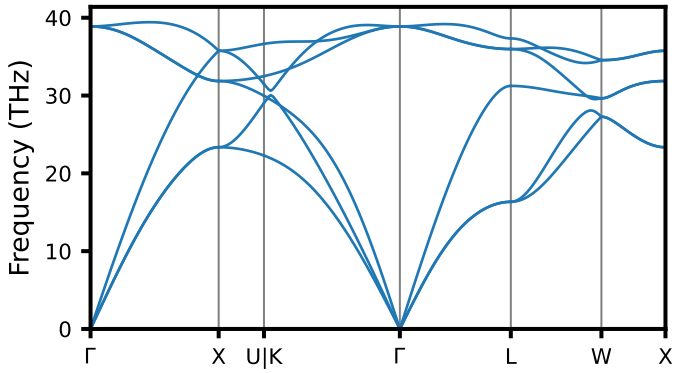

Figure 3.1: Phonon dispersion relation of diamond obtained via Fourier interpolation of the dynamical matrix starting from a 6×6×6 supercell.

observe three acoustic and three optical phonon modes. The phonon frequencies of the acoustic modes go to zero as $\mathbf{q} \to \mathbf{0}$. This is a direct consequence of the ASR discussed in Section 3.3. In practice, it is sometimes necessary to explicitly symmetrize the IFC matrix in order to enforce the ASR. Otherwise, the phonon frequencies at Γ can become finite or even imaginary due to numerical inaccura-

cies.

The accuracy of the interpolation procedure depends heavily on the spatial decay of the IFC matrix. Therefore, the size of the supercell needs to be large enough to accommodate all relevant entries of the IFC matrix. One must in general carefully check whether this is the case and converge the phonon dispersion relation with respect to the supercell size. As an example, Fig. 3.2 shows the decay of the IFC matrix of diamond as a function of distance between atoms for different supercell sizes. The lines roughly follow an exponential decay as the

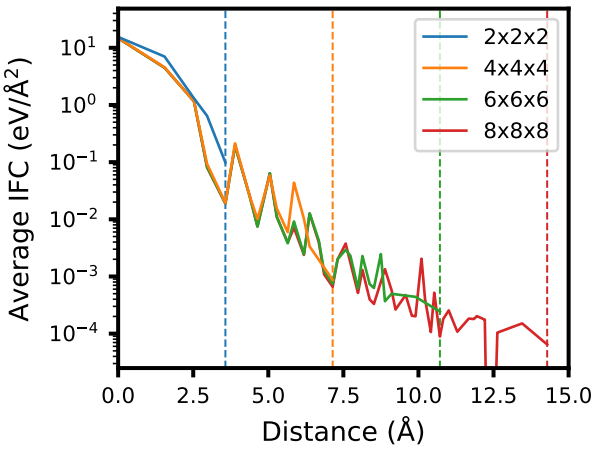

Figure 3.2: IFC matrix of diamond as a function of distance between atoms. For each possible interatomic distance, a data point is obtained by averaging the absolute values of the corresponding IFC matrix elements. Each solid line corresponds to a different supercell size. The dashed lines indicate the maximum distance in each data set.

distance between atoms increases. Differences between lines can be attributed to the non-spherical cutoff that occurs in the periodic supercell.

The convergence of the phonon dispersion relation with respect to the supercell is illustrated in Fig. 3.3 for the same example of diamond. Using a 6×6×6 supercell, one obtains an accurate phonon dispersion relation, showing little to no difference to the 8×8×8 case. Using a 4×4×4 supercell generates a qualitatively correct phonon dispersion, even though it is not as numerically accurate as the 6×6×6 case. The 2×2×2 supercell produces undesirable results. In this case, the IFC matrix is truncated too soon.

3.5 LO-TO Splitting in Polar Materials

Fourier interpolation of the dynamical matrix works well for most systems that only contain one species of atom. Unfortunately, for a polar insulator whose crystal basis contains different atomic species, a collective out-of-phase displacement of the ions can induce a macroscopic electrostatic field. This field gives rise to

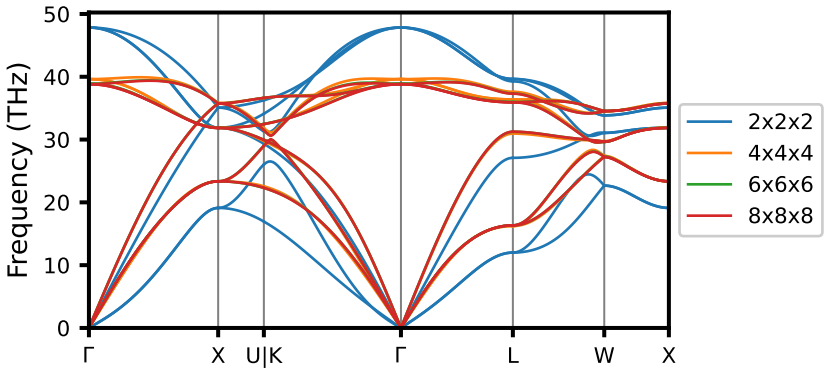

Figure 3.3: Phonon dispersion relation of diamond obtained via Fourier interpolation from different supercell sizes.

long-range contributions to the force constants. In this case, the IFC matrix can no longer be truncated for the purpose of Fourier interpolation. In this section, we briefly illustrate how long-range electrostatic interactions can emerge in the lattice dynamics of polar materials. This leads to the splitting of the longitudinal optical (LO) from the transverse optical (TO) phonon modes.

To illustrate, let us consider an insulator comprised of two differently charged atomic species, A and B, undergoing a lattice vibration that corresponds to an LO phonon mode with $\mathbf{q} \to \mathbf{0}$. As mentioned in Section 3.3, a zone-center optical phonon mode is described by a standing lattice wave. Accordingly, the sublattices pertaining to the atomic species A and B are always displaced in opposite directions, i.e., fully out of phase. This leads to the formation of microscopic dipole moments that all point in the same direction. Under the assumption that the electronic screening of the ionic charges is incomplete, they induce a macroscopic polarization, $\mathbf{P}(\mathbf{q})$, which is accompanied by an electrostatic field, $\mathbf{E}(\mathbf{q})$. We like to mention that the macroscopic polarization should not be defined as the sum of cell-periodic dipoles as this leads to many inconsistencies. A rigorous definition of the macroscopic polarization is given in the modern theory of polarization [80, 81] in terms of the Berry phase [82, 83].

The long-range electrostatic field only appears in the longitudinal case. The two associated transverse modes of this particular phonon are unaffected. Therefore, when looking at the associated frequencies at the Γ-point, one observes a splitting between the LO and TO modes in polar insulators. The principle stays the same when there are multiple ionic species or the material is anisotropic. LO-TO splitting can be attributed to a nonanalytic contribution to the IFC matrix, and we will now show how to calculate it.

The potential energy of the system is expanded up to second order in terms of

the atomic displacements, $\mathbf{u}_\kappa$, and the electric field, $\mathbf{E}$ [84]:

$$\begin{aligned} U = U_0 + \frac{1}{2}\sum_{\kappa\kappa'}\sqrt{m_\kappa m_{\kappa'}}\mathbf{u}_\kappa^\top \mathbf{D}_{\kappa,\kappa'}\mathbf{u}_{\kappa'} \\ - e\sum_\kappa \mathbf{E}^\top \mathbf{Z}_\kappa^\star \mathbf{u}_\kappa - \frac{V_{\mathrm{pc}}}{2}\mathbf{E}^\top \boldsymbol{\chi}\mathbf{E} \\ + \mathcal{O}(3), \end{aligned} \tag{3.34}$$

where we used the following notation to facilitate matrix and vector multiplications:

$$\mathbf{v}^\top \mathbf{T}\mathbf{w} = \sum_{\alpha\beta} v_\alpha T_{\alpha\beta} w_\beta. \tag{3.35}$$

Here, it is understood that the perturbation described by $\mathbf{u}_\kappa(\mathbf{q})$ and $\mathbf{E}(\mathbf{q})$ is due to an optical phonon with $\mathbf{q} \to \mathbf{0}$. The tensor $Z^\star_{\kappa,\alpha\beta}$ is the so-called *Born effective-charge tensor* and $\chi_{\alpha\beta}$ is the electric susceptibility tensor. The susceptibility is related to the *ion-clamped static dielectric permittivity tensor*, $\epsilon^\infty_{\alpha\beta}$:

$$\epsilon^\infty_{\alpha\beta} = \delta_{\alpha\beta} + 4\pi\chi_{\alpha\beta}. \tag{3.36}$$

For brevity, we will henceforth refer to this quantity simply as the *dielectric tensor*. How $\mathbf{Z}^\star_\kappa$ and $\boldsymbol{\epsilon}^\infty$ can be calculated in practice is discussed elsewhere [85, 86].

The first second-order term in Eq. (3.34), which involves the dynamical matrix, $D_{\kappa\alpha,\kappa'\beta}$, can be considered the analytic contribution. According to Eq. (3.9), this term yields the correct phonon spectrum if the crystal is not polarized. That leaves the two remaining terms as the nonanalytic contributions at second order. The first of which involves the Born effective charges and measures the change in macroscopic polarization when an atom is displaced from its equilibrium position in the presence of an external electric field. The second of which involves the electric susceptibility and measures the change in macroscopic polarization solely due to the presence of an external electric field. We aim to rewrite these two contributions as a nonanalytic part of the dynamical matrix in terms of $\mathbf{Z}^\star_\kappa$ and $\boldsymbol{\epsilon}^\infty$.

Both the Born effective charges and the dielectric tensor can be obtained as first derivatives of the macroscopic polarization, which is itself the first derivative of the potential energy with respect to the electric field:

$$P_\alpha = -\frac{1}{V_{\mathrm{pc}}}\left(\frac{\partial U}{\partial E_\alpha}\right)_{\mathbf{u}_\kappa=\mathbf{0}}, \tag{3.37}$$

$$Z^\star_{\kappa,\alpha\beta} = \frac{V_{\mathrm{pc}}}{e}\left(\frac{\partial P_\alpha}{\partial u_{\kappa\beta}}\right)_{\mathbf{E}=\mathbf{0}}, \tag{3.38}$$

$$\epsilon^\infty_{\alpha\beta} = \delta_{\alpha\beta} + 4\pi\left(\frac{\partial P_\alpha}{\partial E_\beta}\right)_{\mathbf{u}_\kappa=\mathbf{0}}. \tag{3.39}$$

Strictly speaking, $\mathbf{P}$ is defined here as the macroscopic polarization per unit-cell volume. Using Eqs. (3.34) and (3.37), we can now write the polarization,

$$\mathbf{P} = \frac{e}{V_{\mathrm{pc}}} \sum_{\kappa} \mathbf{Z}_{\kappa}^{\star} \mathbf{u}_{\kappa} + \chi \mathbf{E}, \tag{3.40}$$

and the electric displacement field, $\mathbf{D}$,

$$\begin{aligned} \mathbf{D} &= \mathbf{E} + 4\pi \mathbf{P} \\ &= \mathbf{E} + \frac{4\pi e}{V_{\mathrm{pc}}} \sum_{\kappa} \mathbf{Z}_{\kappa}^{\star} \mathbf{u}_{\kappa} + 4\pi \chi \mathbf{E} \\ &= \frac{4\pi e}{V_{\mathrm{pc}}} \sum_{\kappa} \mathbf{Z}_{\kappa}^{\star} \mathbf{u}_{\kappa} + \epsilon^{\infty} \mathbf{E}, \end{aligned} \tag{3.41}$$

where we used the fact that χ and, by extension, ϵ^{∞} are symmetric. According to Maxwell's equations, $\boldsymbol{\nabla} \cdot \mathbf{D} = 0$ and $\boldsymbol{\nabla} \times \mathbf{E} = \mathbf{0}$, given that there are no free charges inside the material. In the reciprocal-space description, the nabla operator is replaced by a multiplication with the momentum. In this case, it is the phonon wave vector, $\mathbf{q}$. Therefore:

$$\mathbf{q} \cdot \mathbf{D} = 0 = \frac{4\pi e}{V_{\mathrm{pc}}} \sum_{\kappa} \mathbf{q}^{\mathsf{T}} \mathbf{Z}_{\kappa}^{\star} \mathbf{u}_{\kappa} + \mathbf{q}^{\mathsf{T}} \epsilon^{\infty} \mathbf{E}, \tag{3.42}$$

$$\mathbf{q}\left(\mathbf{q}^{\mathsf{T}} \epsilon^{\infty} \mathbf{E}\right) = -\frac{4\pi e}{V_{\mathrm{pc}}} \mathbf{q} \sum_{\kappa} \mathbf{q}^{\mathsf{T}} \mathbf{Z}_{\kappa}^{\star} \mathbf{u}_{\kappa}, \tag{3.43}$$

$$\underbrace{\mathbf{q}(\mathbf{q}^{\mathsf{T}} \epsilon^{\infty} \mathbf{E}) - \mathbf{E}(\mathbf{q}^{\mathsf{T}} \epsilon^{\infty} \mathbf{q})}_{(\mathbf{q}^{\mathsf{T}} \epsilon^{\infty}) \times (\mathbf{E} \times \mathbf{q}) = \mathbf{0}} = -\frac{4\pi e}{V_{\mathrm{pc}}} \mathbf{q} \sum_{\kappa} \mathbf{q}^{\mathsf{T}} \mathbf{Z}_{\kappa}^{\star} \mathbf{u}_{\kappa} - \mathbf{E}\left(\mathbf{q}^{\mathsf{T}} \epsilon^{\infty} \mathbf{q}\right), \tag{3.44}$$

$$\mathbf{E} = -\frac{4\pi e}{V_{\mathrm{pc}}} \mathbf{q} \sum_{\kappa} \frac{\mathbf{q}^{\mathsf{T}} \mathbf{Z}_{\kappa}^{\star} \mathbf{u}_{\kappa}}{\mathbf{q}^{\mathsf{T}} \epsilon^{\infty} \mathbf{q}}. \tag{3.45}$$

From Eq. (3.34), we can identify the nonanalytic contribution to the zone-center dynamical matrix, which we denote as $\mathbf{D}^{\mathrm{na}}_{\kappa,\kappa'}$, as follows:

$$\frac{1}{2} \sum_{\kappa\kappa'} \sqrt{m_{\kappa} m_{\kappa'}} \mathbf{u}_{\kappa}^{\mathsf{T}} \mathbf{D}^{\mathrm{na}}_{\kappa,\kappa'} \mathbf{u}_{\kappa'} = -e \sum_{\kappa} \mathbf{E}^{\mathsf{T}} \mathbf{Z}_{\kappa}^{\star} \mathbf{u}_{\kappa} - \frac{V_{\mathrm{pc}}}{2} \mathbf{E}^{\mathsf{T}} \chi \mathbf{E}. \tag{3.46}$$

Finally, substituting Eq. (3.45) into Eq. (3.46) allows us to write $\mathbf{D}^{\mathrm{na}}_{\kappa,\kappa'}$ in terms of $\mathbf{Z}_{\kappa}^{\star}$ and ϵ^{∞}:

$$\mathbf{D}^{\mathrm{na}}_{\kappa,\kappa'}(\mathbf{q} \to \mathbf{0}) = \frac{4\pi e^2}{V_{\mathrm{pc}} \sqrt{m_{\kappa} m_{\kappa'}}} \frac{\left(\mathbf{q}^{\mathsf{T}} \mathbf{Z}_{\kappa}\right) \otimes \left(\mathbf{q}^{\mathsf{T}} \mathbf{Z}_{\kappa'}\right)}{\mathbf{q}^{\mathsf{T}} \epsilon^{\infty} \mathbf{q}}. \tag{3.47}$$

Only the LO phonon modes are affected by this nonanalytic contribution to the dynamical matrix. In fact, the eigenvectors corresponding to the TO modes obey the following symmetry relation [87]:

$$\sum_{\kappa} \mathbf{q}^{\mathsf{T}} \mathbf{Z}_{\kappa}^{\star} \mathbf{e}_{\kappa} = \mathbf{0}. \tag{3.48}$$

This leads to a splitting of the otherwise degenerate optical phonon modes close to Γ. The LO phonons acquire more energy due to the coupling with the electric dipole field, and the associated frequencies are related to the TO frequencies via:

$$\omega^2_{\mathrm{LO},\mathbf{q}\to\mathbf{0}} - \omega^2_{\mathrm{TO},\mathbf{q}=\mathbf{0}} = \lim_{\mathbf{q}\to\mathbf{0}} \frac{4\pi e^2}{V_{\mathrm{pc}}} \sum_{\kappa} \frac{|\mathbf{q}^\top \mathbf{Z}_\kappa \mathbf{e}_{\kappa,\mathrm{TO},\mathbf{q}=\mathbf{0}}|^2}{\mathbf{q}^\top \boldsymbol{\epsilon}^\infty \mathbf{q}} \tag{3.49}$$

In anisotropic materials, where $\epsilon^\infty_{\alpha\beta} \neq \epsilon^\infty \delta_{\alpha\beta}$, the splitting also depends on the direction of $\mathbf{q}$ as $\mathbf{q} \to \mathbf{0}$. In other words, the LO phonon frequencies feature discontinuities around the Γ-point. Eq. (3.49) also recovers the correct behavior for vanishing Born effective charges, namely $\omega_{\mathrm{LO},\mathbf{q}=\mathbf{0}} = \omega_{\mathrm{TO},\mathbf{q}=\mathbf{0}}$.

3.6 Long-range Force Constants

In Section 3.5, we have seen how dipole-dipole interactions in polar materials yield a correction to the dynamical matrix at $\mathbf{q} \to \mathbf{0}$. In this section, we present a simple model function, inspired by electrostatics, to treat these long-range interactions also at finite phonon wave vector. This allows us to amend the Fourier-interpolation scheme even in the presence of long-range electrostatic interactions. A comprehensive derivation is given in Ref. [87].

To begin with, let us consider the electrostatic potential, $\phi(\mathbf{r}, \boldsymbol{\xi})$, at location $\mathbf{r}$ generated by a point charge with electric charge Q. The charge is situated at $\boldsymbol{\xi}$ inside a homogeneous dielectric characterized by the dielectric tensor $\boldsymbol{\epsilon}^\infty$. The potential, $\phi(\mathbf{r}, \boldsymbol{\xi})$, is a solution to the anisotropic macroscopic Poisson equation:

$$(\boldsymbol{\nabla}^\top \boldsymbol{\epsilon}^\infty \boldsymbol{\nabla})\phi(\mathbf{r}, \boldsymbol{\xi}) = -4\pi Q \delta^{(3)}(\mathbf{r} - \boldsymbol{\xi}). \tag{3.50}$$

The standard way of solving Eq. (3.50) is by using the Fourier transformation as the differential operators map to simple multiplications in Fourier space. Therefore, the potential on the left-hand side of Eq. (3.50) is expressed in reciprocal space using the inverse Fourier transform,

$$\phi(\mathbf{r}, \boldsymbol{\xi}) = \frac{1}{(2\pi)^3} \int_{\mathbb{R}^3} \mathrm{d}^3 q \, \mathrm{e}^{\mathrm{i}\mathbf{q}\cdot\mathbf{r}} \widetilde{\phi}(\mathbf{q}, \boldsymbol{\xi}), \tag{3.51}$$

$$(\boldsymbol{\nabla}^\top \boldsymbol{\epsilon}^\infty \boldsymbol{\nabla})\phi(\mathbf{r}, \boldsymbol{\xi}) = -\frac{1}{(2\pi)^3} \int_{\mathbb{R}^3} \mathrm{d}^3 q \, \mathrm{e}^{\mathrm{i}\mathbf{q}\cdot\mathbf{r}} (\mathbf{q}^\top \boldsymbol{\epsilon}^\infty \mathbf{q}) \widetilde{\phi}(\mathbf{q}, \boldsymbol{\xi}). \tag{3.52}$$

The reciprocal-space solution, $\widetilde{\phi}(\mathbf{q}, \boldsymbol{\xi})$, is then retrieved by Fourier transforming both sides of Eq. (3.50):

$$\widetilde{\phi}(\mathbf{q}, \boldsymbol{\xi}) = 4\pi Q \frac{\mathrm{e}^{-\mathrm{i}\mathbf{q}\cdot\boldsymbol{\xi}}}{\mathbf{q}^\top \boldsymbol{\epsilon}^\infty \mathbf{q}}, \tag{3.53}$$

which can be substituted back into Eq. (3.51) to obtain the real-space solution:

$$\phi(\mathbf{r}, \boldsymbol{\xi}) = \frac{Q}{2\pi^2} \int_{\mathbb{R}^3} \mathrm{d}^3 q \, \frac{\mathrm{e}^{\mathrm{i}\mathbf{q}\cdot(\mathbf{r}-\boldsymbol{\xi})}}{\mathbf{q}^\top \boldsymbol{\epsilon}^\infty \mathbf{q}}. \tag{3.54}$$

Going from the potential of a point charge in Eq. (3.54) to the potential generated by a dipole with dipole moment $\mathbf{p}$ located at $\boldsymbol{\xi}$ is straight forward [88]:

$$\phi^{\mathrm{d}}(\mathbf{r},\boldsymbol{\xi},\mathbf{p}) = \left[-\frac{1}{Q}\mathbf{p}\cdot\boldsymbol{\nabla}^{\xi'}\phi(\mathbf{r},\boldsymbol{\xi}')\right]_{\xi} = -\frac{\mathrm{i}}{2\pi^2}\int_{\mathbb{R}^3}\mathrm{d}^3q\,\frac{\mathbf{p}\cdot\mathbf{q}}{\mathbf{q}^\top\boldsymbol{\epsilon}^\infty\mathbf{q}}\mathrm{e}^{\mathrm{i}\mathbf{q}\cdot(\mathbf{r}-\boldsymbol{\xi})}. \tag{3.55}$$

The microscopic electric field, $\mathbf{E}^{\mathrm{d}}$, generated by this dipole is obtained as the gradient of its potential:

$$\mathbf{E}^{\mathrm{d}}(\mathbf{r},\boldsymbol{\xi},\mathbf{p}) = \left[-\boldsymbol{\nabla}^{r'}\phi^{\mathrm{d}}(\mathbf{r}',\boldsymbol{\xi},\mathbf{p})\right]_{\mathbf{r}} = -\frac{1}{2\pi^2}\int_{\mathbb{R}^3}\mathrm{d}^3q\,\mathbf{q}\frac{\mathbf{p}\cdot\mathbf{q}}{\mathbf{q}^\top\boldsymbol{\epsilon}^\infty\mathbf{q}}\mathrm{e}^{\mathrm{i}\mathbf{q}\cdot(\mathbf{r}-\boldsymbol{\xi})}. \tag{3.56}$$

We can see that Eq. (3.56) looks similar to Eq. (3.45) with the dipole shifted to $\boldsymbol{\xi}$.

Let us now place another dipole, $\mathbf{p}'$, inside this field at the location $\mathbf{r}$. The potential energy of the resulting dipole-dipole system is then given as $\mathbf{p}'\cdot\mathbf{E}^{\mathrm{d}}$. In a vibrating polar material, each such dipole originates from the displacement of an atom and is proportional to the Born effective-charge tensor. For small atomic displacements, $\mathbf{u}_{l\kappa}$, Eq. (3.38) provides the following linear relationship between the displacement and the induced dipole moment for each atom:

$$\mathbf{p}_{l\kappa} = e\mathbf{Z}^{\star}_{\kappa}\mathbf{u}_{l\kappa}. \tag{3.57}$$

The location of each dipole is then fixed at the respective atomic site, i.e., $\mathbf{r} = \mathbf{R}_{l\kappa}$ and $\boldsymbol{\xi} = \mathbf{R}_{l'\kappa'}$. Substituting $\mathbf{p}$, $\mathbf{p}'$, $\mathbf{r}$ and $\boldsymbol{\xi}$ according to these considerations into the potential energy expression and summing over all pairs of atomic sites yields the total dipole-dipole potential energy of the crystal, U^{dd}:

$$U^{\mathrm{dd}} = -\frac{1}{2}\sum_{l\kappa}\sum_{l'\kappa'}\frac{e^2}{2\pi^2}\int_{\mathbb{R}^3}\mathrm{d}^3q\,\frac{\mathbf{q}^\top\mathbf{Z}^{\star}_{\kappa}\mathbf{u}_{l\kappa}\mathbf{q}^\top\mathbf{Z}^{\star}_{\kappa'}\mathbf{u}_{l'\kappa'}}{\mathbf{q}^\top\boldsymbol{\epsilon}^\infty\mathbf{q}}\mathrm{e}^{\mathrm{i}\mathbf{q}\cdot(\mathbf{R}_{l\kappa}-\mathbf{R}_{l'\kappa'})}, \tag{3.58}$$

where double-counting corrections are accounted for via a factor of $\frac{1}{2}$. By comparing Eq. (3.58) against the second-order term in the Taylor expansion, Eq. (3.2), we can identify the long-range dipole-dipole contribution to the IFC matrix, $\boldsymbol{\Phi}^{\mathrm{LR}}_{l\kappa,l'\kappa'}$:

$$U^{\mathrm{dd}} = -\frac{1}{2}\sum_{l\kappa}\sum_{l'\kappa'}\mathbf{u}^\top_{l\kappa}\boldsymbol{\Phi}^{\mathrm{LR}}_{l\kappa,l'\kappa'}\mathbf{u}_{l'\kappa'}, \tag{3.59}$$

$$\boldsymbol{\Phi}^{\mathrm{LR}}_{l\kappa,l'\kappa'} = \frac{e^2}{2\pi^2}\int_{\mathbb{R}^3}\mathrm{d}^3q\,\frac{\left(\mathbf{q}^\top\mathbf{Z}^{\star}_{\kappa}\right)\otimes\left(\mathbf{q}^\top\mathbf{Z}^{\star}_{\kappa'}\right)}{\mathbf{q}^\top\boldsymbol{\epsilon}^\infty\mathbf{q}}\mathrm{e}^{\mathrm{i}\mathbf{q}\cdot(\mathbf{R}_{l\kappa}-\mathbf{R}_{l'\kappa'})}. \tag{3.60}$$

Following the definition of the dynamical matrix in Eq. (3.7), the corresponding long-range dipole-dipole dynamical matrix, $\mathbf{D}^{\mathrm{LR}}_{\kappa\kappa'}(\mathbf{q})$, is obtained via a Fourier transform:

$$\mathbf{D}^{\mathrm{LR}}_{\kappa\kappa',\mathbf{q}} = \frac{e^2}{2\pi^2\sqrt{m_\kappa m_{\kappa'}}} \times\int_{\mathbb{R}^3}\mathrm{d}^3q'\,\frac{\left(\mathbf{q}'^\top\mathbf{Z}^{\star}_{\kappa}\right)\otimes\left(\mathbf{q}'^\top\mathbf{Z}^{\star}_{\kappa'}\right)}{\mathbf{q}'^\top\boldsymbol{\epsilon}^\infty\mathbf{q}'}\mathrm{e}^{\mathrm{i}\mathbf{q}'\cdot(\tau_\kappa-\tau_{\kappa'})}\sum_{l}\mathrm{e}^{\mathrm{i}\mathbf{R}_l\cdot(\mathbf{q}-\mathbf{q}')}. \tag{3.61}$$

Some care must be taken when performing the sum over all cells. Since the domain of integration encompasses all of reciprocal space, the sum does not evaluate to a single Dirac-delta function confined to the FBZ, but rather to a three-dimensional Dirac comb where the spacing between individual Dirac peaks is equal to reciprocal-lattice vectors, $\mathbf{G}$:

$$\sum_{l} \mathrm{e}^{\mathrm{i}\mathbf{R}_l\cdot(\mathbf{q}-\mathbf{q}')} = \Omega_{\mathrm{BZ}} \sum_{\mathbf{G}}^{\mathrm{pc}} \delta^{(3)}(\mathbf{q}' - \mathbf{q} - \mathbf{G}). \tag{3.62}$$

This is a simple consequence of the fact that $\mathrm{e}^{\mathrm{i}\mathbf{R}_l\cdot\mathbf{G}} = 1$. For improved clarity in this section, the letters "pc" appear above the sum, indicating that it runs over all reciprocal-lattice vectors of the *primitive cell*.

Combining Eqs. (3.61) and (3.62) and performing the integration over $\mathbf{q}'$ yields the following expression for the long-range dynamical matrix:

$$\mathbf{D}^{\mathrm{LR}}_{\kappa\kappa',\mathbf{q}} = \frac{4\pi e^2}{V_{\mathrm{pc}}\sqrt{m_\kappa m_{\kappa'}}} \sum_{\substack{\mathbf{G}\neq-\mathbf{q} \\ \mathbf{K}\equiv\mathbf{q}+\mathbf{G}}}^{\mathrm{pc}} \frac{\left(\mathbf{K}^\top \mathbf{Z}^\star_\kappa\right)\otimes\left(\mathbf{K}^\top \mathbf{Z}^\star_{\kappa'}\right)}{\mathbf{K}^\top \boldsymbol{\epsilon}^\infty \mathbf{K}} \mathrm{e}^{\mathrm{i}\mathbf{K}\cdot(\tau_\kappa-\tau_{\kappa'})}. \tag{3.63}$$

At first glance, Eq. (3.63) looks very similar to Eq. (3.47). However, in Eq. (3.63) appear an additional phase factor and a sum over reciprocal-lattice vectors. Indeed, the nonanalytic, direction-dependent part of the dynamical matrix defined in Eq. (3.47) is recovered from Eq. (3.63) for $\mathbf{G} = \mathbf{0}$ in the limit $\mathbf{q} \to \mathbf{0}$.

Importantly, Eq. (3.63) provides a way to amend the Fourier-interpolation scheme outlined in Section 3.4. Conceptually, the full interpolation procedure works as follows:

1. The IFC matrix is calculated for a certain supercell from finite differences.
2. From this IFC matrix, the dynamical matrix is calculated at the set $\{\mathbf{q}_c\}$ of q-points commensurate with the supercell.
3. At each such q-point, the long-range contribution, $\mathbf{D}^{\mathrm{LR}}_{\kappa\kappa',\mathbf{q}}$, is removed from the dynamical matrix.
4. The resulting short-range dynamical matrix, $\mathbf{D}^{\mathrm{SR}}_{\kappa\kappa',\{\mathbf{q}_c\}}$, is transformed back to the supercell to obtain a short-range IFC matrix, $\boldsymbol{\Phi}^{\mathrm{SR}}_{l\kappa,l'\kappa'}$.
5. For an arbitrary q-point, $\mathbf{q}$, $\boldsymbol{\Phi}^{\mathrm{SR}}_{l\kappa,l'\kappa'}$ is interpolated to $\mathbf{D}^{\mathrm{SR}}_{\kappa\kappa',\mathbf{q}}$.
6. $\mathbf{D}^{\mathrm{LR}}_{\kappa\kappa',\mathbf{q}}$ is calculated and added back to $\mathbf{D}^{\mathrm{SR}}_{\kappa\kappa',\mathbf{q}}$ to obtain the full dynamical matrix at $\mathbf{q}$.

We note that a popular alternative to steps 1. and 2. is to calculate the dynamical matrix directly at the commensurate q-points using DFPT. In this work, however,

we rely on the calculation of the IFC matrix via finite displacements in large supercells. Consequently, after careful consideration, one finds that steps 2.-4. can be simplified by formulating $\mathbf{\Phi}^{\mathrm{SR}}_{l\kappa,l'\kappa'}$ explicitly in the supercell.

The short-range IFC matrix, $\mathbf{\Phi}^{\mathrm{SR}}_{l\kappa,l'\kappa'}$, can be obtained by removing the long-range part, $\mathbf{\Phi}^{\mathrm{LR}}_{l\kappa,l'\kappa'}$ from the IFC matrix obtained from finite differences, i.e.,

$$\mathbf{\Phi}^{\mathrm{SR}}_{l\kappa,l'\kappa'} = \mathbf{\Phi}_{l\kappa,l'\kappa'} - \mathbf{\Phi}^{\mathrm{LR}}_{l\kappa,l'\kappa'}. \tag{3.64}$$

$\mathbf{\Phi}^{\mathrm{LR}}_{l\kappa,l'\kappa'}$ can be obtained from Eq. (3.63) by means of an inverse Fourier transform involving only the set $\{\mathbf{q}_c\}$ of commensurate q-points. This results in a double sum over reciprocal-lattice points:

$$\sum_{\mathbf{q}\in\{\mathbf{q}_c\}} \sum_{\mathbf{G}\neq-\mathbf{q}}^{\mathrm{pc}}$$

In this context, we need to realize that $\mathbf{G}$ are reciprocal-lattice vectors of the *primitive cell* spanning all of reciprocal space, while $\mathbf{q}$ are reciprocal-lattice vectors of the *supercell* confined to its FBZ. Therefore, the entire set of vectors $\mathbf{K} = \mathbf{q} + \mathbf{G}$ can be identified as the reciprocal lattice of the *supercell*, without Γ. This simple trick leads to a very simple expression for the long-range IFC matrix:

$$\mathbf{\Phi}^{\mathrm{LR}}_{l\kappa,0\kappa'} = \frac{4\pi e^2}{V_{\mathrm{pc}}\sqrt{m_\kappa m_{\kappa'}}} \sum_{\mathbf{G}\neq\mathbf{0}}^{\mathrm{sc}} \frac{\left(\mathbf{G}^\top \mathbf{Z}^\star_\kappa\right)\otimes\left(\mathbf{G}^\top \mathbf{Z}^\star_{\kappa'}\right)}{\mathbf{G}^\top \boldsymbol{\epsilon}^\infty \mathbf{G}} e^{i\mathbf{G}\cdot(\mathbf{R}_{l\kappa}-\mathbf{R}_{0\kappa'})}, \tag{3.65}$$

where "sc" indicates the summation over all reciprocal-lattice vectors of the *supercell*.

In general, the short-range matrix, $\mathbf{\Phi}^{\mathrm{SR}}_{l\kappa,l'\kappa'}$, decays faster as a function of distance between atoms than the unmodified IFC matrix, $\mathbf{\Phi}_{l\kappa,l'\kappa'}$. Fig. 3.4 illustrates this for the case of MgO, a prototypical polar material.

Finally, Figs. 3.5 and 3.6 show examples of dispersion relations for polar materials that are obtained using the interpolation technique discussed in this section. Fig. 3.5 highlights the effects of LO-TO splitting in MgO. In this case, the LO-TO splitting is strongly pronounced. Fig. 3.6 shows the phonon dispersion relation of AlN in the wurtzite structure. The wurtzite structure is more anisotropic than cubic crystals. Therefore, in addition to LO-TO splitting, the phonon frequencies are discontinuous at Γ.

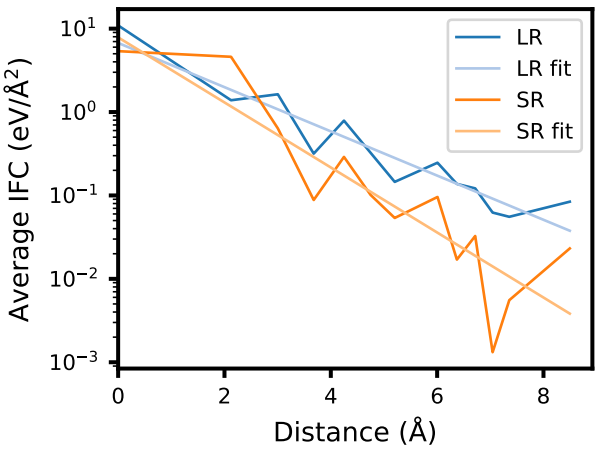

Figure 3.4: $\mathbf{\Phi}_{l\kappa,0\kappa'}$ (blue) and $\mathbf{\Phi}^{\mathrm{LR}}_{l\kappa,0\kappa'}$ (orange) IFC matrices of MgO as functions of distance between atoms. For each possible interatomic distance, a data point is obtained by averaging the absolute values of the corresponding IFC matrix elements. In addition, a linear fit is shown for each data set on the logarithmic scale, indicating the exponential decay. The short-range matrix decays faster.

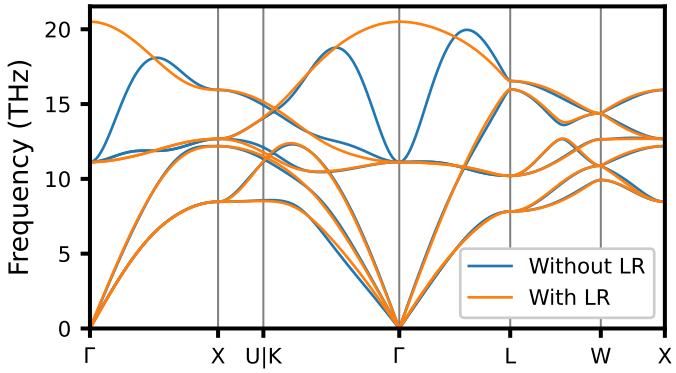

Figure 3.5: Phonon dispersion relation of MgO obtained from a 4×4×4 supercell via Fourier interpolation. The blue lines neglect long-range electrostatic effects. The orange lines include dipole-dipole corrections, which leads to LO-TO splitting.

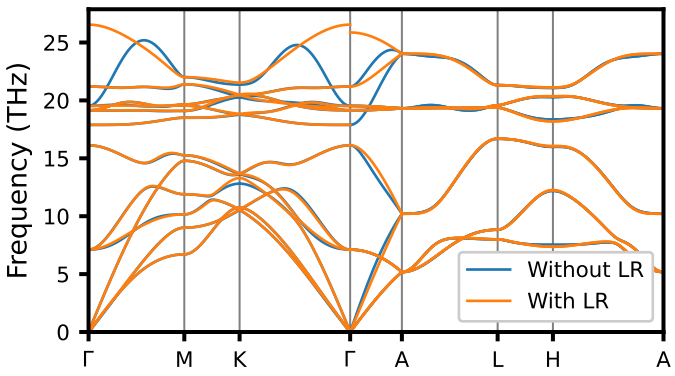

Figure 3.6: Phonon dispersion relation of AlN in the wurtzite structure obtained from a 4×4×4 supercell via Fourier interpolation. The blue lines neglect long-range electrostatic effects. The orange lines include dipole-dipole corrections, which leads to LO-TO splitting and discontinuous phonon frequencies at Γ.

CHAPTER 4

Electron-Phonon Interactions

4.1 Allen-Heine-Cardona Approach

As alluded to in Chapter 1, electron-phonon interactions can have a profound effect on the electronic band structure. Before we delve into the sophisticated theoretical background of this topic, we look at it from a more historical perspective. The earliest ZPR calculations for real materials was performed by Allen, Heine and Cardona (AHC) [89, 90] around 1980. They used Rayleigh-Schrödinger perturbation theory [91, 92] to determine the change of the electronic eigenvalues due to a static phonon perturbation. This method lays the foundation for many modern approaches. In this section, we briefly demonstrate how the AHC theory can be derived. While not technically necessary, this provides context for when we generalize it to the PAW method in Section 4.4.1. The connection to many-body perturbation theory is established in Section 4.3.

To begin with, let us write the fully renormalized energy, $E_{n\mathbf{k}}(T)$, of a KS state as a perturbative expansion in terms of the atomic displacements, $\mathbf{u}_{l\kappa}$:

$$E_{n\mathbf{k}}(T) = \varepsilon_{n\mathbf{k}} + \sum_{l\kappa\alpha} \left(\frac{\partial \varepsilon_{n\mathbf{k}}}{\partial u_{l\kappa\alpha}} \right)_0 \langle u_{l\kappa\alpha} \rangle_T + \Delta\varepsilon_{n\mathbf{k}}(T) + \ldots \tag{4.1}$$

$$\Delta\varepsilon_{n\mathbf{k}}(T) = \frac{1}{2} \sum_{l\kappa\alpha} \sum_{l'\kappa'\beta} \left(\frac{\partial^2 \varepsilon_{n\mathbf{k}}}{\partial u_{l\kappa\alpha}\, \partial u_{l'\kappa'\beta}} \right)_0 \langle u_{l\kappa\alpha} u_{l'\kappa'\beta} \rangle_T \,. \tag{4.2}$$

Here we use the same notational conventions as in the case of phonons, for example, in Eq. (3.2). Furthermore, $\varepsilon_{n\mathbf{k}}$ are the KS eigenvalues of the unperturbed system. The notation $\langle \mathbf{u} \rangle_T$ indicates that the corresponding atomic displacement is given by a thermal expectation value at temperature T.

The first-order term in Eq. (4.1) is often disregarded. A common justification is that the perturbation needs to vanish at linear order for symmetry reasons. However, in the presence of degeneracies this is not necessarily the case. Regardless, we do not comment any further on this point and only consider the second-order term to be non-zero.

Currently, the phonon perturbation in Eq. (4.2) is written as a double sum over individual atomic displacements, $\mathbf{u}_{l\kappa}$. In the end, we would like to express everything in terms of collective phonon excitations. To achieve this goal, we promote each atomic displacement, $\mathbf{u}_{l\kappa}$, to an operator and use Eq. (3.11) to express them in terms of phonon creation and annihilation operators:

$$\hat{\mathbf{u}}_{l\kappa} = \sum_{\nu} \int_{\Omega_{\mathrm{BZ}}} \frac{\mathrm{d}^3 q}{\Omega_{\mathrm{BZ}}} \sqrt{\frac{\hbar}{2m_\kappa \omega_{\nu\mathbf{q}}}} \mathbf{e}_{\kappa,\nu\mathbf{q}} \mathrm{e}^{\mathrm{i}\mathbf{q}\cdot\mathbf{R}_l} \left(\hat{b}_{\nu\mathbf{q}} + \hat{b}^\dagger_{\nu,-\mathbf{q}}\right), \tag{4.3}$$

where we have summed over the phononic degrees of freedom, ν and $\mathbf{q}$. We can now interpret the thermal expectation values in Eq. (4.1) as the expectation value of a multi-particle phonon state at temperature T. Thus,

$$\begin{aligned}\langle u_{l\kappa\alpha} u_{l'\kappa'\beta} \rangle_T = \frac{\hbar}{2} \sum_{\nu\nu'} \int_{\Omega_{\mathrm{BZ}}} \frac{\mathrm{d}^3 q}{\Omega_{\mathrm{BZ}}} \int_{\Omega_{\mathrm{BZ}}} \frac{\mathrm{d}^3 q'}{\Omega_{\mathrm{BZ}}} \frac{e_{\kappa\alpha,\nu\mathbf{q}} e_{\kappa'\beta,\nu'\mathbf{q}'}}{\sqrt{m_\kappa m_{\kappa'} \omega_{\nu\mathbf{q}} \omega_{\nu'\mathbf{q}'}}} \\ \times \mathrm{e}^{\mathrm{i}\mathbf{q}\cdot\mathbf{R}_l + \mathrm{i}\mathbf{q}'\cdot\mathbf{R}_{l'}} \left\langle \left(\hat{b}_{\nu\mathbf{q}} + \hat{b}^\dagger_{\nu,-\mathbf{q}}\right)\left(\hat{b}_{\nu'\mathbf{q}'} + \hat{b}^\dagger_{\nu',-\mathbf{q}'}\right)\right\rangle_T .\end{aligned} \tag{4.4}$$

The expectation value between phonon states results in:

$$\begin{aligned}&\left\langle \left(\hat{b}_{\nu\mathbf{q}} + \hat{b}^\dagger_{\nu,-\mathbf{q}}\right)\left(\hat{b}_{\nu'\mathbf{q}'} + \hat{b}^\dagger_{\nu',-\mathbf{q}'}\right)\right\rangle_T \\ &= \langle \hat{b}_{\nu\mathbf{q}} \hat{b}^\dagger_{\nu',-\mathbf{q}'} + \hat{b}^\dagger_{\nu,-\mathbf{q}} \hat{b}_{\nu'\mathbf{q}'} \rangle_T + \underbrace{\langle \hat{b}_{\nu\mathbf{q}} \hat{b}_{\nu'\mathbf{q}'} + \hat{b}^\dagger_{\nu,-\mathbf{q}} \hat{b}^\dagger_{\nu',-\mathbf{q}'} \rangle_T}_{=0} \\ &= \Omega_{\mathrm{BZ}} \delta_{\nu\nu'} \delta^{(3)}(\mathbf{q} + \mathbf{q}') \langle 2\hat{n}^{\mathrm{p}}_{\nu\mathbf{q}} + 1 \rangle_T \\ &= \Omega_{\mathrm{BZ}} \delta_{\nu\nu'} \delta^{(3)}(\mathbf{q} + \mathbf{q}') \left[2n_{\nu\mathbf{q}}(T) + 1\right],\end{aligned} \tag{4.5}$$

where we used the commutation relation in Eq. (3.13) and the definition of the phonon number operator, Eq. (3.24). Additionally, the number of phonons in each state at temperature T is given by the Bose-Einstein distribution, Eq. (4.17). This allows us to simplify the thermal expectation value:

$$\langle u_{l\kappa\alpha} u_{l'\kappa'\beta} \rangle_T = \hbar \sum_{\nu} \int_{\Omega_{\mathrm{BZ}}} \frac{\mathrm{d}^3 q}{\Omega_{\mathrm{BZ}}} \frac{e_{\kappa\alpha,\nu\mathbf{q}} e^*_{\kappa'\beta,\nu\mathbf{q}}}{\omega_{\nu\mathbf{q}} \sqrt{m_\kappa m_{\kappa'}}} \mathrm{e}^{\mathrm{i}\mathbf{q}\cdot(\mathbf{R}_l - \mathbf{R}_{l'})} \left[n_{\nu\mathbf{q}}(T) + \frac{1}{2}\right]. \tag{4.6}$$

Finally, after substituting Eq. (4.6) back into Eq. (4.2), we obtain:

$$\Delta\varepsilon_{n\mathbf{k}}(T) = \sum_{\nu} \int_{\Omega_{\mathrm{BZ}}} \frac{\mathrm{d}^3 q}{\Omega_{\mathrm{BZ}}} \left[n_{\nu\mathbf{q}}(T) + \frac{1}{2}\right] \partial_{\nu\mathbf{q}} \partial_{\nu,-\mathbf{q}} \varepsilon_{n\mathbf{k}}, \tag{4.7}$$

where we have defined the phonon displacement operator,

$$\partial_{\nu\mathbf{q}} \equiv \sum_{l\kappa\alpha} \sqrt{\frac{\hbar}{2m_\kappa \omega_{\nu\mathbf{q}}}} e_{\kappa\alpha,\nu\mathbf{q}} \mathrm{e}^{\mathrm{i}\mathbf{q}\cdot\mathbf{R}_l} \frac{\partial}{\partial u_{l\kappa\alpha}}, \tag{4.8}$$

following Eq. (3.11). Eq. (4.7) describes the energy shift as a weighted second-order change of the KS eigenvalues due to phonons. The weight is given simply as the number of phonons in each state at the given temperature plus a fixed contribution 1/2 from zero-point vibrations.

What remains is to determine the second derivative of the electronic eigenvalues in terms of the phonon displacement operator. This can be accomplished by differentiating the KS equations, Eq. (2.11), which follows standard perturbation theory. We choose to forgo this part of the derivation as we will perform a more detailed derivation in Section 4.4.1 in the context of the PAW method. Instead, we simply state the final result for the AHC theory:

$$\Delta\varepsilon_{n\mathbf{k}}^{\mathrm{AHC}}(T) \equiv \sum_{\nu} \int_{\Omega_{\mathrm{BZ}}} \frac{\mathrm{d}^3 q}{\Omega_{\mathrm{BZ}}} \big(2n_{\nu\mathbf{q}}(T) + 1\big) \times \mathrm{Re}\left(\sum_{m} \frac{|g_{mn\mathbf{k},\nu\mathbf{q}}|^2}{\varepsilon_{n\mathbf{k}} - \varepsilon_{m\mathbf{k}+\mathbf{q}} + \mathrm{i}\delta} + g^{\mathrm{DW}}_{nn\mathbf{k},\nu\mathbf{q},\nu,-\mathbf{q}} \right), \tag{4.9}$$

with

$$g_{mn\mathbf{k},\nu\mathbf{q}} \equiv \langle \psi_{m\mathbf{k}+\mathbf{q}} | \partial_{\nu\mathbf{q}} \hat{H} | \psi_{n\mathbf{k}} \rangle \,, \tag{4.10}$$

$$g^{\mathrm{DW}}_{mn\mathbf{k},\nu\mathbf{q},\nu'\mathbf{q}'} \equiv \frac{1}{2} \langle \psi_{m\mathbf{k}+\mathbf{q}+\mathbf{q}'} | \partial_{\nu\mathbf{q}} \partial_{\nu'\mathbf{q}'} \hat{H} | \psi_{n\mathbf{k}} \rangle \,. \tag{4.11}$$

$g_{mn\mathbf{k},\nu\mathbf{q}}$ and $g^{\mathrm{DW}}_{mn\mathbf{k},\nu\mathbf{q},\nu'\mathbf{q}'}$ are first and second-order coupling strengths. The former is simply called the electron-phonon matrix element, while the latter is referred to as the Debye-Waller (DW) matrix element. In this case, both are expressed in the basis of KS states. The imaginary shift $\mathrm{i}\delta$ is added artificially to avoid divergent contributions from degenerate states. In the context of many-body perturbation theory, this shift arises naturally from switching on the perturbation adiabatically.

The problem of calculating the band-structure renormalization in the AHC theory essentially reduces to calculating the first and second-order matrix elements. In Section 4.5, we will see how $g^{\mathrm{DW}}_{mn\mathbf{k},\nu\mathbf{q},\nu'\mathbf{q}'}$ can be approximated in terms of $g_{mn\mathbf{k},\nu\mathbf{q}}$. Therefore, only the electron-phonon matrix elements, electronic eigenvalues and phonon frequencies are required at a sufficiently dense set of points throughout the FBZ. The following sections introduce various representations of the electron-phonon matrix element in the PAW method. First, however, we take a step back and look at electron-phonon interactions from the picture of many-body perturbation theory.

4.2 Electron-Phonon Hamiltonian and Matrix Elements

Studying the interaction between electrons and phonons is best done in the language of second quantization. It offers a rigorous and intuitive way of handling

the complexities encountered in many-body theories. In this language, the Hamiltonian describing the interacting electron-phonon system up to second order is given as [25]:

$$\hat{H}_\mathrm{e} + \hat{H}_\mathrm{p} + \hat{H}_\mathrm{ep}^{(1)} + \hat{H}_\mathrm{ep}^{(2)},$$

where $\hat{H}_\mathrm{e}$ and $\hat{H}_\mathrm{p}$ are the free-electron and free-phonon Hamiltonian, defined in Eq. (B.1) and Eq. (3.23), respectively. The term $\hat{H}_\mathrm{ep}^{(1)}$ describes the electron-phonon interaction to first-order in the atomic displacements and is given by:

$$\hat{H}_\mathrm{ep}^{(1)} = \sum_{mn\nu} \int_{\Omega_\mathrm{BZ}} \frac{\mathrm{d}^3k}{\Omega_\mathrm{BZ}} \int_{\Omega_\mathrm{BZ}} \frac{\mathrm{d}^3q}{\Omega_\mathrm{BZ}} g_{mn\mathbf{k},\nu\mathbf{q}} \hat{c}^\dagger_{m\mathbf{k}+\mathbf{q}} \hat{c}_{n\mathbf{k}} \left(\hat{b}_{\nu\mathbf{q}} + \hat{b}^\dagger_{\nu,-\mathbf{q}}\right). \tag{4.12}$$

This combination of creation and annihilation operators describes a scattering process in which an incoming electron with momentum $\mathbf{k}$ is scattered into a final state with momentum $\mathbf{k}+\mathbf{q}$ by either absorbing ($\hat{b}_{\nu\mathbf{q}}$) or emitting ($\hat{b}^\dagger_{\nu,-\mathbf{q}}$) a phonon with wave vector $\mathbf{q}$. The coupling strength of this fundamental scattering process is given by the electron-phonon matrix element, $g_{mn\mathbf{k},\nu\mathbf{q}}$. We have introduced this quantity earlier in Eq. (4.10) expressed in the basis of KS states.

To second-order in the atomic displacements is where the term $\hat{H}_\mathrm{ep}^{(2)}$ contributes:

$$\hat{H}_\mathrm{ep}^{(2)} = \sum_{mn\nu\nu'} \int_{\Omega_\mathrm{BZ}} \frac{\mathrm{d}^3k}{\Omega_\mathrm{BZ}} \int_{\Omega_\mathrm{BZ}} \frac{\mathrm{d}^3q}{\Omega_\mathrm{BZ}} \int_{\Omega_\mathrm{BZ}} \frac{\mathrm{d}^3q'}{\Omega_\mathrm{BZ}} g^\mathrm{DW}_{mn\mathbf{k},\nu\mathbf{q},\nu'\mathbf{q}'} \times \hat{c}^\dagger_{m\mathbf{k}+\mathbf{q}+\mathbf{q}'} \hat{c}_{n\mathbf{k}} \left(\hat{b}_{\nu\mathbf{q}} + \hat{b}^\dagger_{\nu,-\mathbf{q}}\right)\left(\hat{b}_{\nu'\mathbf{q}'} + \hat{b}^\dagger_{\nu',-\mathbf{q}'}\right). \tag{4.13}$$

In this case, the process involves the simultaneous emission or absorption of two phonons with wave vectors $\mathbf{q}$ and $\mathbf{q}'$, respectively. The DW matrix element, $g^\mathrm{DW}_{mn\mathbf{k},\nu\mathbf{q},\nu'\mathbf{q}'}$, was also introduced earlier in Eq. (4.11) in terms of KS states. We like to point out that the truncation of the electron-phonon Hamiltonian at second order follows the harmonic approximation. Therefore, anharmonic contributions to the electron-phonon interaction will not be captured by this description.

4.3 Electron Self-Energy

During the propagation of an electron through a material, the electron can interact with the sea of phonons created by the vibrations of the crystal lattice. This dynamical process can be viewed as a kind of phonon-mediated electron self-interaction that effectively renormalizes the propagator of the electron as well as its energy. In this section, we quickly summarize the electron self-energy on the level of DFT.

Going from the sophisticated set of Hedin-Baym equations [10, 93] to a perturbative theory on the level of DFT requires multiple approximations. They are aptly summarized in Sec. V.B.2 of Ref. [25]. Equivalently, one can employ many-body perturbation theory up to second order to obtain the same results. At

second order in the atomic displacements, the temperature-dependent phonon-induced electron self-energy, $\Sigma_{nn'\mathbf{k}}(\omega, T)$, can be written as a sum of a frequency-dependent and a static part:

$$\Sigma_{nn'\mathbf{k}}(\omega, T) = \Sigma^{\mathrm{FM}}_{nn'\mathbf{k}}(\omega, T) + \Sigma^{\mathrm{DW}}_{nn'\mathbf{k}}(T). \tag{4.14}$$

The frequency-dependent part is commonly referred to as the Fan-Migdal (FM) self-energy [89, 90, 94–97] and the purely static part as the DW self-energy [98–100]. Each term is described by a Feynman diagram involving the exchange of one virtual phonon.

Let us first discuss the FM self-energy, whose Feynman diagram is shown in Fig. 4.1a. In this case, a phonon is spontaneously emitted and later reabsorbed

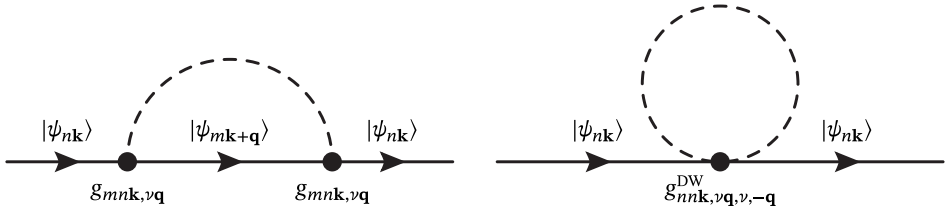

(a) FM process; a phonon with wave vector $\mathbf{q}$ and branch index ν is emitted and later reabsorbed.

(b) DW process; a phonon is simultaneously emitted and reabsorbed. Note that there is no momentum transfer in this case.

Figure 4.1: Feynman-diagrammatic representation of the lowest-order electron-phonon contributions to the band-diagonal electron self-energy in the context of KS DFT. Electronic states (solid lines) interact with phonon states (dashed lines) via the first and second-order electron-phonon matrix elements, $g_{mn\mathbf{k},\nu\mathbf{q}}$ and $g^{\mathrm{DW}}_{mn\mathbf{k},\nu\mathbf{q},\nu'\mathbf{q}'}$, respectively.

by the propagating electron. The intermediate electron and phonon lines correspond to the unperturbed electron and phonon Green's functions, respectively. Each of the two vertices in the Feynman diagram corresponds to a first-order electron-phonon matrix element defined in Eq. (4.10). After combining these ingredients in the usual way, one arrives at an expression for the FM self-energy that is valid only at absolute-zero temperature. Fortunately, there is a standard way of extending this result to finite temperature, namely the Matsubara formalism [101]. Ultimately, this gives the following expression for the FM self-energy:

$$\begin{aligned}\Sigma^{\mathrm{FM}}_{nn'\mathbf{k}}(\omega, T) = \sum_{m\nu} \int_{\Omega_{\mathrm{BZ}}} \frac{\mathrm{d}^3 q}{\Omega_{\mathrm{BZ}}} g^*_{mn\mathbf{k},\nu\mathbf{q}} g_{mn'\mathbf{k},\nu\mathbf{q}} \\ \times \left[\frac{1 - f_{m\mathbf{k+q}}(T) + n_{\nu\mathbf{q}}(T)}{\hbar\omega - \varepsilon_{m\mathbf{k+q}} - \hbar\omega_{\nu\mathbf{q}} + \mathrm{i}\delta} + \frac{f_{m\mathbf{k+q}}(T) + n_{\nu\mathbf{q}}(T)}{\hbar\omega - \varepsilon_{m\mathbf{k+q}} + \hbar\omega_{\nu\mathbf{q}} + \mathrm{i}\delta} \right].\end{aligned} \tag{4.15}$$

$f_{m\mathbf{k+q}}(T)$ and $n_{\nu\mathbf{q}}(T)$ are the Fermi-Dirac and Bose-Einstein distribution functions for the electron and phonon occupancies, respectively. They are defined as

usual:

$$f_{n\mathbf{k}}(T) = \left(\mathrm{e}^{\frac{\varepsilon_{n\mathbf{k}}-\varepsilon_\mathrm{F}}{k_\mathrm{B}T}} + 1\right)^{-1}, \tag{4.16}$$

$$n_{\nu\mathbf{q}}(T) = \left(\mathrm{e}^{\frac{\hbar\omega_{\nu\mathbf{q}}}{k_\mathrm{B}T}} - 1\right)^{-1}, \tag{4.17}$$

where ε_F is the Fermi level. δ is a positive infinitesimal that ensures the correct pole structure in the complex plane.

Next, let us discuss the DW self-energy, whose Feynman diagram is shown in Fig. 4.1b. In this case, the virtual phonon is emitted and reabsorbed simultaneously. This is a second-order scattering process in the sense that the associated coupling, $g^{\mathrm{DW}}_{mn\mathbf{k},\nu\mathbf{q},\nu'\mathbf{q}'}$, defined in Eq. (4.11), contains the *second*-order response of the Hamiltonian to a lattice excitation. At finite temperature, the resulting DW self-energy has the following form:

$$\Sigma^{\mathrm{DW}}_{nn'\mathbf{k}}(T) = \sum_\nu \int_{\Omega_\mathrm{BZ}} \frac{\mathrm{d}^3q}{\Omega_\mathrm{BZ}} g^{\mathrm{DW}}_{nn'\mathbf{k},\nu\mathbf{q},\nu,-\mathbf{q}}\big(2n_{\nu\mathbf{q}}(T)+1\big). \tag{4.18}$$

While the DW self-energy is real, the FM self-energy is complex valued. This is important as we can attribute different physical meaning to the real and imaginary parts of the self-energy. The real part is related to a shift of the quasiparticle poles of the associated electron Green's function. In other words, the electronic quasiparticle excitation energies are renormalized by the electron-phonon interaction. For semiconductors and insulators, this causes a renormalization of the electronic band gap similar to electron-electron corrections from methods related to the GW approximation [10–12]. It is this phonon-induced band-gap renormalization that we are primarily concerned with in this work.

The imaginary part, on the other hand, is related to the linewidth of the associated electron quasiparticle peaks. The inverse of this line width is often interpreted as a quasiparticle lifetime, i.e., the average amount of time the particle remains in the excited state. However, in this work, we do not go further into detail on quantities related to the imaginary part of the self-energy.

In order to obtain the renormalization of the electronic band structure, we evaluate the self-energy at the KS eigenvalue, $\hbar\omega = \varepsilon_{n\mathbf{k}}$, and neglect the off-diagonal components:

$$\Delta\varepsilon_{n\mathbf{k}}(T) \equiv \Delta\varepsilon^{\mathrm{FM}}_{n\mathbf{k}}(T) + \Delta\varepsilon^{\mathrm{DW}}_{n\mathbf{k}}(T), \tag{4.19}$$

with

$$\Delta\varepsilon^{\mathrm{FM}}_{n\mathbf{k}}(T) \equiv \Sigma^{\mathrm{FM}}_{nn\mathbf{k}}(\varepsilon_{n\mathbf{k}}, T) = \sum_{m\nu} \int_{\Omega_\mathrm{BZ}} \frac{\mathrm{d}^3q}{\Omega_\mathrm{BZ}} |g_{mn\mathbf{k},\nu\mathbf{q}}|^2 \times \left[\frac{1 - f_{m\mathbf{k}+\mathbf{q}}(T) + n_{\nu\mathbf{q}}(T)}{\varepsilon_{n\mathbf{k}} - \varepsilon_{m\mathbf{k}+\mathbf{q}} - \hbar\omega_{\nu\mathbf{q}} + \mathrm{i}\delta} + \frac{f_{m\mathbf{k}+\mathbf{q}}(T) + n_{\nu\mathbf{q}}(T)}{\varepsilon_{n\mathbf{k}} - \varepsilon_{m\mathbf{k}+\mathbf{q}} + \hbar\omega_{\nu\mathbf{q}} + \mathrm{i}\delta}\right], \tag{4.20}$$

and

$$\Delta\varepsilon^{\mathrm{DW}}_{n\mathbf{k}}(T) \equiv \Sigma^{\mathrm{DW}}_{nn\mathbf{k}}(T) = \sum_{\nu} \int_{\Omega_{\mathrm{BZ}}} \frac{\mathrm{d}^3 q}{\Omega_{\mathrm{BZ}}} g^{\mathrm{DW}}_{nn\mathbf{k},\nu\mathbf{q},\nu,-\mathbf{q}} \big(2n_{\nu\mathbf{q}}(T) + 1\big). \tag{4.21}$$

Under the assumption that $|\varepsilon_{n\mathbf{k}} - \varepsilon_{m\mathbf{k}+\mathbf{q}}| \gg \hbar\omega_{\nu\mathbf{q}}$, one may neglect the phonon frequencies in the denominators of Eq. (4.20) to recover the perturbative expression of AHC in Eq. (4.9). This approximation effectively removes the possibility of dynamically transferring energy between electrons and phonons. The system is essentially treated on the level of the Born-Oppenheimer or adiabatic approximation with a static external perturbation. For this reason, we refer to Eq. (4.9) as the *adiabatic* AHC theory. Conversely, we choose to call the more general Eqs. (4.19) to (4.21) the *non-adiabatic* AHC theory. We like to point out that since the DW contribution naturally does not allow for momentum transfer, it is the same in both cases.

A special case of the band-structure renormalization occurs at absolute-zero temperature, since even in the ground state does the lattice exhibit zero-point motion that can couple to the electrons. This is the ZPR alluded to in Chapter 1. In this work, we are particularly interested in the ZPR of the electronic band gap of insulators and semiconductors.

4.4 Electron-Phonon Interactions using the PAW Method

In this section, we study electron-phonon physics in the context of the PAW formalism. We discuss two complementary approaches for calculating electron-phonon matrix elements. One is specifically motivated by the need to perform ZPR calculations in the PAW framework while the other seeks to provide an explicit PAW formulation of the electron-phonon matrix element. We refer to the former as the *pseudo* approach and to the latter as the *all-electron* approach. However, it is crucial to note that despite what their names might imply, both are AE approaches in the PAW sense. We will come back to this point when we discuss their differences in Section 4.4.3.

4.4.1 Pseudo Approach

In order to derive a PAW expression for the phonon-induced renormalization of the electronic band structure, we follow the steps initially taken by AHC and employ Rayleigh-Schrödinger perturbation theory. However, instead of starting with the AE KS equations, we first pseudize the problem using the PAW method and take the necessary derivatives afterwards. This will eventually allow us to identify a pseudized version of the electron-phonon matrix element that is compact and easy to compute.

The first part of the derivation is detailed in Section 4.1. Here, we start with Eq. (4.7) and express the second derivative of the electronic eigenvalues in terms of PAW quantities. This allows us to identify PAW versions of the first and second-order electron-phonon matrix elements. We can accomplish this by taking the derivative of the pseudized KS equations. This is precisely the idea behind the PS approach to electron-phonon interactions.

In the PAW framework, the KS eigenvalues are obtained by solving a generalized eigenvalue problem. Thus, let us recapitulate Eq. (2.32), i.e., the PS KS equations after taking the PAW transformation:

$$\widetilde{H}\,|\widetilde{\psi}_{n\mathbf{k}}\rangle = \varepsilon_{n\mathbf{k}}\tilde{S}\,|\widetilde{\psi}_{n\mathbf{k}}\rangle\,. \tag{4.22}$$

Next, let us take the first derivative of Eq. (4.22) with respect to the displacement of atom $(l\kappa)$ and use the chain rule:

$$\frac{\partial\varepsilon_{n\mathbf{k}}}{\partial u_{l\kappa\alpha}}\tilde{S}\,|\widetilde{\psi}_{n\mathbf{k}}\rangle = \left(\frac{\partial\widetilde{H}}{\partial u_{l\kappa\alpha}} - \varepsilon_{n\mathbf{k}}\frac{\partial\tilde{S}}{\partial u_{l\kappa\alpha}}\right)|\widetilde{\psi}_{n\mathbf{k}}\rangle + \left(\widetilde{H} - \varepsilon_{n\mathbf{k}}\tilde{S}\right)|\frac{\partial\widetilde{\psi}_{n\mathbf{k}}}{\partial u_{l\kappa\alpha}}\rangle\,. \tag{4.23}$$

To retrieve the first derivative of the KS eigenvalues, we multiply Eq. (4.23) with $\langle\widetilde{\psi}_{n\mathbf{k}}|$ from the left and use the fact that the PS orbitals are S-orthonormal. This yields:

$$\frac{\partial\varepsilon_{n\mathbf{k}}}{\partial u_{l\kappa\alpha}} = \langle\widetilde{\psi}_{n\mathbf{k}}|\frac{\partial\widetilde{H}}{\partial u_{l\kappa\alpha}} - \varepsilon_{n\mathbf{k}}\frac{\partial\tilde{S}}{\partial u_{l\kappa\alpha}}|\widetilde{\psi}_{n\mathbf{k}}\rangle\,. \tag{4.24}$$

Eq. (4.24) is the well-known Hellmann-Feynman theorem formulated in the PAW framework. However, instead of taking the derivative with respect to a single atomic displacement, we seek the derivative $\partial_{\nu\mathbf{q}}$ that describes a collective excitation. Fortunately, since the transformation in Eq. (4.8) is linear, we can easily restate the Hellmann-Feynman theorem in terms of the phonon displacement operator:

$$\partial_{\nu\mathbf{q}}\varepsilon_{n\mathbf{k}} = \langle\widetilde{\psi}_{n\mathbf{k}}|\partial_{\nu\mathbf{q}}\widetilde{H} - \varepsilon_{n\mathbf{k}}\partial_{\nu\mathbf{q}}\tilde{S}|\widetilde{\psi}_{n\mathbf{k}}\rangle\,. \tag{4.25}$$

The second derivative of the KS eigenvalues is then obtained by further differentiating Eq. (4.24) using $\partial_{\nu,-\mathbf{q}} = \partial^*_{\nu\mathbf{q}}$:

$$\partial_{\nu\mathbf{q}}\partial^*_{\nu\mathbf{q}}\varepsilon_{n\mathbf{k}} = \left(\delta\tilde{\varepsilon}^{\mathrm{FM,a}}_{n\mathbf{k},\nu\mathbf{q}} + c.c.\right) + \delta\tilde{\varepsilon}^{\mathrm{FM,b}}_{n\mathbf{k},\nu\mathbf{q}} + 2\tilde{g}^{\mathrm{DW}}_{nn\mathbf{k},\nu\mathbf{q},\nu,-\mathbf{q}}, \tag{4.26}$$

where we have grouped the resulting terms according to

$$\delta\tilde{\varepsilon}^{\mathrm{FM,a}}_{n\mathbf{k},\nu\mathbf{q}} \equiv \langle\widetilde{\psi}_{n\mathbf{k}}|\partial^*_{\nu\mathbf{q}}\widetilde{H} - \varepsilon_{n\mathbf{k}}\partial^*_{\nu\mathbf{q}}\tilde{S}|\partial_{\nu\mathbf{q}}\widetilde{\psi}_{n\mathbf{k}}\rangle\,, \tag{4.27}$$

$$\delta\tilde{\varepsilon}^{\mathrm{FM,b}}_{n\mathbf{k},\nu\mathbf{q}} \equiv -\partial_{\nu\mathbf{q}}\varepsilon_{n\mathbf{k}}\,\langle\widetilde{\psi}_{n\mathbf{k}}|\partial^*_{\nu\mathbf{q}}\tilde{S}|\widetilde{\psi}_{n\mathbf{k}}\rangle\,, \tag{4.28}$$

and defined

$$\tilde{g}^{\mathrm{DW}}_{mn\mathbf{k},\nu\mathbf{q},\nu'\mathbf{q}'} \equiv \frac{1}{2}\,\langle\widetilde{\psi}_{m\mathbf{k}+\mathbf{q}+\mathbf{q}'}|\partial_{\nu\mathbf{q}}\partial_{\nu'\mathbf{q}'}\widetilde{H} - \varepsilon_{n\mathbf{k}}\partial_{\nu\mathbf{q}}\partial_{\nu\mathbf{q}'}\tilde{S}|\widetilde{\psi}_{n\mathbf{k}}\rangle\,. \tag{4.29}$$

We have labeled the term $\tilde{g}^{\mathrm{DW}}_{n\mathbf{k},\nu\mathbf{q}}$ with the superscript "DW" and the rest of the terms with the superscript "FM". This is because the former is DW-like in the

sense that it contains the second derivative of the Hamiltonian and the PAW overlap operator. Since there is only a single term like this, we call Eq. (4.29) the PS DW matrix element. It is the PS equivalent to the DW matrix element defined in Eq. (4.11). Conversely, the remaining FM-like terms, Eqs. (4.27) and (4.28), contain only products of first derivatives. Our goal is to transform these equations such that a PS equivalent of the electron-phonon matrix element defined in Eq. (4.10) can be identified.

In order to combine Eqs. (4.27) and (4.28), we must first work on the derivative of the state vector, $|\partial_{\nu\mathbf{q}}\widetilde{\psi}_{n\mathbf{k}}\rangle$. To this end, we employ a standard trick in perturbation theory and write the perturbed state vector as a sum over all unperturbed states. Knowing that the PS orbitals are S-orthonormal, we choose $(m\mathbf{k}') \neq (n\mathbf{k})$ and multiply Eq. (4.23) with $\langle\widetilde{\psi}_{m\mathbf{k}'}|$ from the left. Having used the PS KS equations, Eq. (4.22), we obtain:

$$\langle\widetilde{\psi}_{m\mathbf{k}'}|\tilde{S}|\partial_{\nu\mathbf{q}}\widetilde{\psi}_{n\mathbf{k}}\rangle = \frac{\langle\widetilde{\psi}_{m\mathbf{k}'}|\partial_{\nu\mathbf{q}}\widetilde{H} - \varepsilon_{n\mathbf{k}}\partial_{\nu\mathbf{q}}\tilde{S}|\widetilde{\psi}_{n\mathbf{k}}\rangle}{\varepsilon_{n\mathbf{k}} - \varepsilon_{m\mathbf{k}'}}. \tag{4.30}$$

Together with the PAW completeness relation,

$$\sum_n \int_{\Omega_{\mathrm{BZ}}} \frac{\mathrm{d}^3k}{\Omega_{\mathrm{BZ}}} |\widetilde{\psi}_{n\mathbf{k}}\rangle\langle\widetilde{\psi}_{n\mathbf{k}}|\,\tilde{S} = \mathbb{1}, \tag{4.31}$$

it follows that

$$|\partial_{\nu\mathbf{q}}\widetilde{\psi}_{n\mathbf{k}}\rangle = \sum_m{}' \int_{\Omega_{\mathrm{BZ}}} \frac{\mathrm{d}^3k'}{\Omega_{\mathrm{BZ}}} \frac{|\widetilde{\psi}_{m\mathbf{k}'}\rangle\langle\widetilde{\psi}_{m\mathbf{k}'}|\partial_{\nu\mathbf{q}}\widetilde{H} - \varepsilon_{n\mathbf{k}}\partial_{\nu\mathbf{q}}\tilde{S}|\widetilde{\psi}_{n\mathbf{k}}\rangle}{\varepsilon_{n\mathbf{k}} - \varepsilon_{m\mathbf{k}'}} + |\widetilde{\psi}_{n\mathbf{k}}\rangle\langle\widetilde{\psi}_{n\mathbf{k}}|\tilde{S}|\partial_{\nu\mathbf{q}}\widetilde{\psi}_{n\mathbf{k}}\rangle\,. \tag{4.32}$$

The prime above the summation indicates that the case $(m\mathbf{k}') = (n\mathbf{k})$ is to be *excluded*. In addition to the sum over states, Eq. (4.32) features a term that is diagonal in m and n and only contains the PAW overlap operator. This is an artifact of the PAW formalism. Such terms appear in general when using non-orthogonal basis sets or generalized eigenvalue problems with position-dependent overlap operators.

The Bloch theorem dictates that

$$\langle\psi_{\mathbf{k}''}|\hat{O}_{\mathbf{k}'}|\psi_{\mathbf{k}}\rangle \propto \Omega_{\mathrm{BZ}}\delta^{(3)}(\mathbf{k}'' - \mathbf{k}' - \mathbf{k}), \tag{4.33}$$

given that $\hat{O}_{\mathbf{k}'}$ is a lattice-periodic operator. This condition is true for the phonon displacement operator, $\partial_{\nu\mathbf{q}}$. Indeed, the matrix elements involved in Eq. (4.32) adhere to the Bloch theorem, thereby forcing $\mathbf{k}' = \mathbf{k} + \mathbf{q}$ in the summation over states. Moreover, the derivative in the extra PAW term only acts for zone-center phonons, i.e., $\mathbf{q} = \mathbf{0}$.

Using Eq. (4.32) together with the Bloch theorem, it is now possible to calculate $\delta\tilde{\varepsilon}^{\mathrm{FM,a}}_{n\mathbf{k},\nu\mathbf{q}}$ in Eq. (4.27) together with its complex conjugate. However, we can

simplify the result by making the following observation. When adding the band-diagonal PAW extra term to its complex conjugate, we can employ the product rule of differentiation:

$$\langle\widetilde{\psi}_{n\mathbf{k}}|\tilde{S}|\partial_{\nu\mathbf{0}}\widetilde{\psi}_{n\mathbf{k}}\rangle + \langle\partial_{\nu\mathbf{0}}\widetilde{\psi}_{n\mathbf{k}}|\tilde{S}|\widetilde{\psi}_{n\mathbf{k}}\rangle = -\langle\widetilde{\psi}_{n\mathbf{k}}|\partial_{\nu\mathbf{0}}\tilde{S}|\widetilde{\psi}_{n\mathbf{k}}\rangle\,. \tag{4.34}$$

With this, we obtain:

$$\begin{aligned}\delta\tilde{\varepsilon}^{\mathrm{FM,a}}_{n\mathbf{k},\nu\mathbf{q}} + c.c. = 2{\sum_{m}}' \frac{|\langle\widetilde{\psi}_{m\mathbf{k}+\mathbf{q}}|\partial_{\nu\mathbf{q}}\widetilde{H} - \varepsilon_{n\mathbf{k}}\partial_{\nu\mathbf{q}}\tilde{S}|\widetilde{\psi}_{n\mathbf{k}}\rangle|^2}{\varepsilon_{n\mathbf{k}} - \varepsilon_{m\mathbf{k}+\mathbf{q}}} \\ - \Omega_{\mathrm{BZ}}\delta^{(3)}(\mathbf{q})\,\langle\widetilde{\psi}_{n\mathbf{k}}|\partial_{\nu\mathbf{0}}\widetilde{H} - \varepsilon_{n\mathbf{k}}\partial_{\nu\mathbf{0}}\tilde{S}|\widetilde{\psi}_{n\mathbf{k}}\rangle\,\langle\widetilde{\psi}_{n\mathbf{k}}|\partial_{\nu\mathbf{0}}\tilde{S}|\widetilde{\psi}_{n\mathbf{k}}\rangle\,.\end{aligned} \tag{4.35}$$

Furthermore, we recognize that $\langle\widetilde{\psi}_{n\mathbf{k}}|\partial_{\nu\mathbf{0}}\tilde{S}|\widetilde{\psi}_{n\mathbf{k}}\rangle$ also appears in Eq. (4.28). Indeed, after substituting the Hellmann-Feynman theorem from Eq. (4.25) into Eq. (4.28), we find that $\delta\tilde{\varepsilon}^{\mathrm{FM,b}}_{n\mathbf{k},\nu\mathbf{q}}$ gives the exact same contribution as the last term of $\delta\tilde{\varepsilon}^{\mathrm{FM,a}}_{n\mathbf{k},\nu\mathbf{q}}$ in Eq. (4.35).

Before we state the result, we want to briefly discuss degeneracies in the electronic band structure. Since we used non-degenerate Rayleigh-Schrödinger perturbation theory, it is implicitly assumed that $\varepsilon_{m\mathbf{k}+\mathbf{q}} \neq \varepsilon_{n\mathbf{k}}$, except when $(m\mathbf{k}+\mathbf{q}) = (n\mathbf{k})$. The primed sum introduced in Eq. (4.32) excludes these simple degeneracies. However, in general, there will be other symmetry-driven and coincidental degeneracies for which Eq. (4.32) is ill-defined. In the AHC formula presented in Eq. (4.9), this issue is circumvented by having a small imaginary shift in the denominator. Here, it can be introduced to stay consistent with the established formalism. For a proper general treatment of degeneracies one has to resort to degenerate perturbation theory.

At long last, we combine Eqs. (4.7), (4.25), (4.26), (4.28), (4.29) and (4.35) in order to obtain the full adiabatic AHC energy shift in terms of PS PAW quantities:

$$\Delta\tilde{\varepsilon}_{n\mathbf{k}}(T) = \Delta\tilde{\varepsilon}^{\mathrm{FM}}_{n\mathbf{k}}(T) + \Delta\tilde{\varepsilon}^{\mathrm{DW}}_{n\mathbf{k}}(T), \tag{4.36}$$

with

$$\begin{aligned}\Delta\tilde{\varepsilon}^{\mathrm{FM}}_{n\mathbf{k}}(T) \equiv \sum_{\nu m}\int_{\Omega_{\mathrm{BZ}}}\frac{\mathrm{d}^3q}{\Omega_{\mathrm{BZ}}}\,\mathrm{Re}\,\frac{|\tilde{g}_{mn\mathbf{k},\nu\mathbf{q}}|^2}{\varepsilon_{n\mathbf{k}} - \varepsilon_{m\mathbf{k}+\mathbf{q}} + \mathrm{i}\delta}\left[2n_{\nu\mathbf{q}}(T)+1\right] \\ - \sum_{\nu}\tilde{g}_{nn\mathbf{k},\nu\mathbf{0}}\tilde{g}^{\mathrm{S}}_{nn\mathbf{k},\nu\mathbf{0}}\left[2n_{\nu\mathbf{0}}(T)+1\right],\end{aligned} \tag{4.37}$$

$$\Delta\tilde{\varepsilon}^{\mathrm{DW}}_{n\mathbf{k}}(T) \equiv \sum_{\nu}\int_{\Omega_{\mathrm{BZ}}}\frac{\mathrm{d}^3q}{\Omega_{\mathrm{BZ}}}\tilde{g}^{\mathrm{DW}}_{nn\mathbf{k},\nu\mathbf{q},\nu,-\mathbf{q}}\left[2n_{\nu\mathbf{q}}(T)+1\right], \tag{4.38}$$

where we have defined the following matrix elements:

$$\tilde{g}_{mn\mathbf{k},\nu\mathbf{q}} \equiv \langle\widetilde{\psi}_{m\mathbf{k}+\mathbf{q}}|\partial_{\nu\mathbf{q}}\widetilde{H} - \varepsilon_{n\mathbf{k}}\partial_{\nu\mathbf{q}}\tilde{S}|\widetilde{\psi}_{n\mathbf{k}}\rangle\,, \tag{4.39}$$

$$\tilde{g}^{\mathrm{S}}_{mn\mathbf{k},\nu\mathbf{q}} \equiv \langle\widetilde{\psi}_{m\mathbf{k}+\mathbf{q}}|\partial_{\nu\mathbf{q}}\tilde{S}|\widetilde{\psi}_{n\mathbf{k}}\rangle\,. \tag{4.40}$$

We call $\tilde{g}_{mn\mathbf{k},\nu\mathbf{q}}$ the PS electron-phonon matrix element. This choice of matrix element is motivated by the algebraic similarity between Eq. (4.37) and Eq. (4.20). Except for the additional PAW term involving $\tilde{g}^{\mathrm{S}}_{nn\mathbf{k},\nu\mathbf{0}}$, the PS formulas shown in Eqs. (4.36) to (4.38) indeed take the same form as the conventional AHC theory if one substitutes $\tilde{g}_{mn\mathbf{k},\nu\mathbf{q}} \to g_{mn\mathbf{k},\nu\mathbf{q}}$. To better distinguish between $g_{mn\mathbf{k},\nu\mathbf{q}}$ and $\tilde{g}_{mn\mathbf{k},\nu\mathbf{q}}$ in the context of the PAW method, we call the former the AE electron-phonon matrix element. Once again, this is nomenclature and should not distract from the fact that the PS approach also preserves the AE information.

A huge advantage of the PS approach is that $\tilde{g}_{mn\mathbf{k},\nu\mathbf{q}}$ is easy to compute. Essentially, one only requires the derivatives of the already pseudized PAW Hamiltonian and the PAW overlap operator. The same is, in principle, also true for the other matrix elements, $\tilde{g}^{\mathrm{S}}_{mn\mathbf{k},\nu\mathbf{q}}$ and $\tilde{g}^{\mathrm{DW}}_{n\mathbf{k},\nu\mathbf{q}}$. However, in practice, the second derivative appearing in the DW matrix element is rarely evaluated directly. Instead, an approximation is made to express the second derivative as a product of first derivatives similar to the FM contribution. More details on this are available in Section 4.5.

At this point, we need to make an important statement about the PS approach to electron phonon interactions and how it relates to the traditional AE AHC theory. Since the PAW transformation perfectly preserves the AE information in the limit of a complete basis set, the sum of the resulting PS FM and PS DW energy shifts, given by Eqs. (4.36) to (4.38), must be formally identical to the AHC theory in Eq. (4.9). However, as we have pointed out in previous publications [33, 35], the individual FM and DW contributions will generally *not* be identical to their PS counterparts as defined here. The same is true of the individual matrix elements, $g_{mn\mathbf{k},\nu\mathbf{q}}$ and $\tilde{g}_{mn\mathbf{k},\nu\mathbf{q}}$. This might come as a surprise and, indeed, the difference is very subtle. A detailed discussion of this issue is provided in Sections 6.1 and 6.2.

While the PS approach provides a rigorous and easy way of calculating the renormalization of the electronic band structure due to electron-phonon effects in an adiabatic theory, it is not straight forward to generalize this result. For example, it is a priori unclear if the PS matrix elements defined in Eq. (4.39) can be used in the more general self-energy expression in Eq. (4.15). This may limit the applicability of the PS approach compared to a traditional AE approach.

4.4.2 All-Electron Approach

In Section 4.4.1, we have derived the PS approach by first pseudizing the theory using the PAW transformation and *then* taking the atomic derivatives. This leads to a theory based on PS matrix elements, $\tilde{g}_{mn\mathbf{k},\nu\mathbf{q}}$. These are easy to compute but not necessarily equal to the AE matrix elements, $g_{mn\mathbf{k},\nu\mathbf{q}}$.

In 2019, Chaput, Togo and Tanaka [34] presented a different approach to electron-phonon interactions in the PAW framework, wherein the order of operations is reversed, i.e., the PAW transformation is performed after taking the atomic derivatives. We call this the AE approach to electron-phonon interactions within the PAW framework. Essentially, the AE approach tries to find an explicit

computable expression of the AE matrix element, $g_{mn\mathbf{k},\nu\mathbf{q}}$, in terms of PAW quantities. This section presents the necessary steps to arrive at such an expression, closely following Ref. [34] but using our own notation. A comparison between the AE and PS approaches is given in Section 4.4.3.

Let us begin the derivation directly with the AE electron-phonon matrix element, transforming the AE states using the PAW transformation, Eq. (2.28):

$$g_{mn\mathbf{k},\nu\mathbf{q}} = \langle \psi_{m\mathbf{k}+\mathbf{q}} | \partial_{\nu\mathbf{q}} \hat{H} | \psi_{n\mathbf{k}} \rangle = \langle \widetilde{\psi}_{m\mathbf{k}+\mathbf{q}} | \hat{\mathcal{T}}^\dagger (\partial_{\nu\mathbf{q}} \hat{H}) \hat{\mathcal{T}} | \widetilde{\psi}_{n\mathbf{k}} \rangle \,. \tag{4.41}$$

The operator $\hat{H}$ is the usual KS Hamiltonian acting on the AE orbitals, $|\psi_{n\mathbf{k}}\rangle$. We have placed parentheses around the AE operator to emphasize the fact that the phonon displacement operator is only acting on $\hat{H}$ in Eq. (4.41). This is important since the PAW transformation operator, $\hat{\mathcal{T}}$, also depends on the atomic positions. It therefore does not commute with the phonon displacement operator, it being a superposition of atomic derivatives. Knowing this, we can continue with the product rule of differentiation:

$$\begin{aligned} g_{mn\mathbf{k},\nu\mathbf{q}} &= \langle \widetilde{\psi}_{m\mathbf{k}+\mathbf{q}} | \partial_{\nu\mathbf{q}} \widetilde{H} - (\partial_{\nu\mathbf{q}} \hat{\mathcal{T}}^\dagger) \hat{H} \hat{\mathcal{T}} - \hat{\mathcal{T}}^\dagger \hat{H} (\partial_{\nu\mathbf{q}} \hat{\mathcal{T}}) | \widetilde{\psi}_{n\mathbf{k}} \rangle \\ &= \langle \widetilde{\psi}_{m\mathbf{k}+\mathbf{q}} | \partial_{\nu\mathbf{q}} \widetilde{H} - \varepsilon_{n\mathbf{k}} (\partial_{\nu\mathbf{q}} \hat{\mathcal{T}}^\dagger) \hat{\mathcal{T}} - \varepsilon_{m\mathbf{k}+\mathbf{q}} \hat{\mathcal{T}}^\dagger (\partial_{\nu\mathbf{q}} \hat{\mathcal{T}}) | \widetilde{\psi}_{n\mathbf{k}} \rangle \end{aligned} \tag{4.42}$$

where we have used the KS equations to retrieve the corresponding eigenvalues, $\varepsilon_{n\mathbf{k}}$ and $\varepsilon_{m\mathbf{k}+\mathbf{q}}$.

The first term in Eq. (4.42) also appears in the PS electron-phonon matrix element, Eq. (4.39), and is relatively easy to compute. The other two terms involve the derivative of the PAW transformation operator. This is not straight forward to do, nor are such derivatives usually implemented in PAW codes. Therefore, let us simplify the problem. First, instead of working with the phonon displacement operator, $\partial_{\nu\mathbf{q}}$, it is much easier to focus only on a single atomic displacement, seeing as

$$\left(\frac{\partial \hat{\mathcal{T}}^\dagger}{\partial u_{l\kappa\alpha}} \hat{\mathcal{T}} \right)^\dagger = \hat{\mathcal{T}}^\dagger \frac{\partial \hat{\mathcal{T}}}{\partial u_{l\kappa\alpha}} . \tag{4.43}$$

To recover the electron-phonon matrix element in the phonon basis, one simply uses Eq. (4.8). Therefore, the question becomes how to express $\hat{\mathcal{T}}^\dagger \frac{\partial \hat{\mathcal{T}}}{\partial u_{l\kappa\alpha}}$ in terms of computable PAW quantities. The remaining term can be obtained via Hermitian conjugation. For brevity, we combine the atomic indices l and κ in this section into a compound index, a, as we have done in Section 2.4.

Next, let us expand the PAW transformation operator in terms of PAW projector functions, $|\widetilde{p}_{ai}\rangle$, and partial waves, $|\phi_{ai}\rangle$ and $|\widetilde{\phi}_{ai}\rangle$, according to Eq. (2.41):

$$\begin{aligned} \hat{\mathcal{T}}^\dagger \frac{\partial \hat{\mathcal{T}}}{\partial u_{a\alpha}} &= \left(\mathbb{1} + \sum_{bi} |\widetilde{p}_{bi}\rangle \langle \phi_{bi} - \widetilde{\phi}_{bi}| \right) \frac{\partial}{\partial u_{a\alpha}} \left(\sum_{cj} |\phi_{cj} - \widetilde{\phi}_{cj}\rangle \langle \widetilde{p}_{cj}| \right) \\ &= \left(\mathbb{1} + \sum_{i} |\widetilde{p}_{ai}\rangle \langle \phi_{ai} - \widetilde{\phi}_{ai}| \right) \frac{\partial}{\partial u_{a\alpha}} \left(\sum_{j} |\phi_{aj} - \widetilde{\phi}_{aj}\rangle \langle \widetilde{p}_{aj}| \right), \end{aligned} \tag{4.44}$$

Here, we used the fact that $|\phi_{ai}\rangle$ coincides with $|\widetilde{\phi}_{ai}\rangle$ outside the augmentation region of atom a. In other words, $|\phi_{aj} - \widetilde{\phi}_{aj}\rangle$ is non-zero only inside the augmentation region around atom a. Since the augmentation regions around each atom do not overlap, only the terms with $b = a$ and $c = a$ contribute in the sums over atomic sites.

To simplify Eq. (4.44) further, we can make the following observation: The identity operator in the left pair of parentheses in Eq. (4.44) is projected onto $|\phi_{aj} - \widetilde{\phi}_{aj}\rangle$, which is non-zero only within the augmentation region. Assuming that the PAW basis is complete, the identity operator $\mathbb{1}$ can safely be replaced by the completeness relation in Eq. (2.39) inside the augmentation region:

$$\mathbb{1}_a^{\text{aug}} = \sum_i |\widetilde{p}_{ai}\rangle\langle\widetilde{\phi}_{ai}| \,. \tag{4.45}$$

With this, the left pair of parentheses in Eq. (4.44) becomes

$$\sum_i |\widetilde{p}_{ai}\rangle\langle\phi_{ai}| \,.$$

At the same time, we can use the completeness relation inside the right pair of parentheses to simplify the derivative:

$$\frac{\partial}{\partial u_{a\alpha}}\Bigg(\sum_j |\phi_{aj}\rangle\langle\widetilde{p}_{aj}| - \underbrace{\sum_j |\widetilde{\phi}_{aj}\rangle\langle\widetilde{p}_{aj}|}_{=\mathbb{1}_a^{\text{aug}}}\Bigg) = \frac{\partial}{\partial u_{a\alpha}}\Bigg(\sum_j |\phi_{aj}\rangle\langle\widetilde{p}_{aj}|\Bigg). \tag{4.46}$$

Taken together, Eq. (4.44) becomes

$$\hat{\mathcal{T}}^\dagger \frac{\partial \hat{\mathcal{T}}}{\partial u_{a\alpha}} = \sum_i |\widetilde{p}_{ai}\rangle\langle\phi_{ai}|\phi_{ai}\rangle\langle\frac{\partial \widetilde{p}_{ai}}{\partial u_{a\alpha}}| + \sum_i |\widetilde{p}_{ai}\rangle\langle\phi_{ai}|\frac{\partial \phi_{ai}}{\partial u_{a\alpha}}\rangle\langle\widetilde{p}_{ai}| \,. \tag{4.47}$$

Notably, Eq. (4.47) only contains the AE partial waves. In order to make it more consistent with the usual PAW formalism, the PS partial waves can be reintroduced using the following mathematical trick, once again assuming that the PAW basis is complete:

$$0 = \frac{\partial \mathbb{1}_a^{\text{aug}}}{\partial u_{a\alpha}} = \sum_j \frac{\partial}{\partial u_{a\alpha}}\Big(|\widetilde{\phi}_{aj}\rangle\langle\widetilde{p}_{aj}|\Big) = \sum_{ij} |\widetilde{p}_{ai}\rangle\langle\widetilde{\phi}_{ai}| \, \frac{\partial}{\partial u_{a\alpha}}\Big(|\widetilde{\phi}_{aj}\rangle\langle\widetilde{p}_{aj}|\Big). \tag{4.48}$$

Added to Eq. (4.47), this gives:

$$\hat{\mathcal{T}}^\dagger \frac{\partial \hat{\mathcal{T}}}{\partial u_{l\kappa\alpha}} = \sum_{ij} |\widetilde{p}_{l\kappa i}\rangle \, Q_{l\kappa,ij} \, \langle\frac{\partial \widetilde{p}_{l\kappa j}}{\partial u_{l\kappa\alpha}}| + \sum_{ij} |\widetilde{p}_{l\kappa i}\rangle \, R_{l\kappa\alpha,ij} \, \langle\widetilde{p}_{l\kappa j}| \,, \tag{4.49}$$

with

$$Q_{l\kappa,ij} \equiv \langle\phi_{l\kappa i}|\phi_{l\kappa j}\rangle - \langle\widetilde{\phi}_{l\kappa i}|\widetilde{\phi}_{l\kappa j}\rangle \,, \tag{4.50}$$

$$R_{l\kappa\alpha,ij} \equiv \langle\phi_{l\kappa i}|\frac{\partial \phi_{l\kappa j}}{\partial u_{l\kappa\alpha}}\rangle - \langle\widetilde{\phi}_{l\kappa i}|\frac{\partial \widetilde{\phi}_{l\kappa j}}{\partial u_{l\kappa\alpha}}\rangle \,, \tag{4.51}$$

where we have reintroduced the atomic indices, l and κ. $Q_{l\kappa,ij}$ are the augmentation charges already defined in Eq. (2.46). The newly introduced quantity $R_{l\kappa\alpha,ij}$ is anti-Hermitian in the indices i and j as is easily verified:

$$\begin{aligned} R^*_{l\kappa\alpha,ji} &= \langle \phi_{l\kappa j} | \frac{\partial \phi_{l\kappa i}}{\partial u_{l\kappa\alpha}} \rangle^* - \langle \widetilde{\phi}_{l\kappa j} | \frac{\partial \widetilde{\phi}_{l\kappa i}}{\partial u_{l\kappa\alpha}} \rangle^* \\ &= \langle \frac{\partial \phi_{l\kappa i}}{\partial u_{l\kappa\alpha}} | \phi_{l\kappa j} \rangle - \langle \frac{\partial \widetilde{\phi}_{l\kappa i}}{\partial u_{l\kappa\alpha}} | \widetilde{\phi}_{l\kappa j} \rangle \\ &= \underbrace{\frac{\partial Q_{l\kappa ij}}{\partial u_{l\kappa\alpha}}}_{=0} - \left(\langle \phi_{l\kappa i} | \frac{\partial \phi_{l\kappa j}}{\partial u_{l\kappa\alpha}} \rangle - \langle \widetilde{\phi}_{l\kappa i} | \frac{\partial \widetilde{\phi}_{l\kappa j}}{\partial u_{l\kappa\alpha}} \rangle \right) \\ &= -R_{l\kappa\alpha,ij}. \end{aligned} \tag{4.52}$$

Combining equations Eqs. (4.8), (4.42), (4.43) and (4.49) provides a compact expression for the AE electron-phonon matrix element:

$$\begin{aligned} g_{m\mathbf{k}',n\mathbf{k},l\kappa\alpha} &\equiv \langle \widetilde{\psi}_{m\mathbf{k}'} | \frac{\partial \hat{H}}{\partial u_{l\kappa\alpha}} | \widetilde{\psi}_{n\mathbf{k}} \rangle \\ &= \langle \widetilde{\psi}_{m\mathbf{k}'} | \frac{\partial \widetilde{H}}{\partial u_{l\kappa\alpha}} | \widetilde{\psi}_{n\mathbf{k}} \rangle \\ &\quad - \varepsilon_{n\mathbf{k}} \sum_{ij} \langle \widetilde{\psi}_{m\mathbf{k}'} | \frac{\partial \widetilde{p}_{l\kappa i}}{\partial u_{l\kappa\alpha}} \rangle Q_{l\kappa,ij} \langle \widetilde{p}_{l\kappa j} | \widetilde{\psi}_{n\mathbf{k}} \rangle \\ &\quad - \varepsilon_{m\mathbf{k}'} \sum_{ij} \langle \widetilde{\psi}_{m\mathbf{k}'} | \widetilde{p}_{l\kappa i} \rangle Q_{l\kappa,ij} \langle \frac{\partial \widetilde{p}_{l\kappa j}}{\partial u_{l\kappa\alpha}} | \widetilde{\psi}_{n\mathbf{k}} \rangle \\ &\quad + (\varepsilon_{n\mathbf{k}} - \varepsilon_{m\mathbf{k}'}) \langle \widetilde{\psi}_{m\mathbf{k}'} | \widetilde{p}_{l\kappa i} \rangle R_{l\kappa\alpha,ij} \langle \widetilde{p}_{l\kappa j} | \widetilde{\psi}_{n\mathbf{k}} \rangle . \end{aligned} \tag{4.53}$$

The matrix element $g_{m\mathbf{k}',n\mathbf{k},l\kappa\alpha}$ is defined only for a single atomic displacement. However, it is directly linked to $g_{mn\mathbf{k},\nu\mathbf{q}}$ in the phonon representation via Eq. (4.8).

Let us inspect the different contributions to the AE electron-phonon matrix element in Eq. (4.53). The first term in Eq. (4.53) is also found in the PS electron-phonon matrix element, $\tilde{g}_{mn\mathbf{k},\nu\mathbf{q}}$, defined in Eq. (4.39). The second and third terms are very similar to each other. They contain the derivatives of the projector functions. In addition, these terms are closely related to the derivative of the PAW overlap operator that appears in $\tilde{g}_{mn\mathbf{k},\nu\mathbf{q}}$, since

$$\frac{\partial \tilde{S}}{\partial u_{l\kappa\alpha}} = \sum_{ij} |\frac{\partial \widetilde{p}_{l\kappa i}}{\partial u_{l\kappa\alpha}} \rangle Q_{l\kappa,ij} \langle \widetilde{p}_{l\kappa j}| + \sum_{ij} |\widetilde{p}_{l\kappa i}\rangle Q_{l\kappa,ij} \langle \frac{\partial \widetilde{p}_{l\kappa j}}{\partial u_{l\kappa\alpha}}| . \tag{4.54}$$

Finally, the last term in Eq. (4.53) is unique to the AE approach. Indeed, $R_{l\kappa\alpha,ij}$ features derivatives of the AE and PS partial waves. This contribution does not exist in the PS approach.

The biggest advantage of the AE approach is that the corresponding matrix element, $g_{mn\mathbf{k},\nu\mathbf{q}}$, is explicitly calculated. It can therefore be used directly and rigorously in the self-energy expression in Eq. (4.15) and any other equations derived

from many-body perturbation theory. However, there are potential downsides to this approach. We expand on this point in Section 6.2.

4.4.3 Comparing All-Electron and Pseudo Approach

In this section, we discuss the connection between the PS approach introduced in Section 4.4.1 and the AE approach introduced in Section 4.4.2. While both approaches feature PAW formulations of the electron-phonon matrix elements, there are some interesting qualitative differences. The former is designed to solve a particular problem, namely the band-structure renormalization in the adiabatic approximation, while the latter strives to offer a more general solution to the electron-phonon problem. Either way, one has to consider the practical limitations and accept certain trade-offs.

4.4.3.1 Equivalence in the Adiabatic Approximation

Based on the fact that the PS approach was designed to accurately describe the band-structure renormalization in the adiabatic approximation, it should be possible to show that it is equivalent to the AE approach in this particular case. In this section, we document our findings that, indeed, such an equivalence can be proved algebraically starting from the adiabatic AHC theory, Eq. (4.9). The following contains a slightly modified version of Appendix B in Ref. [35].

To begin with, let us state the algebraic difference between the PS and AE matrix elements defined in Eq. (4.39) and Eq. (4.53), respectively. Starting from Eq. (4.42), we can employ the product rule of differentiation to obtain:

$$g_{mn\mathbf{k},\nu\mathbf{q}} = \tilde{g}_{mn\mathbf{k},\nu\mathbf{q}} + \left(\varepsilon_{n\mathbf{k}} - \varepsilon_{m\mathbf{k}+\mathbf{q}}\right) t_{mn\mathbf{k},\nu\mathbf{q}}, \tag{4.55}$$

with

$$t_{mn\mathbf{k},\nu\mathbf{q}} \equiv \langle \widetilde{\psi}_{m\mathbf{k}+\mathbf{q}} | \hat{\mathcal{T}}^\dagger \partial_{\nu\mathbf{q}} \hat{\mathcal{T}} | \widetilde{\psi}_{n\mathbf{k}} \rangle \,. \tag{4.56}$$

We like to remind of the fact that this relation only holds in the limit of a complete PAW basis set. For the remainder of this section, we assume that this is the case.

For simplicity's sake, we focus on the ZPR, but the proof is equally valid at finite temperature. In addition, we assume that the electronic band structure is non-degenerate everywhere. While not strictly necessary, this allows for the removal of the $\mathrm{i}\delta$ term from the denominator of the self-energy expression. Under these assumptions, the FM contribution to the adiabatic ZPR reads

$$\mathrm{ZPR}^{\mathrm{FM}}_{n\mathbf{k}} = \int_{\Omega_{\mathrm{BZ}}} \frac{\mathrm{d}^3 q}{\Omega_{\mathrm{BZ}}} \sum_{\nu} \gamma^{\mathrm{FM}}_{n\mathbf{k},\nu\mathbf{q}}, \tag{4.57}$$

$$\gamma^{\mathrm{FM}}_{n\mathbf{k},\nu\mathbf{q}} \equiv \sum_{m}{}' \frac{|g_{mn\mathbf{k},\nu\mathbf{q}}|^2}{\varepsilon_{n\mathbf{k}} - \varepsilon_{m\mathbf{k}+\mathbf{q}}}, \tag{4.58}$$

where the prime above the sum indicates that the case $(m\mathbf{k}+\mathbf{q}) = (n\mathbf{k})$ is excluded. The DW contribution takes the form

$$\mathrm{ZPR}^{\mathrm{DW}}_{n\mathbf{k}} = \int_{\Omega_{\mathrm{BZ}}} \frac{\mathrm{d}^3 q}{\Omega_{\mathrm{BZ}}} \sum_{\nu} \gamma^{\mathrm{DW}}_{n\mathbf{k},\nu\mathbf{q}}, \tag{4.59}$$

$$\gamma^{\mathrm{DW}}_{n\mathbf{k},\nu\mathbf{q}} \equiv \frac{1}{2} \langle \psi_{n\mathbf{k}} | \partial_{\nu\mathbf{q}} \partial^*_{\nu\mathbf{q}} \hat{H} | \psi_{n\mathbf{k}} \rangle , \tag{4.60}$$

where $\partial^*_{\nu\mathbf{q}} = \partial_{\nu,-\mathbf{q}}$. We define new symbols for the integrands in order to reduce the notational complexity in this section.

In the PS formulation, the terms $\gamma^{\mathrm{FM}}_{n\mathbf{k},\nu\mathbf{q}}$ and $\gamma^{\mathrm{DW}}_{n\mathbf{k},\nu\mathbf{q}}$ are replaced by their respective PS equivalents,

$$\tilde{\gamma}^{\mathrm{FM}}_{n\mathbf{k},\nu\mathbf{q}} \equiv \sum_{m}{}' \frac{|\tilde{g}_{mn\mathbf{k},\nu\mathbf{q}}|^2}{\varepsilon_{n\mathbf{k}} - \varepsilon_{m\mathbf{k}+\mathbf{q}}} - \tilde{g}_{nn\mathbf{k},\nu\mathbf{0}} \langle \widetilde{\psi}_{n\mathbf{k}} | \partial_{\nu\mathbf{0}} \tilde{S} | \widetilde{\psi}_{n\mathbf{k}} \rangle \, \Omega_{\mathrm{BZ}} \delta^{(3)}(\mathbf{q}) \tag{4.61}$$

and

$$\tilde{\gamma}^{\mathrm{DW}}_{n\mathbf{k},\nu\mathbf{q}} \equiv \frac{1}{2} \langle \psi_{n\mathbf{k}} | \partial_{\nu\mathbf{q}} \partial^*_{\nu\mathbf{q}} \widetilde{H} - \varepsilon_{n\mathbf{k}} \partial_{\nu\mathbf{q}} \partial^*_{\nu\mathbf{q}} \tilde{S} | \psi_{n\mathbf{k}} \rangle . \tag{4.62}$$

Note that $\gamma^{\mathrm{DW}}_{n\mathbf{k},\nu\mathbf{q}}$ and $\tilde{\gamma}^{\mathrm{DW}}_{n\mathbf{k},\nu\mathbf{q}}$ are essentially the AE and PS DW matrix elements, respectively.

Our goal is to show that $\gamma^{\mathrm{FM}}_{n\mathbf{k},\nu\mathbf{q}} - \tilde{\gamma}^{\mathrm{FM}}_{n\mathbf{k},\nu\mathbf{q}} = \tilde{\gamma}^{\mathrm{DW}}_{n\mathbf{k},\nu\mathbf{q}} - \gamma^{\mathrm{DW}}_{n\mathbf{k},\nu\mathbf{q}}$ when integrated over the FBZ, which proves that both formulations yield identical results for the adiabatic ZPR. Let us begin by transforming the AE electron-phonon matrix elements in Eq. (4.58) to the PS formulation using Eq. (4.55). To keep track of the different resulting terms, they are divided into three different contributions:

$$\gamma^{\mathrm{FM}}_{n\mathbf{k},\nu\mathbf{q}} = \gamma^{\mathrm{FM,a}}_{n\mathbf{k},\nu\mathbf{q}} + \gamma^{\mathrm{FM,b}}_{n\mathbf{k},\nu\mathbf{q}} + \gamma^{\mathrm{FM,c}}_{n\mathbf{k},\nu\mathbf{q}}, \tag{4.63}$$

$$\gamma^{\mathrm{FM,a}}_{n\mathbf{k},\nu\mathbf{q}} \equiv \sum_{m}{}' \frac{|\tilde{g}_{mn\mathbf{k},\nu\mathbf{q}}|^2}{\varepsilon_{n\mathbf{k}} - \varepsilon_{m\mathbf{k}+\mathbf{q}}}, \tag{4.64}$$

$$\gamma^{\mathrm{FM,b}}_{n\mathbf{k},\nu\mathbf{q}} \equiv \sum_{m}{}' \tilde{g}^*_{mn\mathbf{k},\nu\mathbf{q}} \tilde{t}_{mn\mathbf{k},\nu\mathbf{q}} + c.c., \tag{4.65}$$

$$\gamma^{\mathrm{FM,c}}_{n\mathbf{k},\nu\mathbf{q}} \equiv \sum_{m}{}' (\varepsilon_{n\mathbf{k}} - \varepsilon_{m\mathbf{k}+\mathbf{q}}) |\tilde{t}_{mn\mathbf{k},\nu\mathbf{q}}|^2, \tag{4.66}$$

$$\tilde{t}_{mn\mathbf{k},\nu\mathbf{q}} \equiv \langle \widetilde{\psi}_{m\mathbf{k}+\mathbf{q}} | \hat{\mathcal{T}}^\dagger \partial_{\nu\mathbf{q}} \hat{\mathcal{T}} | \widetilde{\psi}_{n\mathbf{k}} \rangle . \tag{4.67}$$

The term $\gamma^{\mathrm{FM,a}}_{n\mathbf{k},\nu\mathbf{q}}$ is already identical to the first line of Eq. (4.61). Next, let us add and subtract the $(m\mathbf{q}) = (n\mathbf{0})$ contribution to and from $\gamma^{\mathrm{FM,b}}_{n\mathbf{k},\nu\mathbf{q}}$ to complete the sum:

$$\gamma^{\mathrm{FM,b}}_{n\mathbf{k},\nu\mathbf{q}} = \left[\sum_{m} \tilde{g}^*_{mn\mathbf{k},\nu\mathbf{q}} \tilde{t}_{mn\mathbf{k},\nu\mathbf{q}} - \tilde{g}^*_{nn\mathbf{k},\nu\mathbf{0}} \tilde{t}_{nn\mathbf{k},\nu\mathbf{0}} \Omega_{\mathrm{BZ}} \delta^{(3)}(\mathbf{q}) \right] + c.c.. \tag{4.68}$$

Since $\partial_{\nu\mathbf{0}} = \partial^*_{\nu\mathbf{0}}$, we know that $\tilde{g}_{nn\mathbf{k},\nu\mathbf{0}}$ is real, which lets us further modify the terms appearing on the second line of Eq. (4.68):

$$\begin{aligned}
&\tilde{g}^*_{nn\mathbf{k},\nu\mathbf{0}}\tilde{t}_{nn\mathbf{k},\nu\mathbf{0}} + \tilde{t}^*_{nn\mathbf{k},\nu\mathbf{0}}\tilde{g}_{nn\mathbf{k},\nu\mathbf{0}} \\
&= \tilde{g}_{nn\mathbf{k},\nu\mathbf{0}}\left[\tilde{t}_{nn\mathbf{k},\nu\mathbf{0}} + \tilde{t}^*_{nn\mathbf{k},\nu\mathbf{0}}\right] \\
&= \tilde{g}_{nn\mathbf{k},\nu\mathbf{0}}\left\langle\widetilde{\psi}_{n\mathbf{k}}\middle|\partial_{\nu\mathbf{0}}\tilde{S}\middle|\widetilde{\psi}_{n\mathbf{k}}\right\rangle,
\end{aligned}$$

where we used the product rule of differentiation to retrieve the PAW overlap operator. Therefore,

$$\gamma^{\mathrm{FM,b}}_{n\mathbf{k},\nu\mathbf{q}} = \sum_m\left(\tilde{g}^*_{mn\mathbf{k},\nu\mathbf{q}}\tilde{t}_{mn\mathbf{k},\nu\mathbf{q}} + c.c.\right) - \tilde{g}_{nn\mathbf{k},\nu\mathbf{0}}\left\langle\widetilde{\psi}_{n\mathbf{k}}\middle|\partial_{\nu\mathbf{0}}\tilde{S}\middle|\widetilde{\psi}_{n\mathbf{k}}\right\rangle\Omega_{\mathrm{BZ}}\delta^{(3)}(\mathbf{q}). \quad (4.69)$$

Summing Eq. (4.64) and the second line of Eq. (4.69) yields exactly $\tilde{\gamma}^{\mathrm{FM}}_{n\mathbf{k},\nu\mathbf{q}}$, so the difference of the AE and PS FM contributions is simply the entire remainder:

$$\begin{aligned}
&\gamma^{\mathrm{FM}}_{n\mathbf{k},\nu\mathbf{q}} - \tilde{\gamma}^{\mathrm{FM}}_{n\mathbf{k},\nu\mathbf{q}} = \\
&\qquad\sum_m\left[(\varepsilon_{n\mathbf{k}} - \varepsilon_{m\mathbf{k}+\mathbf{q}})\left|\tilde{t}_{mn\mathbf{k},\nu\mathbf{q}}\right|^2 + \tilde{g}^*_{mn\mathbf{k},\nu\mathbf{q}}\tilde{t}_{mn\mathbf{k},\nu\mathbf{q}} + \tilde{t}^*_{mn\mathbf{k},\nu\mathbf{q}}\tilde{g}_{mn\mathbf{k},\nu\mathbf{q}}\right]. \quad (4.70)
\end{aligned}$$

Notice how Eq. (4.70) now contains a sum over all intermediate states, m. This is possible since the case $(m\mathbf{q}) = (n\mathbf{0})$ does not contribute in $\gamma^{\mathrm{FM,c}}_{n\mathbf{k},\nu\mathbf{q}}$.

To show the difference between the AE and PS DW contributions, it is easier to begin in the PS formulation by expanding Eq. (4.62) in terms of the PAW transformation and then applying the differential operators using the product rule. This way, the second derivative of the PAW Hamiltonian contributes 9 terms while the second derivative of the PAW overlap contributes 4. To keep track of all these terms, we once again group them into different contributions:

$$\tilde{\gamma}^{\mathrm{DW}}_{n\mathbf{k},\nu\mathbf{q}} = \gamma^{\mathrm{DW}}_{n\mathbf{k},\nu\mathbf{q}} + \tilde{\gamma}^{\mathrm{DW,a}}_{n\mathbf{k},\nu\mathbf{q}} + \tilde{\gamma}^{\mathrm{DW,b}}_{n\mathbf{k},\nu\mathbf{q}} + \tilde{\gamma}^{\mathrm{DW,c}}_{n\mathbf{k},\nu\mathbf{q}}, \quad (4.71)$$

$$\tilde{\gamma}^{\mathrm{DW,a}}_{n\mathbf{k},\nu\mathbf{q}} \equiv \frac{1}{2}\left\langle\widetilde{\psi}_{n\mathbf{k}}\middle|\,\partial_{\nu\mathbf{q}}\partial^*_{\nu\mathbf{q}}\hat{\mathcal{T}}^\dagger\hat{H}\hat{\mathcal{T}} - \varepsilon_{n\mathbf{k}}\partial_{\nu\mathbf{q}}\partial^*_{\nu\mathbf{q}}\hat{\mathcal{T}}^\dagger\hat{\mathcal{T}}\,\middle|\,\widetilde{\psi}_{n\mathbf{k}}\right\rangle + c.c., \quad (4.72)$$

$$\begin{aligned}
\tilde{\gamma}^{\mathrm{DW,b}}_{n\mathbf{k},\nu\mathbf{q}} \equiv{}& \frac{1}{2}\left\langle\widetilde{\psi}_{n\mathbf{k}}\middle|\,\partial^*_{\nu\mathbf{q}}\hat{\mathcal{T}}^\dagger\hat{H}\partial_{\nu\mathbf{q}}\hat{\mathcal{T}} + \partial_{\nu\mathbf{q}}\hat{\mathcal{T}}^\dagger\hat{H}\partial^*_{\nu\mathbf{q}}\hat{\mathcal{T}}\,\middle|\,\widetilde{\psi}_{n\mathbf{k}}\right\rangle \\
&- \frac{1}{2}\left\langle\widetilde{\psi}_{n\mathbf{k}}\middle|\varepsilon_{n\mathbf{k}}\partial^*_{\nu\mathbf{q}}\hat{\mathcal{T}}^\dagger\partial_{\nu\mathbf{q}}\hat{\mathcal{T}} + \varepsilon_{n\mathbf{k}}\partial_{\nu\mathbf{q}}\hat{\mathcal{T}}^\dagger\partial^*_{\nu\mathbf{q}}\hat{\mathcal{T}}\middle|\widetilde{\psi}_{n\mathbf{k}}\right\rangle, \quad (4.73)
\end{aligned}$$

$$\begin{aligned}
\tilde{\gamma}^{\mathrm{DW,c}}_{n\mathbf{k},\nu\mathbf{q}} \equiv{}& \frac{1}{2}\left\langle\widetilde{\psi}_{n\mathbf{k}}\middle|\,\hat{\mathcal{T}}^\dagger\partial^*_{\nu\mathbf{q}}\hat{H}\partial_{\nu\mathbf{q}}\hat{\mathcal{T}} + \hat{\mathcal{T}}^\dagger\partial_{\nu\mathbf{q}}\hat{H}\partial^*_{\nu\mathbf{q}}\hat{\mathcal{T}}\,\middle|\,\widetilde{\psi}_{n\mathbf{k}}\right\rangle \\
&+ \frac{1}{2}\left\langle\widetilde{\psi}_{n\mathbf{k}}\middle|\partial^*_{\nu\mathbf{q}}\hat{\mathcal{T}}^\dagger\partial_{\nu\mathbf{q}}\hat{H}\hat{\mathcal{T}} + \partial_{\nu\mathbf{q}}\hat{\mathcal{T}}^\dagger\partial^*_{\nu\mathbf{q}}\hat{H}\hat{\mathcal{T}}\middle|\widetilde{\psi}_{n\mathbf{k}}\right\rangle. \quad (4.74)
\end{aligned}$$

The first term on Eq. (4.71) is already the AE DW contribution. Using the KS equations, $\hat{H}\,|\psi_{n\mathbf{k}}\rangle = \varepsilon_{n\mathbf{k}}\,|\psi_{n\mathbf{k}}\rangle$, it is quite easy to show that $\tilde{\gamma}^{\mathrm{DW,a}}_{n\mathbf{k},\nu\mathbf{q}}$ is, in fact, zero. Eqs. (4.73) and (4.74) consist of pairs of terms which are invariant under a sign change of $\mathbf{q}$. For example, the first term in Eq. (4.73) maps onto the second term:

$$\partial^*_{\nu,-\mathbf{q}}\hat{\mathcal{T}}^\dagger\hat{H}\partial_{\nu,-\mathbf{q}}\hat{\mathcal{T}} = \partial_{\nu\mathbf{q}}\hat{\mathcal{T}}^\dagger\hat{H}\partial^*_{\nu\mathbf{q}}\hat{\mathcal{T}}.$$

Since the domain of integration is the FBZ and therefore inversion symmetric around the origin, the sign of the integration variable, $\mathbf{q}$, can be swapped without affecting the result. Hence, by redefining $\mathbf{q} \to -\mathbf{q}$ for only one term of each pair mentioned earlier, we can simplify the contributions from Eq. (4.73),

$$\int_{\Omega_{\mathrm{BZ}}} \frac{\mathrm{d}^3 q}{\Omega_{\mathrm{BZ}}} \tilde{\gamma}^{\mathrm{DW,b}}_{n\mathbf{k},\nu\mathbf{q}} = \int_{\Omega_{\mathrm{BZ}}} \frac{\mathrm{d}^3 q}{\Omega_{\mathrm{BZ}}} \langle \widetilde{\psi}_{n\mathbf{k}} | \partial^*_{\nu\mathbf{q}} \hat{\mathcal{T}}^\dagger \big(\hat{H} - \varepsilon_{n\mathbf{k}}\big) \partial_{\nu\mathbf{q}} \hat{\mathcal{T}} | \widetilde{\psi}_{n\mathbf{k}} \rangle \,, \tag{4.75}$$

and from Eq. (4.74),

$$\int_{\Omega_{\mathrm{BZ}}} \frac{\mathrm{d}^3 q}{\Omega_{\mathrm{BZ}}} \tilde{\gamma}^{\mathrm{DW,c}}_{n\mathbf{k},\nu\mathbf{q}} = \int_{\Omega_{\mathrm{BZ}}} \frac{\mathrm{d}^3 q}{\Omega_{\mathrm{BZ}}} \langle \widetilde{\psi}_{n\mathbf{k}} | \hat{\mathcal{T}}^\dagger \partial^*_{\nu\mathbf{q}} \hat{H} \partial_{\nu\mathbf{q}} \hat{\mathcal{T}} + \partial^*_{\nu\mathbf{q}} \hat{\mathcal{T}}^\dagger \partial_{\nu\mathbf{q}} \hat{H} \hat{\mathcal{T}} | \widetilde{\psi}_{n\mathbf{k}} \rangle \,. \tag{4.76}$$

Each of the matrix elements appearing in Eqs. (4.75) and (4.76) consists of a product of two first-order derivatives. In order to separate them, we insert the complete basis of PS Bloch states,

$$\mathbb{1} = \int_{\Omega_{\mathrm{BZ}}} \frac{\mathrm{d}^3 k}{\Omega_{\mathrm{BZ}}} \sum_m \hat{\mathcal{T}} \, | \widetilde{\psi}_{m\mathbf{k}} \rangle \langle \widetilde{\psi}_{m\mathbf{k}} | \, \hat{\mathcal{T}}^\dagger,$$

in-between the operators. Due to the Bloch theorem, it is sufficient to only involve states at $\mathbf{k}+\mathbf{q}$ to complete the basis in this case. Let us demonstrate this procedure for the first matrix element in Eq. (4.75):

$$\begin{aligned}
\partial^*_{\nu\mathbf{q}} \hat{\mathcal{T}}^\dagger \hat{H} \partial_{\nu\mathbf{q}} \hat{\mathcal{T}} &= \partial^*_{\nu\mathbf{q}} \hat{\mathcal{T}}^\dagger \sum_m \big(\hat{\mathcal{T}} \, | \widetilde{\psi}_{m\mathbf{k}+\mathbf{q}} \rangle \langle \widetilde{\psi}_{m\mathbf{k}+\mathbf{q}} | \, \hat{\mathcal{T}}^\dagger \big) \hat{H} \\
&\quad \times \sum_{m'} \big(\hat{\mathcal{T}} \, | \widetilde{\psi}_{m'\mathbf{k}+\mathbf{q}} \rangle \langle \widetilde{\psi}_{m'\mathbf{k}+\mathbf{q}} | \, \hat{\mathcal{T}}^\dagger \big) \partial_{\nu\mathbf{q}} \hat{\mathcal{T}} \\
&= \sum_{mm'} \partial^*_{\nu\mathbf{q}} \hat{\mathcal{T}}^\dagger \hat{\mathcal{T}} \, | \widetilde{\psi}_{m\mathbf{k}+\mathbf{q}} \rangle \underbrace{\langle \widetilde{\psi}_{m\mathbf{k}+\mathbf{q}} | \tilde{H} | \widetilde{\psi}_{m'\mathbf{k}+\mathbf{q}} \rangle}_{\varepsilon_{m\mathbf{k}+\mathbf{q}} \delta_{mm'}} \langle \widetilde{\psi}_{m'\mathbf{k}+\mathbf{q}} | \, \hat{\mathcal{T}}^\dagger \partial_{\nu\mathbf{q}} \hat{\mathcal{T}} \\
&= \sum_m \varepsilon_{m\mathbf{k}+\mathbf{q}} \partial^*_{\nu\mathbf{q}} \hat{\mathcal{T}}^\dagger \hat{\mathcal{T}} \, | \widetilde{\psi}_{m\mathbf{k}+\mathbf{q}} \rangle \langle \widetilde{\psi}_{m\mathbf{k}+\mathbf{q}} | \, \hat{\mathcal{T}}^\dagger \partial_{\nu\mathbf{q}} \hat{\mathcal{T}}.
\end{aligned}$$

Using this trick to separate the derivatives, Eq. (4.75) becomes

$$\int_{\Omega_{\mathrm{BZ}}} \frac{\mathrm{d}^3 q}{\Omega_{\mathrm{BZ}}} \tilde{\gamma}^{\mathrm{DW,b}}_{n\mathbf{k},\nu\mathbf{q}} = - \int_{\Omega_{\mathrm{BZ}}} \frac{\mathrm{d}^3 q}{\Omega_{\mathrm{BZ}}} \sum_m \big(\varepsilon_{n\mathbf{k}} - \varepsilon_{m\mathbf{k}+\mathbf{q}} \big) \big| \tilde{t}_{mn\mathbf{k},\nu\mathbf{q}} \big|^2. \tag{4.77}$$

Similarly, Eq. (4.76) becomes

$$\int_{\Omega_{\mathrm{BZ}}} \frac{\mathrm{d}^3 q}{\Omega_{\mathrm{BZ}}} \tilde{\gamma}^{\mathrm{DW,c}}_{n\mathbf{k},\nu\mathbf{q}} = \int_{\Omega_{\mathrm{BZ}}} \frac{\mathrm{d}^3 q}{\Omega_{\mathrm{BZ}}} \sum_m \big(g^*_{mn\mathbf{k},\nu\mathbf{q}} t_{mn\mathbf{k},\nu\mathbf{q}} + t^*_{mn\mathbf{k},\nu\mathbf{q}} g_{mn\mathbf{k},\nu\mathbf{q}} \big). \tag{4.78}$$

The final step involves transforming the AE matrix elements in Eq. (4.78) to the PS representation using Eq. (4.55):

$$\begin{aligned}
g^*_{mn\mathbf{k},\nu\mathbf{q}} t_{mn\mathbf{k},\nu\mathbf{q}} + t^*_{mn\mathbf{k},\nu\mathbf{q}} g_{mn\mathbf{k},\nu\mathbf{q}} &= \tilde{g}^*_{mn\mathbf{k},\nu\mathbf{q}} t_{mn\mathbf{k},\nu\mathbf{q}} + t^*_{mn\mathbf{k},\nu\mathbf{q}} \tilde{g}_{mn\mathbf{k},\nu\mathbf{q}} \\
&\quad + 2\big(\varepsilon_{n\mathbf{k}} - \varepsilon_{m\mathbf{k}+\mathbf{q}} \big) \big| \tilde{t}_{mn\mathbf{k},\nu\mathbf{q}} \big|^2.
\end{aligned} \tag{4.79}$$

This allows us to state the difference between the integrated AE and PS DW contributions:

$$\int_{\Omega_{\mathrm{BZ}}} \frac{\mathrm{d}^3 q}{\Omega_{\mathrm{BZ}}} \left(\tilde{\gamma}^{\mathrm{DW}}_{n\mathbf{k},\nu\mathbf{q}} - \gamma^{\mathrm{DW}}_{n\mathbf{k},\nu\mathbf{q}}\right) = \int_{\Omega_{\mathrm{BZ}}} \frac{\mathrm{d}^3 q}{\Omega_{\mathrm{BZ}}} \sum_m \left[(\varepsilon_{n\mathbf{k}} - \varepsilon_{m\mathbf{k}+\mathbf{q}}) |\tilde{t}_{mn\mathbf{k},\nu\mathbf{q}}|^2 + \tilde{g}^*_{mn\mathbf{k},\nu\mathbf{q}} \tilde{t}_{mn\mathbf{k},\nu\mathbf{q}} + \tilde{t}^*_{mn\mathbf{k},\nu\mathbf{q}} \tilde{g}_{mn\mathbf{k},\nu\mathbf{q}} \right]. \tag{4.80}$$

Finally, we are able to compare Eq. (4.80) against Eq. (4.70) and find that

$$\int_{\Omega_{\mathrm{BZ}}} \frac{\mathrm{d}^3 q}{\Omega_{\mathrm{BZ}}} \left(\gamma^{\mathrm{FM}}_{n\mathbf{k},\nu\mathbf{q}} - \tilde{\gamma}^{\mathrm{FM}}_{n\mathbf{k},\nu\mathbf{q}}\right) = \int_{\Omega_{\mathrm{BZ}}} \frac{\mathrm{d}^3 q}{\Omega_{\mathrm{BZ}}} \left(\tilde{\gamma}^{\mathrm{DW}}_{n\mathbf{k},\nu\mathbf{q}} - \gamma^{\mathrm{DW}}_{n\mathbf{k},\nu\mathbf{q}}\right), \tag{4.81}$$

which, of course, implies that the AE and PS ZPR equations are identical.

Note that this equivalence between the AE and PS formulations is no longer valid once the rigid-ion approximation is introduced. This approximation is used to calculate the second-order DW contribution with greater computational efficiency and is detailed in Section 4.5. However, the way this approximation is employed in the PS case is different from how it is employed in the AE case, in the sense that the resulting ZPR expressions are no longer formally equivalent. Furthermore, the proof is only valid in the limit of a complete set of PAW partial waves.

4.4.3.2 Computational Differences

When comparing the AE against the PS approach, one might wonder about the computational characteristics of the respective electron-phonon matrix elements, $g_{mn\mathbf{k},\nu\mathbf{q}}$ and $\tilde{g}_{mn\mathbf{k},\nu\mathbf{q}}$. Even in the case where both approaches are equivalent, as proved in Section 4.4.3.1 for the adiabatic approximation, the practical aspects of using either method should be well understood. In this section, we provide an alternative way of writing the AE and PS matrix elements. This allows us to compare various PAW contributions and formulate tentative qualitative statements about the computational performance. A quantitative study and thorough discussion is presented in Section 6.2.

Let us organize the contributions to the AE electron-phonon matrix element in the same way as done by Chaput, Togo and Tanaka [34]:

$$g_{m\mathbf{k}',n\mathbf{k},l\kappa\alpha} = g^{(\mathrm{V})}_{m\mathbf{k}',n\mathbf{k},l\kappa\alpha} + g^{(\mathrm{D})}_{m\mathbf{k}',n\mathbf{k},l\kappa\alpha} + g^{(\mathrm{P})}_{m\mathbf{k}',n\mathbf{k},l\kappa\alpha} + g^{(\mathrm{R})}_{m\mathbf{k}',n\mathbf{k},l\kappa\alpha}, \tag{4.82}$$

with

$$g^{(\mathrm{V})}_{m\mathbf{k}',n\mathbf{k},l\kappa\alpha} \equiv \langle \widetilde{\psi}_{m\mathbf{k}'} | \frac{\partial \tilde{v}}{\partial u_{l\kappa\alpha}} | \widetilde{\psi}_{n\mathbf{k}} \rangle , \tag{4.83}$$

$$g^{(\mathrm{D})}_{m\mathbf{k}',n\mathbf{k},l\kappa\alpha} \equiv \sum_{l'\kappa'} \sum_{ij} \langle \widetilde{\psi}_{m\mathbf{k}'} | \widetilde{p}_{l'\kappa' i} \rangle \frac{\partial D_{l'\kappa',ij}}{\partial u_{l\kappa\alpha}} \langle \widetilde{p}_{l'\kappa' j} | \widetilde{\psi}_{n\mathbf{k}} \rangle , \tag{4.84}$$

$$\begin{aligned} g^{(\mathrm{P})}_{m\mathbf{k}',n\mathbf{k},l\kappa\alpha} \equiv & \sum_{ij} \langle \widetilde{\psi}_{m\mathbf{k}'} | \frac{\partial \widetilde{p}_{l\kappa i}}{\partial u_{l\kappa\alpha}} \rangle \left(D_{l\kappa,ij} - \varepsilon_{n\mathbf{k}} Q_{l\kappa,ij} \right) \langle \widetilde{p}_{l\kappa j} | \widetilde{\psi}_{n\mathbf{k}} \rangle \\ & + \sum_{ij} \langle \widetilde{\psi}_{m\mathbf{k}'} | \widetilde{p}_{l\kappa i} \rangle \left(D_{l\kappa,ij} - \varepsilon_{m\mathbf{k}'} Q_{l\kappa,ij} \right) \langle \frac{\partial \widetilde{p}_{l\kappa j}}{\partial u_{l\kappa\alpha}} | \widetilde{\psi}_{n\mathbf{k}} \rangle , \end{aligned} \tag{4.85}$$

$$g^{(\mathrm{R})}_{m\mathbf{k}',n\mathbf{k},l\kappa\alpha} \equiv (\varepsilon_{n\mathbf{k}} - \varepsilon_{m\mathbf{k}'}) \sum_{ij} \langle \widetilde{\psi}_{m\mathbf{k}'} | \widetilde{p}_{l\kappa i} \rangle R_{l\kappa\alpha,ij} \langle \widetilde{p}_{l\kappa j} | \widetilde{\psi}_{n\mathbf{k}} \rangle . \tag{4.86}$$

Here, the Hamiltonian is written more explicitly in terms of the pseudopotential, $\tilde{v}$, and the PAW strengths, $D_{l\kappa,ij}$. We have introduced these quantities in Section 2.4. Note that the kinetic-energy term is absent since it does not depend on the atomic coordinates. We also like to mention that $D_{l\kappa,ij}$ contains the non-local part of the PAW Hamiltonian. Therefore, there is an additional sum over atomic sites present in $g^{(\mathrm{D})}$.

Compared to Eq. (4.53), $\frac{\partial \tilde{H}}{\partial u_{l\kappa\alpha}}$ is now split between $g^{(\mathrm{V})}$, $g^{(\mathrm{D})}$ and $g^{(\mathrm{P})}$. The second and third lines of Eq. (4.53) are contained in $g^{(\mathrm{P})}$, and the last line of Eq. (4.53) remains unaltered as $g^{(\mathrm{R})}$. This way, it is easier to make precise statements about the derivatives required to evaluate Eq. (4.82).

Similarly, we reorganize the contributions to the PS electron-phonon matrix element [35]:

$$\tilde{g}_{m\mathbf{k}',n\mathbf{k},l\kappa\alpha} = g^{(\mathrm{V})}_{m\mathbf{k}',n\mathbf{k},l\kappa\alpha} + g^{(\mathrm{D})}_{m\mathbf{k}',n\mathbf{k},l\kappa\alpha} + g^{(\mathrm{Q})}_{m\mathbf{k}',n\mathbf{k},l\kappa\alpha}, \tag{4.87}$$

with

$$\begin{aligned} g^{(\mathrm{Q})}_{m\mathbf{k}',n\mathbf{k},l\kappa\alpha} \equiv & \sum_{ij} \langle \widetilde{\psi}_{m\mathbf{k}'} | \frac{\partial \widetilde{p}_{l\kappa i}}{\partial u_{l\kappa\alpha}} \rangle \left(D_{l\kappa,ij} - \varepsilon_{n\mathbf{k}} Q_{l\kappa,ij} \right) \langle \widetilde{p}_{l\kappa j} | \widetilde{\psi}_{n\mathbf{k}} \rangle \\ & + \sum_{ij} \langle \widetilde{\psi}_{m\mathbf{k}'} | \widetilde{p}_{l\kappa i} \rangle \left(D_{l\kappa,ij} - \varepsilon_{n\mathbf{k}} Q_{l\kappa,ij} \right) \langle \frac{\partial \widetilde{p}_{l\kappa j}}{\partial u_{l\kappa\alpha}} | \widetilde{\psi}_{n\mathbf{k}} \rangle . \end{aligned} \tag{4.88}$$

This is indeed equivalent to Eq. (4.55). The matrix element is expressed using only a single atomic derivative. As usual, the connection to the electron-phonon matrix element in the phonon picture is established via Eq. (4.8).

Notably, the contributions $g^{(\mathrm{P})}$ and $g^{(\mathrm{Q})}$ look very similar, yet differ in an important aspect. Instead of the KS eigenvalues $\varepsilon_{m\mathbf{k}+\mathbf{q}}$ of the intermediate state, Eq. (4.88) features only the KS eigenvalues $\varepsilon_{n\mathbf{k}}$. The AE expression is symmetric, while the PS one is not. This can play an important role in the convergence behavior of the ZPR with respect to the number of intermediate states and is discussed further in Section 6.2.

Eqs. (4.82) to (4.88) provide one way of calculating the AE and PS electron-phonon matrix elements. The derivatives of the potential and PAW strengths can be computed from finite-displacement calculations in supercells. While other means of evaluating the derivatives exist, such as DFPT, we will use the intuitive picture of finite-displacement methods to investigate the computational characteristics of the matrix elements.

Let us think of the atomic derivative as a small rigid displacement of the corresponding atom along a Cartesian direction. Importantly, the sharp $1/r$ cusp of the Coulomb potential also moves in unison with the nucleus that generates it. Smooth PS quantities, such as $\tilde{v}$ and $\widetilde{p}$, are constructed such that the Coulomb cusp is effectively replaced by a smooth pseudopotential that is easily described in terms of only a few plane waves. Hence, small shifts of the nuclear Coulomb potential do not introduce any sharp features in the atomic derivatives of PS quantities. For that reason, the derivatives involved in $g^{(\mathrm{V})}$, $g^{(\mathrm{P})}$ and $g^{(\mathrm{Q})}$ are generally representable in the same PAW basis set used to solve the KS equations. This assumption is also important for calculating forces using the PAW method or other pseudization methods [31, 32].

Let us continue to investigate the effect of an atomic displacement on the remaining terms, $g^{(\mathrm{D})}$ and $g^{(\mathrm{R})}$. The term $g^{(\mathrm{D})}$ is common to both the AE and the PS matrix elements. It involves the derivative of the PAW strengths, $D_{l\kappa,ij}$, which is also routinely computed in force calculations [32] and is well represented in the PAW basis. When the nucleus is displaced from its equilibrium position, both pairs of partial waves involved in the inner product in $D_{l\kappa,ij}$ move in unison. This means that the on-site terms are still well representable using the shifted local basis functions.

The term $g^{(\mathrm{R})}$ involves the matrix $R_{l\kappa\alpha,ij}$ defined in Eq. (4.51). In this case, the perturbed partial waves are projected onto their unperturbed counterparts. Such a term is qualitatively different from the ones discussed so far. Even though the rapid oscillations encoded in the AE partial waves can be accurately represented using the local PAW basis, the same is not necessarily true of their derivative. This is particularly relevant whenever the PAW basis is incomplete, which is the case in practice. Due to this reason, $g^{(\mathrm{R})}$ is likely to have the largest dependence on the PAW basis set out of all the terms discussed so far. However, without a quantitative study, it is very difficult to make any definitive statement about general practical implications.

4.5 Rigid-Ion Approximation

To accurately calculate the band-structure renormalization in the adiabatic AHC framework, one has to compute the FM as well as the DW contribution. While the former only contains first derivatives, the evaluation of the DW matrix element requires the computation of a second derivative for each vibrational degree of freedom. Consequently, a direct computation of the DW term, for example

by means of finite displacements, can be expensive in practice. Therefore, the DW term is often approximated by the so-called rigid-ion approximation (RIA). In this section, we quickly demonstrate the RIA and how it leads to a computationally more tractable formulation of the AHC theory. In addition, we provide a PS formulation of the RIA in the PAW framework.

The basic idea behind the RIA stems directly from the translational invariance of the equilibrium crystal structure. Any rigid translation of *all* atoms of the crystal in the *same* direction cannot have an effect on the electronic band structure. We can express this mathematically as

$$\sum_{l\kappa} \frac{\partial \varepsilon_{n\mathbf{k}}}{\partial u_{l\kappa\alpha}} = \sum_{l\kappa} g_{n\mathbf{k},l\kappa\alpha} = 0. \tag{4.89}$$

Eq. (4.89) is one of multiple manifestations of the ASR. Taking the derivative of Eq. (4.89) with respect to an additional atomic displacement yields yet another sum rule:

$$\sum_{l'\kappa'} g^{\mathrm{DW}}_{n\mathbf{k},l\kappa\alpha,l'\kappa'\beta} + \sum_{l'\kappa'} {\sum_{m\mathbf{k}'}}' \mathrm{Re}\, \frac{g^*_{m\mathbf{k}',n\mathbf{k},l\kappa\alpha} g_{m\mathbf{k}',n\mathbf{k},l'\kappa'\beta}}{\varepsilon_{n\mathbf{k}} - \varepsilon_{m\mathbf{k}'}} = 0, \tag{4.90}$$

where

$$g^{\mathrm{DW}}_{n\mathbf{k},l\kappa\alpha,l'\kappa'\beta} \equiv \frac{1}{2} \langle \psi_{n\mathbf{k}} | \frac{\partial^2 \hat{H}}{\partial u_{l\kappa\alpha}\, \partial u_{l'\kappa'\beta}} | \psi_{n\mathbf{k}} \rangle \tag{4.91}$$

is simply the diagonal DW matrix element written in terms of a single atomic displacement. Once again, the primed sum in Eq. (4.90) indicates that the case $(m\mathbf{k}') = (n\mathbf{k})$ is excluded from the summation.

The RIA is obtained by neglecting the $(l\kappa) \neq (l'\kappa')$ off-diagonal DW matrix elements in Eq. (4.90). This way, only on-site terms are allowed to contribute to the DW energy shift. Importantly, the RIA allows us to express the remaining second-order DW matrix elements in terms of only first-order matrix elements:

$$g^{\mathrm{DW}}_{n\mathbf{k},l\kappa\alpha,l\kappa\beta} \approx -2 \sum_{l'\kappa'} {\sum_{m\mathbf{k}'}}' \mathrm{Re}\, \frac{g^*_{m\mathbf{k}',n\mathbf{k},l\kappa\alpha} g_{m\mathbf{k}',n\mathbf{k},l'\kappa'\beta}}{\varepsilon_{n\mathbf{k}} - \varepsilon_{m\mathbf{k}'}}. \tag{4.92}$$

This significantly reduces the computational cost of the procedure as the first-order electron-phonon matrix elements need to be computed anyway in order to evaluate the FM contribution.

Eq. (4.92) can now be used to approximate the DW term in the AHC theory, Eq. (4.21), which results in the following DW energy shift [25, 35]:

$$\Delta\varepsilon^{\mathrm{DW}}_{n\mathbf{k}}(T) \approx -\int_{\Omega_{\mathrm{BZ}}} \frac{\mathrm{d}^3 q}{\Omega_{\mathrm{BZ}}} \sum_{\nu} {\sum_{m}}' \frac{\Xi_{mn\mathbf{k},\nu\mathbf{q}}}{\varepsilon_{n\mathbf{k}} - \varepsilon_{m\mathbf{k}}} \big(2n_{\nu\mathbf{q}}(T) + 1\big), \tag{4.93}$$

where

$$\Xi_{mn\mathbf{k},\nu\mathbf{q}} \equiv \frac{\hbar}{4\omega_{\nu\mathbf{q}}} \sum_{\kappa\alpha} \sum_{\kappa'\beta} \Theta^{\nu\mathbf{q}}_{\kappa\alpha,\kappa'\beta} g^{0*}_{mn\mathbf{k},\kappa\alpha} g^{0}_{mn\mathbf{k},\kappa'\beta}, \tag{4.94}$$

$$\Theta^{\nu\mathbf{q}}_{\kappa\alpha,\kappa'\beta} \equiv \frac{e_{\kappa\alpha,\nu\mathbf{q}} e^{*}_{\kappa\beta,\nu\mathbf{q}}}{m_\kappa} + \frac{e^{*}_{\kappa'\alpha,\nu\mathbf{q}} e_{\kappa'\beta,\nu\mathbf{q}}}{m_{\kappa'}}, \tag{4.95}$$

$$g^{0}_{mn\mathbf{k},\kappa\alpha} \equiv \sum_{\nu} \sqrt{\frac{2m_\kappa \omega_{\nu\mathbf{0}}}{\hbar}} e_{\kappa\alpha,\nu\mathbf{0}} g_{mn\mathbf{k},\nu\mathbf{0}}. \tag{4.96}$$

Eq. (4.93) now looks similar to the FM contribution. One of the biggest differences between the two is that the electron-phonon matrix elements in Eq. (4.93) are not dependent on the phonon wave vector, $\mathbf{q}$. In fact, the only $\mathbf{q}$-dependent terms are phonon frequencies, eigenvectors and occupancies. This means that the approximated DW contribution is generally much cheaper to calculate than the FM contribution.

We will now summarize how the RIA works in the PS formulation of the electron-phonon interaction. We showed in the past [30, 33] that the RIA can be derived in the PS formulation using the same basic principles as outlined earlier. The ASR in Eq. (4.89) is still fulfilled if the AE electron-phonon matrix element is replaced by its PS counterpart:

$$\sum_{l\kappa} \frac{\partial \varepsilon_{n\mathbf{k}}}{\partial u_{l\kappa\alpha}} = \sum_{l\kappa} \tilde{g}_{n\mathbf{k},n\mathbf{k},l\kappa\alpha} = 0. \tag{4.97}$$

From Eq. (4.97), the steps needed to arrive at the RIA are identical to before. However, just as with the PS formulation of the FM contribution, the DW term acquires an additional contribution due to the S-orthogonality of the PS orbitals:

$$\sum_{l'\kappa'} \tilde{g}^{\mathrm{DW}}_{n\mathbf{k},l\kappa\alpha,l'\kappa'\beta} + \sum_{l'\kappa'} {\sum_{m\mathbf{k}'}}' \mathrm{Re} \frac{\tilde{g}^{*}_{m\mathbf{k}',n\mathbf{k},l\kappa\alpha} \tilde{g}_{m\mathbf{k}',n\mathbf{k},l'\kappa'\beta}}{\varepsilon_{n\mathbf{k}} - \varepsilon_{m\mathbf{k}'}} - \frac{1}{2} \sum_{l'\kappa'} \left(\tilde{g}_{n\mathbf{k},n\mathbf{k},l\kappa\alpha} \tilde{g}^{\mathrm{S}}_{n\mathbf{k},n\mathbf{k},l'\kappa'\beta} + \tilde{g}^{\mathrm{S}}_{n\mathbf{k},n\mathbf{k},l\kappa\alpha} \tilde{g}_{n\mathbf{k},n\mathbf{k},l'\kappa'\beta} \right) = 0, \tag{4.98}$$

where

$$\tilde{g}^{\mathrm{DW}}_{n\mathbf{k},l\kappa\alpha,l'\kappa'\beta} \equiv \frac{1}{2} \langle \psi_{n\mathbf{k}} | \frac{\partial^2 \widetilde{H}}{\partial u_{l\kappa\alpha}\, \partial u_{l'\kappa'\beta}} - \varepsilon_{n\mathbf{k}} \frac{\partial^2 \tilde{S}}{\partial u_{l\kappa\alpha}\, \partial u_{l'\kappa'\beta}} | \psi_{n\mathbf{k}} \rangle, \tag{4.99}$$

$$\tilde{g}_{m\mathbf{k}',n\mathbf{k},l\kappa\alpha} \equiv \langle \widetilde{\psi}_{m\mathbf{k}'} | \frac{\partial \widetilde{H}}{\partial u_{l\kappa\alpha}} - \varepsilon_{n\mathbf{k}} \frac{\partial \tilde{S}}{\partial u_{l\kappa\alpha}} | \widetilde{\psi}_{n\mathbf{k}} \rangle, \tag{4.100}$$

$$\tilde{g}^{\mathrm{S}}_{m\mathbf{k}',n\mathbf{k},l\kappa\alpha} \equiv \langle \widetilde{\psi}_{m\mathbf{k}'} | \frac{\partial \tilde{S}}{\partial u_{l\kappa\alpha}} | \widetilde{\psi}_{n\mathbf{k}} \rangle. \tag{4.101}$$

Eqs. (4.99) to (4.101) are the same PS quantities as defined in Eqs. (4.29), (4.39) and (4.40) but expressed in terms of a single atomic displacement using Eq. (4.8).

Finally, completing the derivation as instructed earlier gives the following RIA to the DW energy shift in the PS formulation [33]:

$$\Delta\tilde{\varepsilon}^{\mathrm{DW}}_{n\mathbf{k}}(T) \approx -\int_{\Omega_{\mathrm{BZ}}} \frac{\mathrm{d}^3 q}{\Omega_{\mathrm{BZ}}} \sum_{\nu} \left(\sum_{m}{}' \frac{\Xi_{mn\mathbf{k},\nu\mathbf{q}}}{\varepsilon_{n\mathbf{k}} - \varepsilon_{m\mathbf{k}}} - \Xi^{\mathrm{S}}_{n\mathbf{k},\nu\mathbf{q}} \right) \left(2n_{\nu\mathbf{q}}(T) + 1\right), \tag{4.102}$$

where

$$\widetilde{\Xi}_{mn\mathbf{k},\nu\mathbf{q}} \equiv \frac{\hbar}{4\omega_{\nu\mathbf{q}}} \sum_{\kappa\alpha} \sum_{\kappa'\beta} \Theta^{\nu\mathbf{q}}_{\kappa\alpha,\kappa'\beta} \tilde{g}^{0*}_{mn\mathbf{k},\kappa\alpha} \tilde{g}^{0}_{mn\mathbf{k},\kappa'\beta}, \tag{4.103}$$

$$\widetilde{\Xi}^{\mathrm{S}}_{n\mathbf{k},\nu\mathbf{q}} \equiv \frac{\hbar}{4\omega_{\nu\mathbf{q}}} \sum_{\kappa\alpha} \sum_{\kappa'\beta} \Theta^{\nu\mathbf{q}}_{\kappa\alpha,\kappa'\beta} \tilde{g}^{0}_{nn\mathbf{k},\kappa\alpha} \tilde{g}^{\mathrm{S}0}_{nn\mathbf{k},\kappa'\beta}, \tag{4.104}$$

$$\tilde{g}^{0}_{mn\mathbf{k},\kappa\alpha} \equiv \sum_{\nu} \sqrt{\frac{2m_\kappa \omega_{\nu\mathbf{0}}}{\hbar}} e_{\kappa\alpha,\nu\mathbf{0}} \tilde{g}_{mn\mathbf{k},\nu\mathbf{0}}, \tag{4.105}$$

$$\tilde{g}^{\mathrm{S}0}_{mn\mathbf{k},\kappa\alpha} \equiv \sum_{\nu} \sqrt{\frac{2m_\kappa \omega_{\nu\mathbf{0}}}{\hbar}} e_{\kappa\alpha,\nu\mathbf{0}} \tilde{g}^{\mathrm{S}}_{mn\mathbf{k},\nu\mathbf{0}}. \tag{4.106}$$

An important question that arises in this context is whether the application of the RIA approximation in the PS framework is consistent with the RIA in the AE framework. At first glance, this seems to be the case. The RIA was motivated from general symmetry considerations, and we apply the same principles in each framework. However, in general, as we have shown in Section 4.4.3.1,

$$\Delta\varepsilon^{\mathrm{DW}}_{n\mathbf{k}}(T) \neq \Delta\tilde{\varepsilon}^{\mathrm{DW}}_{n\mathbf{k}}(T), \tag{4.107}$$

This implies that performing the RIA as shown in this section can introduce an inconsistency between the PS and AE frameworks. Just how large the difference between the two formulations is in practice is difficult to estimate without a numerical study.

4.6 Long-range Electron-phonon Interactions

As we have discussed in Section 3.5, a collective out-of-phase displacement of the ions in a polar material induces dipoles that give long-range electrostatic contributions to the dynamical matrix. Similarly, these induced dipoles also give long-range electrostatic contributions to electron-phonon matrix elements corresponding to LO phonon modes. In fact, the interaction of the involved electrons with the dipole potential causes the matrix elements to diverge in the limit of small phonon wave vectors. The earliest mathematical description of this phenomenon is known as the Fröhlich interaction which originated from considerations by Fröhlich [45] and Vogl [44].

In this section, we present a model for the electron-phonon matrix element that correctly accounts for long-range dipole contribution [46, 47], which are the

predominant contributions at long wavelengths. The derivation closely follows Ref. [46] and builds on concepts and quantities introduced in Sections 3.5 and 3.6. The quadrupole interaction was recently covered in the literature [43, 48–50], but is not covered here.

Much of the work needed to derive the long-range electron-phonon matrix element from electrostatics was done in Section 3.6. Therefore, let us simply recall Eq. (3.55), i.e., the electric potential generated by a dipole inside an anisotropic uniform dielectric:

$$\phi^{\mathrm{d}}(\mathbf{r}, \boldsymbol{\xi}, \mathbf{p}) = -\frac{\mathrm{i}}{2\pi^2} \int_{\mathbb{R}^3} \mathrm{d}^3 q \, \frac{\mathbf{p} \cdot \mathbf{q}}{\mathbf{q}^\top \boldsymbol{\epsilon}^\infty \mathbf{q}} \mathrm{e}^{\mathrm{i}\mathbf{q}\cdot(\mathbf{r}-\boldsymbol{\xi})}. \tag{4.108}$$

However, this time, we need to couple the phonon-induced dipole moment to an electron. To accomplish this, the dipole, $\mathbf{p}$, is first expressed in terms of atomic displacements, just as in Eq. (3.57). Afterwards, it can further be expressed in terms of phonon eigenmodes by using the second-quantized form of the atomic displacements, Eq. (3.11). This involves promoting the dipole moment to an operator that acts on phononic states and has the following form:

$$\hat{\mathbf{p}}_{l\kappa,\nu\mathbf{q}} = e\sqrt{\frac{\hbar}{2m_\kappa \omega_{\nu\mathbf{q}}}} \mathrm{e}^{\mathrm{i}\mathbf{q}\cdot\mathbf{R}_l} \mathbf{Z}^\star_\kappa \mathbf{e}_{\kappa,\nu\mathbf{q}} \left(\hat{b}_{\nu\mathbf{q}} + \hat{b}^\dagger_{\nu,-\mathbf{q}}\right). \tag{4.109}$$

Meanwhile, to couple Eq. (3.55) to an electron, we first multiply with its charge, e. Additionally, the position coordinate, $\mathbf{r}$, needs to be associated with the electron. In second quantization, this is achieved via the electron field operator, $\hat{\Psi}(\mathbf{r})$,

$$\mathbf{r} \to \hat{\Psi}^\dagger(\mathbf{r}) \mathbf{r} \hat{\Psi}(\mathbf{r}),$$

which acts on the electronic multi-particle state. $\hat{\Psi}^\dagger(\mathbf{r})$ and $\hat{\Psi}(\mathbf{r})$ can conveniently be expanded into a basis of single-particle KS states using the electron creation and annihilation operators, respectively:

$$\hat{\Psi}(\mathbf{r}) = \sum_n \int_{\Omega_{\mathrm{BZ}}} \frac{\mathrm{d}^3 k}{\Omega_{\mathrm{BZ}}} \langle \mathbf{r} | \psi_{n\mathbf{k}} \rangle \hat{c}_{n\mathbf{k}}. \tag{4.110}$$

Combining Eqs. (4.108) to (4.110) and summing over all electronic and phononic degrees of freedom lets us formulate the long-range dipole contribution to the electron-phonon Hamiltonian, $\hat{H}^{\mathrm{LR}}_{\mathrm{ep}}$:

$$\begin{aligned} \hat{H}^{\mathrm{LR}}_{\mathrm{ep}} = \sum_{mn} \sum_{l\kappa} \sum_{\nu} \int_{\Omega_{\mathrm{BZ}}} \frac{\mathrm{d}^3 k}{\Omega_{\mathrm{BZ}}} \int_{\Omega_{\mathrm{BZ}}} \frac{\mathrm{d}^3 k'}{\Omega_{\mathrm{BZ}}} \int_{\Omega_{\mathrm{BZ}}} \frac{\mathrm{d}^3 q}{\Omega_{\mathrm{BZ}}} \hat{c}^\dagger_{m\mathbf{k}'} \hat{c}_{n\mathbf{k}} \left(\hat{b}_{\nu\mathbf{q}} + \hat{b}^\dagger_{\nu,-\mathbf{q}}\right) \\ \times \mathrm{i}2e^2 \sqrt{\frac{\hbar}{2m_\kappa \omega_{\nu\mathbf{q}}}} \mathrm{e}^{\mathrm{i}\mathbf{q}\cdot\mathbf{R}_l} \int_{\mathbb{R}^3} \mathrm{d}^3 q' \, \frac{\mathbf{q}'^\top \mathbf{Z}^\star_\kappa \mathbf{e}_{\kappa,\nu\mathbf{q}}}{\mathbf{q}'^\top \boldsymbol{\epsilon}^\infty \mathbf{q}'} \langle \psi_{m\mathbf{k}'} | \mathrm{e}^{\mathrm{i}\mathbf{q}'\cdot(\hat{\mathbf{r}}-\mathbf{R}_{l\kappa})} | \psi_{n\mathbf{k}} \rangle . \end{aligned} \tag{4.111}$$

Since Eq. (4.111) is quite a lengthy expression, let us quickly recapitulate the action of each creation and annihilation operator. $\hat{c}_{n\mathbf{k}}$ removes the incoming electron, $|\psi_{n\mathbf{k}}\rangle$, from the initial multi-particle state. At the same time, $\hat{c}^\dagger_{m\mathbf{k}'}$ adds the outgoing electron, $|\psi_{m\mathbf{k}'}\rangle$, to the final multi-particle state. $\hat{b}_{\nu\mathbf{q}}$ and $\hat{b}^\dagger_{\nu,-\mathbf{q}}$ facilitate the absorption and emission of a phonon, respectively. Momentum conservation ensures that $\mathbf{k}' = \mathbf{k} + \mathbf{q}$, which immediately allows us to drop the $\mathbf{k}'$ integration. The remaining steps in the derivation are identical to the ones performed in Eqs. (3.61) to (3.63), thereby requiring no further comments. Taking all this into consideration, the final expression for the long-range electron-phonon Hamiltonian reads:

$$\hat{H}^{\mathrm{LR}}_{\mathrm{ep}} = \sum_{mn}\sum_{\nu}\int_{\Omega_{\mathrm{BZ}}}\frac{\mathrm{d}^3k}{\Omega_{\mathrm{BZ}}}\int_{\Omega_{\mathrm{BZ}}}\frac{\mathrm{d}^3q}{\Omega_{\mathrm{BZ}}} g^{\mathrm{LR}}_{mn\mathbf{k},\nu\mathbf{q}}\hat{c}^\dagger_{m\mathbf{k}+\mathbf{q}}\hat{c}_{n\mathbf{k}}\left(\hat{b}_{\nu\mathbf{q}} + \hat{b}^\dagger_{\nu,-\mathbf{q}}\right), \tag{4.112}$$

$$g^{\mathrm{LR}}_{mn\mathbf{k},\nu\mathbf{q}} \equiv \mathrm{i}\frac{4\pi}{V_{\mathrm{pc}}}\sum_{\kappa}\sqrt{\frac{\hbar}{2m_\kappa\omega_{\nu\mathbf{q}}}}\sum_{\substack{\mathbf{G}\neq-\mathbf{q}\\ \mathbf{K}\equiv\mathbf{q}+\mathbf{G}}}^{\mathrm{pc}}\frac{\mathbf{K}^\top\mathbf{Z}^\star_\kappa\mathbf{e}_{\kappa,\nu\mathbf{q}}}{\mathbf{K}^\top\boldsymbol{\epsilon}^\infty\mathbf{K}}\langle\psi_{m\mathbf{k}+\mathbf{q}}|\mathrm{e}^{\mathrm{i}\mathbf{K}\cdot(\hat{\mathbf{r}}-\tau_\kappa)}|\psi_{n\mathbf{k}}\rangle\,, \tag{4.113}$$

where we identified the long-range electron-phonon matrix element, $g^{\mathrm{LR}}_{mn\mathbf{k},\nu\mathbf{q}}$, by comparing Eqs. (4.112) and (4.113) against the first-order electron-phonon coupling term in the full Hamiltonian, Eq. (4.12).

From the q/q^2 dependence in Eq. (4.113), we learn that $g^{\mathrm{LR}}_{mn\mathbf{k},\nu\mathbf{q}}$ diverges for LO phonon modes in the limit $\mathbf{q} \to \mathbf{0}$. This is qualitatively different from the long-range dynamical matrix, Eq. (3.63), where the $\mathbf{q} \to \mathbf{0}$ limit converges to a finite value, though in general dependent on the direction of $\mathbf{q}$. In both cases, however, the TO modes do not couple to the electric field since it is orthogonal to the phonon wave vector. The ASR discussed in Section 3.3 ensures that the matrix elements corresponding to acoustic modes go to zero as $\mathbf{q} \to \mathbf{0}$.

Eq. (4.113) is useful in the context of electron-phonon interpolation, where the long-range character of the interaction is difficult to recover. The idea is essentially the same as in Section 3.6 for the case of the dynamical matrix. Given a Fourier-like interpolation procedure for electron-phonon matrix elements, one would first remove the long-range part. This leaves only the short-range part which is amenable to Fourier interpolation. Afterwards, the long-range part is calculated at the interpolated value and added back. In Section 5.2.3, we present a concrete example of this procedure for the case of Wannier interpolation.

CHAPTER 5

Wannier Orbitals

In extended systems, the electronic orbitals are most naturally represented using Bloch functions as discussed in Section 2.2. As eigenstates of the electronic KS Hamiltonian, they inherently obey the translational symmetries of the crystal structure. However, sometimes it can be useful to switch from a fully delocalized representation to a localized one.

Wannier orbitals, introduced by Gregory Wannier in 1937 [38], have become a popular choice for localized basis functions. They have been used extensively in numerous areas. Example applications include the analysis of chemical bonding in solids [102–106], the electric polarization in terms of the Berry-phase [80, 107, 108] and the interpolation of the electronic band structure [109] and electron-phonon matrix elements [36, 37, 40, 42].

In this section, we give a brief introduction to Wannier orbitals. After a general definition in Section 5.1, we show how the electronic band structure and electron-phonon matrix elements can be interpolated using Wannier orbitals in Section 5.2. Finally, we cover the relevant methods of constructing Wannier orbitals in Section 5.3. An extensive review of Wannier orbitals and their applications is given in Ref. [39].

5.1 Definition

Various equally valid definitions of Wannier orbitals exist in the literature. For our purposes, we define Wannier orbitals to be consistent with the normalization convention found in Eq. (14) of Ref. [39]. A general Wannier orbital, $|\mathcal{W}_{al}\rangle$, which is characterized by its Wannier index, a, and a cell index, l, is then given by the linear transformation:

$$|\mathcal{W}_{al}\rangle \equiv \frac{1}{\sqrt{N_\mathrm{c}}} \sum_{n\mathbf{k}} \mathrm{e}^{-\mathrm{i}\mathbf{k}\cdot\mathbf{R}_l} |\psi_{n\mathbf{k}}\rangle U_{na,\mathbf{k}}. \tag{5.1}$$

Eq. (5.1) takes the form of a generalized Fourier transform of Bloch orbitals, $|\psi_{n\mathbf{k}}\rangle$, with the important addition of the Wannier transformation matrix, $U_{an,\mathbf{k}}$. The

Wannier index, a, is used to distinguish between different Wannier orbitals corresponding to a single unit cell of the crystal lattice whose origin is located at $\mathbf{R}_l$. In Eq. (5.1), we implicitly assume that the involved Bloch vectors, $\mathbf{k}$, form a regular grid of N_c points in the FBZ. The resulting Wannier orbitals then populate a periodic supercell comprised of N_c individual primitive cells.

If $U_{an,\mathbf{k}}$ is a unitary matrix of full rank, then it follows immediately that the resulting Wannier orbitals share the same Hilbert space as the original Bloch orbitals. In that case, Eq. (5.1) is fully invertible, allowing the reconstruction of the Bloch orbitals from a set of Wannier orbitals. After inversion, Eq. (5.1) therefore describes the inverse transformation:

$$|\psi_{n\mathbf{k}}\rangle = \frac{1}{\sqrt{N_\mathrm{c}}} \sum_{al} \mathrm{e}^{\mathrm{i}\mathbf{k}\cdot\mathbf{R}_l} |\mathcal{W}_{al}\rangle \, U^\dagger_{an,\mathbf{k}}. \tag{5.2}$$

Note, however, that the Wannier transformation matrix, $U_{an,\mathbf{k}}$, need not be square in general. In fact, it is often useful to generate a set of Wannier orbitals that only span a subspace of the Hilbert space spanned by the original Bloch orbitals. In that case, the Wannier transformation is not invertible as the Hilbert space becomes truncated in the process. Nevertheless, Eq. (5.2) might still be used to generate Bloch orbitals in the truncated Hilbert subspace.

Although naturally, Wannier orbitals are localized objects, in practice, they are often constructed in an environment that obeys periodic boundary conditions, such as in a Born-von-Karmann supercell [79]. In such an environment, there is always some ambiguity in the definition of the spatial center of the Wannier orbital due to the existence of periodic images [110].

Wannier orbitals possess various properties which are quite convenient for our purposes. For one, they form an orthonormal basis set,

$$\langle \mathcal{W}_{al} | \mathcal{W}_{bl'} \rangle = \delta_{ab}\delta_{ll'}, \tag{5.3}$$

given that the original Bloch orbitals are orthonormal as well and the Wannier transformation is unitary. However, the implications are quite important, as not only do Wannier orbitals produce zero overlap when their Wannier indices differ but also when they are located in different cells. This will allow us to construct localized objects, such as the electronic Hamiltonian, using the Wannier representation.

In addition to being orthonormal, Wannier orbitals are also invariant under translations with respect to primitive-lattice vectors. To see this, let us inspect the position-space wave function of a Wannier orbital located in unit cell l:

$$\mathcal{W}_{al}(\mathbf{r}) = \langle \hat{r} | \mathcal{W}_{al} \rangle = \frac{1}{\sqrt{N_\mathrm{c}}} \sum_{n\mathbf{k}} \mathrm{e}^{\mathrm{i}\mathbf{k}\cdot\mathbf{R}_l} \psi_{n\mathbf{k}}(\mathbf{r}) U_{na,\mathbf{k}}. \tag{5.4}$$

Next, we shift the origin by $\mathbf{R}_0 - \mathbf{R}_l$ to translate into unit-cell l and use the Bloch

theorem:

$$\begin{aligned}\mathcal{W}_{al}(\mathbf{r}+\mathbf{R}_0-\mathbf{R}_l) &= \frac{1}{\sqrt{N_c}}\sum_{n\mathbf{k}} e^{i\mathbf{k}\cdot\mathbf{R}_l}\underbrace{\psi_{n\mathbf{k}}(\mathbf{r}+\mathbf{R}_0-\mathbf{R}_l)}_{\psi_{n\mathbf{k}}(\mathbf{r})e^{i\mathbf{k}\cdot(\mathbf{R}_0-\mathbf{R}_l)}} U_{na,\mathbf{k}} \\ &= \frac{1}{\sqrt{N_c}}\sum_{n\mathbf{k}} e^{i\mathbf{k}\cdot\mathbf{R}_0}\psi_{n\mathbf{k}}(\mathbf{r})U_{na,\mathbf{k}} \\ &= \mathcal{W}_{a0}(\mathbf{r}). \end{aligned} \tag{5.5}$$

Evidently, the Wannier orbital in cell l is just a translational copy of the one in cell 0.

It has been shown that Wannier orbitals constructed from energetically isolated manifolds can be exponentially localized in real space [111, 112]. In this case, the overlap between two different Wannier orbitals decreases exponentially fast as the distance between them grows. Having an exponentially fast decay of the overlap is another important aspect of what makes Wannier orbitals attractive in interpolation schemes. Obviously, there is a potential concern to be raised in the case of metallic states, as there is no band gap and the aforementioned localization criterion can therefore never be fulfilled. It is still possible to arrive at a localized Wannier representation in that case, but there is no formal guarantee that the degree of localization can be as good as for insulators or semiconductors. This is an important aspect to consider even when dealing with gapped systems, as the energetically higher-lying states can pose the same problem for the construction of Wannier orbitals. A common way to resolve this issue is through a process known as disentanglement which is discussed in Section 5.3.3.

5.2 Wannier Interpolation

With their high degree of localizability, Wannier orbitals lend themselves perfectly to be used in interpolation schemes. The general idea behind Wannier interpolation is analogous to how Fourier interpolation works. Eqs. (5.1) and (5.2) allow us to transform between the delocalized Bloch representation and the localized Wannier representation. In Section 5.1, we have implicitly assumed that the k-vectors involved in the transformation are commensurate with the supercell that holds the Wannier orbitals, meaning that the transformation is perfectly invertible. If, however, the k-vectors used in Eq. (5.2) are not commensurate with the supercell, the resulting Bloch orbitals are interpolated. The quality of this interpolation depends on the properties of the Wannier orbitals, especially regarding the degree of their localization. This section closely follows Ref. [36] and presents Wannier interpolation schemes for the electronic band structure as well as for electron-phonon matrix elements.

5.2.1 Electronic Band Structure

The first instance where Wannier interpolation is useful is the interpolation of the electronic band structure. For illustration purposes, let us assume that we are interested in calculating the KS eigenvalue spectrum along a certain high-symmetry path in the FBZ. This is a very common scenario that can easily be tackled using traditional methods. However, we will quickly see how an interpolation-based approach can overcome certain limitations and offers more flexibility and computational performance.

In order to calculate the eigenvalue spectrum along a k-point path using DFT, one would usually employ a two-step approach. First, the ground-state charge density is determined using a self-consistent DFT calculation. In this step, the KS equations are solved on a k-point mesh that spans the FBZ and is dense enough to reach convergence with respect to the charge density. Second, the previously obtained charge density is kept constant and the KS equations are solved non-self-consistently for k-points on the path of interest. This procedure, which we refer to as the non self-consistent field (NSCF) scheme for band-structure calculations, is simple, robust and very accurate as the KS eigenvalues are obtained from diagonalizing the KS Hamiltonian.

A potential downside of the NSCF scheme is that its computational cost scales directly with the method used to determine the electronic eigenvalues. For example, this applies to more expensive exchange-correlation functionals, Hartree-Fock hybrid functionals [113] and the GW approximation [10–12]. An interpolation scheme based on Wannier orbitals avoids this issue. The only input required are the electronic orbitals on a sufficiently dense k-point grid or in a sufficiently large supercell.

As a starting point for explaining the Wannier interpolation scheme, we assume that the electronic eigenvalues, $\varepsilon_{n\mathbf{k}}$, and accompanying eigenstates, $|\psi_{n\mathbf{k}}\rangle$, have been obtained on a regular grid of N_c k-points throughout the FBZ. The eigenvalues are given as the expectation value of the electronic Hamiltonian in the Bloch basis:

$$\varepsilon_{n\mathbf{k}} = \langle \psi_{n\mathbf{k}} | \hat{H} | \psi_{n\mathbf{k}} \rangle \,. \tag{5.6}$$

We can now expand the Bloch orbitals in terms of localized Wannier orbitals using Eq. (5.1):

$$\varepsilon_{n\mathbf{k}} = \frac{1}{N_\mathrm{c}} \sum_{abll'} \mathrm{e}^{-\mathrm{i}\mathbf{k}\cdot(\mathbf{R}_l - \mathbf{R}_{l'})} U_{na,\mathbf{k}} H^{\mathcal{W}}_{al,bl'} U^{\dagger}_{bn,\mathbf{k}}, \tag{5.7}$$

where we have introduced the Hamiltonian matrix in the Wannier representation:

$$H^{\mathcal{W}}_{al,bl'} \equiv \langle \mathcal{W}_{al} | \hat{H} | \mathcal{W}_{bl'} \rangle \,. \tag{5.8}$$

These Wannier orbitals populate a supercell that contains exactly N_c primitive cells.

Eq. (5.7) can be simplified further by exploiting the translational symmetry of Wannier orbitals and the Hamiltonian operator:

$$\mathbf{R}_{l_2} - \mathbf{R}_{l_1} = \mathbf{R}_l - \mathbf{R}_0 \quad \Rightarrow \quad H^{\mathcal{W}}_{al_2,bl_1} = H^{\mathcal{W}}_{al,b0}. \tag{5.9}$$

For each summand in Eq. (5.7), we now intend to shift the involved Wannier orbitals such that the index l' references the same unit cell, $l' = 0$. Finally, we can express the electronic eigenvalues in terms of the Wannier-space Hamiltonian matrix as:

$$\varepsilon_{n\mathbf{k}} = \sum_{ab} U_{na,\mathbf{k}} \left[\sum_l H^{\mathcal{W}}_{al,b0} \mathrm{e}^{-\mathrm{i}\mathbf{k}\cdot(\mathbf{R}_l - \mathbf{R}_0)} \right] U^{\dagger}_{bn,\mathbf{k}}. \tag{5.10}$$

Eq. (5.10) is exact as long as the Bloch vector, $\mathbf{k}$, is commensurate with the supercell holding the Wannier orbitals. Otherwise, it provides an interpolation scheme for the electronic eigenvalues at arbitrary k-points. First, the Hamiltonian matrix is constructed in the basis of Wannier orbitals, for example, in a supercell calculation. Next, the quantity in brackets in Eq. (5.10), which describes a simple Fourier interpolation of a single strip of this matrix, is calculated. Finally, the matrices $U_{na,\mathbf{k}}$ and $U^{\dagger}_{bn,\mathbf{k}}$ can be identified as the left and right unitary diagonalizers of the interpolated Hamiltonian matrix. These matrices, together with the eigenvalues, are then obtained by means of a suitable matrix-diagonalization procedure.

This interpolation scheme relies on the assumption that the Hamiltonian matrix in the Wannier representation is a well localized object. More precisely, it must decay fast enough with respect to the real-space distance between the involved Wannier orbitals so that its entries can be neglected beyond a certain cutoff distance. This is analogous to the interpolation of the dynamical matrix in the case of phonons, as explained in Section 3.4. Since the electronic Hamiltonian is a semi-local operator, the quality of the band-structure interpolation depends primarily on the properties of the involved Wannier orbitals. Thus, it is important to optimize the Wannier orbitals with regard to localization.

5.2.2 Electron-phonon Matrix Elements

In Chapter 4, we introduced the electron-phonon matrix element, a pivotal quantity that underpins various kinds of electron-phonon calculations. Many of these calculations require numerous matrix elements to be evaluated throughout the FBZ. A common example are integrals such as in Eq. (4.15) that may require a considerable amount of q-points to be computed numerically. Unfortunately, the direct evaluation of electron-phonon matrix elements through the means of DFPT is computationally demanding. As a result, various interpolation schemes have been developed over the years in the field of electron-phonon physics to provide a tractable way of reaching the desired q-point densities [33, 34, 40, 41, 43, 114]. In this section, we present an interpolation technique for electron-phonon matrix elements that is based on the localized Wannier representation. It can be

considered a combination of the interpolation techniques presented in Section 3.4 and Section 5.2.1.

To begin with, the electron-phonon matrix element is expanded in terms of Wannier orbitals using Eq. (5.2) in complete analogy to Eq. (5.7):

$$\begin{aligned} g_{mn\mathbf{k},\nu\mathbf{q}} &= \langle \psi_{m\mathbf{k}+\mathbf{q}} | \partial_{\nu\mathbf{q}} \hat{H} | \psi_{n\mathbf{k}} \rangle \\ &= \frac{1}{N_\mathrm{c}} \sum_{abll'} \mathrm{e}^{-\mathrm{i}(\mathbf{k}+\mathbf{q})\cdot\mathbf{R}_l + \mathrm{i}\mathbf{k}\cdot\mathbf{R}_{l'}} U_{ma,\mathbf{k}+\mathbf{q}} \langle \mathcal{W}_{al} | \partial_{\nu\mathbf{q}} \hat{H} | \mathcal{W}_{bl'} \rangle U^\dagger_{bn,\mathbf{k}}. \end{aligned} \tag{5.11}$$

Next, we use the definition of the phonon-displacement operator, $\partial_{\nu\mathbf{q}}$, in Eq. (4.8), to rewrite the electron-phonon matrix element in terms of individual atomic displacements:

$$\begin{aligned} g_{mn\mathbf{k},\nu\mathbf{q}} = \frac{1}{N_\mathrm{c}} \sum_{abll'} \sum_{p\kappa\alpha} \sqrt{\frac{\hbar}{2m_\kappa \omega_{\nu\mathbf{q}}}} \mathrm{e}^{-\mathrm{i}(\mathbf{k}+\mathbf{q})\cdot\mathbf{R}_l + \mathrm{i}\mathbf{k}\cdot\mathbf{R}_{l'} + \mathrm{i}\mathbf{q}\cdot\mathbf{R}_p} \\ \times U_{ma,\mathbf{k}+\mathbf{q}} g^{\mathcal{W}}_{al,bl',p\kappa\alpha} U^\dagger_{bn,\mathbf{k}} e_{\kappa\alpha,\nu\mathbf{q}}, \end{aligned} \tag{5.12}$$

$$g^{\mathcal{W}}_{al,bl',p\kappa\alpha} \equiv \langle \mathcal{W}_{al} | \partial_{p\kappa\alpha} \hat{H} | \mathcal{W}_{bl'} \rangle . \tag{5.13}$$

The quantity $g^{\mathcal{W}}_{al,bl',p\kappa\alpha}$ is the electron-phonon matrix element in the Wannier representation. Notice how both the electronic and phononic part of the Wannier-space matrix element are localized in real space. To recapitulate, ν and $\mathbf{q}$ are the branch index and wave vector characterizing the involved phonon. $\omega_{\nu\mathbf{q}}$ and $e_{\kappa\alpha,\nu\mathbf{q}}$ are then phonon angular frequencies and eigenvectors, respectively, which can be obtained by diagonalizing the dynamical matrix as described in Section 3.1. The derivative $\partial_{p\kappa\alpha}$ denotes a displacement of atom κ with mass m_κ in cell p along a Cartesian direction labeled by α.

The Wannier-space electron-phonon matrix element, $g^{\mathcal{W}}_{al,bl',p\kappa\alpha}$, obeys similar translational symmetries as the Hamiltonian matrix in Eq. (5.9):

$$\left.\begin{aligned} \mathbf{R}_{l_1} - \mathbf{R}_p &= \mathbf{R}_l - \mathbf{R}_0 \\ \mathbf{R}_{l_2} - \mathbf{R}_p &= \mathbf{R}_{l'} - \mathbf{R}_0 \end{aligned}\right\} \quad \Rightarrow \quad g^{\mathcal{W}}_{al_1,bl_2,p\kappa\alpha} = g^{\mathcal{W}}_{al,bl',0\kappa\alpha}. \tag{5.14}$$

In other words, it is invariant under a simultaneous translation of both Wannier orbitals and the atomic perturbation by a primitive-lattice vector. This is a simple consequence of the discrete translational symmetries of the Wannier orbitals and the Hamiltonian with respect to the underlying Bravais lattice. Using Eq. (5.14), we aim to shift each matrix element appearing in Eq. (5.12) such that the atomic phonon perturbation is moved to unit cell $p = 0$. Since this process is slightly more involved, let us apply the modifications step by step on the relevant part of Eq. (5.12):

$$\sum_{l_1 l_2 p} \mathrm{e}^{-\mathrm{i}(\mathbf{k}+\mathbf{q})\cdot\mathbf{R}_{l_1} + \mathrm{i}\mathbf{k}\cdot\mathbf{R}_{l_2} + \mathrm{i}\mathbf{q}\cdot\mathbf{R}_p} g^{\mathcal{W}}_{al_1,bl_2,p\kappa\alpha}. \tag{5.15}$$

The cell labels for the Wannier orbitals have been renamed to match the conditions present in Eq. (5.14). Let us now add and subtract the term $i\mathbf{k}\cdot\mathbf{R}_p$ to and from the exponent in Eq. (5.15) and rearrange the terms:

$$\sum_{l_1 l_2 p} e^{-i(\mathbf{k}+\mathbf{q})\cdot(\mathbf{R}_{l_1}-\mathbf{R}_p)} e^{i\mathbf{k}\cdot(\mathbf{R}_{l_2}-\mathbf{R}_p)} g^{\mathcal{W}}_{al_1,bl_2,p\kappa\alpha}. \tag{5.16}$$

At this point, we can shift the matrix element according to Eq. (5.14) and redefine the summation indices:

$$\sum_{ll' p} e^{-i(\mathbf{k}+\mathbf{q})\cdot(\mathbf{R}_l-\mathbf{R}_0)} e^{i\mathbf{k}\cdot(\mathbf{R}_{l'}-\mathbf{R}_0)} g^{\mathcal{W}}_{al,bl',0\kappa\alpha}. \tag{5.17}$$

Finally, we assume that the number of cells involved in the sum over p is the same as in the sum over l and l', namely N_c. With this, the electron-phonon matrix element reads:

$$\begin{aligned} g_{mn\mathbf{k},\nu\mathbf{q}} = \sum_{abll'} \sum_{\kappa\alpha} \sqrt{\frac{\hbar}{2m_\kappa \omega_{\nu\mathbf{q}}}} e^{-i(\mathbf{k}+\mathbf{q})\cdot(\mathbf{R}_l-\mathbf{R}_0)} e^{i\mathbf{k}\cdot(\mathbf{R}_{l'}-\mathbf{R}_0)} \\ \times U_{ma,\mathbf{k}+\mathbf{q}} g^{\mathcal{W}}_{al,bl',0\kappa\alpha} U^{\dagger}_{bn,\mathbf{k}} e_{\kappa\alpha,\nu\mathbf{q}}. \end{aligned} \tag{5.18}$$

Eq. (5.18) provides a recipe for interpolating $g_{mn\mathbf{k},\nu\mathbf{q}}$ to arbitrary k- and q-points given $g^{\mathcal{W}}_{al,bl',0\kappa\alpha}$. However, it is much more involved than the simple interpolation of the band structure presented in Section 5.2.1. For one, instead of a single sum over cells, Eq. (5.18) requires a double sum to be evaluated. In addition, it requires the knowledge of the phonon frequencies and eigenvectors at $\mathbf{q}$ and the Wannier transformation matrices at $\mathbf{k}$ and $\mathbf{k}+\mathbf{q}$. The former can be obtained by diagonalizing the dynamical matrix at $\mathbf{q}$, while the latter can be obtained by diagonalizing the interpolated Hamiltonian matrix, Eq. (5.10), once at $\mathbf{k}$ and once at $\mathbf{k}+\mathbf{q}$. It is important to note that, since no approximations have been made, Eq. (5.18) is exact if $\mathbf{k}$ and $\mathbf{q}$ are commensurate with the supercell holding the Wannier orbitals and the phonon perturbation.

5.2.3 Polar Materials

The interpolation procedure for the electron-phonon matrix element outlined in Section 5.2.2 is a valuable tool for efficiently calculating matrix elements on fine grids. Unfortunately, the electron-phonon matrix element diverges for LO phonons in the limit of small phonon wave vectors in polar materials due to long-range electrostatic interactions. A direct application of the interpolation scheme outlined in Section 5.2.2 is likely to cause termination wiggles, i.e., the Gibbs phenomenon [115]. It is therefore not expected to yield accurate results at small phonon wave vectors.

In Section 4.6, we have already presented a long-range model for the electron-dipole interaction. Based on this, an interpolation strategy similar to the one dis-

cussed in Section 3.6 can be implemented. In this section, we provide a formulation of the long-range electron-phonon matrix element in the Wannier representation. This is particularly useful if one already starts the calculation in the Wannier picture in a supercell, as is the case in the present work.

To begin with, let us expand the Bloch orbitals in Eq. (4.113) using Eq. (5.2):

$$\begin{aligned} g^{\mathcal{L}}_{mn,\nu}(\mathbf{k},\mathbf{q}) = & \\ & \mathrm{i}\frac{4\pi e^2}{N_\mathrm{c} V_\mathrm{uc}} \sum_\kappa \sqrt{\frac{\hbar}{2m_\kappa \omega_{\nu\mathbf{q}}}} \sum_{\mathbf{G}\neq -\mathbf{q}} \frac{(\mathbf{q}+\mathbf{G})\cdot \mathbf{Z}^\star_\kappa \cdot \mathbf{e}_{\kappa,\nu\mathbf{q}}}{(\mathbf{q}+\mathbf{G})\cdot \epsilon^\infty \cdot (\mathbf{q}+\mathbf{G})} \mathrm{e}^{-\mathrm{i}(\mathbf{q}+\mathbf{G})\cdot\tau_\kappa} \\ & \times \sum_{abll'} \mathrm{e}^{-\mathrm{i}(\mathbf{k}+\mathbf{q})\cdot(\mathbf{R}_l-\mathbf{R}_0)} U_{ma,\mathbf{k}+\mathbf{q}} g^{\mathcal{L}q}_{ab,ll'}(\mathbf{q}+\mathbf{G}) U^\dagger_{bn,\mathbf{k}} \mathrm{e}^{\mathrm{i}\mathbf{k}\cdot(\mathbf{R}'_l-\mathbf{R}_0)}, \end{aligned} \tag{5.19}$$

where we have defined the auxiliary quantity,

$$g^{\mathcal{L}q}_{ab,ll'}(\mathbf{q}) \equiv \langle \mathcal{W}_{al} | \mathrm{e}^{\mathrm{i}\mathbf{q}\cdot\hat{\mathbf{r}}} | \mathcal{W}_{bl'} \rangle , \tag{5.20}$$

as a q-dependent Wannier-space overlap matrix element. We now proceed to investigate the translational symmetry properties of $g^{\mathcal{L}q}_{ab,ll'}(\mathbf{q})$. Let us rewrite the abstract scalar product between Wannier orbitals in Eq. (5.20) as an integral in position space:

$$g^{\mathcal{L}q}_{ab,ll'}(\mathbf{q}+\mathbf{G}) = \int_{\mathbb{R}^3} \mathrm{d}^3 r\, \mathcal{W}^*_{al}(\mathbf{r}) \mathcal{W}_{bl'}(\mathbf{r}) \mathrm{e}^{\mathrm{i}(\mathbf{q}+\mathbf{G})\cdot\mathbf{r}}. \tag{5.21}$$

Exploiting the translational symmetries of the involved Wannier orbitals, it is possible to shift the auxiliary matrix element such that one of the two Wannier orbitals is now located in cell $l = 0$:

$$\mathbf{R}_{l''} - \mathbf{R}_0 = \mathbf{R}_l - \mathbf{R}_{l'} \quad \Rightarrow \quad \begin{cases} \mathcal{W}^*_{al}(\mathbf{r}) = \mathcal{W}^*_{al''}(\mathbf{r} - \mathbf{R}_{l'} + \mathbf{R}_0) \\ \mathcal{W}_{bl'}(\mathbf{r}) = \mathcal{W}_{b0}(\mathbf{r} - \mathbf{R}_{l'} + \mathbf{R}_0) \end{cases}, \tag{5.22}$$

where the cell index l'' is chosen such that it fulfills this condition. Shifting the integration variable accordingly, Eq. (5.21) can be expressed as:

$$\begin{aligned} g^{\mathcal{L}q}_{ab,ll'}(\mathbf{q}+\mathbf{G}) &= \int_{\mathbb{R}^3} \mathrm{d}^3 r\, \mathcal{W}^*_{al''}(\mathbf{r} - \mathbf{R}_{l'} + \mathbf{R}_0) \mathcal{W}_{b0}(\mathbf{r} - \mathbf{R}_{l'} + \mathbf{R}_0) \mathrm{e}^{\mathrm{i}(\mathbf{q}+\mathbf{G})\cdot\mathbf{r}} \\ &= \int_{\mathbb{R}^3} \mathrm{d}^3 r\, \mathcal{W}^*_{al''}(\mathbf{r}) \mathcal{W}_{b0}(\mathbf{r}) \mathrm{e}^{\mathrm{i}(\mathbf{q}+\mathbf{G})\cdot(\mathbf{r}+\mathbf{R}_{l'}-\mathbf{R}_0)} \\ &= \langle \mathcal{W}_{al''} | \mathrm{e}^{\mathrm{i}(\mathbf{q}+\mathbf{G})\cdot\hat{\mathbf{r}}} | \mathcal{W}_{b0} \rangle \, \mathrm{e}^{\mathrm{i}(\mathbf{q}+\mathbf{G})\cdot(\mathbf{R}_{l'}-\mathbf{R}_0)} \\ &= g^{\mathcal{L}q}_{ab,l''0}(\mathbf{q}+\mathbf{G}) \mathrm{e}^{\mathrm{i}\mathbf{q}\cdot(\mathbf{R}_{l'}-\mathbf{R}_0)}, \end{aligned} \tag{5.23}$$

where the ket state is now restricted to one unit cell.

We can now substitute Eq. (5.23) back into Eq. (5.19) and perform the summation over l'. However, since this gives a relatively lengthy expression, we first

focus solely on the exponential factors that depend on l and l' and show that the summation indeed simplifies the result:

$$\begin{aligned}&\sum_{ll'} g^{\mathcal{L}q}_{ab,ll'}(\mathbf{q}+\mathbf{G})\mathrm{e}^{-\mathrm{i}(\mathbf{k}+\mathbf{q})\cdot(\mathbf{R}_l-\mathbf{R}_0)}\mathrm{e}^{\mathrm{i}\mathbf{k}\cdot(\mathbf{R}_{l'}-\mathbf{R}_0)}\\ &= N_\mathrm{c}\sum_{l''} g^{\mathcal{L}q}_{ab,l''0}(\mathbf{q}+\mathbf{G})\mathrm{e}^{-\mathrm{i}(\mathbf{k}+\mathbf{q})\cdot(\mathbf{R}_{l''}-\mathbf{R}_0)}.\end{aligned} \tag{5.24}$$

At this point, the only cell index that appears in the previous expression is l'', which obeys the translation condition specified in Eq. (5.22) and can be renamed to l. The final result is inferred from Eqs. (5.19), (5.23) and (5.24):

$$\begin{aligned}&g^{\mathcal{L}}_{mn,\nu}(\mathbf{k},\mathbf{q}) = \\ &\quad \mathrm{i}\frac{4\pi e^2}{V_\mathrm{uc}}\sum_\kappa \sqrt{\frac{\hbar}{2m_\kappa\omega_{\nu\mathbf{q}}}}\sum_{\mathbf{G}\neq-\mathbf{q}}\frac{(\mathbf{q}+\mathbf{G})\cdot\mathbf{Z}^\star_\kappa\cdot\mathbf{e}_{\kappa,\nu\mathbf{q}}}{(\mathbf{q}+\mathbf{G})\cdot\boldsymbol{\epsilon}^\infty\cdot(\mathbf{q}+\mathbf{G})}\mathrm{e}^{-\mathrm{i}(\mathbf{q}+\mathbf{G})\cdot\boldsymbol{\tau}_\kappa}\\ &\qquad\qquad \times\sum_{abl}\mathrm{e}^{-\mathrm{i}(\mathbf{k}+\mathbf{q})\cdot(\mathbf{R}_l-\mathbf{R}_0)}U_{ma,\mathbf{k}+\mathbf{q}}g^{\mathcal{L}q}_{ab,l0}(\mathbf{q}+\mathbf{G})U^\dagger_{bn,\mathbf{k}}.\end{aligned} \tag{5.25}$$

Evidently, Eq. (5.25) requires only a single summation over all cells. This way, only a thin slice of the entire Wannier-space matrix needs to be evaluated, analogous to the interpolation of the electronic Hamiltonian, Eq. (5.10).

The long-range matrix element, $g^{\mathcal{L}}_{mn,\nu}(\mathbf{k},\mathbf{q})$, is a quantity that lives in the Bloch picture. It depends on the Bloch vector, $\mathbf{k}$, and on the phonon wave vector, $\mathbf{q}$. The corresponding Wannier-space representation of this matrix element should have no such dependence. Unfortunately, the auxiliary matrix element $g^{\mathcal{L}q}_{ab,l0}(\mathbf{q})$ appearing in Eq. (5.25) does not qualify as it contains a phase factor that depends directly on $\mathbf{q}$. Therefore, it is now time to find a complete Wannier representation of the long-range matrix element that satisfies this criterion. To this end, we seek to transform the long-range matrix elements, $g^{\mathcal{L}}_{mn,\nu}(\mathbf{k},\mathbf{q})$, at all $\mathbf{k}$ and $\mathbf{q}$ vectors that are commensurate with the supercell into a pure Wannier-space matrix element, $g^{\mathcal{L}\mathcal{W}}_{ab,l0,\kappa\alpha}$. This allows us to find $g^{\mathcal{L}\mathcal{W}}_{ab,l0,\kappa\alpha}$ in terms of $g^{\mathcal{L}q}_{ab,l0}(\mathbf{G})$, where $\mathbf{G}$ are reciprocal lattice vectors. The criterion of commensurability ensures that the resulting Wannier-space matrix elements are computable, as there is a one-to-one mapping between the unit cell and the supercell under these conditions.

We begin by manipulating Eq. (5.25), with the goal of transforming both sides of the equation such that the right-hand side ends up in a pure Wannier representation. First, we multiply with the adjoint unitary Wannier rotation matrices

to remove them from the right-hand side:

$$\sum_{mn} U^{\dagger}_{am,\mathbf{k}+\mathbf{q}} g^{\mathcal{L}}_{mn,\nu}(\mathbf{k},\mathbf{q}) U_{nb,\mathbf{k}} = \mathrm{i}\frac{4\pi e^2}{V_{\mathrm{uc}}} \sum_{\kappa} \sqrt{\frac{\hbar}{2m_\kappa \omega_{\nu\mathbf{q}}}} \sum_{\mathbf{G}\neq-\mathbf{q}} \frac{(\mathbf{q}+\mathbf{G})\cdot\mathbf{Z}^{\star}_{\kappa}\cdot\mathbf{e}_{\kappa,\nu\mathbf{q}}}{(\mathbf{q}+\mathbf{G})\cdot\boldsymbol{\epsilon}^{\infty}\cdot(\mathbf{q}+\mathbf{G})} \times \mathrm{e}^{-\mathrm{i}(\mathbf{q}+\mathbf{G})\cdot\tau_\kappa} \sum_{l} \mathrm{e}^{-\mathrm{i}(\mathbf{k}+\mathbf{q})\cdot(\mathbf{R}_l-\mathbf{R}_0)} g^{\mathcal{L}q}_{ab,l0}(\mathbf{q}+\mathbf{G}). \quad (5.26)$$

Next, we are free to multiply away the unitary matrix of phonon eigenvectors in a similar manner:

$$\sum_{\nu} \sqrt{\frac{2m_\kappa\omega_{\nu\mathbf{q}}}{\hbar}} e^{*}_{\kappa\alpha,\nu\mathbf{q}} \sum_{mn} U^{\dagger}_{am,\mathbf{k}+\mathbf{q}} g^{\mathcal{L}}_{mn,\nu}(\mathbf{k},\mathbf{q}) U_{nb,\mathbf{k}} = \mathrm{i}\frac{4\pi e^2}{V_{\mathrm{uc}}} \sum_{\mathbf{G}\neq-\mathbf{q}} \frac{\sum_\beta (q_\beta+G_\beta) Z^{\star}_{\kappa,\beta\alpha}}{(\mathbf{q}+\mathbf{G})\cdot\boldsymbol{\epsilon}^{\infty}\cdot(\mathbf{q}+\mathbf{G})} \times \mathrm{e}^{-\mathrm{i}(\mathbf{q}+\mathbf{G})\cdot\tau_\kappa} \sum_{l} \mathrm{e}^{-\mathrm{i}(\mathbf{k}+\mathbf{q})\cdot(\mathbf{R}_l-\mathbf{R}_0)} g^{\mathcal{L}q}_{ab,l0}(\mathbf{q}+\mathbf{G}). \quad (5.27)$$

Finally, we perform two inverse Fourier transforms from the set of commensurate $\mathbf{q}$ and $\mathbf{k}$ inside the FBZ, to the lattice vector $\mathbf{R}_l - \mathbf{R}_0$, i.e., the Fourier factor takes the form

$$\mathrm{e}^{\mathrm{i}(\mathbf{k}+\mathbf{q})\cdot(\mathbf{R}_l-\mathbf{R}_0)}. \quad (5.28)$$

On the right-hand side, this leads to an expression containing:

$$\sum_{\mathbf{k}\in\mathrm{sc}} \mathrm{e}^{\mathrm{i}(\mathbf{k}+\mathbf{q})\cdot(\mathbf{R}_l-\mathbf{R}_{l'})} = \delta_{ll'}, \quad (5.29)$$

where we denoted the condition of commensurability with the supercell as $\mathbf{k} \in \mathrm{sc}$. Ultimately, the discrete Fourier transform results in

$$\sum_{\mathbf{k},\mathbf{q}\in\mathrm{sc}} \mathrm{e}^{\mathrm{i}(\mathbf{k}+\mathbf{q})\cdot(\mathbf{R}_l-\mathbf{R}_0)} \sum_{\nu} \sqrt{\frac{2m_\kappa\omega_{\nu\mathbf{q}}}{\hbar}} e^{*}_{\kappa\alpha,\nu\mathbf{q}} \sum_{mn} U^{\dagger}_{am,\mathbf{k}+\mathbf{q}} g^{\mathcal{L}}_{mn,\nu}(\mathbf{k},\mathbf{q}) U_{nb,\mathbf{k}} = \mathrm{i}\frac{4\pi e^2}{V_{\mathrm{uc}}} \sum_{\mathbf{q}\in\mathrm{sc}} \sum_{\substack{\mathbf{G}\in\mathrm{uc}\\ \mathbf{G}\neq-\mathbf{q}}} \frac{\sum_\beta (q_\beta+G_\beta) Z^{\star}_{\kappa,\beta\alpha}}{(\mathbf{q}+\mathbf{G})\cdot\boldsymbol{\epsilon}^{\infty}\cdot(\mathbf{q}+\mathbf{G})} \mathrm{e}^{-\mathrm{i}(\mathbf{q}+\mathbf{G})\cdot\tau_\kappa} g^{\mathcal{L}q}_{ab,l0}(\mathbf{q}+\mathbf{G}). \quad (5.30)$$

The set of $\mathbf{q}$ vectors contains all reciprocal-lattice vectors commensurate with the *supercell* inside the FBZ, while $\mathbf{G}$ runs over all reciprocal-lattice vectors commensurate with the *primitive cell* (except for $\mathbf{G} = -\mathbf{q}$). Combining the two sums into one with the new variable running over *all* reciprocal-lattice vectors commensurate with the supercell, leads to the long-range electron-phonon matrix

element in the pure Wannier representation:

$$g^{\mathcal{LW}}_{ab,ll',\kappa\alpha} \equiv \mathrm{i}\frac{4\pi e^2}{V_{\mathrm{uc}}} \sum_{\substack{\mathbf{G}\in\mathrm{sc}\\ \mathbf{G}\neq\mathbf{0}}} \frac{\sum_\beta G_\beta Z^\star_{\kappa,\beta\alpha}}{\mathbf{G}\cdot\epsilon^\infty\cdot\mathbf{G}} \mathrm{e}^{-\mathrm{i}\mathbf{G}\cdot\tau_\kappa} g^{\mathcal{L}q}_{ab,l0}(\mathbf{G})\delta_{ll'}. \tag{5.31}$$

In practice, Eq. (5.31) is evaluated using a truncated Ewald sum [116]. Additionally, the following approximation is employed to enable the calculation of the auxiliary matrix elements, $g^{\mathcal{L}q}_{ab,ll'}(\mathbf{q})$:

$$g^{\mathcal{L}q}_{ab,ll'}(\mathbf{q}) = \langle \mathcal{W}_{al}|\mathrm{e}^{\mathrm{i}\mathbf{q}\cdot\hat{\mathbf{r}}}|\mathcal{W}_{bl'}\rangle \approx \langle \mathcal{W}_{al}|\mathcal{W}_{bl'}\rangle = \delta_{ab}\delta ll' \tag{5.32}$$

$$\Rightarrow \langle \Psi_{m\mathbf{k}+\mathbf{q}}|\mathrm{e}^{\mathrm{i}\mathbf{q}\cdot(\hat{\mathbf{r}}-\tau_\kappa)}|\Psi_{n\mathbf{k}}\rangle \approx \sum_a U_{ma,\mathbf{k}+\mathbf{q}} U^\dagger_{an,\mathbf{k}}. \tag{5.33}$$

This trick simplifies Eq. (5.31) even further as the matrix element becomes fully diagonal in both the Wannier-orbital index and the cell index. In addition, when employing the interpolation scheme at arbitrary $\mathbf{k}$ and $\mathbf{q}$ vectors, one can reuse the Wannier transformation matrices from the diagonalization of the Wannier-interpolated Hamiltonian, Eq. (5.10). The reason this approximation works well is related to the fact that we add and subtract the same kind of contribution for each data point. In a sense, it is not so important what the long-range contribution looks like exactly, as long as it reproduces the original data points, which is guaranteed by the commensurability condition.

At this point, we quickly outline the interpolation procedure for electron-phonon matrix elements including long-range electrostatic contributions. This is similar to the case of phonons in Section 3.6.

1. The Wannier-space electron-phonon matrix elements, $g^{\mathcal{W}}_{al,bl',p\kappa\alpha}$, are calculated in the supercell according to Eq. (5.13).
2. The long-range Wannier-space electron-phonon matrix elements, $g^{\mathcal{LW}}_{ab,ll',\kappa\alpha}$, are calculated in the supercell according to Eq. (5.31) and subtracted from the $g^{\mathcal{W}}_{al,bl',p\kappa\alpha}$.
3. The resulting short-range electron-phonon matrix elements are Wannier interpolated to the primitive cell using Eq. (5.18). This can in principle be done for arbitrary $\mathbf{k}$ and $\mathbf{q}$.
4. Finally, the long-range electron-phonon matrix elements are calculated at the relevant $\mathbf{k}$ and $\mathbf{q}$ vectors using Eq. (5.25) and added to the interpolated short-range matrix elements.

5.3 Wannierization

Probably the most critical aspect when it comes to Wannier orbitals is their construction from a given Bloch manifold, a process which we refer to as Wannierization. There are numerous ways to approach this task and each comes with

different advantages and disadvantages. In principle, the process of Wannierization is the process of determining a suitable Wannier transformation matrix, $U_{na,\mathbf{k}}$. In the context of this work, suitability implies that the Wannier orbitals are decently localized, have a well-defined center and span a Hilbert space that is sufficiently similar to one spanned by a certain subset of Bloch orbitals.

The determination of the Wannier transformation matrix is an exceedingly difficult task that often involves a lot of trial and error. In a time when automation and high-throughput computing is constantly gaining traction, having a procedure that relies heavily on human input is becoming progressively more controversial. Human time is arguably more important than machine time, so it is crucial to employ Wannierization methods that require as little human intervention as possible while still producing reliable results. This section discusses different Wannierization schemes and compares their computational characteristics against each other.

5.3.1 Wannier Orbitals Via Projections

Arguably the simplest way of constructing Wannier orbitals is by projecting the original Bloch orbitals, $|\psi_{n\mathbf{k}}\rangle$ onto a set of localized trial functions, $|\chi_a\rangle$. These can be hydrogen-like, atomic orbitals or constitute of the partial waves or projector functions of a PAW dataset. Whatever the case, the Wannierization procedure is always the same.

First, the overlap matrix between N_B Bloch and N_W trial orbitals is determined for each k-point:

$$A_{na,\mathbf{k}} \equiv \langle \psi_{n\mathbf{k}} | \chi_a \rangle \,. \tag{5.34}$$

Using this overlap matrix as a transformation, we arrive at a set of intermediate Wannier-like orbitals:

$$|\mathcal{W}^\mathrm{I}_{a,\mathbf{k}}\rangle = \sum_n |\psi_n\rangle A_{na,\mathbf{k}}. \tag{5.35}$$

However, in general, the states $|\mathcal{W}^\mathrm{I}_{a,\mathbf{k}}\rangle$ need not be orthonormal, as we have not imposed any orthogonality constraint on the trial functions. In fact, most convenient trial functions will likely not be orthogonal between different lattice sites. Trying to directly use $A_\mathbf{k}$ as a Wannier transformation matrix is therefore in general not possible. To remedy this issue, the intermediate states need to be orthonormalized. Formally, a possible Wannier transformation matrix that produces orthonormalized orbitals is given by:

$$U_{na,\mathbf{k}} = \sum_b A_{nb,\mathbf{k}} \left(S_\mathbf{k}^{-\frac{1}{2}} \right)_{ba}, \tag{5.36}$$

$$S_{ab,\mathbf{k}} = \left(A^\dagger_\mathbf{k} A_\mathbf{k} \right)_{ab}. \tag{5.37}$$

It can easily be shown that such an expression leads to orthonormal Wannier orbitals assuming that the Bloch orbitals are properly normalized. At this point,

the overlap matrix is decomposed using a singular-value decomposition (SVD):

$$A_{na,\mathbf{k}} = \sum_{mb} \bar{Z}_{nm,\mathbf{k}} \sigma_{b,\mathbf{k}} \delta_{mb} Z^{\dagger}_{ba,\mathbf{k}}, \tag{5.38}$$

where $Z_{\mathbf{k}}$ and $\bar{Z}_{\mathbf{k}}$ are unitary matrices of rank N_{W} and N_{B}, respectively. The scalars $\sigma_{a,\mathbf{k}}$ are the singular values of the matrix $A_{\mathbf{k}}$ and δ_{ij} is the Kronecker delta. Substituting Eq. (5.38) into Eq. (5.37) yields

$$S_{ab,\mathbf{k}} = \sum_{mncd} Z_{ac,\mathbf{k}} \sigma_{c,\mathbf{k}} \delta_{cm} \underbrace{\left(\bar{Z}^{\dagger} \bar{Z}\right)_{mn,\mathbf{k}}}_{\delta_{mn}} \sigma_{d,\mathbf{k}} \delta_{nd} Z^{\dagger}_{db,\mathbf{k}} = \sum_{c} Z_{ac,\mathbf{k}} \sigma^2_{c,\mathbf{k}} Z^{\dagger}_{cb,\mathbf{k}}, \tag{5.39}$$

which is readily inverted to obtain

$$\left(S_{\mathbf{k}}^{-\frac{1}{2}}\right)_{ab} = \sum_{c} Z_{ac,\mathbf{k}} \frac{1}{\sigma_{c,\mathbf{k}}} Z^{\dagger}_{cb,\mathbf{k}}, \tag{5.40}$$

where we used the fact that $Z_{\mathbf{k}}$ is unitary.

Finally, it is possible to write the Wannier transformation matrix for orthonormal Wannier orbitals using Eqs. (5.36), (5.38) and (5.40):

$$\begin{aligned} U_{na,\mathbf{k}} &= \sum_{b} A_{nb,\mathbf{k}} \left(S_{\mathbf{k}}^{-\frac{1}{2}}\right)_{ba} \\ &= \sum_{mbc} \bar{Z}_{nm,\mathbf{k}} \sigma_{b,\mathbf{k}} \delta_{mb} \underbrace{\left(Z^{\dagger}_{\mathbf{k}} Z_{\mathbf{k}}\right)_{bc}}_{\delta_{bc}} \frac{1}{\sigma_{c,\mathbf{k}}} Z^{\dagger}_{ca,\mathbf{k}} \\ &= \sum_{mb} \bar{Z}_{nm,\mathbf{k}} \delta_{mb} Z^{\dagger}_{ba,\mathbf{k}}. \end{aligned} \tag{5.41}$$

This result is quite simple and only requires a single SVD at each k-point. The main reason for using an SVD over an incremental procedure such as Gram-Schmidt orthonormalization is that the former preserves the symmetries of the original trial functions during the Wannierization process while the latter does not. To illustrate how a Gram-Schmidt procedure would break the symmetry, let us consider simple hydrogenic 1s orbitals situated on different atoms. When trying to model these using Wannier orbitals via the projection technique, it is possible to already provide hydrogenic orbitals as trial functions with the correct radial symmetries. At this point, the intermediate states, $|w^{\mathrm{I}}_{a,\mathbf{k}}\rangle$, would still exhibit the correct symmetries, but they would not be orthogonal. This fact should be intuitively clear since the hydrogen-1s wave function does not exhibit any nodes. A Gram-Schmidt procedure does not alter the orientation of the first state vector it considers but instead reorients the second state vector such that it is orthogonal to the first one. It then continues to reorient all other state vectors one at a time until all vectors are orthogonal to each other. In the case of the 1s orbitals, the first one would remain nodeless while the second one must logically acquire at least one

node in order to become orthogonal to the first one. Thus, the radial characters of the first and second Wannier orbitals are qualitatively different, having broken the original symmetries.

A major advantage of the projection scheme outlined in this section is the possibility to tune certain properties of Wannier orbitals by changing the initial trial functions. The latter can be placed at specific positions with specific orbital characters, for example as an sp-2 or sp-3 bonding orbital between two carbon atoms. Roughly speaking, the shape, location and orientation of the trial wave functions will mostly be preserved during the Wannierization process. However, some intuition might be required to set up the trial functions.

When generating Wannier orbitals in a supercell, the preservation of symmetry is of great importance to the interpolation procedures outlined in Section 5.2. Each cell must contain a perfect translational copy of the Wannier orbitals in any other cell, while preserving the ordering of the individual orbitals within each cell. The projection scheme offers a simple and robust way of achieving this goal directly in the supercell. If all trial functions obey the translational symmetry constraints, the Wannier orbitals obtained via the projection and SVD follow suit.

A major disadvantage of this method is the amount of knowledge and intuition required by the user in order to properly Wannierize a set of bands. If the character of a particular electronic band structure is not well understood, it becomes extremely difficult to properly Wannierize it using the projection technique, as it is unclear which trial functions should be selected. Furthermore, certain electronic bands might mix and hybridize profoundly as a function of the Bloch vector, making it even more difficult to distill their character. Additionally, the pool of available trial functions might not include the desired functions for a particular situation, which necessitates implementation efforts to include additional projection targets.

In practice, the sum of these disadvantages makes it exceedingly difficult to properly Wannierize electronically complex systems. The projection technique is therefore ill-suited for the purpose of Wannier interpolation whenever the available trial functions are insufficient to describe the relevant bands in the electronic band structure.

5.3.2 Automatic Wannier Orbitals Using the Density Matrix

A common criticism against most Wannierization approaches is that they require an inconveniently high level of human input. The projection scheme outlined in the previous section is a prime example of such a method whose Wannierization quality depends fully on external parameters, i.e. the choice of trial functions. In those situations where the electronic band structure is not well understood or where parameter optimization is cumbersome, an automatic Wannierization approach becomes appealing.

One such way of generating Wannier orbitals from only a minimal set of parameters is to use selected columns of the density matrix (SCDM) [117–119]. It

requires only a few parameters and relies heavily on information found within the electronic one-particle density matrix. In many aspects, the SCDM method can be regarded as a truly complementary approach to the projection-based approach shown in Section 5.3.1. This section quickly summarizes the core concepts behind the SCDM method.

First, let us define the one-particle density matrix, $\mathcal{P}_{\mathbf{k}}$, for a particular k-point, $\mathbf{k}$:

$$\mathcal{P}_{\mathbf{k}}(\mathbf{r_1}, \mathbf{r_2}) \equiv \sum_n \psi_{n\mathbf{k}}(\mathbf{r}_1)\psi^*_{n\mathbf{k}}(\mathbf{r}_2), \tag{5.42}$$

where $\mathbf{r}_1$ and $\mathbf{r}_2$ are positions in real space. In practice, the portion of real-space filling the unit cell would be discretized using a dense regular grid consisting of N_r grid points, $\mathbf{r}^\mathrm{r}_i$, that are distinguished by the index, i. The density matrix at a specific k-point can then be written using two such real-space indices, i and j:

$$\mathcal{P}_{\mathbf{k},ij} \equiv \mathcal{P}_{\mathbf{k}}\left(\mathbf{r}^\mathrm{r}_\mathbf{i}, \mathbf{r}^\mathrm{r}_\mathbf{j}\right). \tag{5.43}$$

It is well-know that for gapped systems the one-particle density matrix in an isolated manifold decays exponentially fast in its off-diagonal elements [120]. Incidentally, the density matrix also contains all the necessary information governing the quantum-mechanical ground state of the system. As such, there must exist columns in this matrix that describe exponentially localized functions and also correctly capture the electronic character of the underlying states. These columns can then act as convenient blueprints for the construction of localized basis functions used in the Wannierization process. The only remaining question is how to choose suitable columns.

The strategy employed by Damle, Lin and Ying involves a rank-revealing QR decomposition, i.e., a QR decomposition with column pivoting (QRCP) that reveals the numerical rank of the matrix [121–123] and is inspired by a matrix-compression technique known as interpolative decomposition [124]. The QRCP of a complex matrix A can be written as:

$$A\Pi = QR, \tag{5.44}$$

where Q is unitary and R is upper triangular. What sets a QRCP apart from a regular QR decomposition is the permutation matrix, Π, which selects columns from A during the decomposition process such that R is well-conditioned. Incidentally, the first few columns of $A\Pi$ are columns with large norms and minimal overlap amongst each other, which is perfect for our purposes. Therefore, one could perform a QRCP on the one-particle density matrix, $\mathcal{P}_{\mathbf{k}}$, and use the first N_W columns of the permuted matrix to construct Wannier orbitals. In practice, however, the size of the density matrix renders a QRCP operation prohibitively expensive.

Fortunately, instead of explicitly constructing the entire density matrix for each k-point, it is sufficient to only apply the QRCP to a matrix, $P^\dagger_{\mathbf{k}_0}$, which consists

of the real-space wave functions of the Bloch orbitals at a reference or anchor k-point, $\mathbf{k_0}$:

$$P_{\mathbf{k}} \equiv \begin{pmatrix} \psi_{1\mathbf{k}}(\mathbf{r}_1) & \psi_{2\mathbf{k}}(\mathbf{r}_1) & \cdots & \psi_{N_\mathrm{B}\mathbf{k}}(\mathbf{r}_1) \\ \psi_{1\mathbf{k}}(\mathbf{r}_2) & \psi_{2\mathbf{k}}(\mathbf{r}_2) & \cdots & \psi_{N_\mathrm{B}\mathbf{k}}(\mathbf{r}_2) \\ \vdots & \vdots & \ddots & \vdots \\ \psi_{1\mathbf{k}}(\mathbf{r}_{N_\mathrm{r}}) & \psi_{2\mathbf{k}}(\mathbf{r}_{N_\mathrm{r}}) & \cdots & \psi_{N_\mathrm{B}\mathbf{k}}(\mathbf{r}_{N_\mathrm{r}}) \end{pmatrix}, \tag{5.45}$$

and

$$\mathcal{P}_{\mathbf{k}} = P_{\mathbf{k}} P_{\mathbf{k}}^\dagger. \tag{5.46}$$

A short argument for why the decomposition of $P_{\mathbf{k}}^\dagger$ is sufficient can be based on the fact that the QR decomposition of a matrix is essentially unique. More precisely, if A is a matrix of full rank and the diagonal entries of R are required to be positive, then the decomposition $A = QR$ is unique. Therefore, since $P_{\mathbf{k}}^\dagger$ certainly has full rank, its QRCP is unique:

$$P_{\mathbf{k}}^\dagger \Pi_{\mathbf{k}} = Q_{\mathbf{k}} R_{\mathbf{k}}. \tag{5.47}$$

Multiplying Eq. (5.47) with $P_{\mathbf{k}}$ from the left yields:

$$\mathcal{P}_{\mathbf{k}} \Pi_{\mathbf{k}} = Q'_{\mathbf{k}} R_{\mathbf{k}}, \tag{5.48}$$

$$Q'_{\mathbf{k}} \equiv P_{\mathbf{k}} Q_{\mathbf{k}}. \tag{5.49}$$

The matrix $Q'_{\mathbf{k}}$ has orthonormal columns as long as the original Bloch orbitals are orthogonal and properly normalized in real space:

$$Q'^\dagger_{\mathbf{k}} Q'_{\mathbf{k}} = Q^\dagger_{\mathbf{k}} \underbrace{P^\dagger_{\mathbf{k}} P_{\mathbf{k}}}_{\mathbb{1}} Q_{\mathbf{k}} = \mathbb{1}. \tag{5.50}$$

Therefore, Eq. (5.48) takes the form of a valid QRCP of $\mathcal{P}_{\mathbf{k}}$. Since the density matrix is generally not of full rank, however, this decomposition is generally not unique. Fortunately, we are only interested in a subset of N_W linearly independent columns, with $N_\mathrm{W} \leq N_\mathrm{B}$, where N_B is the number of original Bloch orbitals, i.e., the rank of the density matrix. Under these circumstances, the relevant $N_\mathrm{B} \times N_\mathrm{B}$ block of the matrix $Q'_{\mathbf{k}}$ is unitary and the QRCP is unique. Therefore, one may perform a QRCP of the matrix $P_{\mathbf{k}}^\dagger$ in place of the computationally more involved QRCP of the matrix $\mathcal{P}_{\mathbf{k}}$ in order to determine the permutation matrix.

In principle, one could perform a QRCP of $P_{\mathbf{k}}^\dagger$ to determine the permutation matrix at each k-point. However, in doing so, the selected columns of the density matrix will in general differ between k-points. As the choice of column directly determines the spatial properties of the corresponding Wannier orbital, this could potentially affect the quality of the Wannierization. Therefore, Damle, Lin and Ying propose to only perform one QRCP at the Γ-point and reuse that permutation matrix at all remaining k-points. To the best of our knowledge, there is nothing inherently special about the Γ-point in this context, so other k-points could be equally chosen. This strategy of picking an *anchor* point is very simple and stable, in the sense that complications due to different column selections

are completely avoided. That being said, there is no guarantee that it will always work in practice.

The final step of the SCDM-based Wannierization procedure is the creation of orthonormalized Wannier orbitals from the selected columns of the matrices $P_{\mathbf{k}}^{\dagger}$. To this end, we can employ the SVD, the same way the Wannier orbitals created by the projection scheme in Section 5.3.1 are orthonormalized. In this context, the selected columns of $P_{\mathbf{k}}^{\dagger}$ act as the projection matrix, $A_{na,\mathbf{k}}$, even though the former is not obtained by means of projection.

5.3.3 Disentanglement

A fundamental issue with Wannierization schemes that is deeply connected to the very nature of Wannier orbitals is the disentanglement problem. The problem arises whenever one tries to Wannierize electronic bands that mix or hybridize with others. In such a case, we say that the bands are *entangled*, and now the challenge is to find a way to disentangle them such that the Wannierization process yields a good description of the relevant subset of bands.

So far, we have established that a set of Wannier orbitals can be obtained from a given Bloch manifold by means of a unitary transformation. We have also implicitly assumed that the Bloch orbitals spanning that manifold belong to an energetically isolated region, i.e., they are bounded by band gaps from below and above. The disentanglement problem does not appear in this case because the map between the Bloch and Wannier representations of that isolated part of the Hilbert space is bijective. A good example of such a case would be the Wannierization of the valence bands below the Fermi level in an insulator or semiconductor.

In the context of electron-phonon physics, one is often interested in processes that occur at or around the band gap. A classic example is the renormalization of the electronic band gap due to lattice vibrations, which involves electronic states below *and* above the band gap. While the valence states are guaranteed to be bounded from below, there is no guarantee for the existence of another band gap above the Fermi level. As such, the involved conduction-band states belong to a region in Hilbert space that is generally *not* energetically isolated. This is important when trying to construct Wannier orbitals for the purpose of electron-phonon interpolation as the band structure needs to be described very accurately.

A rather simple solution is to introduce a sharp energy cutoff, so that only states with a KS eigenvalue, $\varepsilon_{n\mathbf{k}}$, inside a certain energy window are considered for Wannierization. However, there are multiple issues with this selection criterion. First, as a global Fourier-like transformation, the Wannier interpolation of the band structure is very likely to exhibit spurious oscillations when sharp cutoffs are introduced. These termination wiggles are the well-known Gibbs phenomenon [115]. Second, a sharp cutoff can coincide with a region of degeneracy in the band structure, potentially breaking the symmetry with respect to unitary transformations in that subspace. This can once again result in termination wiggles or other undesirable artifacts.

A better strategy is to smoothen the cutoff such that it allows for the inclusion of higher-lying states. This can be achieved by assigning a weight, $f_{n\mathbf{k}}$, to each KS state when calculating the projection matrix or the SCDM:

$$A_{na,\mathbf{k}} \to A_{na,\mathbf{k}} f_{n\mathbf{k}}. \tag{5.51}$$

If one is interested in an energy window, $f_{n\mathbf{k}}$ can be modeled by a Gaussian or similarly localized function. Otherwise, if one wants to Wannierize the band structure up to a certain energy, the Fermi distribution function or complementary error function are good choices. In any case, by specifying a smooth cutoff criterion, the degeneracy problem is solved and termination wiggles are much less pronounced.

In this work, we make use of the complementary error function to describe the smooth cutoff. This way, the weights are defined as:

$$f_{n\mathbf{k}}(\mu, \sigma) \equiv \frac{1}{2} \operatorname{erfc}\Big(\frac{\varepsilon_{n\mathbf{k}} - \mu}{\sigma}\Big), \tag{5.52}$$

$$\operatorname{erfc}(x) \equiv \frac{2}{\pi} \int_x^\infty \mathrm{e}^{-t^2}\, \mathrm{d}t\,. \tag{5.53}$$

The parameters μ and σ determine the location and spread of the smooth cutoff edge, respectively, and must be chosen carefully by the user.

CHAPTER 6

Results

In the scope of this work, an extensive amount of effort has been dedicated to implementing the theoretical concepts outlined in Chapters 3 to 5 into the VASP code. In order to test the implementation and answer interesting questions regarding the PAW formulation of the electron-phonon problem, we have subsequently conducted calculations on semiconductors and insulators. Here, we report the results of these calculations.

First, in Section 6.1, we focus on the Wannier-interpolation approach and its applicability to ZPR calculation in the adiabatic AHC theory. Second, in Section 6.2, we present results obtained with an alternative electron-phonon implementation that has recently been implemented in VASP. In this case, we were able to find interesting aspects about the relationship between AE and PS approaches in the context of ZPR calculations. Finally, we show our most recent results showing the difference between the AE and PS formulation regarding the general electron self-energy.

6.1 Electron-Phonon Interactions using Wannier Orbitals

In this section, I present excerpts of Ref. [33], which reports and discusses the calculation of the adiabatic AHC ZPR using Wannier orbitals and the PAW method. In accordance with the rules imposed by the University of Vienna on cumulative dissertations, I provide here additional details regarding the publication.

The original work, titled "Electron-phonon interactions using the projector augmented-wave method and Wannier functions", was published in Physical Review B in May 2020. Copyright is held by the American Physical Society. With the help of my coauthors, Martijn Marsman, Cesare Franchini and Georg Kresse, I have contributed a majority of the work. In particular, I have produced all numerical results, conducted the analysis and have written most of the original manuscript. The underlying code was written in large part by me. My coauthors

contributed with constructive feedback, theoretical understanding and expertise. I have also relied on them for guidance on academic writing. Additionally, they provided corrections to the final draft of the manuscript.

The theory section of the publication is covered sufficiently in Chapters 3 to 5 and is not included here. Instead, we focus solely on the methodology used, the results and the conclusion. This part of the research work was financially supported by the Austrian Science Fund (FWF) No. I2460-N36.

6.1.1 Results and Discussion

Before the Wannier-interpolation scheme discussed in Section 5.2 can be used in practice, a few conditions must be met. In particular, the Wannier-space matrix elements involving the PAW Hamiltonian, its derivative and the derivative of the PAW overlap operator need to spatially decay sufficiently fast so that the sums in Eqs. (5.10) and (5.18) converge. Additionally, the set of Wannier functions used for interpolation must closely match the electronic character of the target range of bands included in the transformation. It is important to verify these criteria independently for each material. Otherwise, the quality of the interpolation might deteriorate.

In this section, attention is initially placed on diamond, owing mostly to its extensive coverage in literature. Afterwards, phonon-induced band-gap renormalizations are calculated for a set of semiconductors. We also take the opportunity to compare our results with the ones obtained by Karsai [58] using a stochastic one-shot method. The latter has recently also been implemented in VASP providing a solid ground for comparison.

6.1.1.1 Diamond

In diamond, the Wannier-projection process is straight forward. The four highest valence bands and the four lowest conduction bands can be spanned by one s-like and three p-like Wannier orbitals on each atom. With two atoms per primitive cell, the number of bands that can be spanned is eight. Four of which are in the valence band, while the other four are in the conduction band.

All calculations on diamond are performed using the PBE [64, 65] PAW potential with the default electronic cutoff of 400 eV. The lattice parameter is set to the experimental value of 3.567 Å [125].

Small sections of the Wannier-space matrices of the Hamiltonian, its derivative and the derivative of the PAW overlap are visualized in Fig. 6.1 (the unperturbed overlap matrix is the identity matrix). The matrix elements corresponding to the atom at which the perturbation occurs are located in the first four rows (or columns) starting from the top left corner of the shown section. One can clearly see that, after taking the derivative with respect to that atom, only matrix elements involving atoms around that perturbation have significant contributions.

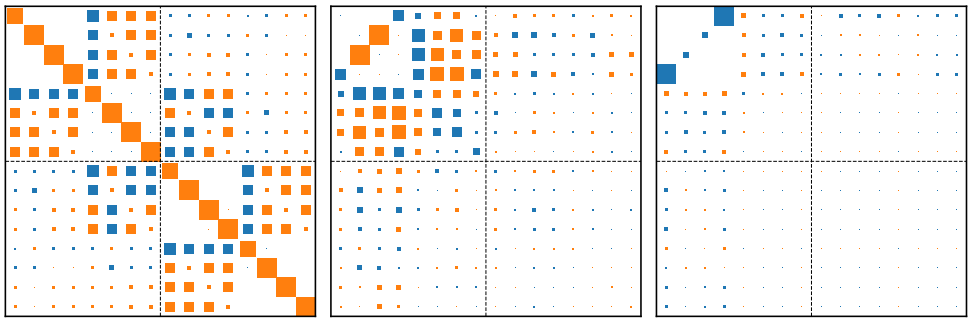

Figure 6.1: Numerical structure of various Wannier matrices for diamond. The three figures show parts of the real-valued matrices $\langle \widetilde{\mathcal{W}}_{al} | \widetilde{H} | \widetilde{\mathcal{W}}_{bl'} \rangle$ (left), $\langle \widetilde{\mathcal{W}}_{al} | \partial_{000} \widetilde{H} | \widetilde{\mathcal{W}}_{bl'} \rangle$ (middle) and $\langle \widetilde{\mathcal{W}}_{al} | \partial_{000} \widetilde{S} | \widetilde{\mathcal{W}}_{bl'} \rangle$ (right). The dashed lines separate regions corresponding to different unit cells (indices l and l'), while the rows and columns of colored squares correspond to the different Wannier orbitals (indices a and b; in this case, 1 s-like and 3 p-like orbitals per atom). The area of each square is proportional to the absolute value of the corresponding matrix element, while the color indicates positive (orange) and negative (blue) values.

This supports the claim that the real-space sums appearing in Eq. (5.18) can be truncated at a fairly small radius without jeopardizing their convergence.

A meaningful way of quantifying the spatial decay of these matrix elements is to study their absolute values as a function of distance between the associated Wannier centers in the periodic supercell. Fig. 6.2 shows this dependency on distance for the Hamiltonian, its derivative and the derivative of the PAW overlap operator. Clearly, the data decay roughly exponentially with the distance.

Finally, we would like to showcase the importance of the supercell size and the number of q-points in the convergence of an observable. The size of the supercell is relevant because the number of Wannier orbitals is directly tied to the number of atoms in our implementation. Therefore, the Wannier-space cutoff radius is implicitly given by the size of the supercell and is implemented using a minimum-image convention within the periodic supercell. In our studies, we use 4×4×4, 5×5×5 and 6×6×6 supercells comprised of primitive unit cells, each containing two atoms.

We calculate the ZPR of the direct band gap of diamond using Eqs. (4.36), (4.37) and (4.93). The FBZ integrals are approximated by sums over a dense q-point mesh. Here, we simply choose the mesh to contain the q-points commensurate with the supercell and subdivide it in all three reciprocal-lattice directions in order to increase the q-point density.

The ZPR of the direct gap as a function of the FBZ sampling density is shown in Fig. 6.3 for different supercell sizes. Based on these calculations, the most well-converged result for the ZPR of the direct gap of diamond is −427 meV for the 6×6×6 supercell.

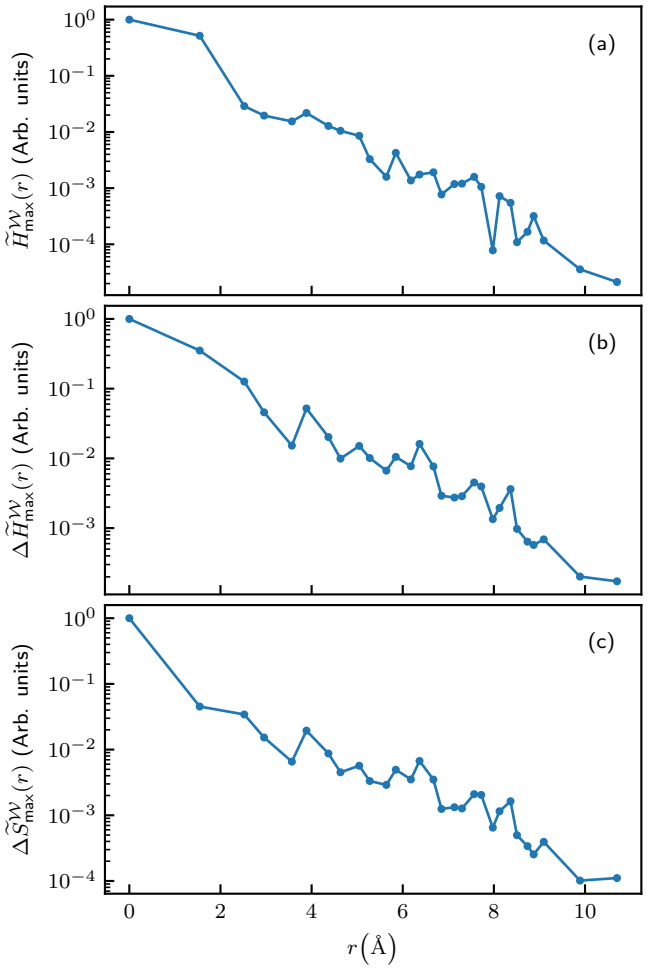

Figure 6.2: Various Wannier-space matrix elements for diamond plotted as functions of the distance between the corresponding Wannier centers. For each possible distance, only the largest absolute value is shown. A logarithmic scale is used to highlight the exponential spatial decay. Panel (a) shows the unperturbed PAW Hamiltonian matrix, $\widetilde{H}^{\mathcal{W}}_{\max}(r) \equiv \max_{\{al\}} \langle \widetilde{\mathcal{W}}_{al} | \widetilde{H} | \widetilde{\mathcal{W}}_{00} \rangle$, with $|\boldsymbol{\xi}_{la} - \boldsymbol{\xi}_{00}| = r$. Panel (b) shows the Hamiltonian matrix for a particular mono-atomic perturbation, $\Delta\widetilde{H}^{\mathcal{W}}_{\max}(r) \equiv \max_{\{al\}} \langle \widetilde{\mathcal{W}}_{al} | \partial_{000}\widetilde{H} | \widetilde{\mathcal{W}}_{00} \rangle$, with $|\boldsymbol{\xi}_{la} - \mathbf{R}_{00}| = r$. Finally, (c) is the same as (b) but showing the perturbed PAW overlap matrix.

Judging from the available data, we conclude that cell sizes beyond a 6×6×6 supercell would not significantly change the result for diamond. We also note that q-point convergence is reached independent of the original cell size at around 10^5 q-points inside the FBZ.

Finally, we also calculate the temperature-dependent direct and indirect band gap of diamond using a 5×5×5 supercell at fixed volume. The results are shown

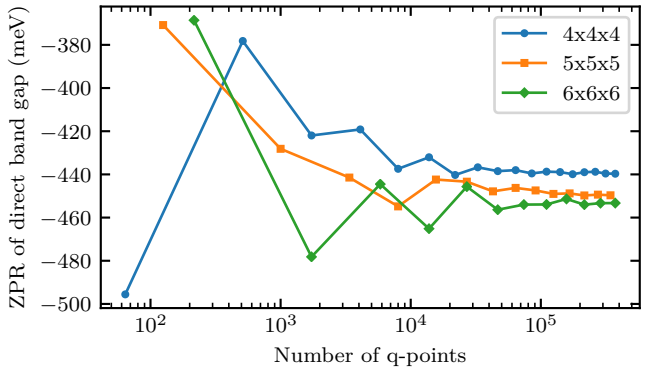

Figure 6.3: Convergence of the renormalization of the direct band gap of diamond as a function of cell size and q-point density. The number of q-points is determined as the number of q-points commensurate with the supercell times the number of subdivisions in one direction cubed.

in Fig. 6.4. For the sake of comparison, experimental as well as other ab-initio results are included. The experimental data sets are fitted with an analytical function advocated in [127], claimed to be superior to fits based on the Varshni equation [128]. The ab-initio data from Karsai correspond to one-shot calculations for a 5×5×5 supercell using DFT (extracted from the LDA and PBE data sets in Fig. 3 and 5 in [58], respectively). Lastly, the data set produced by Antonius *et al.* [17], using the same underlying methodology as presented here, is shown.

The results are satisfactory as there is good agreement with the other ab-initio data sets. In the case of the direct gap, our results tend to agree quite well with the results published by Antonius *et al.*. This is to be expected since the underlying computational methods are essentially the same. The deviation from the experimental data at high temperatures is a result of the neglect of the volume expansion as a function of the temperature (quasi-harmonic effects) as discussed in reference [58].

6.1.1.2 Band-gap Renormalization in other Materials

The present algorithm has also been employed to calculate the ZPR of band gaps for AlAs, AlP, AlSb, BN, C, GaN, GaP, Si and SiC. These materials share the same zincblende (or diamond) structure but with different lattice parameters. Appropriate Wannier orbitals can again be obtained by a projection on one s-like and three p-like orbitals. Again, PBE potentials and default electronic cutoff radii are used and ZPRs corresponding to degenerate bands are averaged. The computational parameters are summarized in Table 6.1. The lattice parameters are chosen in accordance with the ones in [58] in order to maximize the comparability of the data.

With the exception of GaN, all of these materials feature an indirect band

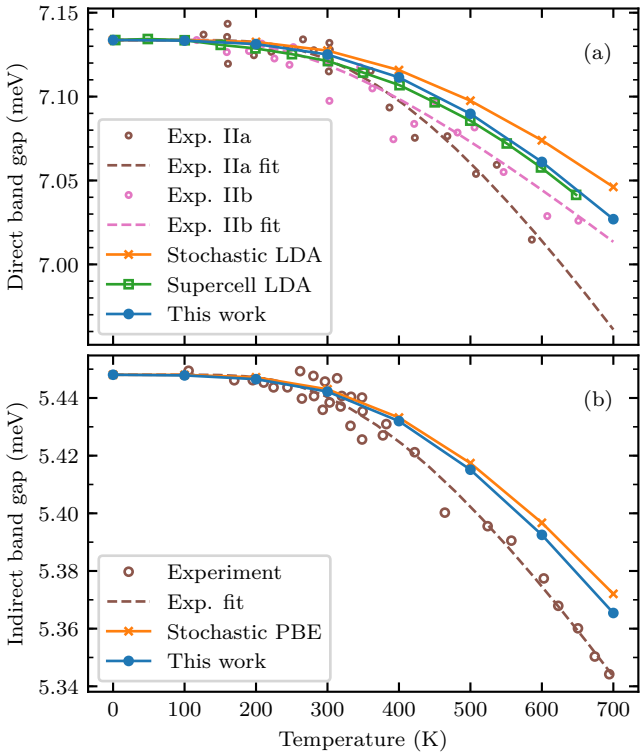

Figure 6.4: Temperature dependence of the direct and indirect band gap of diamond, with the present results obtained from a 5×5×5 supercell. The data corresponding to the stochastic one-shot method (orange crosses) were taken from [58], while the ones for a reference super-cell calculation (green squares) were extracted from [17]. The experimental data for the direct gap correspond to samples IIa and IIb in [126] and for the indirect gap, the data are taken from [127]. Experimental data sets are fitted with the analytic function proposed in [127]. All curves are shifted as to coincide with the fitted experimental data at zero temperature (in panel (a), with respect to data set IIa).

gap. In order to determine the precise location of the band transition inside the FBZ, Wannier-interpolation is used to calculate the electronic band structure along finely sampled high-symmetry lines. These data are then scanned for the conduction-band minimum and the valence-band maximum. The total ZPR is then the difference between the respective energy shifts.

Calculations are performed for 4×4×4 and 5×5×5 supercells. All results are converged with respect to the number of q-points. Table 6.2 shows the final results for the aforementioned materials.

A closer look at the data reveals that the ZPR increases with cell size, lowering the band gap, except for GaP where the ZPR stays the same. This is consistent with the convergence behavior shown in Fig. 6.3, indicating that the 4×4×4

Table 6.1: List of computational parameters for the simulated materials.

	Lattice parameter (Å)	Plane-wave cutoff (eV)	Reference
AlAs	5.661	240	[129]
AlP	5.463	255	[130]
AlSb	6.136	240	[131]
BN	3.616	400	[132]
C	3.567	400	[125]
GaN	4.535	400	[58]
GaP	5.451	255	[133]
Si	5.431	245	[134]
SiC	4.358	400	[135]

Table 6.2: Band-gap renormalization due to zero-point lattice vibrations for a selection of materials obtained via the presented algorithm. All results are converged with respect to the number of q-points. Supercell sizes are given in parentheses. Theoretical literature values are presented for BN [136], C [137, 138], GaN [139], Si [59, 138] and SiC [57]. In addition, experimental results are presented for AlSb [100], C [95, 140] and Si [95, 100]. Energies are in eV.

	ZPR (4×4×4)	ZPR (5×5×5)	Theory	Exp.
AlAs	-0.048	-0.056	–	–
AlP	-0.057	-0.065	–	–
AlSb	-0.032	-0.039	–	-0.039
BN	-0.294	-0.321	-0.262	–
			-0.331	–
C	-0.344	-0.368	-0.330	-0.340
			-0.343	-0.370
			-0.379	–
GaN	-0.090	-0.095	-0.127	–
GaP	-0.049	-0.049	–	–
Si	-0.044	-0.055	-0.058	-0.050
			-0.060	-0.064
			-0.064	–
SiC	-0.113	-0.120	-0.109	–

Table 6.3: Zero-point band-gap renormalizations calculated via the presented AHC algorithm compared to ones calculated with the one-shot method. Results for the one-shot method are taken from table 3 in [58], with the exception of SiC. Only q-points commensurate with the respective supercell are included to maximize the comparability of the two methods. The converged results from Table 6.2 are shown once more in the last column for the sake of comparison. Energies are in eV.

	4×4×4		5×5×5		5×5×5
	AHC	One shot	AHC	One shot	Converged
AlAs	-0.050	-0.051	-0.055	-0.063	-0.056
AlP	-0.060	-0.062	-0.067	-0.070	-0.065
AlSb	-0.041	-0.050	-0.039	-0.043	-0.039
BN	-0.257	-0.269	-0.290	-0.294	-0.321
C	-0.396	-0.363	-0.337	-0.320	-0.368
GaN	-0.086	-0.102	-0.095	-0.094	-0.095
GaP	-0.047	-0.072	-0.044	-0.057	-0.049
Si	-0.054	-0.064	-0.054	-0.065	-0.055
SiC	-0.104	-0.104	-0.130	-0.120	-0.120

supercell is insufficiently large to reach convergence. The mean absolute difference in the ZPRs between the 4×4×4 and 5×5×5 cell is about 11 meV, which also agrees favorably with the results obtained for the direct gap of diamond.

Finally, we compare our ZPR results with the ones from Ref. [58], which is summarized in Table 6.3. Since the data sets are generated by fundamentally different methods, it is desirable to tune the computational parameters in order to maximize comparability. The lattice parameters are already chosen to be identical and the PBE potential is used in both cases. In the one-shot method, only phonon modes at the Γ-point of the supercell are included in the calculation. This is equivalent to sampling only q-points in the primitive cell's FBZ that are commensurate with the supercell. Therefore, the integrals appearing in Eqs. (4.37) and (4.102) are restricted to sums over these commensurate q-points in the second and fourth column of Table 6.3. This restriction also applies to finding the location of the conduction-band minimum.

Even with these modifications, there are still fundamental differences in the methodology that cannot be easily accounted for. The one-shot method implicitly includes anharmonic contributions that are completely absent from second-order perturbation theory. Moreover, AHC theory relies on the rigid-ion approximation to evaluate the DW self-energy, which induces errors. Probably most problematic, however, is the issue of convergence with respect to the number of virtual orbitals that arises in methods based on Wannier interpolation. In principle, one needs to include all occupied and unoccupied orbitals in sums over states, such as the ones appearing in Eqs. (4.37) and (4.102). The set of Wannier functions only spans a

small subspace of the full Hilbert space. This has potential ramifications for the accuracy of the method. Unfortunately, it is very difficult to estimate bounds on the error induced by neglecting higher-lying states in the perturbational calculations. A numerical comparison with a different method integrated in the same software package is obviously valuable.

We need to report that the values for the ZPR of SiC as listed in reference [58] are erroneous, as subsequent calculations have shown. The values presented here have been recalculated using the one-shot method yielding −104 meV and −120 meV for 4×4×4 and 5×5×5 supercells, respectively.

The agreement between both data sets is remarkably good, especially in light of the aforementioned differences in methodology. The mean relative error between the data sets is about 11 % for the smaller cell while for the larger cell it is approximately 9 %.

Generally, the one-shot method yields systematically larger absolute band-gap renormalizations (with the exception of C and SiC). We relate this to the fact that the one-shot method implicitly accounts for excitations in all unoccupied states, whereas in the present perturbational calculations, we limit the calculations to 8 bands per unit cell.

We relate this to the fact that the one shot-method does not require a summation over states, and in the present perturbational calculations, we truncate the calculation to 8 bands per unit cell. We note that perturbation theory is not variational, implying that the inclusion of more bands does not necessarily increase the ZPR, although usually this is the case.

6.1.2 Conclusion

In this paper, the zero-point and finite-temperature renormalizations of the electronic bands due to electron-phonon interactions are derived and determined in the PAW framework. As usual in the AHC method, we define the electron-phonon matrix element as the second derivative of the one-electron energies in the adiabatic (Born–Oppenheimer) approximation, *i.e.*, neglecting explicit frequency dependencies of the external perturbation. Since the PAW method yields a generalized eigenvalue problem, the second derivatives of the eigenvalues also involve an eigenvalue-dependent "non-Hermitian" matrix element. This matrix element lacks some symmetries that are usually present in all-electron formulations, and we have discussed this issue at some length.

An important characteristic of the present method is that the actual implementation does not rely on linear-response theory. Instead, the first-order change of the Hamiltonian is determined by small finite displacements. This makes the method broadly applicable to any functional, including hybrid functionals as well as more complicated exchange-correlation functionals, where higher-order derivatives of the functionals are not readily computable. Finite differences, however, also imply the use of supercells. To mitigate this problem, the orbitals are transformed to a Wannier representation using a projection scheme. This has the

added advantage that a Wannier interpolation of the electron-phonon matrix elements is readily possible. This interpolation is, as a matter of fact, again adapted to the PAW method.

Using the developed method, numerical calculations are performed on diamond and a selection of binary compounds. To begin with, convergence tests are performed on diamond showing that a 5×5×5 supercell and the Γ-point suffice to determine reliable electron-phonon matrix elements. These can then be interpolated to much larger supercells and thus much denser wave-vector grids. We find that interpolation to about a million q-points suffices for results converged to few meV for the ZPR. The temperature-dependence of the direct and indirect band gaps of diamond are then studied. Our findings follow the same trends as other computational studies, underestimating the temperature dependence of the band-gap renormalization (this has previously been related to the neglect of the thermal expansion [58] and this previous assessment remains unchallenged). In addition, band-gap renormalizations have been calculated for a set of binary compounds. The results obtained by Wannier interpolation to many q-points compare very well with the available computational and experimental results found in the literature. A comparison of the one-shot method with the values obtained without interpolation to a finer q-point grid shows excellent agreement for the band-gap renormalization at wave vectors commensurate with the supercell. Not only does the excellent numerical agreement between the different methods serve as a proof-of-concept for the two implementations, it also shows that, within the set of tested materials, the employed approximations of all methods seem to be well justified. Typically, errors introduced by using a finite supercell, by neglecting interpolation to a fine wave-vector grid, or by the rigid-ion approximation all amount to about 10 % in total. Hence, if absolute accuracy is not an issue, most methods will yield reasonably reliable results. Specifically, our present implementation of the Wannier-interpolation method gives good estimates of the band-structure renormalization at zero and finite temperature compared to other codes, while taking full advantage of the numerical convenience of the PAW method.

As an outlook, it is important to remember that one of the strengths of the Wannier-interpolation method lies in the efficient calculation of the imaginary part of the electron self-energy. Future endeavors will focus on a PAW formulation of the fully frequency-dependent self-energy in second quantization. In addition, the inclusion of phonon-induced long-range dielectric effects (Fröhlich-like terms) that prominently occur in polar materials will be necessary [46, 47] in order to obtain accurate results for polar materials.

6.2 Zero-Point Renormalization in Semiconductors and Insulators

In this section, we present excerpts of Ref. [35]. It pertains to the band-gap ZPR of various semiconductors and insulators using the PAW method. Again, in ac-

cordance with the rules imposed by the University of Vienna on cumulative dissertations, I provide here additional details regarding the publication.

The original work, published in Physical Review B in September 2022, is titled "Zero-point renormalization of the band gap of semiconductors and insulators using the projector augmented wave method". Copyright is held by the American Physical Society. I have contributed the majority of the work and composed the majority of the text comprising the final manuscript. The numerical calculations were also performed by me, and I am in large part responsible for the analysis. My coauthors, Henrique Miranda, Laurent Chaput, Atsushi Togo, Carla Verdi, Martijn Marsman, and Georg Kresse, have helped finalize the research paper. Notably, the underlying code was developed mainly by Henrique Miranda, Laurent Chaput and Atsushi Togo. Major contributions to the appendix regarding this implementation were provided by Henrique Miranda and Laurent Chaput. All coauthors provided guidance, theoretical understanding and expertise.

As with the publication presented in Section 6.1, the theory is covered in Chapters 3 to 5. Here, we focus solely on the methodology used, the results and the conclusion. The computational approach used in this publication is different from the Wannier-based approach presented so far. In fact, an alternative electron-phonon implementation is used to calculate the band-gap ZPR. A rough outline of this new code is given in Section 6.2.1. For details, we refer to Ref. [34] and Ref. [35].

6.2.1 Computational approach

The implementation used to calculate the ZPR is based on the non-adiabatic AHC formulas in Eqs. (4.20) and (4.93) and utilizes finite atomic displacements in large supercells to evaluate the involved derivatives, $\partial_{l\kappa\alpha}$, numerically. Most of the code is implemented directly in VASP, but the derivatives are computed using a complementary python program. The ZPR can both be evaluated using the PS and the AE electron-phonon matrix elements defined in Sections 4.4.1 and 4.4.2. In either case, a series of perturbations consisting of single atomic displacements, $\partial_{l\kappa\alpha}$, are performed in large supercells. From these calculations, both the interatomic force constants and the changes of the self-consistent KS potential are computed in the supercell and written to disk. In VASP, the supercell potentials and force constants are read from disk, mapped to the primitive cell and evaluated between Bloch states corresponding to $\mathbf{k}$ and $\mathbf{k}+\mathbf{q}$ according to Eq. (4.10). Note that VASP recalculates on-the-fly the Bloch orbitals on the required dense k-point grid. In order to reconstruct the operator $\partial_{\nu\mathbf{q}}$, linear combinations involving the phonon eigenvectors, Eq. (4.8), are built. This allows to compute $\partial_{\nu\mathbf{q}}\widetilde{H}$, the derivative of the pseudopotential, $\partial_{\nu\mathbf{q}}\widetilde{V}$, and other related quantities. Details are given in Appendix C and in Ref. [34]. The computation of the electron-phonon matrix elements using the derivative of the potential known in a supercell requires an interpolation procedure, which is detailed in Appendix C.1. There, it is also shown that the procedure becomes exact when $\mathbf{k}$ and $\mathbf{q}$ are commensu-

rate with the supercell used in the calculation. For the related case of phonons, a derivation is also given in Ref. [141].

For ionic compounds, the long-range part of the potential derivatives contained in the electron-phonon matrix element must be treated explicitly. To this end, a strategy similar to the one presented in Ref. [46] is employed. Details are given in Section 4.6 and Appendix C.2.

Ultimately, the procedure outlined above allows to obtain both matrix elements, $g_{mn\mathbf{k},\nu\mathbf{q}}$ and $\tilde{g}_{mn\mathbf{k},\nu\mathbf{q}}$, at arbitrary $\mathbf{k}$ and $\mathbf{q}$ vectors. In order to estimate the integral over the FBZ in Eqs. (4.20) and (4.93), an extrapolation towards an infinitely dense q-point grid is necessary. It is assumed that at sufficiently dense q-point sampling densities, n_q, the ZPR depends linearly on $n_\mathrm{q}^{-1/3}$, so that the final ZPR can be extrapolated from this linear regime [138].

6.2.2 Results

6.2.2.1 AE versus PS formulation

First, we present a comparison between the AE and PS approaches discussed in Section 4.4. To this end, we calculate the non-adiabatic band-gap ZPR for a few materials, namely MgO-rs, AlAs-zb, ZnS-zb and C-cd. Here and in the following, the suffixes -rs, -zb, -cd and -w are used to denote the rock salt, zincblende, cubic diamond and wurtzite crystal structures, respectively. For each of the four materials, two electron-phonon calculations are performed, one using the AE matrix elements and one using the PS matrix elements. Both commence from the same 4×4×4 supercell calculation to determine the force-constants and the change of the self-consistent KS potential. In our experience, the convergence of the ZPR with respect to the number of bands is largely independent of the convergence with respect to the number of q-points used to sample the phononic states. Since we aim to highlight the difference between the AE and PS approach, we only use a relatively coarse 8×8×8 q-point mesh to sample the phononic states in each electron-phonon calculation. This is identical to the 8×8×8 k-point mesh used to diagonalize the electronic KS Hamiltonian in the primitive cell. The smearing parameter, δ, appearing in the denominator of Eq. (4.20) is set to 10 meV. The converged results for the non-adiabatic band-gap ZPR are listed in Table 6.4 together with the PAW potentials used and the electronic cut-off energies. We opt to use the labels of the POTCAR files distributed with VASP to distinguish between different PAW potentials. Additional information that characterizes these PAW potentials is provided in Table 6.9. The convergence behavior with respect to the number of bands is shown in Figs. 6.5 and 6.6. Each panel shows the non-adiabatic band-gap ZPR as a function of the maximum number of included intermediate states. The secondary x-axis atop each panel displays the average KS energy associated with each intermediate state relative to the Fermi level. Panels (a), (b) and (c) of Fig. 6.5 show the ZPR of MgO, AlAs and ZnS, respectively, while Fig. 6.6 is dedicated to diamond.

Table 6.4: Comparison of the non-adiabatic band-gap ZPR converged with respect to the number of bands between AE and PS methods. In addition, the used PAW potentials (POTCAR) and plane-wave cutoffs (E_{cut}) are listed.

material	POTCAR	E_{cut} (eV)	ZPR AE	ZPR PS
AlAs-zb	Al As	600	-64	-64
C-cd	C	1500	-334	-338
C-cd	C_GW_new	2400	-331	-338
C-cd	C_h_GW	3000	-337	-337
MgO-rs	Mg O_s	600	-272	-273
ZnS-zb	Zn S	800	-46	-46

It is known that the convergence of the ZPR with respect to the number of bands is slow and non-monotonic [18], requiring many conduction-band states to reach convergence. However, in Figs. 6.5 and 6.6, we observe that the PS method converges appreciably faster than the AE method. In order to understand why the ZPR converges slowly in the first place, let us consider the FM contribution in the adiabatic approximation. The relevant quantity is the integrand $\gamma^{\text{FM}}_{n\mathbf{k},\nu\mathbf{q}}$ in Eqs. (4.57) and (4.58). When written using the one-particle Green's function, $\left(\varepsilon_{n\mathbf{k}} - \hat{H}\right)^{-1}$, the integrand becomes:

$$\gamma^{\text{FM}}_{n\mathbf{k},\nu\mathbf{q}} = \sum_{m}{}' \langle\psi_{n\mathbf{k}}|\partial_{\nu-\mathbf{q}}\hat{H}|\psi_{m\mathbf{k}+\mathbf{q}}\rangle \langle\psi_{m\mathbf{k}+\mathbf{q}}|\left(\varepsilon_{n\mathbf{k}} - \hat{H}\right)^{-1}\partial_{\nu\mathbf{q}}\hat{H}|\psi_{n\mathbf{k}}\rangle\,. \tag{6.1}$$

In this form, it becomes clear that the sum over all intermediate states, $|\psi_{m\mathbf{k}+\mathbf{q}}\rangle$, can be considered an expansion of the perturbed AE potential present in $\partial_{\nu\mathbf{q}}\hat{H}$ in terms of KS orbitals. Since the KS orbitals at high energies essentially behave like free electrons, the sum eventually becomes a plane-wave expansion at high energies. Unfortunately, the true AE potential and its derivative can change rapidly in proximity to the nuclei. Thus, in general, a considerable amount of plane waves is required to accurately represent the change of the AE potential. This explains the origin of the slow convergence of the ZPR with respect to the number of intermediate states. Similar arguments can be made to discuss the convergence of the DW part of the ZPR.

Let us now attempt to explain the difference in convergence behavior between the AE and PS approaches as seen in Figs. 6.5 and 6.6. In the PS approach, the PS FM term is calculated by replacing the integrand $\gamma^{\text{FM}}_{n\mathbf{k},\nu\mathbf{q}}$ in Eq. (4.57) by its PS counterpart, $\tilde{\gamma}^{\text{FM}}_{n\mathbf{k},\nu\mathbf{q}}$, defined in Eq. (4.61). The two integrands differ only by a substitution $g_{mn\mathbf{k},\nu\mathbf{q}} \to \tilde{g}_{mn\mathbf{k},\nu\mathbf{q}}$ and by the last term in Eq. (4.61). This term has been carefully checked to be negligible for all materials considered here. Therefore, the difference in convergence behavior between the AE and PS approaches is directly related to the difference between the corresponding electron-phonon matrix el-

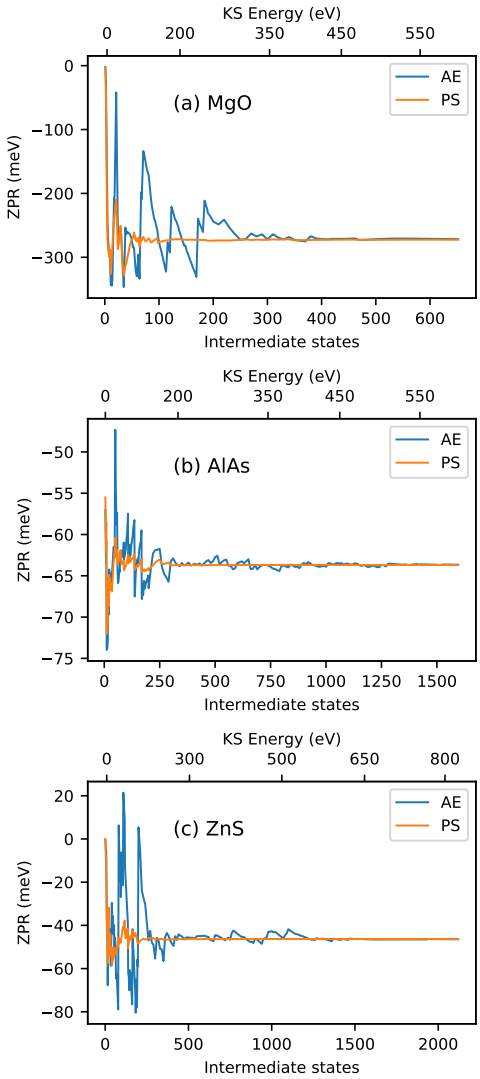

Figure 6.5: Convergence behavior of the non-adiabatic ZPR with respect to the maximum number of included intermediate states for both the AE and PS method for (a) MgO, (b) AlAs and (c) ZnS. The second x-axis scale above each panel displays the average KS energy with respect to the Fermi level that corresponds to the number of bands. The PS method converges much faster and smoother than the AE method, but both eventually converge to approximately the same value.

ements. As a side note, the individual FM and DW terms generally converge to completely different values in the two formulations, as discussed in Ref. [33].

In the PAW method, slow plane-wave convergence is usually avoided since the sharp AE potential is replaced by a smooth pseudopotential that requires fewer plane waves to be described accurately. In the case of the PS electron-phonon matrix element, this pseudization is kept intact as we pseudize the or-

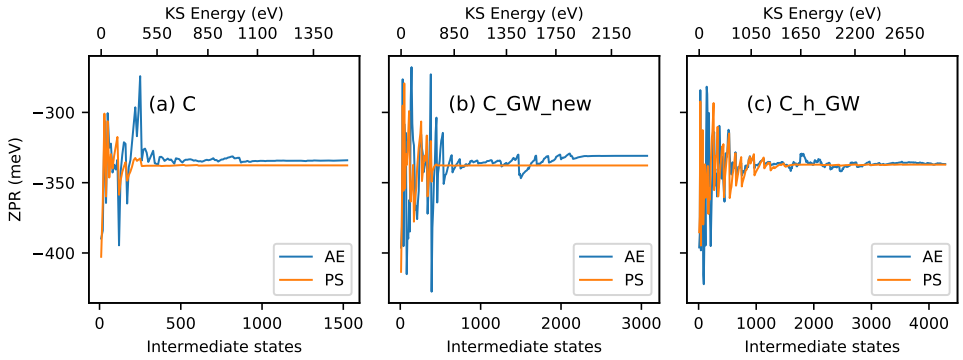

Figure 6.6: Same as Fig. 6.5 but for diamond and using three different PAW potentials: C (a), C_GW_new (b) and C_h_GW (c). AE and PS methods converge to approximately the same result only in panel (c). The AE results depend more strongly on the PAW potential.

bitals and potentials first, and only describe the interaction of the PS orbitals with the pseudopotentials and their derivatives. Although the pseudized electron-phonon term, Eq. (4.87), contains one-center corrections — as happens for any operator after the PAW transformation — these one-center terms are calculated in such a manner that the ionic potential and partial waves move rigidly in unison with the PAW sphere when the corresponding atom is displaced. As a consequence, there are no partial derivatives of the AE potential. This explains the comparatively faster convergence in the PS case.

On the other hand, in the case of the AE electron-phonon matrix element, the change of the AE potential is essentially reconstructed from the available information inside the PAW spheres using Eqs. (4.82) to (4.86). This reintroduces the slow convergence as discussed earlier. To see how this manifests in practice, let us inspect the difference between the AE and PS matrix elements given in Eq. (4.55). It factorizes into two parts: an energy difference, $\left(\varepsilon_{n\mathbf{k}} - \varepsilon_{m\mathbf{k}+\mathbf{q}}\right)$, and the term $t_{mn\mathbf{k},\nu\mathbf{q}}$ that contains the change of the AE partial waves (see Eq. (4.86)). The energy difference causes this contribution to converge slowly as it scales linearly with the KS energy of the intermediate state, while $t_{mn\mathbf{k},\nu\mathbf{q}}$ provides a numerical reconstruction of the perturbed AE potential. In contrast, no such scaling is present in the PS method as the corresponding matrix elements do not contain the KS energy of the intermediate state.

If one were to artificially set $\left(\varepsilon_{n\mathbf{k}} - \varepsilon_{m\mathbf{k}+\mathbf{q}}\right) = 1$ in Eqs. (4.85) and (4.86), the fast convergence behavior of the PS method should be recovered. We have conducted this numerical test for the carbon potential corresponding to panel (a) of Fig. 6.6 and indeed found that the modified ZPR calculation converges as fast as in the PS case. Once again, this is not a coincidence as the reconstruction of the AE information contained in $t_{mn\mathbf{k},\nu\mathbf{q}}$ is not required in the PS method.

For diamond, as observed in panels (a) and (b) of Fig. 6.6, both methods converge to slightly different values. In our implementation, Eq. (4.82) can be seen as

a reconstruction formula to obtain the AE quantity, Eq. (4.10). That both methods do not converge to the same value indicates that this reconstruction in the term $t_{mn\mathbf{k},\nu\mathbf{q}}$ has failed. More precisely, it is most likely the contribution $g^{(\mathrm{R})}$ in Eq. (4.86), which contains the derivative of the AE partial waves, $|\phi_j\rangle$, projected onto other partial waves, $\langle\phi_i|$, that is responsible for the discrepancy. Unfortunately, it is entirely possible that the corresponding partial-wave basis is not sufficiently complete to describe the potential derivative induced by the phonon perturbation, especially at high energies. In general, pseudopotential methods, the PAW method and other linearized methods have been designed to describe total energies, forces, and one-electrons energies close to the Fermi-level with great accuracy [142]. In contrast, electron-phonon matrix elements are, strictly speaking, not observables. Hence, it is reasonable to assume that the reconstruction of the AE orbital might fail for certain pseudopotentials, especially at higher energies where the partial-wave basis is not sufficiently complete. An important exception are the diagonal matrix elements ($\varepsilon_{m\mathbf{k}+\mathbf{q}} = \varepsilon_{n\mathbf{k}}$) which describe the first-order change of the electronic eigenvalues. In this case, the AE and PS electron-phonon matrix elements are strictly identical and the contribution from Eq. (4.86) is zero. Similar issues related to the completeness of the local PAW basis were previously encountered in the context of linear optical properties [86] and are also commonly observed for NMR calculations in all-electron codes [143].

In panel (b) of Fig. 6.6, we have tried to improve upon the calculations performed in panel (a) by using a different pseudopotential that features more partial waves, but this did not improve the agreement. It is difficult to say why this is the case exactly. First, there is no guarantee that the ZPR converges monotonically with respect to the number of local basis functions. Second, a systematic convergence study becomes unfeasible due to the technical challenges of pseudopotential generation, as increasing the local basis-set size usually requires tuning other parameters.

In panel (c), we instead used a pseudopotential with a smaller core radius for the PAW spheres, a local pseudopotential that follows the all-electron potential down to 0.8 Bohr radii, and a partial-wave basis that contains three partial waves and accurately restores the scattering properties up to 500 eV above the vacuum level. This effectively shifts a portion of the AE information from the local basis onto the plane-wave grid and improves the completeness of the partial wave basis. The drawback of such a potential is that an even larger number of states is required to converge the ZPR with respect to the number of intermediate states. In panel (c), the AE and PS methods agree on the final result, as reported in Table 6.4. Remarkably, the values computed using the PS approach seem to be quite insensitive to the choice of the pseudopotential, which motivates our choice to calculate the ZPR using the PS approach.

6.2.2.2 Evaluation of ZPR for selected materials

In light of the above results and discussion, from here on we have calculated the ZPR using the PS approach. We now proceed to present converged non-adiabatic ZPR calculations for several materials listed in Table 6.5. Important computational parameters, such as the choice of the PAW potential and the plane-wave cutoff, are reported. In addition, the table also lists the size of the supercell and

Table 6.5: PAW potentials (POTCAR), plane-wave cutoffs (E_{cut}) and supercell sizes used for all materials studied. In addition, the finest k/q-point grid size used to extrapolate the ZPR towards infinity is listed for each material (max. grid). This grid size is used for both electrons and phonons. The names of the PAW potentials correspond to the labels of the POTCAR files distributed with VASP.

material	POTCAR	E_{cut} (eV)	supercell	max. grid
AlAs-zb	Al As	240	4×4×4	64×64×64
AlN-w	Al N_s	279	4×4×2	48×48×48
AlP-zb	Al P	255	4×4×4	64×64×64
AlSb-zb	Al Sb	240	4×4×4	64×64×64
BN-zb	B N_s	319	4×4×4	64×64×64
BaO-rs	Ba_sv O_s	283	4×4×4	64×64×64
BeO-w	Be O_s	350	4×4×2	48×48×48
C-cd	C	600	4×4×4	48×48×48
CaO-rs	Ca_sv O_s	350	4×4×4	64×64×64
CdS-zb	Cd S	274	4×4×4	64×64×64
CdSe-zb	Cd Se	274	4×4×4	64×64×64
CdTe-zb	Cd Te	274	4×4×4	64×64×64
GaN-w	Ga_d N_s	283	4×4×2	64×64×64
GaN-zb	Ga_d N_s	350	4×4×4	64×64×64
GaP-zb	Ga_d P	283	4×4×4	64×64×64
Li2O	Li_sv O	499	4×4×4	64×64×64
LiF-rs	Li_sv F	499	4×4×4	64×64×64
MgO-rs	Mg O	500	4×4×4	64×64×64
Si-cd	Si	245	4×4×4	64×64×64
SiC-zb	Si C	400	4×4×4	64×64×64
SiO2-t	Si O_s	283	3×3×4	48×48×48
SnO2-t	Sn_d O_s	283	3×3×4	48×48×48
SrO-rs	Sr_sv O_s	283	4×4×4	64×64×64
TiO2-t	Ti_sv O_s	283	3×3×4	32×32×32
ZnO-w	Zn O_s	283	4×4×2	64×64×64
ZnS-zb	Zn S	277	4×4×4	64×64×64
ZnSe-zb	Zn Se	277	4×4×4	64×64×64
ZnTe-zb	Zn Te	400	4×4×4	64×64×64

the maximum number of k/q-points used to extrapolate the ZPR towards infinity. Additional information regarding the pseudopotentials is listed in Table 6.9. The materials were chosen from a recent publication by Miglio *et al.* [20] in order to make a detailed comparison.

All calculations were performed using the PBE flavor of density-functional-theory approximation [64, 65], except AlN, BN and C, where LDA was used [62]. This is done for consistency with the calculations reported by Miglio *et al.*, as different density-functional-theory approximations can translate into slight differences in the ZPR results. For reason of consistency, we also chose a smearing parameter of $\delta = 10$ meV for all compounds and the same band-gap transitions as in Ref. [20]. Lattice parameters are optimized to minimize the DFT total-energy functional. The Born effective-charge tensor and macroscopic ion-clamped static dielectric tensor used to calculate the long-range electrostatic contributions in our interpolation scheme are calculated from DFPT [86]. We leave the special treatment of the dynamic quadrupoles in the long-range interaction as proposed in [48, 49] for a future work. Lattice parameters as well as the relevant components of the Born effective-charge and dielectric tensor are reported in Tables 6.6 to 6.8.

Table 6.6: Lattice constants (in Å), dielectric constants and Born effective charges for cubic materials.

material	a	ϵ^{∞}_{xx}	$Z^{\star}_{xx}$
AlAs-zb	4.053	9.526	2.154
AlP-zb	3.893	8.118	2.245
AlSb-zb	4.407	12.035	1.827
BN-zb	2.535	4.534	1.866
BaO-rs	3.968	4.238	2.722
CaO-rs	3.421	3.768	2.346
CdS-zb	4.190	6.227	2.235
CdSe-zb	4.379	8.386	2.319
CdTe-zb	4.680	9.304	2.302
GaN-zb	3.215	6.059	2.669
GaP-zb	3.891	10.583	2.206
Li2O	3.268	2.918	0.903
LiF-rs	2.867	2.049	1.052
MgO-rs	2.978	3.128	1.969
SiC-zb	3.096	6.993	2.690
SrO-rs	3.682	3.781	2.431
ZnS-zb	3.851	5.905	2.022
ZnSe-zb	4.055	7.345	2.102
ZnTe-zb	4.372	9.030	2.087

Our results for the band-gap ZPR are reported in Table 6.10, together with

Table 6.7: Lattice constants (in Å) and components of the dielectric tensor and Born effective-charge tensor for symmetry-inequivalent directions for hexagonal materials.

material	a	c	ϵ^{∞}_{xx}	ϵ^{∞}_{zz}	$Z^{\star}_{xx}$	$Z^{\star}_{zz}$
AlN-w	3.091	4.947	4.372	4.592	2.504	2.665
BeO-w	2.712	4.404	3.044	3.108	1.788	1.848
GaN-w	3.219	5.244	5.855	6.035	2.621	2.761
ZnO-w	3.284	5.301	5.242	5.227	2.109	2.162

Table 6.8: Same as Table 6.7 but for tetragonal materials.

material	a	c	ϵ^{∞}_{xx}	ϵ^{∞}_{zz}	$Z^{\star}_{xx}$	$Z^{\star}_{xy}$	$Z^{\star}_{zz}$
SiO2-t	4.231	2.700	3.369	3.556	3.807	0.401	4.041
SnO2-t	4.831	3.246	4.675	4.909	4.097	0.519	4.474
TiO2-t	4.587	2.954	7.404	8.738	6.341	1.030	7.621

the corresponding results from Miglio *et al.* Given the differences in the pseudopotentials and the different methodological details, the comparison between the ZPR results is excellent. For most materials, the relative difference is only within a few percent, except for some compounds that feature a particularly small ZPR, such as ZnTe and CdSe. Concerning LiF, missing in Ref. [20], we note that Nery *et al.* [19] report a non-adiabatic band-gap ZPR for LiF of −1149 meV. This agrees well with our value of −1231 meV.

The values for the ZPR in Table 6.10 range from a few meV to over 1 eV in the case of LiF. We can observe an overall trend that materials involving light atoms also feature a large total ZPR. This is in line with previous findings by Karsai *et al.* [58]. However, a definitive statement would require a more thorough analysis. Additionally, Nery *et al.* [19] showed that for the strongly polar materials LiF and MgO, long-range Fröhlich-like interactions account for a considerable portion of the total ZPR. Although we did not look at the Fröhlich contribution separately for the present materials, we still expect this to be the case for other polar materials.

With the choice $\delta = 10\,\text{meV}$ for the smearing parameter, some small numerical errors occur. To gauge the size of these errors, we have investigated the convergence behavior of the ZPR with respect to δ for MgO and CdTe. The latter has a particularly small total ZPR that is of the same order of magnitude as δ. The errors are about 1 meV and 0.5 meV for MgO and CdTe, respectively.

In order to reaffirm the correctness of our results, we conducted a more thorough analysis on ZnO-w for which the relative and absolute differences are comparatively large. First, we compare our computational setup with the one used by Miglio *et al.* in Ref. [20]. While small differences exist in the lattice parameters,

Table 6.9: List of PAW potentials used in this work. The first column (POTCAR) contains the label of the potential from VASP's PAW database. The second column (valence) shows which local orbitals are treated as valence. The cutoff radii, r_{cut}, for the s, p, d and f channels are reported in columns three to six if applicable. If there is more than one channel for a single angular-momentum quantum number, the corresponding cutoff radii are listed as $n \times r_{\text{cut}}$ if they are the same or as a comma-separated list otherwise. The final column contains the radius r_{core} below which the AE potential is replaced by a local pseudopotential. All radii are given in atomic units.

POTCAR	valence	$r_{\text{cut}}(s)$	$r_{\text{cut}}(p)$	$r_{\text{cut}}(d)$	$r_{\text{cut}}(f)$	r_{core}
Al	3s3p3d	2×1.9	2×1.9	1.9	–	1.900
As	4s4p4d4f	2×2.1	2×2.1	2.1	2.1	2.100
B	2s2p3d	2×1.5	2×1.7	1.7	–	1.700
Ba_sv	5s6s5p5d	2×2.8	2×2.7	2×2.7	–	2.516
Be	2s2p3d	2×1.9	2×1.9	1.5	–	1.900
C	2s2p3d	2×1.2	2×1.5	1.5	–	1.500
C_GW_new	2s2p	3×1.1	3×1.5	1.5, 1.6	1.4	1.600
C_h_GW	2s2p	3×1.0	3×1.1	2×1.1	–	0.804
Ca_sv	3s4s3p3d	2×2.3	2×2.3	2×2.3	–	1.808
Cd	4d5s	2×2.3	2×2.3	2×2.3	–	2.054
F	2s2p3d	2×1.2	2×1.52	1.5	–	1.520
Ga_d	3d4s4p	2×2.3	2.1, 2.3	2×2.3	2.3	2.300
Li_sv	1s2s2p3d	1.4, 1.7	1.4	1.4	–	1.700
Mg	3s3d	2×2.0	2×2.0	2.0	–	1.506
N_s	2s2p	2×1.5	2×1.85	–	–	0.803
O	2s2p3d	2×1.2	2×1.52	1.5	–	1.520
O_s	2s2p	2×1.5	2×1.85	–	–	0.804
P	3s3p3d	2×1.9	2×1.9	1.9	–	1.900
S	3s3p3d	2×1.9	2×1.9	1.9	–	1.900
Sb	5s5p5d4f	2×2.3	2×2.3	2.3	2.3	2.300
Se	4s4p4d4f	2×2.1	2×2.1	2.1	2.1	2.100
Si	3s3p3d	2×1.9	2×1.9	1.9	–	1.900
Sn_d	4d5s5p	2×2.5	2×2.5	2×2.5	2.5	2.500
Sr_sv	4s5s4p4d	2×2.48	2×2.5	2×2.5	–	2.201
Te	5s5p5d4f	2×2.3	2×2.3	2.3	2.3	2.300
Ti_sv	3s4s3p3d4f	1.8, 2.3	2×2.3	2×2.3	2.3	2.300
Zn	3d4s	2×2.3	2×2.3	2×2.3	–	1.828

Born effective charges and the dielectric tensor, we find that those differences only account for a change in the ZPR of about 3 meV. Likewise, increasing the supercell size in our calculation from 4×4×2 to 5×5×3 increases the total ZPR by only 2 meV.

Table 6.10: Band-gap ZPR (in meV) obtained in the framework of non-adiabatic AHC theory for various materials. The values are compared against the ones reported by Miglio *et al.* [20].

material	ZPR this work	ZPR Ref. [20]	rel. diff.	abs. diff.
AlAs-zb	-74	-74	0.2 %	0
AlN-w	-377	-399	5.5 %	22
AlP-zb	-96	-93	2.9 %	3
AlSb-zb	-52	-51	1.8 %	1
BN-zb	-402	-406	0.9 %	4
BaO-rs	-277	-271	2.4 %	6
BeO-w	-726	-699	3.9 %	27
C-cd	-323	-330	2.0 %	7
CaO-rs	-357	-341	4.8 %	16
CdS-zb	-67	-70	3.8 %	3
CdSe-zb	-29	-34	15.2 %	5
CdTe-zb	-19	-20	7.4 %	1
GaN-w	-171	-189	9.5 %	18
GaN-zb	-163	-176	7.6 %	13
GaP-zb	-69	-65	5.7 %	4
Li2O	-569	-573	0.6 %	4
LiF-rs	-1231	–	–	–
MgO-rs	-533	-524	1.6 %	9
Si-cd	-58	-56	4.1 %	2
SiC-zb	-175	-179	2.1 %	4
SiO2-t	-583	-585	0.4 %	2
SnO2-t	-232	-215	7.9 %	17
SrO-rs	-323	-326	1.0 %	3
TiO2-t	-349	-337	3.5 %	12
ZnO-w	-175	-157	11.2 %	18
ZnS-zb	-88	-88	0.2 %	0
ZnSe-zb	-43	-44	3.1 %	1
ZnTe-zb	-25	-22	14.4 %	3

Next, we investigate the effect of using different pseudopotentials on the ZPR. The AHC band-gap ZPR of ZnO reported in Ref. [20] was calculated in Abinit [144] using ONCVPSP-type pseudopotentials from the Pseudo-Dojo database v0.3 [145]. Here, we attempt to replicate the result of Ref. [20], and we perform additional calculations using the EPH module in Abinit 9.6.2 which uses a similar approach to interpolate the electron-phonon potential to dense q-point meshes. We use the Dojo pseudopotentials in their standard and high variants, as well as two other types denoted FHI98pp and HGH following the denominations in Ref. [146].

The results of our Abinit calculations are summarized in Table 6.11. The HGH

Table 6.11: Comparison between different norm-conserving pseudopotentials used in our Abinit calculations of the band-gab ZPR of ZnO-w (in meV). The row labeled "infinity" contains the extrapolated values.

dense grid	FHI98pp	Dojo-std.	Dojo-high	HGH
4×4×4	-81	-88	-88	-84
8×8×8	-106	-116	-116	-110
12×12×12	-117	-129	-129	-122
16×16×16	-124	-137	-137	-129
24×24×24	-133	-148	-148	-139
32×32×32	-139	-153	-154	-146
48×48×48	-145	-162	-162	-152
64×64×64	-149	-166	-166	-158
infinity	-160	-175	-178	-175

as well as both Dojo calculations yield very similar values when extrapolated to an infinitely dense q-point grid, in excellent agreement with the ones obtained by VASP using the PAW method (175 meV). The FHI98pp pseudopotential is an outlier in the set which is in line with the Δ test results [146]. We conclude that the ZPR value for ZnO agrees well with the one obtained using the new EPH module in Abinit [144, 147]. This approach bypasses DFPT computations of the electron-phonon potential on dense q-point meshes and is thus more attractive from a computational point of view. The value of the ZPR for ZnO-w reported in Ref. [20] is an outlier in the otherwise satisfactory agreement with our current results. The remaining differences are likely to be related to substantially different pseudopotentials. We consider the present agreement to be a strong validation of the results obtained in Ref. [20] as well as a thorough validation of our present VASP implementation.

6.2.2.3 Comparison with prior work

In this section, we compare against two publications by Karsai *et al.* [58] and Engel *et al.* [33] that calculated the band-gap ZPR using VASP, and we highlight their shortcomings. While the approaches used in both cases employ the adiabatic Born-Oppenheimer approximation and rely on finite displacements in supercells, they differ substantially in how the ZPR is calculated. Let us first briefly review the characteristics of each method.

In Ref. [58], the change of the band structure was determined directly from a single frozen phonon that represents a stochastically average displacement [16]. Since the band structure is calculated exactly for the frozen-phonon structure, no summation over intermediate states is required. Additionally, this method implicitly captures contributions to the ZPR that correspond to higher-order terms

in the electron-phonon interaction (anharmonicities in the ion-ion interactions are neglected, though). The disadvantage of the supercell approach is that momentum transfers are restricted to wave vectors that are commensurate with the supercell. In order to sample small momentum transfers, one might need to increase the supercell size, in particular for polar materials. Presently, a simple method to accurately account for the long-range electrostatic contributions to the electron-phonon interaction does not exist in this approach, so one must rely on brute-force convergence tests and potentially huge supercells.

In Ref. [33], the ZPR was calculated from second-order perturbation theory in the harmonic approximation. Similar to the present work, this method relies on the AHC approach and the rigid-ion approximation to calculate the DW contribution. In contrast to the present work, the electron-phonon matrix elements were calculated using a Wannier-interpolation scheme. While this allows for a very fine sampling of the FBZ, only a comparatively small number of intermediate states has been used. Convergence of the ZPR with respect to the number of bands is generally fairly challenging in Wannier-interpolation schemes, since conduction bands are not easily localized. Finally, even though long-range electrostatic contributions can, in principle, be included in such an interpolation scheme, a working implementation was not available then, and these contributions are hence missing in Ref. [33].

Table 6.12 lists results for the band-gap ZPR from both prior publications and the present work for selected semiconductors and insulators. The reported literature values correspond to calculations using a 5×5×5 supercell and were extracted from Table III in Ref. [33], while the first column collects the present results from Table 6.10. In addition, column two of Table 6.12 also provides results calculated within the adiabatic AHC approximation using the present PS method, but employing supercell sizes and computational parameters that match closely those of Ref. [58]. Specifically, for column two and four, no interpolation to a dense q-point grid was performed, so the k/q-point grids are commensurate with the 5×5×5 supercell. Convergence with respect to the number of intermediate states was obtained by summing over numerous bands as done everywhere else in this work. We are now in a position to compare and assess the implications of the various approximations.

First, we note that the last three columns of Table 6.12 are remarkably close but deviate significantly from the first column. The last three columns have been obtained for identical supercell sizes (one-shot method) and q-point samplings. Besides using the adiabatic approximation, all three are obviously not converged with respect to the considered momentum transfers. For non-polar materials (C and Si) and materials with a large dielectric screening (AlSb) the resulting errors are small. However, for the more polar materials with a small dielectric constant and large Born effective charges, the errors are not acceptable. The errors can well reach a factor two and are typically at least 50 %. Clearly, this confirms prior observations that an accurate treatment of the long-range electrostatic interactions is required in polar materials [19].

Table 6.12: Band-gap ZPR in meV. Column one shows the converged ZPR from this work (Table 6.10). Column two shows the adiabatic ZPR without q-point interpolation and hence without long-range electrostatic contributions. Columns three and four reproduce results from prior publications by Karsai *et al.* and Engel *et al.*, respectively, and correspond to 5×5×5 supercell calculations; in both cases, long-range electrostatic contributions are missing. The table includes information about whether a method employs the harmonic or adiabatic approximations, and whether it is converged with respect to the conduction-band states and q-points.

	ZPR			
	this work AHC	this work AHC	Ref. [58] one-shot	Ref. [33] AHC
adiabatic	no	yes	yes	yes
q-point conv.	yes	no	no	no
harmonic	yes	yes	partly	yes
band conv.	yes	yes	yes	no
AlAs-zb	-74	-57	-63	-55
AlP-zb	-96	-70	-70	-67
AlSb-zb	-44	-43	-43	-39
BN-zb	-402	-290	-294	-290
C-cd	-323	-320	-320	-337
GaN-zb	-163	-87	-94	-95
GaP-zb	-61	-52	-57	-44
Si-cd	-58	-54	-65	-54
SiC-zb	-175	-121	-120	-130

The second interesting assessment is the comparison of the stochastic one-shot method (third column) and the adiabatic AHC approach (second column). The results are remarkably close, with absolute errors hardly exceeding 10 meV (Si-cd). The one-shot method always consistently increases the ZPR for the materials considered here. The good agreement means that in this case the harmonic approximation in the electron-phonon interaction in combination with the rigid-ion approximation is quite well justified. One could potentially add the corrections obtained by the one-shot method compared to the adiabatic AHC back to the q-point converged results to correct for the rigid-ion approximation and anharmonic effects in the electron-phonon interaction.

The final comparison is between column two (AHC converged with respect to intermediate conduction bands) and the AHC approach using Wannier orbitals. The latter is not converged with respect to the intermediate states. Clearly, the relative errors are between 5 % and 10 % but can approach 15 % as for GaP-zb. A systematic trend is not observed. Generally, as shown in Fig. 6.5, the convergence

of the ZPR with respect to the intermediate states can be fairly erratic, with outliers often exceeding 10 % of the converged ZPR. Note that the magnitude of the "oscillations" also depends strongly on the used PAW potentials, as exemplified in Fig. 6.6. Hard accurate PAW potentials (C_h_GW) or the AE PAW approach result in larger jumps than softer PAW potentials. This makes the Wannier approach somewhat unpredictable. Used with care and in combination with soft PAW potentials, it can give a fairly reliable estimate of the ZPR using little computational resources. The downside of this approach is that one needs to be particularly careful when constructing the Wannier orbitals, and validation against converged AHC calculations will likely be required to ascertain the reliability of the results.

6.2.3 Conclusion

The present work determines the ZPR of the band gaps of 28 semiconductors and insulators using the PAW method. As shown, one can derive two different expressions for the electron-phonon matrix element in the PAW method. We have explained in detail how this is possible. Essentially, it depends on whether the atomic derivatives are performed before or after the PAW transformation. The PAW transformation and completeness relation can either be used at the beginning of the derivation, transforming the AE Hamiltonian to the PAW form, or alternatively after taking the derivatives of the AE Hamiltonian with respect to the ionic positions. We have termed the former description PS PAW electron-phonon matrix element and the latter AE PAW electron-phonon matrix element. The latter version describes how the electron-phonon matrix element changes as the nuclear cusp, Z/r, moves against the AE orbitals. The PS version replaces the Z/r cusp and the AE orbitals by the corresponding pseudized quantities.

On first sight, one would expect the AE description to be preferable for the determination of the ZPR, since it is fundamentally more accurate. However, in practice, we find a more rapid convergence of the ZPR with respect to the number of intermediate conduction-band states in the PS formulation. Moreover, in the case of diamond, the local partial-wave expansion does not seem sufficiently complete to perform the reconstruction of the full potential in the AE formulation. Only a reduction of the radial cutoff for the local basis yields results consistent with PS calculations. It remains to be seen if the PS formulation can be employed successfully for other observables. In general, one should carefully investigate whether a simple substitution of the AE matrix element with the PS one yields accurate results.

The second issue we have addressed in the present work is the comparison between different approaches implemented in VASP. The new reference method is based on the AHC approach, can use very dense k-point grids and can account for the energy transfer during phonon emission and absorption. The other two considered approaches are the supercell-based one-shot method and Wannier interpolation. The one-shot method imposes a specific phonon pattern in a su-

percell and determines the induced band-gap changes compared to the ground-state structure. This approach is in some aspects more accurate than the AHC approach adopted in the present work, since it includes higher-order electron-phonon interactions and avoids the rigid-ion approximation. Remarkably, for the materials considered here, the corrections are always below 10 meV, which we consider to be acceptable. The disadvantage of the one-shot approach is that it neglects the energy transfer upon phonon emission and absorption, and at the often considered cell sizes it neglects important long-range contributions. This can lead to sizable errors for polar materials. The second method is also based on the AHC approach but replaces the reevaluation of the KS orbitals at a very dense k-point grid by a Wannier interpolation. While this approach appears to introduce errors of about 10 %, the errors can be much larger in some cases and for hard potentials. The main source of these errors is related to the small number of conduction-band states that one can include in the Wannier approach.

Finally, we have compared our ZPR results with the results of Miglio *et al.* [20] for the same set of materials. The agreement between the two different first-principles codes is overall good, but we find a few cases where the discrepancy is approaching 10 % or even 20 % for materials with a very small ZPR. We have picked one of the outliers (ZnO) and carefully reevaluated the ZPR using Abinit for several pseudopotentials. The reevaluation greatly improved the agreement with our data. As to why the new values using Abinit are improved compared to VASP, we have speculated that this is either related to more careful convergence tests in the present work, an unfortunate choice of pseudopotentials in the original work or recent improvements in the Abinit code. In summary, we are confident that our present PAW results can serve as a very stringent test for other implementations.

6.3 All-Electron vs. Pseudo Approach

In Section 6.2, we show results that highlight differences between the AE and PS approaches to electron-phonon interactions. In particular, we show for a few materials that the converged ZPR is largly unaffected by the method chosen. In this section, we conduct further numerical studies that highlight differences between the AE and PS approaches.

6.3.1 Perturbative Contributions in Diamond

We provide numerical evidence that the AE FM and DW contributions to the ZPR in Eqs. (4.20) and (4.93) differ significantly from their PS counterparts, Eqs. (4.37) and (4.102). To this end, we pick diamond as an example system. Specifically, we provide further details for the calculation performed in panel (a) of Fig. 6.6 by splitting each ZPR into its FM and DW contributions. The result is shown in Fig. 6.7.

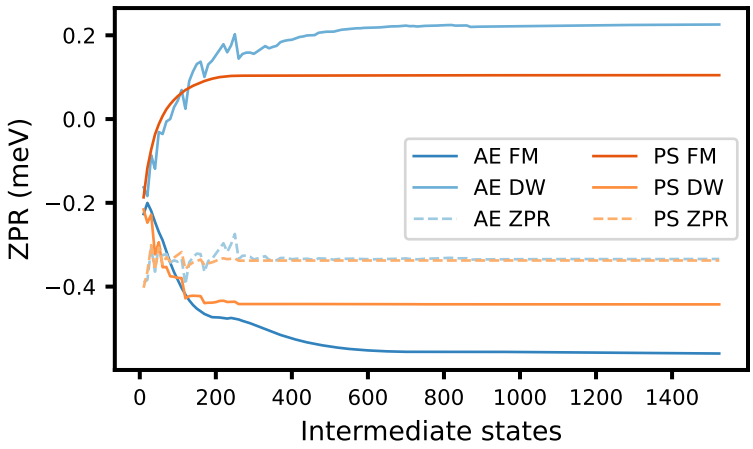

Figure 6.7: Same as panel (a) of Fig. 6.6 but the AE and PS ZPR is decomposed into the FM and DW contributions and the PS FM and AE DW contributions, respectively. Blue and orange lines correspond to AE and PS data, respectively.

In addition to the differences in the convergence already discussed in Section 6.2, Fig. 6.7 reveals stark differences between the different contributions. For example, the AE FM contribution converges to about −560 meV while the PS DW contribution converges to about 105 meV. An similar difference exists in the DW case, where the AE and PS approaches converge to about 226 meV and −442 meV, respectively. This poses no problem for ZPR calculations, since only the sum of FM and DW contributions is a physically meaningful quantity. In Section 4.4.3.1 we even prove the equivalence between AE and PS approaches for calculating the ZPR in the adiabatic approximation. However, it is important to keep in mind that generally one cannot simply substitute the AE matrix elements with the PS matrix elements.

6.3.2 Electron Self-Energy in LiF

The PS approach detailed in Section 4.4.1 was never designed to calculate quantities beyond the adiabatic band-structure renormalization. Still, based on the numerical evidence provided in Section 6.2, we argue that the PS approach can be used in the non-adiabatic case, where it shows a superior convergence behavior compared to the AE approach. However, we now proceed to show an example where the PS approach fails to produce the correct result.

We compute the imaginary part of the band-diagonal frequency-dependent electron self-energy at zero temperature. Since the DW contribution is real, this is just the imaginary part of Eq. (4.15) for $n' = n$ and $T = 0$. The calculations are performed on LiF, a particularly polar insulator that features a large band-gap ZPR. The computational strategy is the same as in Section 6.2. Each calculation starts in a 4×4×4 supercell and the electron-phonon potential is interpolated to

the unit cell. Here, however, we study the self-energy as a function of frequency, ω. In order to decrease the already high computational cost, we forgo the computation of the long-range electron-phonon interaction detailed in Section 4.6. This does not affect the conclusion we draw from the outcome.

Calculations are performed for five different combinations of Li and F pseudopotentials. They are listed in Table 6.13. The combination Li_AE F_AE acts

Table 6.13: Same as Table 6.9 but for different Li and F potentials. The Li_AE POTCAR is a special case. It provides a true AE potential and does not contain any PAW information.

POTCAR	valence	$r_{\text{cut}}(s)$	$r_{\text{cut}}(p)$	$r_{\text{cut}}(d)$	r_{core}
F_AE	1s2p3d	0.4	0.45	0.6	0.600
F_h_GW	2s2p	2×0.8	3×1.05	2×1.05	0.805
F_nc	2s2p3d	2×1.3	2×1.52	1.5	1.520
Li_AE	–	–	–	–	0.000
Li_sv_GW	1s1s2p	2×1.2, 2×1.3	2×1.5	1.5	1.003
Li_sv_nc	1s1s2p3d	2×1.35	2×2.05	2.05	2.050

as a best-effort reference for a true AE calculation. The Li_AE POTCAR does not contain any PAW information and reproduces the true Z/r nature of the Coulomb potential. The F_AE POTCAR, while not a full Z/r potential, uses a considerably smaller cutoff radius for the local pseudopotential than the others. Employing the Li_AE F_AE POTCAR therefore results in a PAW transformation that is close to the identity operator. This way, the differences between AE and PS matrix elements should in principle be negligible. We refer to the calculation using the Li_AE F_AE POTCAR as the *reference* calculation.

Figs. 6.8 and 6.9 show the imaginary part of the electron self-energy of the VBM and CBM of LiF, respectively. In each figure, the panels (a1), (a2), (a3) and (a4) show the imaginary part of the self-energy calculated with the AE matrix elements. Each panel focuses on a different region of the same quantity. Similarly, the panels (b1), (b2), (b3) and (b4) show the imaginary part of the self-energy calculated with the PS matrix elements.

The first observation is that regardless of which kind of matrix element is used, the reference calculation produces approximately the same result. As mentioned earlier, this is important, since it establishes a baseline for both methods that the other pseudopotentials can be compared against. Another important observation is that the AE results all approximately agree with the reference calculation in the studied energy range. This is a strong indication that the AE approach reproduces the correct result from the available PAW information. As mentioned in Section 4.4.2, this is in principle what it is designed to do. A small exception is seen in panel (a2) of Fig. 6.8, where the peak produced by the reference data is seemingly shifted to the right compared to the remaining data. This is most likely related to the F_AE POTCAR used in the reference calculation. It was generated

based on an ionized F atom with atomic energy levels that differ from the other F POTCARs. The convergence with respect to the plane-wave cutoff was verified carefully.

While the AE data agree well with one another, the same is not true for the PS data. In most cases, the reference calculation cannot be reproduced by the other pseudopotentials using the PS matrix elements. A noteworthy exception to this is shown in panel (b3) of both Figs. 6.8 and 6.9. At the KS eigenvalue, as indicated by the dashed line, the imaginary part of the self-energy is approximately the same regardless of pseudopotential and method used. This is consistent with our findings in Section 6.2 for the band-structure renormalization, which is the *real* part of the self-energy evaluated at the KS eigenvalue. It begs the question whether the PS approach could be used in general to calculate quasiparticle lifetimes with good accuracy. That is because the average lifetime $\tau_{n\mathbf{k}}$ an electron (or hole) spends in a state $|\psi_{n\mathbf{k}}\rangle$ is directly related to the imaginary part of the electron self-energy [25]:

$$\frac{1}{\tau_{n\mathbf{k}}} = \frac{2}{\hbar}\left|\operatorname{Im}\Sigma^{\mathrm{FM}}_{nn\mathbf{k}}\left(\frac{\varepsilon_{n\mathbf{k}}}{\hbar}, T\right)\right|. \tag{6.2}$$

Following Fermi's golden rule, the lifetimes are often expressed in terms of Dirac delta functions:

$$\begin{aligned}\frac{1}{\tau_{n\mathbf{k}}} = \frac{2\pi}{\hbar}\int_{\Omega_{\mathrm{BZ}}}\frac{\mathrm{d}^3q}{\Omega_{\mathrm{BZ}}}\left|g_{mn\mathbf{k},\nu\mathbf{q}}\right|^2 \\ \times\Big[\big(1-f_{n\mathbf{k}}(T)+n_{\nu\mathbf{q}}(T)\big)\delta\big(\varepsilon_{n\mathbf{k}}-\varepsilon_{m\mathbf{k}+\mathbf{q}}-\hbar\omega_{\nu\mathbf{q}}\big) \\ +\big(f_{n\mathbf{k}}(T)+n_{\nu\mathbf{q}}(T)\big)\delta\big(\varepsilon_{n\mathbf{k}}-\varepsilon_{m\mathbf{k}+\mathbf{q}}+\hbar\omega_{\nu\mathbf{q}}\big)\Big].\end{aligned} \tag{6.3}$$

Given any state $|\psi_{n\mathbf{k}}\rangle$ (in this case, the VBM or CBM), the delta functions severely restrict the allowed scattering processes. More precisely, the allowed electronic excitation energies, $\varepsilon_{n\mathbf{k}}-\varepsilon_{m\mathbf{k}+\mathbf{q}}$, are of the same order of magnitude as the phonon energies, $\hbar\omega$. Since the phonon frequencies are bounded from above and generally much smaller than the energies of electrons, only a comparatively narrow interval of electronic states contributes to the quasiparticle lifetime of $|\psi_{n\mathbf{k}}\rangle$. Therefore, the difference between the AE and PS matrix elements, given in Eq. (4.55), is naturally suppressed in this quantity as $\varepsilon_{n\mathbf{k}} - \varepsilon_{m\mathbf{k}+\mathbf{q}}$ never grows beyond the maximum phonon energy. Based on this explanation, we expect the PS matrix elements to be a good substitute for the AE matrix elements when calculating quasiparticle lifetimes. However, without a rigorous proof or a more thorough numerical study, we cannot make a definitive claim.

Returning to Figs. 6.8 and 6.9, it is clear that the PS approach fails for frequencies ω much smaller or larger than $\varepsilon_{n\mathbf{k}}$. To be clear, the PS data in Figs. 6.8 and 6.9 was obtained by simply substituting the AE matrix element with the PS one. Judging by the outcome, this is certainly incorrect. Contrary to the discrepancies found in Fig. 6.6, which arise due to computational shortcomings in the AE approach, the stark differences seen in Figs. 6.8 and 6.9 are primarily related

to the inadequate use of the PS matrix elements. It is unknown whether an alternative formulation exists that could extend the validity of the PS approach also to the more general case. A potential candidate for such a formulation could arise from a proper field-theoretical derivation of electron-phonon interactions purely within the PAW framework. Unfortunately, such an endeavor is exceedingly difficult due to the presence of a generalized eigenvalue problem. Nevertheless, the imaginary part of the electron self-energy is not, strictly speaking, an observable. Although, some properties such as lifetimes are clearly accessible to experimental probes. Whether the PS approach fails to reproduce the correct AE results for any particular physical observable remains to be seen.

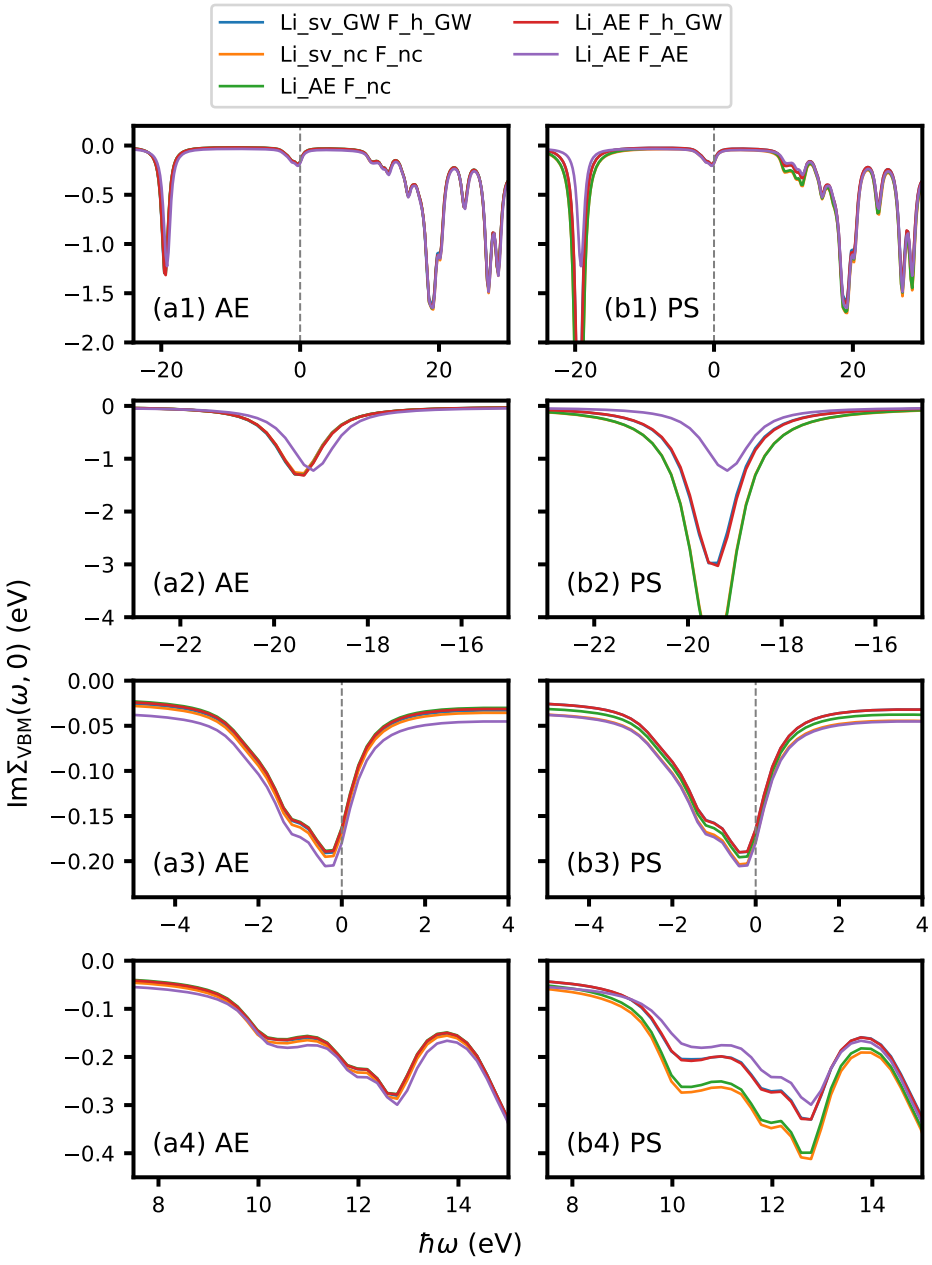

Figure 6.8: Imaginary part of the electron self-energy at the VBM of LiF as a function of frequency, ω. The self-energy is calculated with AE matrix elements [left, (a) panels] and with the PS matrix elements [right, (b) panels] using different pseudopotentials. The energy scales are shifted so the zero coincides with the VBM, indicated by the dashed line. The AE data shows a higher transferability between different pseudopotentials compared to the PS data.

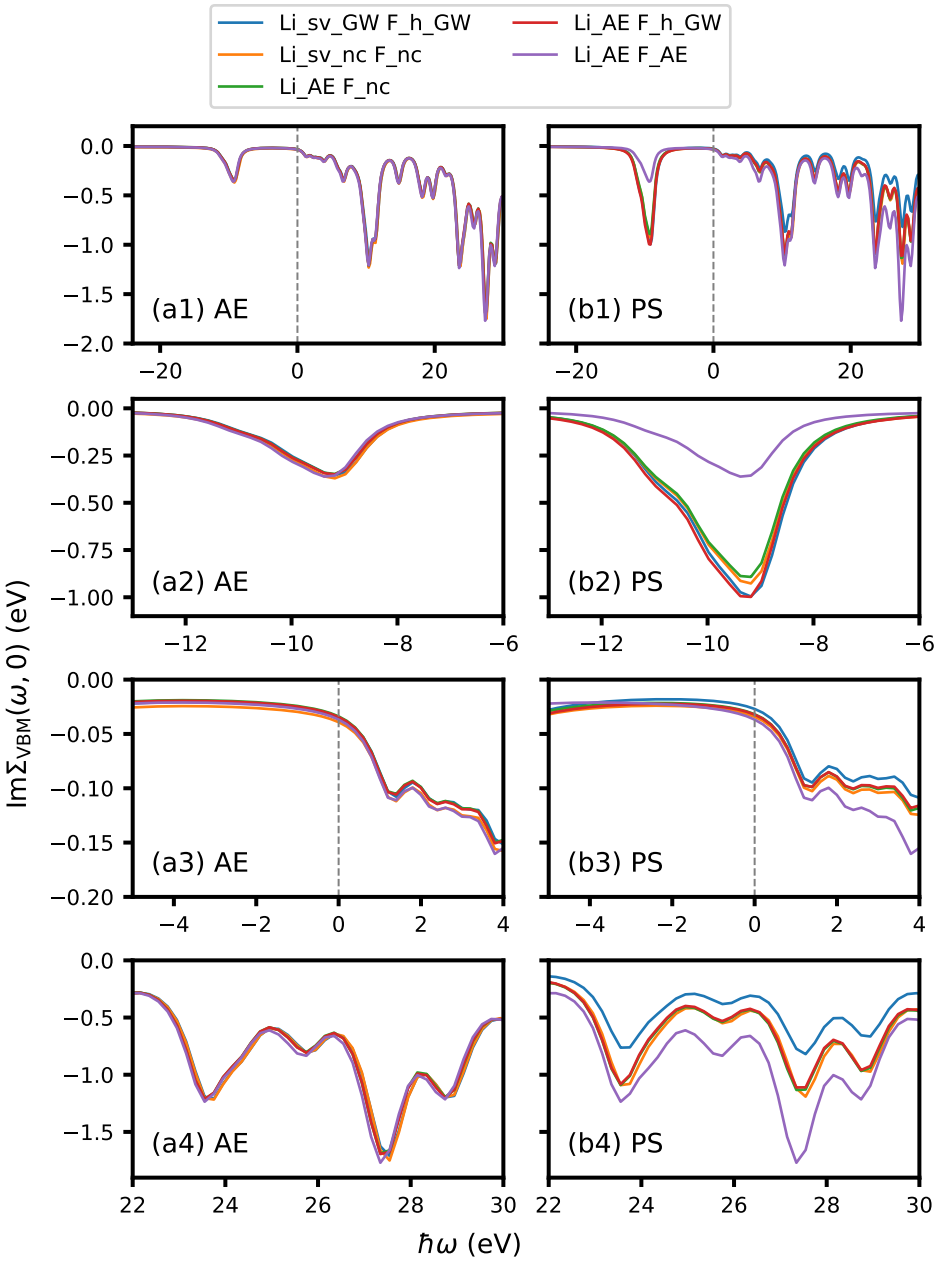

Figure 6.9: Same as Fig. 6.8 but for the CBM.

Chapter 7

Conclusion

The present work set out to implement electron-phonon interactions in VASP in order to calculate the phonon-induced renormalization of the electronic band structure. To accomplish this goal multiple challenges had to be overcome.

First and foremost, the electron-phonon problem was formulated in the theoretical framework of the PAW method. Depending on when the phonon perturbation is introduced, two formulations arise in this context, the AE and the PS approach. We derived both formulations and discussed their differences. Numerical tests were conducted on semiconductors and insulators that reveal the numerical characteristics of the two approaches in the context of the ZPR. This is of paramount importance as the research provides important insights into the inner workings of the electron-phonon problem in the context of the PAW method.

While the PS approach promises a faster numerical convergence for ZPR calculations, its applicability to other observables remains an open question, at least partially. We provide numerical evidence that the PS approach can be used for non-adiabatic ZPR calculations with good accuracy. However, we also show that the imaginary part of the electron self-energy cannot be accurately computed with the PS electron-phonon matrix elements. In this case, only the AE matrix elements produce consistent results for the set of investigated pseudopotentials.

Even though it is not an observable, the imaginary part of the self-energy reveals a fundamental problem with the PS approach. It is designed to solve one particular problem, namely the band-structure renormalization in the adiabatic case. In any other case, great care must be taken when substituting the AE matrix elements with the PS matrix elements.

The AE approach is in principle an exact formulation of the electron-phonon matrix element in terms of PAW quantities. This makes the approach applicable to all kinds of electron-phonon calculations that leverage perturbation theory. Unfortunately, the local basis inside the PAW augmentation spheres is far from complete in practice. As we show in the case of diamond, this can lead to a stronger dependence on the pseudopotential compared to the PS approach. This is most likely caused by numerical inaccuracies arising from the derivatives of

the AE partial waves. In the case of the band-structure renormalization, the AE approach also takes longer to converge with respect to the number of intermediate states. We link this difference in convergence behavior to terms in the AE matrix element that scale with the energy difference between the incoming and outgoing states.

Ultimately, each approach has its advantages and disadvantages. It is important to keep their differences in mind and choose the appropriate method based on the situation. Our understanding and numerical evidence regarding this matter are still limited. We hope to conduct further studies in the future that show a comparison between the AE and PS approaches for more materials and other observables. Another potential outlook is the development of a more general PS approach that can be rigorously extended to the full electron self-energy.

The second achievement of the present work is the development of a Wannier interpolation procedure. With the help of localized Wannier orbitals, we were able to interpolate electronic band-structures and electron-phonon matrix elements. While not a novel approach, our implementation is based on supercells and finite differences. This allows for an easy extension of the interpolation procedure to more complicated density-functional approximations, such as hybrid functionals. Unfortunately, this research avenue was not explored in this work but is without question an interesting future prospect.

In the context of Wannier interpolation, we have implemented the SCDM algorithm for the generation of Wannier orbitals. It exploits the physical properties of the density matrix and requires only a minimal set of parameters. The SCDM method is an important step forward in making Wannier interpolation more user-friendly. It also opens the door for fully automatic Wannierization.

While the Wannier approach is not particularly well-suited for the calculation of the band-structure renormalization due to the required large number of intermediate states, it can be an efficient tool in calculating states around the Fermi level. This is, for example, required for transport calculations based on the Boltzmann transport equation. In these calculations, the energy range for the intermediate states is usually quite narrow but the required q-point meshes are considerably denser. With the computational machinery of Wannier interpolation put in place, this is yet another interesting research area that can be explored in the future.

The third contribution to the VASP code and a key ingredient in the electron-phonon interpolation procedure is the inclusion of long-range electrostatic interactions. We have included the correct non-analytic dipole-dipole contribution to the dynamical matrix for phonons and the dipole contribution for electron-phonon matrix elements. This allows the entire interpolation machinery to be applied to polar materials.

Finally, an alternative electron-phonon implementation has been integrated in VASP, at least partially, which allows the accurate calculation of the band-structure renormalization. We have used this new implementation to calculate the band-gap ZPR of numerous materials. The results agree well with contempo-

rary literature. In addition, we were able to compare against our prior works and highlight former shortcomings due to technical or methodological limitations.

The new electron-phonon implementation will provide a solid foundation for further development. It can coexist with the Wannier-based approach as both have their advantages and disadvantages. Most importantly, either approach can act as a numerical benchmark for the other.

Ultimately, the present work concludes with a bright outlook towards the future. The computational machinery developed in this work is a tremendous step forward in matching the electron-phonon capabilities of other popular, feature-rich codes such as *ABINIT* and *Quantum ESPRESSO*.

APPENDIX A

Abstract

A.1 English Version

We study the phonon-induced renormalization of the electronic band gap using the projector-augmented wave (PAW) method. In the PAW formalism, two distinct types of electron-phonon matrix elements can be defined in the lowest order of perturbation theory. These matrix elements are categorized as “all-electron” (AE) or “pseudo” (PS) depending on whether the atomic derivatives are taken before or after the PAW transformation, respectively. The advantages and disadvantages of the two approaches are carefully analyzed and compared against each other. The theoretical considerations are supplemented by numerical calculations of the band-gap renormalization for numerous semiconductors and insulators. Our findings reveal that the PS approach exhibits faster convergence with respect to the number of unoccupied intermediate states. The required electron-phonon matrix elements are computed in the Vienna Ab-initio Simulation Package (VASP) using interpolation techniques. Specifically, one implementation is based on a Fourier-like interpolation scheme that relies on localized Wannier orbitals. An alternative, newer implementation uses just the standard Bloch orbitals to achieve interpolation, thus eliminating the need for a localized basis set. Both implementations utilize finite atomic displacements in a supercell. Our final results are compared with recent literature, demonstrating satisfactory agreement.

A.2 German Version

Wir untersuchen die phononeninduzierte Renormalisierung der elektronischen Bandlücke mit Hilfe der PAW-Methode (projector-augmented wave). Im PAW-Formalismus können zwei verschiedene Arten von Elektron-Phonon-Matrixelementen in der niedrigsten Ordnung der Störungstheorie definiert werden. Diese Matrixelemente werden als “all-electron” (AE) oder “pseudo” (PS) kategorisiert,

je nachdem, ob die atomaren Ableitungen vor oder nach der PAW-Transformation genommen werden. Die Vor- und Nachteile der beiden Ansätze werden sorgfältig analysiert und gegeneinander abgewogen. Die theoretischen Überlegungen werden durch numerische Berechnungen der Renormalisierung der Bandlücke für zahlreiche Halbleiter und Isolatoren ergänzt. Unsere Ergebnisse zeigen, dass der PS-Ansatz eine schnellere Konvergenz in Bezug auf die Anzahl der unbesetzten Zwischenzustände aufweist. Die benötigten Elektron-Phonon-Matrixelemente werden im Vienna Ab-initio Simulation Package (VASP) mit Hilfe von Interpolationsverfahren berechnet. Konkret basiert eine Implementierung auf einem Fourier-ähnlichen Interpolationsschema, welches sich auf lokalisierte Wannier-Orbitale stützt. Eine alternative, neuere Implementierung verwendet für die Interpolation nur die üblichen Bloch-Orbitale, wodurch die Notwendigkeit eines lokalisierten Basissatzes entfällt. Beide Implementierungen verwenden finite atomare Auslenkungen in einer Superzelle. Unsere Endergebnisse werden mit der aktuellen Literatur verglichen und zeigen eine zufriedenstellende Übereinstimmung.

Appendix B

Electrons in Second Quantization

In the context of many-body theory, we can describe the system of independent KS electrons using the language of second quantization. In this case, we can write the electronic Hamiltonian, $\hat{H}_\mathrm{e}$, as:

$$\hat{H}_\mathrm{e} = \sum_n \int_{\Omega_\mathrm{BZ}} \frac{\mathrm{d}^3 k}{\Omega_\mathrm{BZ}} \hat{n}^\mathrm{e}_{n\mathbf{k}} \varepsilon_{n\mathbf{k}}, \tag{B.1}$$

$$\hat{n}^\mathrm{e}_{n\mathbf{k}} \equiv \hat{c}^\dagger_{n\mathbf{k}} \hat{c}_{n\mathbf{k}}, \tag{B.2}$$

where $\hat{c}^\dagger_{n\mathbf{k}}$ and $\hat{c}_{n\mathbf{k}}$ are the electron creation and annihilation operators, respectively. They obey the canonical commutation relations:

$$\left[\hat{c}_{n\mathbf{k}}, \hat{c}^\dagger_{n'\mathbf{k}'}\right] = \Omega_\mathrm{BZ} \delta_{nn'} \delta^{(3)}(\mathbf{k}' - \mathbf{k}) \mathbb{1}, \tag{B.3}$$

$$\left[\hat{c}_{n\mathbf{k}}, \hat{c}_{n'\mathbf{k}'}\right] = 0, \tag{B.4}$$

$$\left[\hat{c}^\dagger_{n\mathbf{k}}, \hat{c}^\dagger_{n'\mathbf{k}'}\right] = 0. \tag{B.5}$$

This ensures that the multi-particle states are properly normalized. $\hat{n}^\mathrm{e}_{n\mathbf{k}}$ is the so-called *number operator* for the electrons, which counts the number of electrons with band index n and Bloch vector $\mathbf{k}$ in the corresponding multi-particle state.

Appendix C

New Electron-Phonon Code: Implementation Details

This appendix is a slightly modified excerpt of the appendices found in Ref. [35]. It gives implementation details to the new electron-phonon code used in that publication, which is summarized in Section 6.2

C.1 Parlinski supercell interpolation theorems for electron-phonon interactions

This appendix provides the electron-phonon equivalent of the Parlinski interpolation theorem for phonons [141]. In our approach, we are computing the derivatives of the potentials appearing in Eqs. (4.83) and (4.84) from finite displacements of atoms in supercell calculations (See Ref. [34]). This supercell approach prevents us from accessing the quantities $d\tilde{v}/d\mathbf{R}_\kappa$ and $dD_{ij}/d\mathbf{R}_\kappa$. Indeed, having periodic boundary conditions in the supercell implies that when a finite displacement is applied to atom κ, $\mathbf{R}_\kappa \to \mathbf{R}_\kappa + \mathbf{u}$, every supercell-periodic repetition of this atom is also displaced, $\mathbf{R}_{\mathbf{L}\kappa} \to \mathbf{R}_{\mathbf{L}\kappa} + \mathbf{u}$, with $\mathbf{R}_{\mathbf{L}\kappa} = \mathbf{R}_\kappa + \mathbf{L}$, and $\mathbf{L}$ the supercell lattice vectors. Consequently, the quantities we obtain from finite differences are

$$\sum_{\mathbf{L}} \frac{d\tilde{v}(\mathbf{r})}{d\mathbf{R}_{\mathbf{L}\kappa}} \text{ and } \sum_{\mathbf{L}} \frac{dD_{ij}}{d\mathbf{R}_{\mathbf{L}\kappa}}, \tag{C.1}$$

rather than just $d\tilde{v}/d\mathbf{R}_\kappa$ and $dD_{ij}/d\mathbf{R}_\kappa$.

The same aliasing problem appears in the computation of the phonon spectrum when the force constants are obtained from finite differences of forces. In terms of forces, the dynamical matrix is given as

$$D_{\kappa\alpha,\kappa'\alpha'}(\mathbf{q}) = -\frac{1}{\sqrt{M_\kappa M_{\kappa'}}} \sum_{l'} e^{i\mathbf{q}\cdot\mathbf{R}_{l'}} \frac{\partial \mathbf{F}_{l'\kappa'\alpha'}}{\partial \mathbf{R}_{\kappa\alpha}}, \tag{C.2}$$

with $\mathbf{F}_{l'\kappa'\alpha'}$ the force on atom κ' in primitive cell l' in the Cartesian direction α'. In this case, instead of $\partial\mathbf{F}_{l'\kappa'\alpha'}/\partial\mathbf{R}_{\kappa\alpha}$, one has $\sum_{\mathbf{L}}\partial\mathbf{F}_{l'\kappa'\alpha'}/\partial\mathbf{R}_{\mathbf{L}\kappa\alpha}$, which is obtained from the supercell calculations.

The problem at hand is therefore to obtain as accurately as possible the aforementioned derivatives, $\partial/\partial\mathbf{R}_\kappa$, knowing only the periodic derivatives $\sum_{\mathbf{L}}\partial/\partial\mathbf{R}_{\mathbf{L}\kappa}$. For phonons, by defining a proper interpolation of the dynamical matrix, Parlinski [141] has shown that it is possible to obtain exact results for wave vectors $\mathbf{q}$ that are commensurate with the supercell, $e^{i\mathbf{q}\cdot\mathbf{L}} = 1$. In the following for the electron-phonon coupling, we propose interpolations which also become exact for those commensurate wave vectors.

At first, for a given atom κ at position $\mathbf{R}_\kappa$, and a given location $\mathbf{r}$ in the supercell, we define the set of supercell lattice vectors, $\mathbf{L}$, that minimize the distance between $\mathbf{R}_\kappa$ and the image of $\mathbf{r}$ in the neighboring supercell,

$$\{\mathbf{L}\}_{\kappa,\mathbf{r}} = \underset{\mathbf{L}}{\operatorname{argmin}}\,||\mathbf{r}+\mathbf{L}-\mathbf{R}_\kappa||. \tag{C.3}$$

$\mathbf{r}+\mathbf{L}$ are the so-called minimal images of $\mathbf{r}$ around $\mathbf{R}_\kappa$. Then, if V is the crystal volume and V_S the volume of the supercell, the interpolations are defined saying that the volume integration/summation is replaced by an integration/summation over the supercell volume of the same quantities, but computed with the periodic derivatives, and averaged over their minimal images around atom κ. This gives

$$\begin{aligned}\mathbf{g}^{(V)}_{n\mathbf{k},n'\mathbf{k}'}(\mathbf{R}_\kappa) &= \int_V d^3\mathbf{r}\,\widetilde{\psi}^*_{n\mathbf{k}}(\mathbf{r})\frac{d\tilde{v}(\mathbf{r})}{d\mathbf{R}_\kappa}\widetilde{\psi}_{n'\mathbf{k}'}(\mathbf{r})\\ &\longrightarrow \int_{V_S} d^3\mathbf{r}\,\frac{1}{|\{\mathbf{L}\}_{\kappa,\mathbf{r}}|}\sum_{\{\mathbf{L}\}_{\kappa,\mathbf{r}}}\widetilde{\psi}^*_{n\mathbf{k}}(\mathbf{r}+\mathbf{L})\left(\sum_{\mathbf{L}'}\frac{d\tilde{v}(\mathbf{r}+\mathbf{L})}{d\mathbf{R}_{\mathbf{L}'\kappa}}\right)\widetilde{\psi}_{n'\mathbf{k}'}(\mathbf{r}+\mathbf{L}),\end{aligned} \tag{C.4}$$

$$\begin{aligned}\mathbf{g}^{(D)}_{n\mathbf{k},n'\mathbf{k}'}(\mathbf{R}_\kappa) &= \sum_{\kappa'\in V}\sum_{LL'}\langle\widetilde{\psi}_{n\mathbf{k}}|\widetilde{p}_{\kappa'L}\rangle\frac{dD^{\kappa'}_{L,L'}}{d\mathbf{R}_\kappa}\langle\widetilde{p}_{\kappa'L'}|\widetilde{\psi}_{n'\mathbf{k}'}\rangle\\ &\longrightarrow \sum_{\kappa'\in V_S}\sum_{LL'}\frac{1}{|\{\mathbf{L}\}_{\kappa,\mathbf{R}_{\kappa'}}|}\sum_{\{\mathbf{L}\}_{\kappa,\mathbf{R}_{\kappa'}}}\langle\widetilde{\psi}_{n\mathbf{k}}|\widetilde{p}_{\mathbf{L}\kappa'L}\rangle\left(\sum_{\mathbf{L}'}\frac{dD^{\mathbf{L}\kappa'}_{LL'}}{d\mathbf{R}_{\mathbf{L}'\kappa}}\right)\langle\widetilde{p}_{\mathbf{L}\kappa'L'}|\widetilde{\psi}_{n'\mathbf{k}'}\rangle.\end{aligned} \tag{C.5}$$

In Eqs. (C.4) and (C.5), the definitions of $\mathbf{g}^{(V)}$ and $\mathbf{g}^{(D)}$ are recalled, and the interpolation is defined with the arrow $\longrightarrow$.

That the above interpolations become exact for wave vectors $\mathbf{k}$ and $\mathbf{k}'$ commensurate with the supercell is shown using the Bloch theorem and the periodicity of the potential. Indeed, if $V_S(\mathbf{L}')$ is the volume of the supercell with origin at $\mathbf{L}'$, then the interpolation for $\mathbf{g}^{(V)}$ can be written as

$$\sum_{\mathbf{L}'}\int_{V_S(\mathbf{L}')} d^3\mathbf{r}\,\widetilde{\psi}^*_{n\mathbf{k}}(\mathbf{r})\frac{d\tilde{v}(\mathbf{r})}{d\mathbf{R}_\kappa}\widetilde{\psi}_{n'\mathbf{k}'}(\mathbf{r})\frac{1}{|\{\mathbf{L}\}_{\kappa,\mathbf{r}}|}\sum_{\{\mathbf{L}\}_{\kappa,\mathbf{r}}}e^{i(\mathbf{k}'-\mathbf{k})\cdot(\mathbf{L}-\mathbf{L}')}, \tag{C.6}$$

where the exponential becomes equal to 1 for commensurate wave vectors. The interpolation of $\mathbf{g}^{(D)}$ can be written the same way:

$$\sum_{\mathbf{L}'} \sum_{\kappa' \in V_S(\mathbf{L}')} \sum_{LL'} \langle \widetilde{\psi}_{n\mathbf{k}} | \widetilde{p}_{\kappa' L} \rangle \frac{dD^{\kappa'}_{L,L'}}{d\mathbf{R}_\kappa} \langle \widetilde{p}_{\kappa' L'} | \widetilde{\psi}_{n'\mathbf{k}'} \rangle \frac{1}{|\{\mathbf{L}\}_{\kappa,\mathbf{R}_{\kappa'}}|} \sum_{\{\mathbf{L}\}_{\kappa,\mathbf{R}_{\kappa'}}} e^{i(\mathbf{k}'-\mathbf{k})\cdot(\mathbf{L}-\mathbf{L}')}, \tag{C.7}$$

which becomes equal to $\mathbf{g}^{(D)}$ for commensurate wave vectors.

C.2 Treatment of the long-range part of the potential derivative

In ionic systems, the potential derivative in Eq. (4.10) may have contributions at long wavelengths, and therefore the interpolation defined in the previous section may become inaccurate. In such a case, we may write

$$\mathbf{g}^{\kappa}_{n\mathbf{k},n'\mathbf{k}'} = \langle \psi_{n\mathbf{k}} | \frac{\partial \hat{v}^{\mathcal{S}}_\kappa}{\partial \mathbf{R}_\kappa} | \psi_{n'\mathbf{k}'} \rangle + \langle \psi_{n\mathbf{k}} | \frac{\partial \hat{v}^{\mathcal{L}}_\kappa}{\partial \mathbf{R}_\kappa} | \psi_{n'\mathbf{k}'} \rangle, \tag{C.8}$$

with

$$v^{\mathcal{S}}_\kappa(\mathbf{r}) = v(\mathbf{r}) - v^{\mathcal{L}}_\kappa(\mathbf{r}), \tag{C.9}$$

where $v^{\mathcal{L}}_\kappa$ is a potential with a long range behavior approximately equal to the one of v. Consequently, $v^{\mathcal{S}}_\kappa$ is a short-range potential to which our interpolation procedure may be applied. This concept is explored in Section 4.6. In Section 5.2.3, it is shown how the long-range electron-phonon matrix element can be expressed in terms of Wannier orbitals. Here, we provide a direct description of the long-range electron-phonon potential. In the PAW formulation, this generally includes the PAW strength parameters, D_{ij}, defined in Eq. (2.48).

The AE orbitals, $\psi_{n\mathbf{k}}$, are unknown and therefore the orbitals in Eq. (4.113) have to be expressed in terms of the PS orbitals, $\widetilde{\psi}_{n\mathbf{k}}$. We have

$$\begin{aligned}\langle \psi_{n\mathbf{k}} | e^{i(\mathbf{q}+\mathbf{G})\cdot(\hat{\mathbf{r}}-\mathbf{R}_\kappa)} | \psi_{n'\mathbf{k}'} \rangle = \\ \langle \widetilde{\psi}_{n\mathbf{k}} | e^{i(\mathbf{q}+\mathbf{G})\cdot(\hat{\mathbf{r}}-\mathbf{R}_\kappa)} | \widetilde{\psi}_{n'\mathbf{k}'} \rangle + \sum_{ij} \langle \widetilde{\psi}_{n\mathbf{k}} | \widetilde{p}_i \rangle Q^\kappa_{ij}(\mathbf{q}+\mathbf{G}) \langle \widetilde{p}_j | \widetilde{\psi}_{n'\mathbf{k}'} \rangle,\end{aligned} \tag{C.10}$$

with

$$\begin{aligned} Q^\kappa_{ij}(\mathbf{q}+\mathbf{G}) &= \langle \phi_i | e^{i(\mathbf{q}+\mathbf{G})\cdot(\hat{\mathbf{r}}-\mathbf{R}_\kappa)} | \phi_j \rangle - \langle \widetilde{\phi}_i | e^{i(\mathbf{q}+\mathbf{G})\cdot(\hat{\mathbf{r}}-\mathbf{R}_\kappa)} | \widetilde{\phi}_j \rangle & \text{(C.11)} \\ &= \int_{S_{\kappa_i}} d^3r \left(\phi^*_i(\mathbf{r}) \phi_j(\mathbf{r}) - \widetilde{\phi}^*_i(\mathbf{r}) \widetilde{\phi}_j(\mathbf{r}) \right) e^{i(\mathbf{q}+\mathbf{G})\cdot(\mathbf{r}-\mathbf{R}_{\kappa_i})} e^{i(\mathbf{q}+\mathbf{G})\cdot(\mathbf{R}_{\kappa_i}-\mathbf{R}_\kappa)}. & \text{(C.12)} \end{aligned}$$

S_{κ_i} is the atomic sphere around atom κ_i. However, the functions in the integral depend only on $\mathbf{r} - \mathbf{R}_{\kappa_i}$. Therefore, it can be evaluated in the sphere located

at the origin. Using $\phi_i(\mathbf{r}) = R_{n_i l_i}(r) S_{l_i m_i}(\hat{r})$ (See the appendices in Ref. [34]) and the Rayleigh expansion formula, we obtain

$$Q_{ij}^{\kappa}(\mathbf{q}+\mathbf{G}) = 4\pi e^{i(\mathbf{q}+\mathbf{G})\cdot(\mathbf{R}_{\kappa_i}-\mathbf{R}_{\kappa})} \sum_{l=0}^{\infty} \sum_{m=-l}^{l} i^l S_{lm}(\widehat{\mathbf{q}+\mathbf{G}}) q_{ij}^{l}(|\mathbf{q}+\mathbf{G}|) C_{l_i l_j m_i m_j}^{lm}, \tag{C.13}$$

where

$$q_{ij}^{l}(|\mathbf{q}+\mathbf{G}|) = \int dr r^2 \left(R_{n_i l_i}(r) R_{n_j l_j}(r) - \widetilde{R}_{n_i l_i}(r) \widetilde{R}_{n_j l_j}(r) \right) j_l(|\mathbf{q}+\mathbf{G}| r), \tag{C.14}$$

with the spherical Bessel functions j_l and the Gaunt coefficients,

$$C_{l_i l_j m_i m_j}^{lm} = \int d\hat{r}\, S_{l_i m_i}(\hat{r}) S_{lm}(\hat{r}) S_{l_j m_j}(\hat{r}). \tag{C.15}$$

This gives

$$\begin{aligned} \langle \psi_{n\mathbf{k}} | \frac{\partial \hat{v}_{\kappa}^{\mathcal{L}}}{\partial \mathbf{R}_{\kappa}} | \psi_{n'\mathbf{k}'} \rangle = \\ (-e)\frac{4\pi}{\Omega} \sum_{\mathbf{G}\neq -\mathbf{q}} \langle \widetilde{\psi}_{n\mathbf{k}} | \frac{-i(\mathbf{q}+\mathbf{G})^{\top} \mathbf{Z}_{\kappa}^{\star} e^{i(\mathbf{q}+\mathbf{G})\cdot(\hat{\mathbf{r}}-\mathbf{R}_{\kappa})}}{(\mathbf{q}+\mathbf{G})\cdot\epsilon^{\infty}\cdot(\mathbf{q}+\mathbf{G})} | \widetilde{\psi}_{n'\mathbf{k}'} \rangle \\ + (-e)\frac{4\pi}{\Omega} \sum_{\mathbf{G}\neq -\mathbf{q}} \langle \widetilde{\psi}_{n\mathbf{k}} | \widetilde{p}_i \rangle \frac{-i(\mathbf{q}+\mathbf{G}) \mathbf{Z}_{\kappa}^{\star} \sum_{ij} Q_{ij}^{\kappa}(\mathbf{q}+\mathbf{G})}{(\mathbf{q}+\mathbf{G})\cdot\epsilon^{\infty}\cdot(\mathbf{q}+\mathbf{G})} \langle \widetilde{p}_j | \widetilde{\psi}_{n'\mathbf{k}'} \rangle . \end{aligned} \tag{C.16}$$

The quantities $\sum_{\mathbf{L}'} d\tilde{v}/d\mathbf{R}_{\mathbf{L}'\kappa}$ and $\sum_{\mathbf{L}'} dD_{ij}/d\mathbf{R}_{\mathbf{L}'\kappa}$, which appear in Eqs. (C.4) and (C.5), are the change of the PAW potential when an atom κ is moved in every periodic repetition of the supercell with lattice vectors $\mathbf{L}$. When the Poisson equation is solved with such periodic boundary conditions, its solution can be written as

$$\sum_{\mathbf{L}} \frac{dv^{\mathcal{L}}(\mathbf{r})}{d\mathbf{R}_{\mathbf{L}\kappa}} = (-e)\frac{d}{d\mathbf{R}_{\kappa}} \cdot \frac{4\pi \mathbf{Z}_{\kappa}^{\star}}{V_S} \sum_{\mathbf{K}\neq 0} \frac{e^{i\mathbf{K}\cdot(\mathbf{r}-\mathbf{R}_{\kappa})}}{\mathbf{K}\cdot\epsilon^{\infty}\cdot\mathbf{K}}, \tag{C.17}$$

where $\mathbf{K}$ are the reciprocal-lattice vectors of the supercell. To obtain the PAW representation of this potential, once again we write

$$\langle \psi_{n\mathbf{k}} | e^{i\mathbf{K}\cdot(\mathbf{r}-\mathbf{R}_{\kappa})} | \psi_{n'\mathbf{k}'} \rangle = \langle \widetilde{\psi}_{n\mathbf{k}} | e^{i\mathbf{K}\cdot(\mathbf{r}-\mathbf{R}_{\kappa})} | \widetilde{\psi}_{n'\mathbf{k}'} \rangle + \sum_{ij} \langle \widetilde{\psi}_{n\mathbf{k}} | \widetilde{p}_i \rangle Q_{ij}^{\kappa}(\mathbf{K}) \langle \widetilde{p}_j | \widetilde{\psi}_{n'\mathbf{k}'} \rangle . \tag{C.18}$$

Therefore,

$$\begin{aligned} \langle \psi_{n\mathbf{k}} | \sum_{\mathbf{L}} \frac{d\hat{v}^{\mathcal{L}}}{d\mathbf{R}_{\mathbf{L}\kappa}} | \psi_{n'\mathbf{k}'} \rangle = \langle \widetilde{\psi}_{n\mathbf{k}} | (-e)\frac{4\pi Q_{\kappa}}{V_S} \sum_{\mathbf{K}\neq 0} \frac{-i\mathbf{K}}{\mathbf{K}\cdot\epsilon^{\infty}\cdot\mathbf{K}} e^{i\mathbf{K}\cdot(\hat{\mathbf{r}}-\mathbf{R}_{\kappa})} | \widetilde{\psi}_{n'\mathbf{k}'} \rangle \\ + \sum_{ij} \langle \widetilde{\psi}_{n\mathbf{k}} | \widetilde{p}_i \rangle (-e)\frac{4\pi Q_{\kappa}}{V_S} \sum_{\mathbf{K}\neq 0} \frac{-i\mathbf{K}}{\mathbf{K}\cdot\epsilon^{\infty}\cdot\mathbf{K}} Q_{ij}^{\kappa}(\mathbf{K}) \langle \widetilde{p}_j | \widetilde{\psi}_{n'\mathbf{k}'} \rangle . \end{aligned} \tag{C.19}$$

Comparing with Eqs. (4.83) and (4.84), this last equation shows that we can use the equation of the previous section to perform the interpolation procedure by making the substitutions

$$\sum_{\mathbf{L}} \frac{d\tilde{v}(\mathbf{r})}{d\mathbf{R}_{\mathbf{L}\kappa}} \longleftarrow \sum_{\mathbf{L}} \frac{d\tilde{v}(\mathbf{r})}{d\mathbf{R}_{\mathbf{L}\kappa}} - \frac{4\pi e^2 \mathbf{Z}^{\star}_{\kappa}}{V_S} \sum_{\mathbf{K}\neq 0} \frac{-\mathrm{i}\mathbf{K}}{\mathbf{K}\cdot\boldsymbol{\epsilon}^{\infty}\cdot\mathbf{K}} \mathrm{e}^{\mathrm{i}\mathbf{K}\cdot(\mathbf{r}-\mathbf{R}_{\kappa})}, \tag{C.20}$$

$$\sum_{\mathbf{L}} \frac{dD_{ij}}{d\mathbf{R}_{\mathbf{L}\kappa}} \longleftarrow \sum_{\mathbf{L}} \frac{dD_{ij}}{d\mathbf{R}_{\mathbf{L}\kappa}} - \frac{4\pi e^2 \mathbf{Z}^{\star}_{\kappa}}{V_S} \sum_{\mathbf{K}\neq 0} \frac{-\mathrm{i}\mathbf{K}}{\mathbf{K}\cdot\boldsymbol{\epsilon}^{\infty}\cdot\mathbf{K}} Q^{\kappa}_{ij}(\mathbf{K}). \tag{C.21}$$

Glossary

AE all-electron. 16, 17, 18, 19, 20, 21, 45, 49, 50, 51, 52, 53, 54, 55, 56, 57, 58, 59, 61, 62, 83, 93, 94, 95, 96, 97, 98, 102, 107, 108, 109, 110, 111, 112, 113, 115, 116, 125

AHC Allen, Heine and Cardona. 39, 41, 45, 48, 49, 53, 59, 60, 83, 90, 91, 93, 103, 105, 106, 107, 108

ASR acoustic sum rule. 27, 28, 60, 61, 64

CBM conduction-band minimum. 15, 110, 111, 114

DFPT density-functional perturbation theory. 4, 35, 59, 69, 100, 104

DFT density-functional theory. 2, 4, 5, 7, 8, 9, 10, 11, 14, 16, 42, 43, 68, 87, 100

DW Debye-Waller. 41, 42, 43, 44, 45, 46, 47, 49, 54, 55, 57, 59, 60, 61, 62, 90, 95, 96, 105, 108, 109

FBZ first Brillouin zone. 13, 14, 15, 24, 27, 28, 35, 36, 41, 54, 56, 66, 68, 69, 74, 85, 86, 88, 90, 94, 105

FM Fan-Migdal. 43, 44, 46, 47, 49, 53, 55, 59, 60, 61, 95, 96, 108, 109

GGA generalized-gradient approximation. 11, 16

IFC interatomic force constants. 5, 24, 27, 28, 29, 30, 34, 35, 36

KS Kohn-Sham. 5, 9, 10, 11, 12, 14, 15, 16, 18, 39, 41, 42, 43, 44, 45, 46, 47, 50, 55, 58, 59, 63, 65, 68, 81, 82, 93, 94, 95, 96, 97, 108, 111, 121

LDA local-density approximation. 11, 16, 87, 100

LO longitudinal optical. 30, 32, 33, 36, 37, 38, 62, 71

NSCF non self-consistent field. 68

PAW projector-augmented-wave. 3, 4, 5, 16, 17, 18, 19, 20, 21, 22, 39, 41, 45, 46, 47, 48, 49, 50, 51, 52, 53, 55, 57, 58, 59, 60, 76, 83, 84, 85, 86, 91, 92, 94, 95, 96, 97, 98, 99, 102, 104, 107, 108, 110, 112, 115, 125, 126

PBE Perdew, Burke and Ernzerhof. 11, 84, 87, 90, 100

PS pseudo. 17, 18, 19, 20, 21, 46, 47, 48, 49, 50, 51, 52, 53, 54, 55, 56, 57, 58, 59, 60, 61, 62, 83, 93, 94, 95, 96, 97, 98, 99, 105, 107, 108, 109, 110, 111, 112, 113, 115, 116, 125

QRCP QR decomposition with column pivoting. 79, 80

RIA rigid-ion approximation. 60, 61, 62

SCDM selected columns of the density matrix. 78, 79, 81, 82, 116

SVD singular-value decomposition. 77, 78, 81

TO transverse optical. 30, 32, 33, 36, 37, 38

VBM vallence-band maximum. 15, 110, 111, 113

ZPR zero-point renormalization. 2, 3, 5, 39, 45, 53, 54, 57, 58, 83, 85, 87, 88, 89, 90, 91, 92, 93, 94, 95, 96, 97, 98, 99, 100, 101, 102, 103, 104, 105, 106, 107, 108, 109, 115, 116

Bibliography

[1]M. Park, X. Zhang, M. Chung, G. Less, and A. Sastry, "A review of conduction phenomena in li-ion batteries", Journal of Power Sources **195**, 7904–7929 (2010).

[2]F. Zheng, J. Jiang, B. Sun, W. Zhang, and M. Pecht, "Temperature dependent power capability estimation of lithium-ion batteries for hybrid electric vehicles", Energy **113**, 64–75 (2016).

[3]F. Khan, S.-H. Baek, and J. H. Kim, "Wide range temperature dependence of analytical photovoltaic cell parameters for silicon solar cells under high illumination conditions", Applied Energy **183**, 715–724 (2016).

[4]J.-E. Moser, "Slow recombination unveiled", Nature Materials **16**, 4–6 (2016).

[5]J. J. Urban, "One model to rule them all", Nature Materials **16**, 157 (2016).

[6]Y. Pei, X. Shi, A. LaLonde, H. Wang, L. Chen, and G. J. Snyder, "Convergence of electronic bands for high performance bulk thermoelectrics", Nature **473**, 66 (2011).

[7]Z. M. Gibbs, H. Kim, H. Wang, R. L. White, F. Drymiotis, M. Kaviany, and G. Jeffrey Snyder, "Temperature dependent band gap in pbx (x = s, se, te)", Applied Physics Letters **103**, 262109 (2013).

[8]Y. Tang, Z. M. Gibbs, L. A. Agapito, G. Li, H.-S. Kim, M. B. Nardelli, S. Curtarolo, and G. J. Snyder, "Convergence of multi-valley bands as the electronic origin of high thermoelectric performance in cosb3 skutterudites", Nature Materials **14**, 1223 (2015).

[9]G. Tan, F. Shi, S. Hao, L.-D. Zhao, H. Chi, X. Zhang, C. Uher, C. Wolverton, V. P. Dravid, and M. G. Kanatzidis, "Non-equilibrium processing leads to record high thermoelectric figure of merit in pbte-srte", Nature Communications **7**, 12167 (2016).

[10] L. Hedin, "New method for calculating the one-particle green's function with application to the electron-gas problem", eng, Physical Review series I **139**, 796–823 (1965).

[11] M. Shishkin and G. Kresse, "Implementation and performance of the frequency-dependent *GW* method within the paw framework", Phys. Rev. B **74**, 035101 (2006).

[12] M. Shishkin and G. Kresse, "Self-consistent *GW* calculations for semiconductors and insulators", Phys. Rev. B **75**, 235102 (2007).

[13] A. Marini, "Ab Initio Finite-Temperature Excitons", Physical Review Letters **101**, 106405 (2008).

[14] S. Poncé, G. Antonius, Y. Gillet, P. Boulanger, J. Laflamme Janssen, A. Marini, M. Côté, and X. Gonze, "Temperature dependence of electronic eigenenergies in the adiabatic harmonic approximation", Physical Review B **90**, 214304 (2014).

[15] M. Zacharias and F. Giustino, "One-shot calculation of temperature-dependent optical spectra and phonon-induced band-gap renormalization", Phys. Rev. B **94**, 075125 (2016).

[16] M. Zacharias and F. Giustino, "Theory of the special displacement method for electronic structure calculations at finite temperature", Phys. Rev. Research **2**, 013357 (2020).

[17] G. Antonius, S. Poncé, P. Boulanger, M. Côté, and X. Gonze, "Many-body effects on the zero-point renormalization of the band structure", Phys. Rev. Lett. **112**, 215501 (2014).

[18] F. Giustino, S. G. Louie, and M. L. Cohen, "Electron-phonon renormalization of the direct band gap of diamond", Phys. Rev. Lett. **105**, 265501 (2010).

[19] J. P. Nery, P. B. Allen, G. Antonius, L. Reining, A. Miglio, and X. Gonze, "Quasiparticles and phonon satellites in spectral functions of semiconductors and insulators: cumulants applied to the full first-principles theory and the fröhlich polaron", Phys. Rev. B **97**, 115145 (2018).

[20] A. Miglio, V. Brousseau-Couture, E. Godbout, G. Antonius, Y.-H. Chan, S. G. Louie, M. Côté, M. Giantomassi, and X. Gonze, "Predominance of non-adiabatic effects in zero-point renormalization of the electronic band gap", npj Computational Materials **6**, 167 (2020).

[21] H. Kawai, K. Yamashita, E. Cannuccia, and A. Marini, "Electron-electron and electron-phonon correlation effects on the finite-temperature electronic and optical properties of zinc-blende gan", Phys. Rev. B **89**, 085202 (2014).

[22] E. Cannuccia and A. Marini, "Effect of the quantum zero-point atomic motion on the optical and electronic properties of diamond and trans-polyacetylene", Physical Review Letters **107**, 255501 (2011).

[23] E. Cannuccia and A. Marini, "Zero point motion effect on the electronic properties of diamond, trans-polyacetylene and polyethylene", The European Physical Journal B **85**, 320 (2012).

[24] S. Poncé, G. Antonius, P. Boulanger, E. Cannuccia, A. Marini, M. Côté, and X. Gonze, "Verification of first-principles codes: comparison of total energies, phonon frequencies, electron–phonon coupling and zero-point motion correction to the gap between abinit and qe/yambo", Computational Materials Science **83**, 341–348 (2014).

[25] F. Giustino, "Electron-phonon interactions from first principles", Rev. Mod. Phys. **89**, 015003 (2017).

[26] G. Kresse and J. Hafner, "Ab initio molecular dynamics for liquid metals", Phys. Rev. B **47**, 558–561 (1993).

[27] G. Kresse and J. Hafner, "Ab initio molecular-dynamics simulation of the liquid-metal–amorphous-semiconductor transition in germanium", Phys. Rev. B **49**, 14251–14269 (1994).

[28] G. Kresse and J. Furthmüller, "Efficiency of ab-initio total energy calculations for metals and semiconductors using a plane-wave basis set", Computational Materials Science **6**, 15–50 (1996).

[29] G. Kresse and J. Furthmüller, "Efficient iterative schemes for ab initio total-energy calculations using a plane-wave basis set", Phys. Rev. B **54**, 11169–11186 (1996).

[30] M. Engel, "Electron-phonon interactions using wannier-fourier interpolation", MSc Thesis (University of Vienna, Vienna, 2017).

[31] P. E. Blöchl, "Projector augmented-wave method", Phys. Rev. B **50**, 17953–17979 (1994).

[32] G. Kresse and D. Joubert, "From ultrasoft pseudopotentials to the projector augmented-wave method", Phys. Rev. B **59**, 1758–1775 (1999).

[33] M. Engel, M. Marsman, C. Franchini, and G. Kresse, "Electron-phonon interactions using the projector augmented-wave method and wannier functions", Phys. Rev. B **101**, 184302 (2020).

[34] L. Chaput, A. Togo, and I. Tanaka, "Finite-displacement computation of the electron-phonon interaction within the projector augmented-wave method", Phys. Rev. B **100**, 174304 (2019).

[35] M. Engel, H. Miranda, L. Chaput, A. Togo, C. Verdi, M. Marsman, and G. Kresse, "Zero-point renormalization of the band gap of semiconductors and insulators using the projector augmented wave method", Phys. Rev. B **106**, 094316 (2022).

[36] F. Giustino, J. R. Yates, I. Souza, M. L. Cohen, and S. G. Louie, "Electron-phonon interaction via electronic and lattice wannier functions: superconductivity in boron-doped diamond reexamined", Phys. Rev. Lett. **98**, 047005 (2007).

[37] F. Giustino, M. L. Cohen, and S. G. Louie, "Electron-phonon interaction using wannier functions", Phys. Rev. B **76**, 165108 (2007).

[38] G. H. Wannier, "The structure of electronic excitation levels in insulating crystals", Phys. Rev. **52**, 191–197 (1937).

[39] N. Marzari, A. A. Mostofi, J. R. Yates, I. Souza, and D. Vanderbilt, "Maximally localized wannier functions: theory and applications", Rev. Mod. Phys. **84**, 1419–1475 (2012).

[40] M. Calandra, G. Profeta, and F. Mauri, "Adiabatic and nonadiabatic phonon dispersion in a wannier function approach", Phys. Rev. B **82**, 165111 (2010).

[41] W. Li, "Electrical transport limited by electron-phonon coupling from boltzmann transport equation: an ab initio study of si, al, and MoS_2", Phys. Rev. B **92**, 075405 (2015).

[42] A. Eiguren and C. Ambrosch-Draxl, "Wannier interpolation scheme for phonon-induced potentials: application to bulk MgB_2, W, and the (1×1) H-covered W(110) surface", Physical Review B **78**, 045124 (2008).

[43] G. Brunin, H. P. C. Miranda, M. Giantomassi, M. Royo, M. Stengel, M. J. Verstraete, X. Gonze, G.-M. Rignanese, and G. Hautier, "Phonon-limited electron mobility in si, gaas, and gap with exact treatment of dynamical quadrupoles", Phys. Rev. B **102**, 094308 (2020).

[44] P. Vogl, "Microscopic theory of electron-phonon interaction in insulators or semiconductors", Phys. Rev. B **13**, 694–704 (1976).

[45] H. Fröhlich, "Electrons in lattice fields", Advances in Physics **3**, 325–361 (1954).

[46] C. Verdi and F. Giustino, "Fröhlich electron-phonon vertex from first principles", Phys. Rev. Lett. **115**, 176401 (2015).

[47] J. Sjakste, N. Vast, M. Calandra, and F. Mauri, "Wannier interpolation of the electron-phonon matrix elements in polar semiconductors: polar-optical coupling in gaas", Phys. Rev. B **92**, 054307 (2015).

[48] G. Brunin, H. P. C. Miranda, M. Giantomassi, M. Royo, M. Stengel, M. J. Verstraete, X. Gonze, G.-M. Rignanese, and G. Hautier, "Electron-phonon beyond fröhlich: dynamical quadrupoles in polar and covalent solids", Phys. Rev. Lett. **125**, 136601 (2020).

[49] V. A. Jhalani, J.-J. Zhou, J. Park, C. E. Dreyer, and M. Bernardi, "Piezoelectric electron-phonon interaction from ab initio dynamical quadrupoles: impact on charge transport in wurtzite gan", Phys. Rev. Lett. **125**, 136602 (2020).

[50] J. Park, J.-J. Zhou, V. A. Jhalani, C. E. Dreyer, and M. Bernardi, "Long-range quadrupole electron-phonon interaction from first principles", Phys. Rev. B **102**, 125203 (2020).

[51] S. Baroni, S. de Gironcoli, A. Dal Corso, and P. Giannozzi, "Phonons and related crystal properties from density-functional perturbation theory", Rev. Mod. Phys. **73**, 515–562 (2001).

[52]C. Patrick and F. Giustino, "Quantum nuclear dynamics in the photophysics of diamondoids", Nature Communications **4**, 2006 (2013).

[53]B. Monserrat, N. D. Drummond, C. J. Pickard, and R. J. Needs, "Electron-phonon coupling and the metallization of solid helium at terapascal pressures", Phys. Rev. Lett. **112**, 055504 (2014).

[54]M. Zacharias, M. Scheffler, and C. Carbogno, "Fully anharmonic nonperturbative theory of vibronically renormalized electronic band structures", Phys. Rev. B **102**, 045126 (2020).

[55]A. Kundu, M. Govoni, H. Yang, M. Ceriotti, F. Gygi, and G. Galli, "Quantum vibronic effects on the electronic properties of solid and molecular carbon", Phys. Rev. Materials **5**, L070801 (2021).

[56]B. Monserrat, N. D. Drummond, and R. J. Needs, "Anharmonic vibrational properties in periodic systems: energy, electron-phonon coupling, and stress", Phys. Rev. B **87**, 144302 (2013).

[57]B. Monserrat and R. J. Needs, "Comparing electron-phonon coupling strength in diamond, silicon, and silicon carbide: first-principles study", Phys. Rev. B **89**, 214304 (2014).

[58]F. Karsai, M. Engel, G. Kresse, and E. Flage-Larsen, "Electron-phonon coupling in semiconductors within the gw approximation", New Journal of Physics **20**, 123008 (2018).

[59]B. Monserrat, "Vibrational averages along thermal lines", Phys. Rev. B **93**, 014302 (2016).

[60]P. Hohenberg and W. Kohn, "Inhomogeneous electron gas", Phys. Rev. **136**, B864–B871 (1964).

[61]P. A. M. Dirac, "Note on exchange phenomena in the thomas atom", Mathematical Proceedings of the Cambridge Philosophical Society **26**, 376–385 (1930).

[62]D. M. Ceperley and B. J. Alder, "Ground state of the electron gas by a stochastic method", Phys. Rev. Lett. **45**, 566–569 (1980).

[63]J. P. Perdew and A. Zunger, "Self-interaction correction to density-functional approximations for many-electron systems", Phys. Rev. B **23**, 5048–5079 (1981).

[64]J. P. Perdew, K. Burke, and M. Ernzerhof, "Generalized gradient approximation made simple", Phys. Rev. Lett. **77**, 3865–3868 (1996).

[65]J. P. Perdew, K. Burke, and M. Ernzerhof, "Generalized gradient approximation made simple [phys. rev. lett. 77, 3865 (1996)]", Phys. Rev. Lett. **78**, 1396–1396 (1997).

[66]F. Bloch, "Über die quantenmechanik der elektronen in kristallgittern", Zeitschrift für Physik **52**, 555–600 (1929).

[67]R. Gross and A. Marx, *Festkörperphysik* (Oldenbourg Wissenschaftsverlag, 2012).

[68] L. J. Sham and M. Schlüter, "Density-functional theory of the energy gap", Physical review letters **51**, 1888 (1983).

[69] A. Görling, "Exchange-correlation potentials with proper discontinuities for physically meaningful kohn-sham eigenvalues and band structures", Physical Review B **91**, 245120 (2015).

[70] R. Godby, M. Schlüter, and L. Sham, "Accurate exchange-correlation potential for silicon and its discontinuity on addition of an electron", Physical review letters **56**, 2415 (1986).

[71] L. Sham and M. Schlüter, "Density-functional theory of the band gap", Physical Review B **32**, 3883 (1985).

[72] P. Borlido, J. Schmidt, A. W. Huran, F. Tran, M. A. L. Marques, and S. Botti, "Exchange-correlation functionals for band gaps of solids: benchmark, reparametrization and machine learning", npj Computational Materials **6**, 96 (2020).

[73] F. Tran and P. Blaha, "Accurate band gaps of semiconductors and insulators with a semilocal exchange-correlation potential", Phys. Rev. Lett. **102**, 226401 (2009).

[74] E. Wimmer, H. Krakauer, M. Weinert, and A. J. Freeman, "Full-potential self-consistent linearized-augmented-plane-wave method for calculating the electronic structure of molecules and surfaces: O_2 molecule", Phys. Rev. B **24**, 864–875 (1981).

[75] B. Wei, Q. Sun, C. Li, and J. Hong, "Phonon anharmonicity: a pertinent review of recent progress and perspective", Science China Physics, Mechanics & Astronomy **64**, 117001 (2021).

[76] O. Hellman and I. A. Abrikosov, "Temperature-dependent effective third-order interatomic force constants from first principles", Phys. Rev. B **88**, 144301 (2013).

[77] J. Klarbring, O. Hellman, I. A. Abrikosov, and S. I. Simak, "Anharmonicity and ultralow thermal conductivity in lead-free halide double perovskites", Phys. Rev. Lett. **125**, 045701 (2020).

[78] T. Sun, X. Shen, and P. B. Allen, "Phonon quasiparticles and anharmonic perturbation theory tested by molecular dynamics on a model system", Phys. Rev. B **82**, 224304 (2010).

[79] N. W. Ashcroft and N. D. Mermin, *Solid state physics* (Harcourt, 1976).

[80] R. Resta, "Macroscopic polarization in crystalline dielectrics: the geometric phase approach", Rev. Mod. Phys. **66**, 899–915 (1994).

[81] R. Resta and D. Vanderbilt, "Theory of polarization: a modern approach", in *Physics of ferroelectrics: a modern perspective* (Springer Berlin Heidelberg, Berlin, Heidelberg, 2007), pp. 31–68.

[82] S. Pancharatnam, "Generalized theory of interference, and its applications", Proceedings of the Indian Academy of Sciences - Section A **44**, 247–262 (1956).

[83]M. V. Berry, "Quantal phase factors accompanying adiabatic changes", Proceedings of the Royal Society of London. A. Mathematical and Physical Sciences **392**, 45–57 (1984).

[84]W. Cochran and R. Cowley, "Dielectric constants and lattice vibrations", Journal of Physics and Chemistry of Solids **23**, 447–450 (1962).

[85]S. Baroni and R. Resta, "Ab initio calculation of the macroscopic dielectric constant in silicon", Phys. Rev. B **33**, 7017–7021 (1986).

[86]M. Gajdo š, K. Hummer, G. Kresse, J. Furthmüller, and F. Bechstedt, "Linear optical properties in the projector-augmented wave methodology", Phys. Rev. B **73**, 045112 (2006).

[87]X. Gonze and C. Lee, "Dynamical matrices, born effective charges, dielectric permittivity tensors, and interatomic force constants from density-functional perturbation theory", Phys. Rev. B **55**, 10355–10368 (1997).

[88]B. B. Laud, *Electromagnetics* (Wiley Eastern, 1987).

[89]P. B. Allen and V. Heine, "Theory of the temperature dependence of electronic band structures", Journal of Physics C: Solid State Physics **9**, 2305 (1976).

[90]P. B. Allen and M. Cardona, "Theory of the temperature dependence of the direct gap of germanium", Phys. Rev. B **23**, 1495–1505 (1981).

[91]J. Rayleigh, *The theory of sound* (Dover, 1945).

[92]E. Schrödinger, "Quantisierung als eigenwertproblem", Annalen der Physik **385**, 437–490 (1926).

[93]G. Baym, "Field-theoretic approach to the properties of the solid state", Annals of Physics **14**, 1–42 (1961).

[94]H. Y. Fan, "Temperature dependence of the energy gap in semiconductors", Phys. Rev. **82**, 900–905 (1951).

[95]M. Cardona, "Renormalization of the optical response of semiconductors by electron–phonon interaction", physica status solidi (a) **188**, 1209–1232 (2001).

[96]A. Migdal, "Interaction between electrons and lattice vibrations in a normal metal", Sov. Phys. JETP **7**, 996–1001 (1958).

[97]S. Engelsberg and J. R. Schrieffer, "Coupled electron-phonon system", Phys. Rev. **131**, 993–1008 (1963).

[98]E. Antončík, "On the theory of temperature shift of the absorption curve in non-polar crystals", Cechoslovackij fiziceskij zurnal **5**, 449–461 (1955).

[99]J. P. Walter, R. R. L. Zucca, M. L. Cohen, and Y. R. Shen, "Temperature dependence of the wavelength-modulation spectra of gaas", Phys. Rev. Lett. **24**, 102–104 (1970).

[100]M. Cardona and M. L. W. Thewalt, "Isotope effects on the optical spectra of semiconductors", Rev. Mod. Phys. **77**, 1173–1224 (2005).

[101] G. D. Mahan, *Many-particle physics*, eng, 2. ed., Physics of solids and liquids (Plenum Pr., New York, 1990).

[102] H. Abu-Farsakh and A. Qteish, "Ionicity scale based on the centers of maximally localized wannier functions", Phys. Rev. B **75**, 085201 (2007).

[103] D. E. Usvyat, R. A. Evarestov, and V. P. Smirnov, "Wannier functions and chemical bonding in crystals with the perovskite-like structure: srtio3, batio3, pbti3, and lamno3", International Journal of Quantum Chemistry **100**, 352–359 (2004).

[104] F. Corsetti and A. A. Mostofi, "System-size convergence of point defect properties: the case of the silicon vacancy", Phys. Rev. B **84**, 035209 (2011).

[105] Y.-S. Lee, M. B. Nardelli, and N. Marzari, "Band structure and quantum conductance of nanostructures from maximally localized wannier functions: the case of functionalized carbon nanotubes", Phys. Rev. Lett. **95**, 076804 (2005).

[106] M. Boero, M. Parrinello, S. Hüffer, and H. Weiss, "First principles study of propene polymerization in ziegler−natta heterogeneous catalysis", Journal of the American Chemical Society **122**, 501–509 (2000).

[107] R. D. King-Smith and D. Vanderbilt, "Theory of polarization of crystalline solids", Phys. Rev. B **47**, 1651–1654 (1993).

[108] D. Vanderbilt and R. D. King-Smith, "Electric polarization as a bulk quantity and its relation to surface charge", Phys. Rev. B **48**, 4442–4455 (1993).

[109] I. Souza, N. Marzari, and D. Vanderbilt, "Maximally localized wannier functions for entangled energy bands", Phys. Rev. B **65**, 035109 (2001).

[110] N. Marzari and D. Vanderbilt, "Maximally localized generalized wannier functions for composite energy bands", Phys. Rev. B **56**, 12847–12865 (1997).

[111] C. Brouder, G. Panati, M. Calandra, C. Mourougane, and N. Marzari, "Exponential localization of wannier functions in insulators", Phys. Rev. Lett. **98**, 046402 (2007).

[112] G. Panati and A. Pisante, "Bloch bundles, marzari-vanderbilt functional and maximally localized wannier functions", Communications in Mathematical Physics **322**, 835–875 (2013).

[113] A. D. Becke, "Density-functional thermochemistry. iii. the role of exact exchange", The Journal of Chemical Physics **98**, 5648–5652 (1993).

[114] L. A. Agapito and M. Bernardi, "Ab initio electron-phonon interactions using atomic orbital wave functions", Phys. Rev. B **97**, 235146 (2018).

[115] E. Hewitt and R. E. Hewitt, "The gibbs-wilbraham phenomenon: an episode in fourier analysis", Archive for History of Exact Sciences **21**, 129–160 (1979).

[116] P. P. Ewald, "Die berechnung optischer und elektrostatischer gitterpotentiale", Annalen der Physik **369**, 253–287 (1921).

[117] A. Damle, L. Lin, and L. Ying, "Compressed representation of kohn–sham orbitals via selected columns of the density matrix", Journal of Chemical Theory and Computation **11**, 1463–1469 (2015).

[118] A. Damle, L. Lin, and L. Ying, "Scdm-k: localized orbitals for solids via selected columns of the density matrix", Journal of Computational Physics **334**, 1–15 (2017).

[119] A. Damle and L. Lin, "Disentanglement via entanglement: a unified method for wannier localization", Multiscale Modeling & Simulation **16**, 1392–1410 (2018).

[120] M. Benzi, P. Boito, and N. Razouk, "Decay properties of spectral projectors with applications to electronic structure", SIAM Rev. **55**, 3–64 (2013).

[121] G. H. Golub, "Numerical methods for solving linear least squares problems", Numerische Mathematik **7**, 206–216 (1965).

[122] P. Businger and G. H. Golub, "Linear least squares solutions by householder transformations", Numerische Mathematik **7**, 269–276 (1965).

[123] T. F. Chan, "Rank revealing qr factorizations", Linear Algebra and its Applications **88-89**, 67–82 (1987).

[124] H. Cheng, Z. Gimbutas, P. G. Martinsson, and V. Rokhlin, "On the compression of low rank matrices", SIAM Journal on Scientific Computing **26**, 1389–1404 (2005).

[125] T. Hom, W. Kiszenik, and B. Post, "Accurate lattice constants from multiple reflection measurements. II. Lattice constants of germanium silicon, and diamond", Journal of Applied Crystallography **8**, 457–458 (1975).

[126] S. Logothetidis, J. Petalas, H. M. Polatoglou, and D. Fuchs, "Origin and temperature dependence of the first direct gap of diamond", Phys. Rev. B **46**, 4483–4494 (1992).

[127] K. P. O'Donnell and X. Chen, "Temperature dependence of semiconductor band gaps", Applied Physics Letters **58**, 2924–2926 (1991).

[128] Y. Varshni, "Temperature dependence of the energy gap in semiconductors", Physica **34**, 149–154 (1967).

[129] M. Ettenberg and R. J. Paff, "Thermal expansion of alas", Journal of Applied Physics **41**, 3926–3927 (1970).

[130] D. Richman, "Vapor phase growth and properties of aluminum phosphide", Journal of The Electrochemical Society **115**, 945–947 (1968).

[131] G. Giesecke and H. Pfister, "Präzisionsbestimmung der Gitterkonstanten von $A^{III}B^{V}$-Verbindungen", Acta Crystallographica **11**, 369–371 (1958).

[132] K. Eichhorn, A. Kirfel, J. Grochowski, and P. Serda, "Accurate structure analysis with synchrotron radiation. An application to borazone, cubic BN", Acta Crystallographica Section B **47**, 843–848 (1991).

[133] P. Deus, U. Voland, and H. A. Schneider, "Thermal expansion of gap within 20 to 300 k", physica status solidi (a) **80**, K29–K32 (1983).

[134] C. R. Hubbard, H. E. Swanson, and F. A. Mauer, "A silicon powder diffraction standard reference material", Journal of Applied Crystallography **8**, 45–48 (1975).

[135] Z. Li and R. C. Bradt, "Thermal expansion of the cubic (3c) polytype of sic", Journal of Materials Science **21**, 4366–4368 (1986).

[136] G. Antonius, S. Poncé, E. Lantagne-Hurtubise, G. Auclair, X. Gonze, and M. Côté, "Dynamical and anharmonic effects on the electron-phonon coupling and the zero-point renormalization of the electronic structure", Phys. Rev. B **92**, 085137 (2015).

[137] J. H. Lloyd-Williams and B. Monserrat, "Lattice dynamics and electron-phonon coupling calculations using nondiagonal supercells", Phys. Rev. B **92**, 184301 (2015).

[138] S. Poncé, Y. Gillet, J. Laflamme Janssen, A. Marini, M. Verstraete, and X. Gonze, "Temperature dependence of the electronic structure of semiconductors and insulators", The Journal of Chemical Physics **143**, 102813 (2015).

[139] H. Kawai, K. Yamashita, E. Cannuccia, and A. Marini, "Electron-electron and electron-phonon correlation effects on the finite-temperature electronic and optical properties of zinc-blende gan", Phys. Rev. B **89**, 085202 (2014).

[140] R. Pässler, "Parameter sets due to fittings of the temperature dependencies of fundamental bandgaps in semiconductors", physica status solidi (b) **216**, 975–1007 (1999).

[141] K. Parlinski, Z. Q. Li, and Y. Kawazoe, "First-principles determination of the soft mode in cubic ZrO_2", Phys. Rev. Lett. **78**, 4063–4066 (1997).

[142] O. K. Andersen, "Linear methods in band theory", Phys. Rev. B **12**, 3060–3083 (1975).

[143] G. A. de Wijs, R. Laskowski, P. Blaha, R. W. A. Havenith, G. Kresse, and M. Marsman, "Nmr shieldings from density functional perturbation theory: gipaw versus all-electron calculations", The Journal of Chemical Physics **146**, 064115 (2017).

[144] X. Gonze, B. Amadon, G. Antonius, F. Arnardi, L. Baguet, J.-M. Beuken, J. Bieder, F. Bottin, J. Bouchet, E. Bousquet, N. Brouwer, F. Bruneval, G. Brunin, T. Cavignac, J.-B. Charraud, W. Chen, M. Côté, S. Cottenier, J. Denier, G. Geneste, P. Ghosez, M. Giantomassi, Y. Gillet, O. Gingras, D. R. Hamann, G. Hautier, X. He, N. Helbig, N. Holzwarth, Y. Jia, F. Jollet, W. Lafargue-Dit-Hauret, K. Lejaeghere, M. A. Marques, A. Martin, C. Martins, H. P. Miranda, F. Naccarato, K. Persson, G. Petretto, V. Planes, Y. Pouillon, S. Prokhorenko, F. Ricci, G.-M. Rignanese, A. H. Romero, M. M. Schmitt, M. Torrent, M. J. van Setten, B. Van Troeye, M. J. Verstraete, G. Zérah, and J. W. Zwanziger, "The abinitproject:

impact, environment and recent developments", Computer Physics Communications **248**, 107042 (2020).

[145] M. van Setten, M. Giantomassi, E. Bousquet, M. Verstraete, D. Hamann, X. Gonze, and G.-M. Rignanese, "The pseudodojo: training and grading a 85 element optimized norm-conserving pseudopotential table", Computer Physics Communications **226**, 39–54 (2018).

[146] K. Lejaeghere, G. Bihlmayer, T. Björkman, P. Blaha, S. Blügel, V. Blum, D. Caliste, I. E. Castelli, S. J. Clark, A. Dal Corso, S. de Gironcoli, T. Deutsch, J. K. Dewhurst, I. Di Marco, C. Draxl, M. Dułak, O. Eriksson, J. A. Flores-Livas, K. F. Garrity, L. Genovese, P. Giannozzi, M. Giantomassi, S. Goedecker, X. Gonze, O. Grånäs, E. K. U. Gross, A. Gulans, F. Gygi, D. R. Hamann, P. J. Hasnip, N. A. W. Holzwarth, D. Iuşan, D. B. Jochym, F. Jollet, D. Jones, G. Kresse, K. Koepernik, E. Küçükbenli, Y. O. Kvashnin, I. L. M. Locht, S. Lubeck, M. Marsman, N. Marzari, U. Nitzsche, L. Nordström, T. Ozaki, L. Paulatto, C. J. Pickard, W. Poelmans, M. I. J. Probert, K. Refson, M. Richter, G.-M. Rignanese, S. Saha, M. Scheffler, M. Schlipf, K. Schwarz, S. Sharma, F. Tavazza, P. Thunström, A. Tkatchenko, M. Torrent, D. Vanderbilt, M. J. van Setten, V. Van Speybroeck, J. M. Wills, J. R. Yates, G.-X. Zhang, and S. Cottenier, "Reproducibility in density functional theory calculations of solids", Science **351**, aad3000 (2016).

[147] A. H. Romero, D. C. Allan, B. Amadon, G. Antonius, T. Applencourt, L. Baguet, J. Bieder, F. Bottin, J. Bouchet, E. Bousquet, F. Bruneval, G. Brunin, D. Caliste, M. Côté, J. Denier, C. Dreyer, P. Ghosez, M. Giantomassi, Y. Gillet, O. Gingras, D. R. Hamann, G. Hautier, F. Jollet, G. Jomard, A. Martin, H. P. C. Miranda, F. Naccarato, G. Petretto, N. A. Pike, V. Planes, S. Prokhorenko, T. Rangel, F. Ricci, G.-M. Rignanese, M. Royo, M. Stengel, M. Torrent, M. J. van Setten, B. Van Troeye, M. J. Verstraete, J. Wiktor, J. W. Zwanziger, and X. Gonze, "ABINIT: Overview and focus on selected capabilities", The Journal of Chemical Physics **152**, 124102 (2020).